



HAL
open science

Micromilling mechanism : research and realization

Jinsheng Wang

► **To cite this version:**

Jinsheng Wang. Micromilling mechanism : research and realization. Other. Université Paul Verlaine - Metz, 2009. English. NNT : 2009METZ001S . tel-01752613

HAL Id: tel-01752613

<https://hal.univ-lorraine.fr/tel-01752613>

Submitted on 29 Mar 2018

HAL is a multi-disciplinary open access archive for the deposit and dissemination of scientific research documents, whether they are published or not. The documents may come from teaching and research institutions in France or abroad, or from public or private research centers.

L'archive ouverte pluridisciplinaire **HAL**, est destinée au dépôt et à la diffusion de documents scientifiques de niveau recherche, publiés ou non, émanant des établissements d'enseignement et de recherche français ou étrangers, des laboratoires publics ou privés.



AVERTISSEMENT

Ce document est le fruit d'un long travail approuvé par le jury de soutenance et mis à disposition de l'ensemble de la communauté universitaire élargie.

Il est soumis à la propriété intellectuelle de l'auteur. Ceci implique une obligation de citation et de référencement lors de l'utilisation de ce document.

D'autre part, toute contrefaçon, plagiat, reproduction illicite encourt une poursuite pénale.

Contact : ddoc-theses-contact@univ-lorraine.fr

LIENS

Code de la Propriété Intellectuelle. articles L 122. 4

Code de la Propriété Intellectuelle. articles L 335.2- L 335.10

http://www.cfcopies.com/V2/leg/leg_droi.php

<http://www.culture.gouv.fr/culture/infos-pratiques/droits/protection.htm>



UNIVERSITE DE METZ



NORTHEASTERN UNIVERSITY



ECOLE DOCTORALE EMMA

Énergie, Mécanique, Matériaux

DOCTORAL DISSERTATION

SUBMITTED TO

UNIVERSITY OF METZ

FOR THE DEGREE OF DOCTOR OF PHILOSOPHY

OF UNIVERSITY OF METZ

MAJOR : MECHANICAL ENGINEERING

BY

Jinsheng WANG

MICROMILLING MECHANISM RESEARCH AND REALIZATION

DEFENSE ON 13 January 2009 TO THE JURY COMPOSED BY :

P. PICART Reporter
Y. YAO Reporter
J. ANTOINE Examiner
M. WANG Examiner, President
G. ABBA Thesis supervisor
Y. GONG Thesis supervisor

THIS WORK WAS DONE WITH THE SUPPORT OF FRENCH CHINESE DOCTORAL COLLEGE

Laboratoire de Génie Industriel et
de Production Mécanique (LGIPM),
Université de METZ,
Île du Sauley, F-57045 METZ Cedex 1

Laboratory of Advanced Manufacturing
and Automation (LAMA),
Northeastern University,
Shenyang, Liaoning, 110004, China

To my parents, Yangao Wang and Liying Sun.

Acknowledgements

I would like to express my gratitude towards my supervisor and co-supervisors, professor Gabriel ABBA from LGIPM, UPV in France and professor Yadong GONG from LAMA, NEU in China. This dissertation would not have been possible without their guidance, financial support and encouragement. I appreciate their insightful comments at every stage of this work, their assistance in writing, their patience, understanding and great help not only on my research, but also on many important aspects in my life.

I am also deeply grateful to my previous doctor supervisor, professor Guangqi CAI from LAMA, NEU in China, for his illuminative guidance to this interesting research field. But due to the accident of his physical condition, I can't accept his kindly supervision furthermore. I hope he can recover soon.

I gratefully acknowledge the financial support from LGIPM, UPV in France and LAMA, NEU in China. The major grants of this research are Chinese 985-II foundation, Northeastern University PhD foundation (200705), French Research Ministry foundation, and Lorraine Region Council research foundation.

I would like to thank professor László TÓTH and Mr. Arman HASANI at Laboratoire de Physique et Mécanique des Matériaux (LPMM) of UPV for their support on the OFHC copper preparation, and Professor Weiping TONG at Laboratory of Electromagnetic Processing of Materials (EPM) of NEU for his processing on ultra fine grain steel, and Dr. Kangying ZHU for her help on providing martensite material.

My appreciation also goes to the support staff in LGIPM of UPV, ENSAM and ENIM, especially to Dr. Jean-francois Antoine for his kindly discussions and endless help on this research, to Drs. Alain D'ACUNTO, Christophe LESCALIER, Francois LEONARD, and Patrick ZATTARIN for their sincerely help on my work and life, to Mrs. Nora DEHAS, Véronique ERNEST for their daily care and support. The same acknowledgement gives to the staff in LAMA

of NEU, especially to professor Jiashun SHI for his long time cooperation and guidance on this research, to professors Yongxian LIU, Suoxian YUAN, Ming HU, Ping ZOU, Lei ZHANG and Drs. Wenyuan TIAN and Yaoman ZHANG for their focuses on this work, to technicians Mr. Wei WANG and Mr. Jianwei MIAO for their assistants on the experiments. Meanwhile, my best wishes are given to Madam SIN for her kindly helps on my life.

I also want to thank all my former and current colleagues in the research group for their technical assistance, perspectives and friendship, especially to Kui CHEN, Jianfeng CAO, Jintai MI, Jia LIN, Yancheng ZHANG, Jun CHENG, Jian QIU and Dajian ZHAO. In addition, I would like to thank my best friends at NEU, UPV, ENSAM and ENIM over the years, notably Xuefeng BI, Rity LY, Somasundar KANNAN, Sandra ZIMMER, Cyril NICOLAS and Marius MIHALUTA.

I am truly grateful to my family, especially my parents Mr. Yangao WANG and Mrs. Liying SUN for their unconditioned love, endless encouragement, patience, and support during this work and throughout my life.

Abstract

The miniaturization of machine components plays a very important role in the future technological development of a broad spectrum of products owing to various advantages: low material cost, portability, implant, lower power consumption and higher heat transfer since their surface-to-volume ratio is very high. In particular, one of the manufacturing processes for miniature parts is micromilling. Micromilling is flexible to process a variety of metallic alloys, composites, polymers and ceramic materials to form functional devices. It is suitable for accommodating individual components rather than large batch sizes, and has the ability to monitor the in-process quality of components so that problems can be corrected during fabrication. It is capable of fabricating 3D freeform surfaces, which is especially important for the production of micro-injection molds. Furthermore, it does not require very expensive setups as lithographic and masks.

This dissertation focuses on several aspects of micromilling operation in order to improve its performances and efficiency. The literature survey of the current efforts in micro-mechanical machining investigated various aspects such as research directions, limitations, similarities and differences between macro and micro in order to understand the fundamental knowledge of micro mechanical machining.

A Micro Machine Tool (MMT) test-bed was developed for the micromilling experimental study based on an expert system. The MMT test-bed is driven by ultra precision linear motors with high resolution linear encoders as feedback. A high speed electro-spindle, a CCD stereo microscope and a precision dynamometer are equipped. An open numerical control system and Human-Machine Interface (HMI) with G code compatibility are developed. The evaluation test results, including positional accuracy test and machining performance test, show its excellent performances.

In the micro mechanical machining, the workpiece microstructure effects must be considered. In this research, the multi-phase and single-phase polycrystalline materials are chosen as the micromilling workpieces. Through the modeling and experimental study, their effects to the cutting force, surface generation, surface roughness, and chip formation issues are discussed in detail.

An exact micromill flute trajectories model is developed including the effects of tool radial error motion and rotor vibration. New method is proposed to measure and calculate the tool tip radial error motion and vibration cost-effectively. The flute trajectories are simulated under different parameters setting. The parameter effects are discussed. Based on the trajectories analysis, their effects to chip thickness, cutting force, slot width (machining error), surface quality and tool breakage are investigated. The experimental results validate the model predictions well.

The wavy type chip has been found by the FEM simulation and micromilling experiments. The chip formation mechanism is studied quantitatively by means of hybrid analytical-FEM approach. The “Tool Rake Moment” M_{Tool} and “Shear Band Moment” M_{Work} are calculated, it is proved that the main reasons of wavy chip generation are the variations of the tool chip contact length l_T and shear band length l_S . The Merchant model (MM model) and Arcona-Dow model (AD model) are adopted respectively to calculate the M_{Work} as a comparison. The AD model shows a good performance in the microcutting scale. The chip velocity analysis reflects the chip acquires additional angular acceleration when the segment generation. The chip angular acceleration is calculated via two approaches, FEM and chip moments calculation, respectively. The agreement of these two approaches validates the chip moments calculation.

A back propagation Neural Network (NN) model is developed to predict the effects of spindle speed (n), feedrate (f) and axial depth of cut (a_P) on average surface roughness value (R_a) in the micromilling process. The Taguchi’s approach is utilized for the design of experiment (DoE) to acquire enough training information with minimal experiment number to train the NN model. Finally, the NN model gives a good prediction of the surface roughness value, and the single factor and two-factor interaction effects to R_a are discussed.

Finally, conclusions are drawn and some recommendations for future work are provided.

Contents

1	Introduction	1
1.1	Motivations	2
1.2	Research objectives	4
1.2.1	Literature review on the micro-mechanical machining . .	5
1.2.2	Development of the micro machine tool	6
1.2.3	Workpiece microstructure influences	6
1.2.4	Micromill tip trajectory investigation	6
1.2.5	Wavy chip formation analysis	7
1.2.6	Surface roughness prediction based on the Neural Network	8
1.3	Methodologies	8
2	Literature Review	11
2.1	Micro-cutting equipments development	17
2.1.1	Tungsten carbide micro-tools	17
2.1.2	Precision machine tools	19
2.1.3	Micro machine tool/micro factories	20
2.2	Micro-cutting mechanism characteristics	23
2.2.1	Chip formation and minimum chip thickness	23
2.2.2	Cutting forces in micro-machining	26
2.2.3	Effect of workpiece material (grain size)	28
2.2.4	Tool wear and burrs	29
2.3	Micro-cutting auxiliary processes	31
2.3.1	Testing and modeling	31
2.3.2	Handling and assembly	32
2.4	Micro-machining from macro-machining knowledge	33
2.4.1	Cutting forces	33

2.4.2	Feed rate estimation	35
2.4.3	Instability (Chatter)	36
2.4.4	Run-out/unbalance	37
2.4.5	Sensing methods	38
2.4.6	Process optimization and monitoring	39
2.5	Conclusions	40
3	Micro Machine Tool (MMT) Development	41
3.1	Introduction	41
3.2	Key technologies of MMT	42
3.2.1	Feeding system	42
3.2.2	Spindle system	44
3.2.3	Sensing system	44
3.2.4	Control system	45
3.2.5	Monitor system	45
3.3	Structural configurations and selections reduction	46
3.4	Prototype development	52
3.4.1	Feeding system	53
3.4.2	Spindle system	54
3.4.3	Control system.	54
3.4.4	Human machine interface (HMI)	55
3.4.5	Microscope monitoring system	56
3.4.6	Dynamometer	58
3.4.7	Other components	59
3.5	MMT prototype test	60
3.5.1	Positional accuracy test	61
3.5.2	Micromilling experimental tests	62
3.6	Conclusions	63
4	Workpiece Microstructure Effects in Micromilling	67
4.1	Introduction	67
4.2	Modeling of micromilling multi-phase polycrystalline material	68
4.2.1	Conventional cutting model	68
4.2.2	Micro Cutting features	69
4.2.3	Calculations of h_m and h_r	71

4.2.4	Micromilling Model	72
4.3	Experiments of micromilling multi-phase polycrystalline material	74
4.3.1	Experimental setup	74
4.3.2	Experimental results	75
4.4	Micromilling single-phase polycrystalline material research	79
4.4.1	Workpiece material	79
4.4.2	Experimental design	81
4.4.3	Experimental surface roughness result and discussion . . .	83
4.5	Conclusions	84
5	Micromill Tip Trajectories Investigation	87
5.1	Introduction	87
5.2	Model development	89
5.3	Measuring method	90
5.3.1	Measurement setup	91
5.3.2	Tool tip radial error motion	92
5.3.3	Tool unbalance	93
5.4	Vibration analysis	96
5.4.1	Rotor dynamic model	96
5.4.2	Natural frequency and tool tip vibration	96
5.5	Validation of measurement and calculation	98
5.5.1	Validation test setup	98
5.5.2	Static test results	99
5.5.3	Dynamic test results	99
5.6	Trajectories investigation	100
5.6.1	Trajectories without feeding	101
5.6.2	Trajectories With Feeding	106
5.6.3	Parameters Analysis	107
5.7	Experimental Study	110
5.7.1	Experimental design	110
5.7.2	Cutting forces and chip thickness	111
5.7.3	Slot width and surface quality	112
5.7.4	Tool breakage	114
5.8	Conclusions	114

6	Wavy Chip Formation Analysis	117
6.1	Introduction	117
6.2	FEM Model	119
6.2.1	Material constitutive model	120
6.2.2	Friction model	121
6.2.3	Simulation setup	121
6.3	Simulation results and experimental validations	123
6.3.1	Simulation results	123
6.3.2	Experimental results	124
6.4	Chip formation process	125
6.4.1	Chip formation process	126
6.5	Tool edge radius effect	131
6.6	Chip moments calculations	132
6.6.1	Modeling of the chip formation	132
6.6.2	M_{Tool} calculation	133
6.6.3	M_{Work} calculation	135
6.7	Chip moments calculation results	139
6.8	Chip velocity analysis	143
6.9	Chip angular acceleration analysis	143
6.10	Conclusions	147
7	Surface Roughness Prediction Based on Neural Network	151
7.1	Introduction	151
7.2	Experimental works	153
7.2.1	Experimental Conditions	153
7.2.2	Design of Experiments	153
7.3	Neural Network Model	155
7.3.1	Neural Network Structure	155
7.3.2	Neural Network Performances	157
7.4	Results and Discussions	159
7.4.1	Single Factor Influence	159
7.4.2	Interaction Effect	160
7.5	Conclusion	162

8	Conclusions and Perspectives	164
8.1	Conclusions	164
8.2	Perspectives for future work	166

List of Figures

1.1	Functionality and applications for the miniaturized components .	2
1.2	Dimensional size of micro mechanical machining	3
1.3	Thesis motivation	4
1.4	Thesis objectives	5
1.5	Research methodology	9
2.1	Cutting tool materials	18
2.2	Tungsten carbide micro-end mill with two flutes	18
2.3	SEM figure of micro-cutting tools	19
2.4	Commercial ultra precision machine tools	21
2.5	Micro-machines	22
2.6	Effect of the minimum chip thickness	24
2.7	Chip thickness and force relationship for Pearlite [1]	25
2.8	Tool vibration and frequency spectra for machining Pearlite . . .	27
2.9	Micro-cutting forces in feed direction	34
2.10	Flank wear of edge radiused macro-tool	35
2.11	Chip Generations due to vibration	36
3.1	Directed edge and force flows inside machine tool	46
3.2	Machine tool hierarchy with graph theory	47
3.3	Sample set of structural components with kinematic functionalities	48
3.4	Connectivity of tool to ground structural chain	48
3.5	Connectivity of part to ground structural chain	50
3.6	Reduction of configurations with functional requirements	50
3.7	Reduced set of MMT configurations	51
3.8	Reduction of configuration set with expert design rules	52
3.9	Three-axis MMT system	53

3.10	MX80L micro feeding unit	54
3.11	MX80L structure	54
3.12	Z axis	55
3.13	MMT control system	56
3.14	Multi-closed-loop control scheme	56
3.15	MNCS structure	57
3.16	HMI of MMT prototype	58
3.17	CCD microscope scheme	59
3.18	Calibration comparison between cutting force sensors [2]	59
3.19	The entire dynamometer system	60
3.20	Positional accuracy test data for Z axis	61
3.21	The micro slab surface figures from optical profiler	63
3.22	Micro column	64
3.23	Micro thin wall array	65
3.24	Micro hexagonal spark	65
4.1	Conventional Orthogonal Cutting	68
4.2	Orthogonal micro cutting	70
4.3	Micro cutting zone	70
4.4	Material compression strain-stress curve	72
4.5	Micromilling process	73
4.6	Micromill with cutting edge	74
4.7	Microstructure of Al6061-T6	75
4.8	Tangential cutting force	76
4.9	Micromilled bottom surface	78
4.10	Chips in micromilling	79
4.11	ECAP principle [3]	80
4.12	Grain shape and size evolution during ECAP	81
4.13	OFHC copper with different grain size	82
4.14	R_a experimental results	84
5.1	Geometric comparison between (a) macro mill and (b) micromill	88
5.2	Tool tip dimensions comparison	90
5.3	Trajectory model hierarchical structure	91
5.4	Measurement setup	91

5.5	Measuring points distribution	92
5.6	Tool shank radial error motion measurement	93
5.7	Tool tip radial error motion	94
5.8	Tool unbalance calculation principle	95
5.9	Tool unbalance calculation results	95
5.10	Cutter/spindle system model	96
5.11	Tool tip vibration bode diagram	97
5.12	Laser test scheme	99
5.13	Laser test setup	100
5.14	Laser point location under microscope	101
5.15	Static test results comparison	102
5.16	Dynamic laser test	103
5.17	Frames and vectors in the tool tip plane	104
5.18	Tool tip trajectories simulation without feeding	105
5.19	Tool tip trajectories simulation with feeding	106
5.20	Slot width varying with θ and ϕ	108
5.21	Flute angle θ influence to the slot width	109
5.22	Feed angle ϕ influence to the slot width	110
5.23	Chip thickness and cutting force	112
5.24	Frequency analysis of the experiment cutting forces	113
5.25	Slot width comparison between experiment and model	113
5.26	Bottom surface and tool tip	114
5.27	Tool breakage fracture in the first series experiments	115
6.1	FEM model	122
6.2	The wavy type chip formation in micromilling simulation	124
6.3	The top burr on the down milling side of the micromilled slot	125
6.4	The section view of the wavy chip	125
6.5	The first segment formation process	127
6.6	The second segment formation process	128
6.7	The third segment formation process	130
6.8	The fourth segment formation process	130
6.9	The entire chip formation process	131
6.10	Indentation FEM model	132
6.11	The displacement contour of the indentation process	133

6.12	Chip cantilever modeling	134
6.13	M_{Tool} and tool rake normal pressure	134
6.14	M_{Work} and shear plane normal stress	135
6.15	Micromilling force in one cut-edge	138
6.16	M_{Tool} Vs $M_{Work-MM}$ and M_{Tool} Vs $M_{Work-AD}$	139
6.17	M_{Tool} , $M_{Work-AD}$ and $M_{Tool} - M_{Work-AD}$ variations	140
6.18	σ_{tn_equ} and σ_{wn_aver} variations	141
6.19	Variation of l_T and l_S	141
6.20	Chip velocity before 1st segment	144
6.21	Chip velocity after 1st segment	144
6.22	Chip velocity before 2nd segment	145
6.23	Chip velocity after 2nd segment	145
6.24	Chip moment inertia	147
6.25	Chip angular acceleration	148
7.1	Slot bottom surface measurement example	153
7.2	Neural network structure	155
7.3	Training error epoches	157
7.4	R_a comparison between prediction and experiment	158
7.5	Experimental slots	158
7.6	Main effect of R_a	159
7.7	Interaction Effects of spindle speed and feedrate on R_a	161
7.8	Interaction Effects of spindle speed and axial depth on R_a	162
7.9	Interaction Effects of feedrate and axial depth on R_a	162

List of Tables

2.1	Survey of micro-mechanical machining research	13
3.1	Declared connectivity between sample structural components . .	49
3.2	Linear motor specifications	55
3.3	Dynamometer comparison	60
3.4	The positional accuracy of the MMT prototype	62
4.1	Al6061-T6 material characteristics and calculated results	75
4.2	Experimental setup	83
4.3	Experimental design and R_a results	83
5.1	Tool geometry	92
5.2	LK-G10 specification	98
5.3	Feed Angle Influences to Micromilling, When $\theta = \pm 90^\circ$	109
5.4	Experimental plan for the tool tip trajectories model	111
6.1	Al6061-T6 material constants in JC model	120
6.2	Simulation and experimental parameters	123
7.1	Experimental R_a results for NN training	154
7.2	Experimental validation of NN R_a Prediction	159

Chapter 1

Introduction

Highly accurate miniaturized components are increasingly in demand for various industries such as aerospace, biomedical, electronics, environmental, communications, and automotive (See Fig.1.1). This miniaturization will provide micro-systems that promise to enhance health care, quality of life and economic growth in such applications as micro-channels for lab-on-chips, shape memory alloy stents, fluidic graphite channels for fuel cell applications, subminiature actuators and sensors, and medical devices [4–8]. In fact, the possibilities of the miniaturization are expanding into more complex systems owing to shifting from 2D components to 3D microstructures and from silicon to other materials, such as glass, polymers and metallic alloys. There are several benefits of miniaturization such as a good heat transfer rate due to high surface area to volume ratios, the possibility for non-invasive medical applications (i.e. hearing aid), increasing throughput and sensitivity for micro fluidic channels, reduction in space, material, and energy requirements and portability enable point of care testing [9]. The micro products can be fabricated with more expensive materials with better properties since they require a small amount of materials. They are also easy to transport and store due to the small size of the products.

Micro-component fabrication requires reliable and repeatable methods, with accurate analysis tools. Many common methods of manufacturing miniature components have been based on semi-conductor processing techniques, where silicon materials are photo-etched through chemical or dry processes, usually in large batch production. Numerous researchers have investigated the feasibility of using other fabrication processes, such as LIGA (a photo-lithography method using a synchrotron), laser, ultrasonic, ion beam, micro forming, and micro-

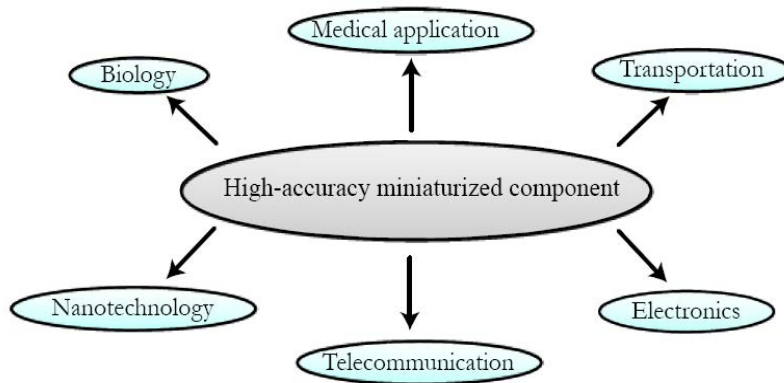


Figure 1.1: Functionality and applications for the miniaturized components

electro discharge machining method, to manufacture commercially viable micro-components [6, 10–13]. However, the majority of these methods are slow, and limited to a few silicon-based materials and essentially planar geometries. The broad commercialization of micro-systems is inhibited by low productivity and by the inability to manufacture in small batch sizes cost effectively.

Micro-mechanical machining is another fabrication method for creating miniature devices and components with features that range from tens of micrometers to a few millimeters in size (Fig.1.2). Recently, there has been strong interest in fabricating micro-meso-scale components through mechanical cutting processes [1]. Even though the mechanical micro-machining process may not be capable of obtaining the smallest feature sizes as with lithographic processes, mechanical cutting processes are very important in bridging the macro domain and the nano- and microdomains for making functional components. This is especially true for complex microstructures requiring a variety of materials, interfaces and functional shapes to form micro-systems that function with the macro-domain.

1.1 Motivations

The knowledge of the macro-mechanical machining has been well researched and established during last several decades. For micro-mechanical machining, there is a lack of knowledge developed. The translation of the wealth of knowledge developed for macro machining operations to micro-processes is

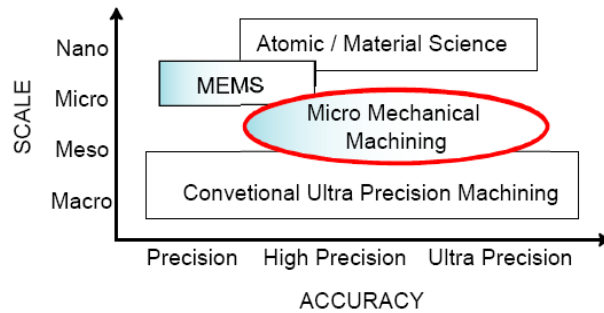


Figure 1.2: Dimensional size of micro mechanical machining

critical, both for the efficient development of practical micro-processes and for the understanding of the limitations of its application. Mechanically removing material using carbide tools can produce countless desired feature shapes and sizes. The micro-cutting process is challenging; however, the experiences learned from macro-processes provide a valuable resource for future micro-machining research. Therefore, it is necessary to research both macro and micro knowledge in machining processes.

Micro-mechanical-machining techniques bring many advantages to the fabrication of micro-sized features. One of the advantages of micro-mechanical machining is flexibility [7]. In contrast to conventional machining, micro-mechanical machining can be easily modified to fulfill the production and operation requirements (i.e. Reconfigurable Manufacturing Systems). Further, they do not require very expensive setups of lithographic methods. They can produce micro-components cost effectively because there is no need for expensive masks. The process is suitable for accommodating individual components rather than large batch sizes, and has the ability to monitor the in-process quality of components so that problems can be corrected during fabrication. It is capable of fabricating 3D freeform surfaces, which is especially important for the production of micro-injection molds. Moreover, it can process a variety of metallic alloys, composites, polymers and ceramic materials to form functional devices. Therefore, it is necessary to investigate the micromechanical machining in depth, see Fig.1.3.

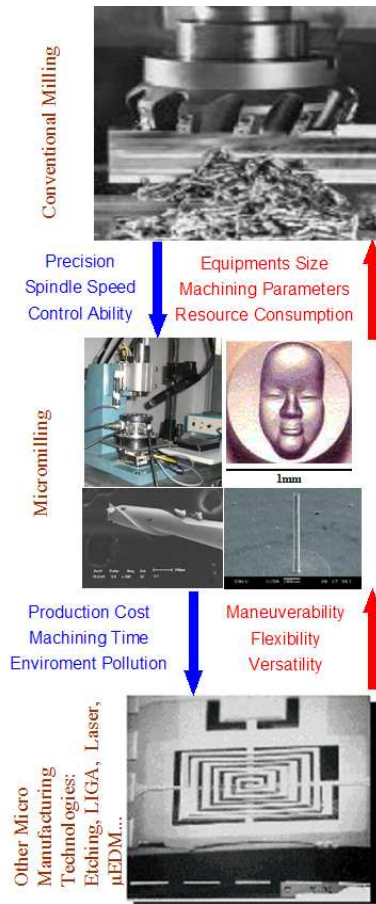


Figure 1.3: Thesis motivation

1.2 Research objectives

The objectives of this research are to translate some knowledge of the macro domain into micro machining processes for the efficient fabrication of miniaturized products (Fig.1.4). There are a number of issues that influence micro-mechanical machining processes: cutting forces, dynamics and stability, chip formation, and machine tools. Several subjects (literature review of the state-of-art micro milling operations, development of the micro machine tool, workpiece microstructure influences, micromill tip trajectory investigation, wavy chip formation analysis in micromilling operation via FEM-analytical approach, surface roughness prediction based on the neural network and design of experiment) are focused in this thesis in order to accelerate the micro-mechanical machining technology in both quality and productivity at the Laboratory of Advanced Manu-

facturing and Automation (LAMA), Northeastern University (NEU) in China, and Laboratoire de Génie Industriel et de Production Mécanique (LGIPM), Université Paul Verlaine (UPV) de Metz in France.

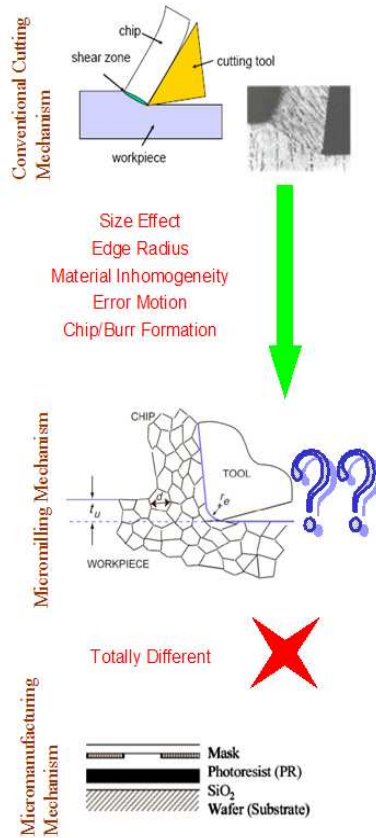


Figure 1.4: Thesis objectives

1.2.1 Literature review on the micro-mechanical machining

Understanding the fundamentals of micro-mechanical machining is essential to fabricate miniaturized products efficiently. It is very important to know the current limitations and research directions of the micro-mechanical machining operations. The focus will be on micro-milling because this machining process is the most flexible for creating 3D surfaces from a variety of engineering materials, such as steel, ceramics, bio-materials. Traditionally, ultra-precision machining uses diamond tool-cutting operations, but because of the high demand for machining ferrous materials, a micro-milling operation using carbide

tools is considered better suited to achieve these ends. In addition, the state of the art of the micro-milling operation will be examined for its transfer of knowledge from the macro-cutting domain to the micro-domain.

1.2.2 Development of the micro machine tool

In order to achieve the micromilling experimental operation, a Micro Machine Tool (MMT) test bed was developed. Meanwhile, the key technologies of MMT are discussed in detail. The test bed is driven by ultra precision linear motors with high resolution linear encoders as feedback. It is equipped with a high speed electro-spindle and a CCD stereo microscope as a monitoring device. The entire machine is controlled by an open numerical control system based on motion controller. The Human-Machine Interface (HMI) software is developed with G code compatibility. Then the evaluation tests, including positional accuracy test and machining performance test, have been done on the MMT, and the results are very satisfactory and show its excellent performances.

1.2.3 Workpiece microstructure influences

In the macro scale, the workpiece is regarded as isotropic, but in the micro scale manufacturing process, it could be considered as inhomogeneous due its microstructure effects. In this research, the multi-phase and single-phase polycrystalline materials are chosen as the micromilling workpiece. Through the modeling and experimental study, the cutting force, surface generation, roughness, and chip formation issues are discussed in detail.

1.2.4 Micromill tip trajectory investigation

In the micromilling operation, due to the special geometric features of the micromill, its tip trajectories under high speed rotation are obviously different from the common sense. In this work, a model considering tool radial error motion and rotor vibration is developed to analyze the tool tip trajectories and their effects. Based on the tool shank measurement results, new methods are proposed to calculate the tool tip radial error motion and tool unbalance as the inputs of the trajectories model. Then the model predicts the trajectories of the tool center and each flute exactly. And their effects to chip thickness, cutting force, slot width (machining error), surface quality and tool breakage

are analyzed too. The experimental results agree well with the model predictions. This analysis shows the single flute cutting condition always occur in the micromilling process. Two parameters, flute angle and feed angle, are important to the machining error and tool wear issues. This model is useful to do error compensation and machining variables optimization in the micromilling operation.

1.2.5 Wavy chip formation analysis

In mechanical micromachining, understanding the chip formation mechanics is critical to optimize the machining parameters, in order to minimize the burrs on the workpieces and improve their performances. An entire slot micromilling process on Al6061-T6 by one flute carbide cutter is simulated by means of FEM, and under this machining parameters set, the chip is found to be wavy type composed by many segments. The simulation is validated by experimental observation of the burr and chip morphology and the cutting force. Through the detailed analysis on the simulation results, the wavy chip formation process is described from the viewpoint of chip velocity, together with the variations of the tool chip contact length (l_T) and the shear band length (l_S). Then the chip formation mechanism is studied quantitatively by means of hybrid analytical-FEM approach. After calculating and analyzing the chip moments, including the “Tool Rake Moment” M_{Tool} and “Shear Band Moment” M_{Work} , it is proved that the main reasons of wavy chip generation are the variations of the l_T and l_S . The Merchant model (MM model) and Arcona-Dow model (AD model) are adopted respectively to calculate the M_{Work} as a comparison. The AD model shows a good performance in the microcutting scale. In the wavy segment generation occasion, the average chip velocity magnitude in chip bending process is much greater than the one before chip bending which is about the cutting speed. The chip root velocity is almost constant in the entire micromilling process, and the chip tip velocity increases too much in the chip bending instant due to the chip angular acceleration. The chip angular acceleration is acquired respectively from FEM and analytical model based on the M_{Tool} and M_{Work_AD} calculations. The excellent agreement of these two approaches validates the correctness of the chip moments calculations.

1.2.6 Surface roughness prediction based on the Neural Network

This study is to analyze the effects of spindle speed (n), feedrate (f) and axial depth of cut (a_P) on average surface roughness parameters (R_a) in the micromilling operation. Compared with the conventional milling operation, the non-linearity of micromilling is more obviously because of the minimum chip thickness, tool radial error motion and workpiece inhomogeneous inherent. In this work, the experimental design adopts the Taguchi's approach to acquire enough training information with minimal experiment number. Based on the experimental results, a neural network model is developed, trained and used to predict the bottom surface roughness in the micromilling operation. Finally, the effects of the single machining parameter and their interactions are analyzed in detail.

1.3 Methodologies

In this thesis, in order to understand the micromilling mechanism topics, such as cutting force, surface generation, metal phase effects, grain size effects, edge radius effects and tool error motion influences, The corresponding mechanism models are built. The models are validated by simulation and experimental approaches. The model-based simulation and Finite Element Method (FEM) are used in this research. The experimental works contain the machine tool development, tool choice, workpiece preparation, sensor calibration, design of experiment and experimental conclusions. Finally, the goal of this thesis is to apply the micromilling technique into diverse fields as MEMS, micro die and mold, biomedical, defense and other applications. The thesis methodologies are shown in Fig.1.5.

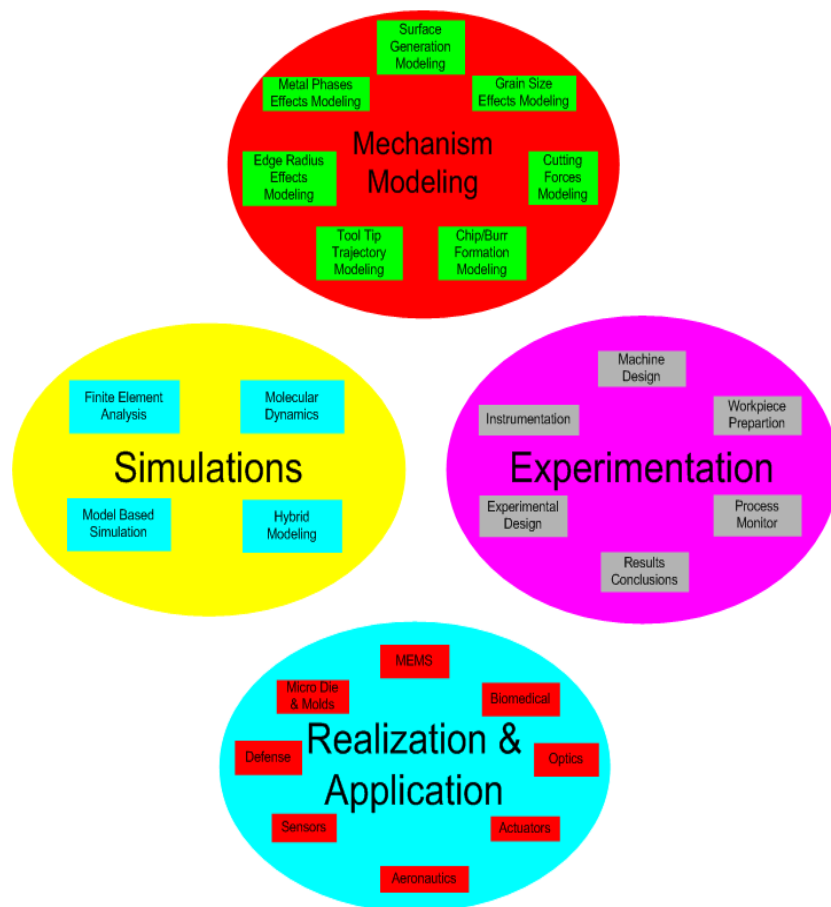


Figure 1.5: Research methodology

Chapter 2

Literature Review

In this chapter, the state of the art in micro-mechanical machining is reviewed. Its focus will be on micro-milling because this machining process is the most flexible [7] for creating 3D surfaces from a variety of engineering materials. Traditionally, ultra-precision machining uses diamond tool-cutting operations, but because of the high demand for machining ferrous materials [13], a micro-milling operation using carbide tools is considered better suited to achieve these ends. In addition, the state of the art will be examined for its transfer of knowledge from the macro-cutting domain to the micro-domain. In particular, research and its applications will be examined for, where macro-cutting knowledge has both succeeded and failed when applied to micro-cutting. Finally, suggestions will be made about macro-cutting knowledge that needs further research to be applied to micro-cutting and is anticipated to improve the quality of micro-mechanical processing.

The micro-cutting of steel has recently received strong research interest with the advent of miniaturized systems using a variety of materials, especially for biomedical applications. Several research laboratories and universities [9,14–20] have active research programs in micromachining. According to Sandia [14], the need to fill the gap between nano/micro- and macro-domains is becoming an increasingly important research topic.

Several survey papers on micro-machining have addressed the importance of micro-fabrication techniques. Hesselbach et al. [21] examined the international state of the art in micro-production technology from the perspective of how German industry fits within its limitations and economic potential. While outlining different fabrication processes, they draw the conclusion that in the

micro-cutting area, there is the need to fabricate steel micro-molds for injection molding or embossing processes. The paper also briefly summarizes micro-assembly and metrology.

Masuzawa [13] examined non-photo etching technologies for micro-machining, and classified the basic machining phenomena of the processes required to fabricate microstructures as: force, vaporization, ablation, dissolution, deformation, solidification, lamination, and re-composition. He examined their advantages and disadvantages, and listed publications that address the production of different feature types. He concluded that the size of micro-features currently being requested is $100\mu m$, with micro-machining technology in the research stage being able to create $5\mu m$ features. In the near future, requested feature sizes are expected to be reduced to $50\mu m$, with a research capability of $2\mu m$ features.

Alting et al. [12] broadly examined the field of microengineering, from the design and development stages to modeling and fabrication, with a focus on how microproducts and their production systems can be designed. In their discussion of micro-mechanical cutting processes, the authors found major challenges to be that high cutting forces limit the accuracy and size due to the deflection of tools and work pieces, and that tool wear on the edge radius also influences cutting forces. The paper also described microfabrication systems, such as the micro-factory [17] and concluded that many benefits will come from applying a systematic approach to micro-engineering, with the achievement of complete process integration a fundamental issue.

Liu et al. [1] presented a survey of the mechanics of micro-machining processes, focused on chip formation as influenced by minimum chip thickness, elastic-plastic deformation, and the non-homogeneity in micro-work pieces. This paper suggested that research is necessary in the modeling of the micro-machining process that will address thermal effects, dynamics, improved methods for estimating minimum chip thickness, and the nano-micro-meso continuum.

Chae et al. [22] reviewed the microcutting in various aspects, from the equipments to the mechanisms. They found the miniature tungsten carbide tools are widely used in the micro mechanical machining. The micro machine tools and precision machine tools are primary test beds of microcutting. The important mechanism researches include the cutting forces, feed rate estimation, instability, run-out effect. They recommended the future research directs will be concentrated on the micro tools and machines developments, micro-cutting

mechanism deeper research, real-time monitoring, and workpiece quality testing.

Dornfeld et al. [23] reviewed some of the main drivers, developments and future requirements in the field of micromanufacturing as related to the machining process from the perspective of the recent research and development literature. For the purposes of this paper micromachining includes creation of precise two and three dimensional workpieces with dimensions in the range of a few tens of nanometers to some few millimeters by cutting using defined geometry cutting tools. This paper also included topics of process physics, including materials and microstructural effects, machine tools, tooling and sensing, workpiece and design issues, software and simulation tools, and other issues, e.g. surface and edge finish, and outlook for future developments.

The consensus that can be derived from these survey papers are that micro-cutting technology is important to the fabrication of 3D structures (i.e. high aspect ratio and complex geometries) using a variety of materials, especially steel. Very little has been studied on micro-machining with tungsten carbide tools, nor have the macro-phenomena such as chatter, tool wear, monitoring, and work piece handling and testing been sufficiently investigated on a micro-scale. In the following section, the details of micro-cutting tools and machine tools, micro-cutting, and auxiliary processes are examined. The micro-fabrication research papers surveyed are summarized in Table.2.1, categorized by their research areas.

Table 2.1: Survey of micro-mechanical machining research

Research areas	Approaches	Remarks	Reference
Micro-tools	Ultrasonic vibration grinding to fabricate, $11\mu m$ pins and $17\mu m$ flat drill. Focused ion beam to fabricate $25\mu m$ end mills. Evaluate various shaped carbide tools with FEM.	Recommendation: compress force for grinding force. Very expensive to fabricate. No helix angle tool causes poor surface finish.	[14, 24, 25]

(continued on next page)

Table.2.1(Continued)

Research areas	Approaches	Remarks	References
Precision machine tools	Spindle speed $\sim 140,000rpm$; Accuracy: $0.1\mu m$; Fly cutter machining spindle; Spindle speed: $40,000rpm$ or $170,000rpm$; Accuracy: $0.3\mu m$ Vertical machine center, spindle speed: $15,000rpm$	Micro-milling: $70\mu m$ fin, $100\mu m$ slot; Hydrostatic/aerostatic bearings; Spindle lubricant controller: prevent the thermal effect of the spindle; Pallet loading capacity: 150 kg	[26-29]
Miniature machine tools (micro-factories)	Surveys of micro-factories; Micro-factory concept; desk-top factory, palm-top machine tools, mobile factory, on-site production facility; Micro-machine tool, Spindle speed $\sim 200,000rpm$; Voice coil motors $\sim 5Gs$ acceleration in each direction spindle speed $\sim 160,000rpm$; 5 axis micro-milling machine; Development from micro-machine tool to micro-assembly device;	Advantages from micro-factories; Main goal: saving energy and economizing; $225 \times 150 \times 175mm^3$ machine footprint, $0.5\mu m$ encoder resolution; $180 \times 180 \times 300mm^3$ machine footprint, tri-load cell mounted; $294 \times 220 \times 328mm^3$ machine footprint, $50nm$ x, y, z feed resolution; $130 \times 160 \times 85mm^3$ machine footprint, backlash compensation algorithm;	[9, 17, 18, 30, 31]

(continued on next page)

Table.2.1(Continued)

Research areas	Approaches	Remarks	References
Chip formation and minimum chip thickness	Orthogonal micro-machining FEM Cutting test with copper; Analytical model for shear stress; Cutting test with copper; FE simulation Grain size effect; Examination of the chip formation with SEM when the tool cutting edge radius is fixed; Dynamic chip thickness; Process parameters, dynamic vibration, elastic recovery; Friction effect between a work piece and tool; Measuring the edge radius with SEM;	The ratio of tool edge radius to the depth of cut: 0.2-1; Under $1\mu m$ depth of cut: elastic recovery of the material; Critical chip thickness: 0.2-0.35 times tool radius; The ductile mode cutting is mainly determined by the undeformed chip thickness; Chip load and force relationship for pearlite; Friction coefficients: 0.2-0.4;	[32-37]
Micro-cutting forces	Relationship between cutting force and chip thickness; Analytical model for cutting force; Evaluation of the cutting force the undeformed chip thickness; Analytical model chip thickness Aluminum cutting test;	Cutting force is nonlinear due to minimum chip thickness; Minimizing tool deflection error; The mean force; Considering negative rake angle of the tool;	[25, 38-40]
Materials	Influence of the work piece material to the cutting force aluminum and silicon; Effect of the work piece material to the surface roughness; Pre-requirement for micro-cutting; Mapping the micro-structure Examining vibration caused by non-homogeneous materials;	The work piece is heterogeneous; Quenching and tempering the steel to obtain the homogenized work piece; Ductile iron: three distinct metallurgical; The changing crystallography and orientation affects shear angle and strength;	[34, 35, 38, 41, 42]

(continued on next page)

Table.2.1(Continued)

Research areas	Approaches	Remarks	References
Tool deflection	Measuring static deflection and bending stress; Cutting force; NC machining simulator;	Compensating the errors by redefining the depth of cut; Increasing the negative rake angle of the tool; Simulator calculates the static deflection of the tool;	[37, 43, 44]
Instabilities	Tool vibration and frequency spectrum;	Very low feed rates result in instability due to elastic deflection of the work piece;	[45, 46]
Burring	Burr formation in milling and drilling; Cutting process in brass and stainless steel, burr removing method;	Reductions in burr formation increase the tool life; Polymeric material and electro-chemical polishing techniques;	[47, 48]
Tool wear	Using cutting force neural network model; Using lamp and SEM; Using SEM; Shaping single crystal diamond tools;	Predicting tool wear; Monitoring tool wear; Monitoring tool wear; Utilization of the effect of tool wear;	[43, 49–51]
Dynamic testing	Isolation Dynamic test system 1-100 kHz; Dynamic measurement system static measurements; Dynamic model for micro-manipulator; Energy method Superposition of three different sinusoidal inputs;	Piezoelectric shaker and laser vibrometer; Micro-grating interferometer and electro static actuator; Frequency domain curve fitting; The identification model errors from different static/dynamic coefficients;	[52–54]
Metrology	LED instead of laser based stroboscopic interferometer;	Small amplitude $2\mu m$;	[53]
Handling and assembly	Piezo type gripper SMA micro-gripper;	Holding micro-structures;	[54, 55]

This chapter is organized as follows: Section 2.1 surveys the primary equipments used for micro-cutting operation, including the precision machine tool, micro machine tool, and cutting tools. Section 2.2 expresses the special characteristics of micro-cutting mechanism, such as minimum chip thickness, work-piece effects, tool wear etc. In Section 2.3, the auxiliary processes in the micro-

cutting of micro-components, such as testing, handling and assembly, is examined. Section 2.4 examines the effectiveness and challenges associated with macro-machining processes when they are applied to predicting the behavior of micromachining operations.

2.1 Micro-cutting equipments development

Precision cutting tools and machine tools are critical to micro-mechanical cutting processes, since the surface quality and feature size of the micro-structures are dependent on them. The majority of micro-machine tools are based on conventional ultra-precision machines with high rigidity that are operated under a temperature-controlled environment. There has been strong interest by various research groups [9, 18–20, 31] to build small-scale machine tools to fabricate micro-size components. The motivation for building miniature machine tools is derived from minimizing cost and size while increasing flexibility. However, the accuracy of these micro-machine tools is not yet on a par with conventional ultra-precision machine tools due to their lack of rigidity, base vibration and accuracy [9]. Tungsten carbide cutting tools are generally used for the micro-mechanical cutting process, due to their hardness over a broad range of temperatures. This section examines the equipment necessary to fabricate accurate and repeatable micro-components.

2.1.1 Tungsten carbide micro-tools

The size of precision micro-cutting tools (henceforth referred to as micro-tools) determines the limit of the size and accuracy of micro-structure features. Smaller tools have decreased thermal expansion relative to their size, increased static stiffness from their short structure, increased dynamic stability from their higher natural frequency, and potential for decreased cost due to smaller quantities of material [56].

Diamond tools are often used for ultra-precision machining, but have a limited ability to machine ferrous materials. The high chemical affinity between diamond and ferrous materials causes severe wear [51, 57], limiting its use to nonferrous micro-mechanical machining operations. Therefore, micro-tools such as micro-end mills and drills are generally made from tungsten carbide (WC), which has high hardness and strength (Fig.2.1) at high temperatures [57]. To

improve the wear resistance characteristics of micro-tools, very small grain size tungsten carbide (i.e. $< 600nm$) is fused together to form the tool. Cobalt is typically used as a binder and its content influences tool hardness. Smaller cobalt content makes the carbide harder, but at the expense of higher brittleness. Commercially available micro-end mills can be as small as $50\mu m$ in diameter, with their helix angle fabricated by grinding. Fig.2.2 depicts a typical two-fluted micro-end mill.

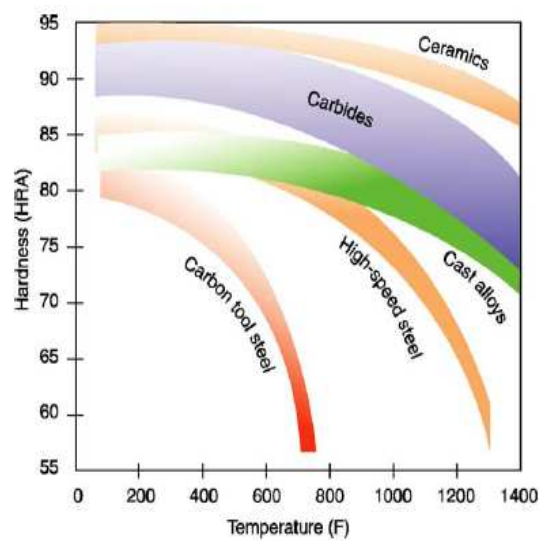


Figure 2.1: Hardness of cutting tool materials as a function of temperature [57]

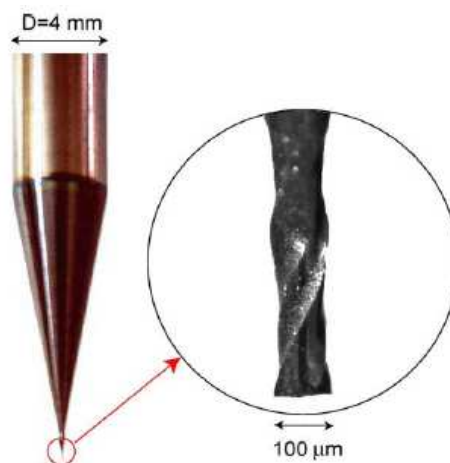


Figure 2.2: Tungsten carbide micro-end mill with two flutes

Micro-tools of less than $50\mu m$ need a zero helix angle to improve their rigid-

ity [14, 48] and to mitigate the limitations of fabrication techniques. Onikura et al. [24] used ultrasonic vibration grinding to reduce the grinding forces and produced an $11\mu\text{m}$ diameter micro-carbide tool. Sandia Labs has developed a $25\mu\text{m}$ diameter carbide end mill tool with five cutting edges using focused ion beam machining, as shown in Fig.2.3. This end mill tool was used to fabricate micro-channels with a $25\mu\text{m}$ depth and width [58]. Schaller et al. [48] fabricated micro-tungsten carbide tools using diamond-grinding disks. These tools are shaped into the single-edge end mills and their diameters range from 35 to $120\mu\text{m}$. Fang et al. [25] investigated various micro-carbide tool geometries (i.e. triangular and semi-circular bases) using finite element method and experimentally verified their predictions. They found that the semi-circular-based mills are better than triangular or the conventional two fluted end-mills. They also concluded that when there is no helix angle on the micro-tools, poor chip evacuation may result in a poor surface finish.

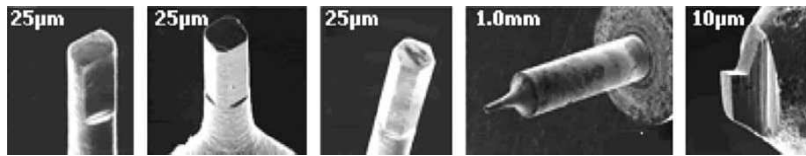


Figure 2.3: Scanning electron micrograph (SEM) of micro-cutting tools [59]

The material and geometry of micro-tools are important factors in micro-mechanical machining operations. The feature size is limited by the size of the micro-tools, and tungsten carbide tools are generally suitable for machining a variety of engineering materials. Several researchers have investigated the fabrication of micro-tools under $50\mu\text{m}$ in diameters, making the cutting edges by intersecting two planes without a helix angle.

2.1.2 Precision machine tools

The size and quality of micro-products depends on the properties of the machine tools used to produce them, including their overall accuracy and their dynamic performance. The capabilities and quality of the machine tool is vital to such product requirements as size, accuracy, surface roughness and dimensional repeatability. The three main systems of precision machine tools are the spindle,

a precision stage and a controller.

In micro-machining applications, the rotational speed of the spindle should be very high to maintain acceptable productivity, since the small tool diameter decreases the chip removal rate. When the torque requirements are high, electric motors with hybrid-angular contact bearings are used. This limits the maximum speed to approximately $80,000rpm$ in the commercial products, since friction in the contact bearing results in the thermal expansion of the spindle. In the laboratory level, the spindle speed can achieve about $500,000rpm$ with magnetic bearing. When a higher spindle speed is required, air bearing spindles with air turbines are typically used, but they produce very low torque. Air bearing spindles that exceed $200,000rpm$ are commercially available. Often to achieve higher speeds, ultra-precision machine tools are retrofitted with high-speed spindles that fit in the conventional tool holder interfaces.

An ultra-precision stage (i.e. XY table) is necessary to achieve high accuracies when fabricating micro-structures. Linear drive motors and a control system are commonly used in ultra-precision machine tools. Compared to conventional drive mechanisms such as ball screws, linear motors have no accumulative errors from friction and the motor-coupling, no loss of accuracy due to wear, and no backlash. They can also provide very high accelerations [60]. The typical accuracy for ultra-precision machine tools using linear drive systems is $\pm 1\mu m$ [13,61].

Ultra-precision macro-machine tools have several advantages including high rigidity, damping and the ability to actuate precisely based on precision sensors and actuators [62]. However, the large scale and precisely controlled machining environment may add very high costs for the fabrication of miniature components. Examples of commercially available precision micro-machining centers are depicted in Fig.2.4.

2.1.3 Micro machine tool/micro factories

Since micro-structures are very small, several researchers and companies are trying to scale down the machine tools necessary to produce micro-components [9,17–20,30]. Micro-machine tools do not necessarily have to be large to achieve the required precision [9], and several benefits from this miniaturization include reduction in energy, space, materials and cost.

Micro-machine tools are cost-effective when compared with ultra-precision

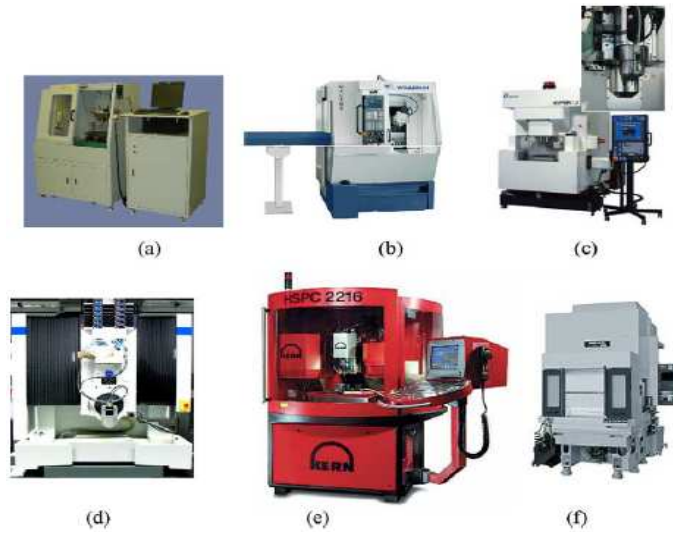


Figure 2.4: Commercial ultra precision machine tools: (a) DT-110 [26]; (b) W-408MT [63]; (c) Hyper2j [28]; (d) Kugler [27]; (e) Kern [61]; (f) Mori Seiki [29]

machine tools and require smaller amounts of materials when fabricated. Therefore, machining centers can be constructed with more expensive materials that exhibit better engineering properties. Micro machine tools have higher natural frequencies compared with conventional macro-machines, due to substantially smaller mass. This translates into a wide range of spindle speeds to fabricate components without regenerative chatter instability. In addition, smaller machine tools have lower vibration amplitudes relative to the conventional machining loads [9]. Fig.2.5 illustrates miniature micro-machine tools.

The portability of such systems is beneficial. Miniature machines introduced the new concept of small footprint factories known as micro-factories [17]. For example, the small size of the machines allows for their deployment to any building or site. Micro-factories may be suitable for the production of micro-components during military or space exploration applications, since the accessibility of large machine tools is very difficult. Miniature factories can also have significant energy savings since the energy requirements are lower.

Micro-factory actuators are either piezoelectric (i.e. flexure designs) or voice coil actuators, in order to achieve sub-micrometer accuracies. They use high-speed air bearing spindles, as used in the majority of ultra-precision machines. Further, micro-factories can have different cells with different functionalities

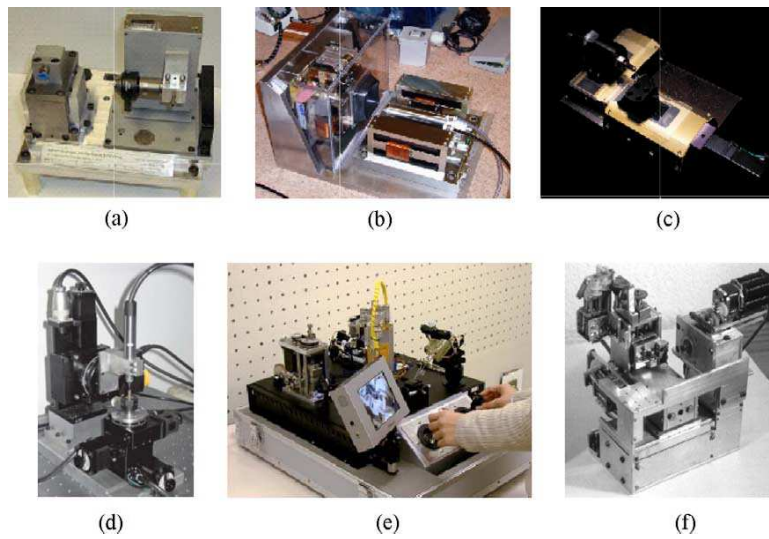


Figure 2.5: Micro-machines (a) 1st generation miniature machine of UIUC [30]; (b) 2nd generation miniature machine of UIUC [30]; (c) commercial miniature machine [64]; (d) 5-axis miniature machine [18]; (e) micro-factory [9]; (f) micro-machine tool [20]

such as micro-lathe, micro-milling, and micro-press. The micro-factory developed in Japan [17] exhibits a two-fingered tweezer-robot and miniature CCD cameras to manipulate micro-components.

There are challenges associated with the development of micro-machine tools. They require accurate sensors and actuators, which must be small enough to implant within the machines. The structural rigidity of micro-machine tools is less than those of precision machines. In addition, the micro-machine tools can be excited by external disturbances; therefore, micro-factories require vibration isolation to achieve desired tolerances.

The accuracy and small features of micro-components are dependent on the machine tools that produce them. Tungsten carbide micro-tools provide the flexibility to fabricate both ferrous and nonferrous components. Conventional ultra-precision machine tools can produce the desired tolerances; however, in order to produce microcomponents cost effectively, the reduced cost potential of micro-factories holds a promising future for research. Further studies are needed to improve the rigidity of micro-factories. Also, integrated processing is still a significant challenge [12].

2.2 Micro-cutting mechanism characteristics

The principals of micro-machining are similar to those of conventional cutting operations. The surface of the work piece is mechanically removed using micro-tools. Unlike conventional macro-machining processes, micro-machining displays different characteristics due to its significant size reduction. Most chip formation investigations are derived from macro-ultra-precision diamond and hardened steel cutting operations, with numerous publications on the effect of round edges and minimum chip thickness [30, 65–69]. Often, the edge radius of the tools is relatively larger than the chip thickness to prevent plastic deformations or breakage of the micro-tools. In contrast to the conventional sharp-edge cutting model, chip shear in micro-machining occurs along the rounded tool edge [33]. As a result, cutting has a large negative rake angle, which affects the magnitude of the ploughing and shearing forces. Therefore, a relatively large volume of material has to become fully plastic for a relatively small amount of material to be removed, resulting in a significant increase in specific energy [66]. Further, when the chip thickness is below a critical chip thickness, chips may not be generated during the cutting process; instead, the work piece material elastically deforms. For annealed steels, this results in a saw-toothed chip formation caused by high-frequency force fluctuation (over 10 kHz) [70]. The increase in cutting forces leads to accelerated tool wear, large tool deflection, and a built-up edge [38, 71]. It is also well known that non-homogenous materials have a profound influence on the surface roughness and the cutting force in micro-scale machining [71].

2.2.1 Chip formation and minimum chip thickness

Chip formation is a dynamic process that is often nonlinear in nature. Understanding micro-chip formation is important in an accurate prediction of cutting forces. Since a chip may not form when the depth of cut is less than a minimum chip thickness, finding the minimum chip thickness has received much attention [38, 52, 71].

In macro-machining, the feed per tooth (i.e. depth of cut) is generally deeper than the cutting tool edge radius. Therefore, macro-chip formation models are based on the assumption that the cutting tools completely remove the surface of the work piece and generate the chips. According to Davies [72, 73], the

material flow pattern at low cutting speed is highly inhomogeneous, which affects segmented chip formation. This strain localization is due to the instability in the thermoplastic behavior of materials with changing temperatures. In contrast, Konig et al. [74] found that periodic fracture caused chip formation. The chip thickness variation in milling operations, $h(\phi)$ can be approximated as $h(\phi) = c \sin \phi$, where ϕ is the angle of immersion (angle of the tool) and c is the feed rate (mm/rev-tooth) [75]. However, simple scaling of the chip thickness variation model cannot be used for micro-machining. The small depth of cut due to the small feed rate and edge radius of the tool cause a large negative rake angle. This phenomenon causes ploughing, a rough surface and elastic recovery of the work piece. Liu et al. [45, 46] and Kim et al. [52] demonstrated that there is elastic-deformation of the work piece during the micro-machining process.

The concept of minimum chip thickness is that the depth of cut or feed must be over a certain critical chip thickness before a chip will form. Fig.2.6 depicts the chip formation with respect to chip thickness. When the uncut chip thickness, h , is less than a critical minimum chip thickness, h_m , as shown in Fig.2.6(a), elastic deformation occurs and the cutter does not remove any work piece material. As the uncut chip thickness approaches the minimum chip thickness, chips are formed by shearing of the work piece, with some elastic deformation still occurring, as illustrated in Fig.2.6(b). As a result, the removed depth of the work piece is less than the desired depth. However, when the uncut chip thickness increases beyond the minimum chip thickness, the elastic deformation phenomena decreases significantly and the entire depth of cut is removed as a chip, Fig.2.6(c) [45, 46, 52].

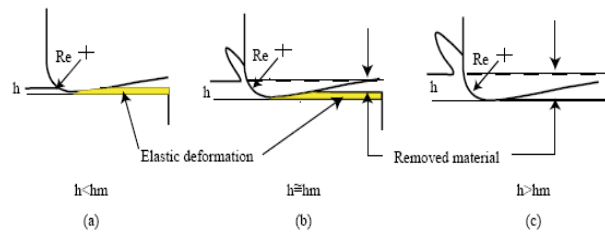


Figure 2.6: Schematic of the effect of the minimum chip thickness (R_e , radius of cutting tool; h , undeformed chip thickness; h_m , minimum chip thickness)

The relationship between the tool radius and minimum chip thickness depends on the cutting edge radius and the material of the work piece. It is

very difficult to directly measure the minimum chip thickness during the process, in spite of knowing the tool edge radius. Researchers have estimated the minimum chip thickness either through finite element (FE) or experimental predictions [34,35]. Moriwaki et al. [32] used the FE method to analyze orthogonal micromachining with the effect of the tool edge radius. Their FE analysis showed good agreement with experimental cutting of copper with a sharp diamond tool. Vogler et al. [34,35] determined the minimum chip thickness of steel by using an FE simulation tool. They reported the critical chip thickness is 0.2 and 0.3 times the edge radius for pearlite and ferrite, respectively. Liu et al. [1] experimentally examined chip formation and micro-cutting forces. They concluded that a sudden change in thrust forces could be used to determine the minimum chip thickness. This sudden change in thrust forces was explained by a shifting from plowing/sliding dominant forces to shearing dominant forces as shown in Fig.2.7.

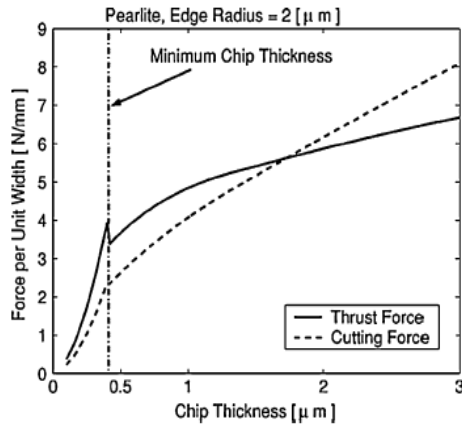


Figure 2.7: Chip thickness and force relationship for Pearlite [1]

Since the minimum chip thickness is dependent on material properties, Son et al. [37] determined the minimum chip thickness based on the tool edge radius and the friction coefficient between the work piece and tool. They analytically formulated that the minimum chip thickness can be approximated as $h_m = R_e(1 - \cos(\pi/4 - \beta/2))$, where β is a friction angle (i.e. Frictional Force/Normal Force = F_u/F_v) between the tool and the uncut-chip work piece, and R_e is the cutting tool edge radius. They also observed that a continuous chip is generated at the minimum chip thickness, producing the best surface finish.

In micro-mechanical machining, it is important to identify the minimum chip

thickness prior to the cutting process, because the chip formation depends on the minimum chip thickness. The minimum chip thickness is influenced by the edge radius of cutting tool and by the work piece material.

2.2.2 Cutting forces in micro-machining

The cutting force is directly related to chip formation. The cutting force also determines the tool deflection and bending stress that limits the feed rate [43, 76]. Well developed analytical cutting force models help operators choose the right cutting conditions for their system. There are two components to cutting forces namely, shearing and plowing forces. Since the chip thickness in micromachining applications can be comparable in size to the edge radius of the tool, the conventional sharp-edged theorem cannot be applied in micro-machining operations due to their large negative rake angle. In addition, the elastic-plastic deformation of the work piece also changes the cutting forces in micro-machining operations.

Kim et al. [33] showed analytically the differences in cutting forces between macro-machining and micro-machining processes. In the macro-model, shear takes place along a shear plane; whereas in micro-machining, the shear stress rises continuously around the cutting edge. Their orthogonal micro-cutting force analytical model considered the elastic recovery of the work piece along the clearance face of the tool and the plowing effect by the tool edge radius. They estimated the elastic effects by simulating the cutting forces based on four separate regions. They found it matched closely with the experimental work of Moriwaki et al. [32] and Lucca et al. [69], and concluded that the cutting forces are different from the sharp-edge model.

Liu et al. [1] found that the forced vibration of the tool and the elastic recovery of the work piece contribute to the magnitude of the cutting force at low feed rates. They proposed the micro-end milling process as having three types of mechanisms: only elastic deformation (the uncut chip thickness is smaller than the minimum chip thickness); elastic and shearing deformation; and, shearing deformation (the uncut chip thickness is greater than the minimum chip thickness). They have used the elastic recovery rate, based on the results from Jardret et al.'s work [77], in order to quantify different types of deformations. In addition, Liu et al. [1] also investigated the effect of low feed rate. They performed cutting at various feed rates and found that very low feed rates re-

sulted in instability due to the elastic deflection of the work piece. This, in turn, creates variation in chip thickness, which results in chatter. Fig.2.8 depicts the instability at different feed rates, where the second and third row graphs show the instability.

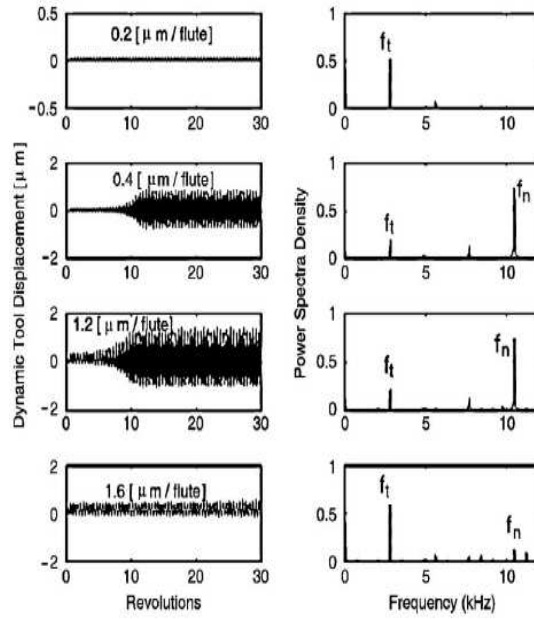


Figure 2.8: Tool vibration and frequency spectra for machining Pearlite

Ni et al. [78] investigated the effect of static tool deflection by assuming the tool as a simple cantilever beam. Their model corrected the actual depth of cut by subtracting the deflection of the cutting tool from the commanded depth of the cut. Dow et al. [43] compensated for the deflection errors in micro-tools by predicting the cutting and thrust forces. Since at micro-scales, cutting force influences tool deflection and tool deflection influences the cutting force, cutting force models should include this coupling.

Bao et al. [40] developed an analytical micro-machining cutting force model for the calculation of chip thickness by considering the trajectory of the tool tip, but did not consider the negative rake angle effect, elastic-plastic work piece, or the deflection of tool (they used relatively large diameter tools). According to the Thusty's works, it is not desirable to apply conventional macro-models [79,80] to the micro-machining process when the ratio between the feed per tooth to tool edge radius is greater than 0.1.

In micro-mechanical machining, the depth of cut is often less than the critical minimum chip thickness to avoid tool breakage and to maintain desired tolerances. This causes a large negative rake angle between the tool and work piece. Conventional sharp-edge macro-cutting models cannot be used to predict cutting forces in micro-machining applications. In addition, the work piece materials elastic-plastic effects and the static deflection of the tool cannot be discounted in micro-cutting force analysis.

2.2.3 Effect of workpiece material (grain size)

In micro-machining, the nature of the workpiece must be considered in order to fabricate accurate micro-parts, as the depth of cut is sometimes less than the grain size in the workpiece material. The assumption of homogeneity in work piece material properties is no longer valid. Because micro-grain-structure size is often of the same order of magnitude as the cutter radius of curvature, the grain structures will affect the overall cutting properties [41]. The assumption in macro-mechanical machining is always that the materials are isotropic and homogenous. This is a distinct difference between micro- and macromechanical machining. The changing crystallography during the cutting process also causes variation in the micro-cutting force and generates vibration. This vibration is difficult to eliminate by changing the machine tool design or process conditions, because it originates from the work piece. Therefore, an averaged constant cutting coefficient cannot be used for micro-machining applications due to tool geometry, small grain size, and non-uniformity of the workpiece material.

Lee et al. [42, 81] examined vibration caused by nonhomogeneous materials (i.e. aluminum single crystal with (110) and (111) plane) in precision machining operations. They found that changing crystallography and grain orientation affects shear angle and strength. Grum et al. [41] analyzed the cutting force in turning-related to work piece material and hardness. Using different aluminum and silicon alloys, they observed different microstructures significantly influence the magnitude of the cutting force, both in their static and dynamic components. When the cutting tool engages from one metallurgical phase to another, the cutting conditions change, causing machining errors, vibration, or accelerated tool wear.

Vogler et al. [71] used a three-step monitoring process for determining the cutting force of different metallurgical materials, especially steel. In steel, the

toughness of ferrite and pearlite grains differs, affecting the machined surface roughness. Their first step was the generation of a microstructural mapping using FE simulation. Step two was the determination of the location of the cutting edge. The cutting coefficients change depending on which material phase is engaged with the cutting edge. The final step was the estimation of the cutting coefficients by using an average chip thickness. With a defined cutting coefficient, an instantaneous chip thickness can be used to predict the cutting force.

To overcome non-homogeneity in work piece material, Weule et al. [38] suggested micro-machining with uniform material. They quenched and tempered SAE 1045 steel with different temperatures ranging from 180 to 600°C in order to obtain a homogenized work piece. They also showed that an increase in the feed rate would improve the surface finish. This conclusion is in agreement with the instability due to low feed rate observed by Liu et al. [1].

The workpiece in micro-machining should be regarded as a non-homogenous material since the grain size is comparable to chip size. If possible, treatment of the workpiece should be considered to provide uniform microstructural properties, allowing for better cutting force prediction.

2.2.4 Tool wear and burrs

The small depth of cut in micro-machining significantly increases friction between the tool and the work piece, resulting in thermal growth and wear. As a result, the increased radius of the tool decreases the quality of the produced part and increases the rate at which tools fail [82, 83]. In addition, the suppression of burr development in micro-machining is very important because unlike in macro-machining, post-processing cannot always be applied to remove burrs on miniature fabricated parts.

While tool wear monitoring has been extensively studied on the macro-scale, very limited work has been conducted at the micro-scale. Tansel et al. [49, 84] developed neural networks to predict tool wear using cutting force and wear data. The neural networks estimated tool condition in the micro-machining of aluminum and steel, with slower tool wear rates for aluminum than in steel. This phenomenon is in agreement with tool wear in the soft/hard work piece cutting observed by Weule et al. [38]. However, the neural network approach requires extensive experimental data and is often inconsistent for different material and

cutting conditions. Rahman et al. [85] investigated the micromilling of copper. They concluded the wear of a $1mm$ diameter tool depended on the tool helix angle and the depth of cut. Their experiments found a small depth of cut ($0.15mm$) has a higher tool wear rate than a larger depth of cut ($0.25mm$). They interpreted this phenomenon as resulting from a continuous chip being removed-up the helix of the micro-tool, increasing the force on its rake face.

Dow et al. [43] observed that as cutting tools wear, the edge of the cutting tool becomes flat. This flat area can be monitored with a scanning electron microscope (SEM) image of the tool edge. However, the applicability of this method is limited by the long and difficult set-up of the SEM. The influence of the tool size on tool wear was investigated by Weinert et al. [50], who also used an SEM to measure the tool wear. Mitsubishi [86] investigated the relationship between the coolant pressure and tool wear in micro-machining. Their experimental results showed there is no relationship between the amount of wear and the coolant pressure.

In milling, the kinematics of the tool as it exits from the work piece significantly affects burr formation due to plastic deformation (i.e. bending) of chips rather than shearing [47]. Weule et al. [38] reported that burrs frequently occur when micro-machining hard materials because of increased tool wear. Schaller et al. [48] examined ways to remove burrs from brass and stainless steel micro-parts. To minimize burring, they coated brass with a cyanacrylate polymeric material. The polymeric material filled voids around the edges of the work piece, where burrs form, allowing the cutting tool always to be engaged with the work piece or the cyanacrylate layer. After machining, the cyanacrylate is removed with acetone in an ultrasonic bath. For stainless steel, they used electro-chemical polishing techniques to remove burrs. This post-processing to minimize micro-burrs can be expensive but necessary.

The motivation for high-speed micro-machining is the reduction of production time in creating complex 3D shapes by maximizing material removal rates. It is important to understand the relationship between the micro-cutting tool and the work piece in order to produce the desired microcomponent. Cutting force prediction and measurement need meticulous care during their analysis so that the effect of built-up edge, run-out, tool deflection, and instability are included. Most of the papers surveyed have individually investigated these effects on tools with diameters greater than $200\mu m$, but a more comprehensive

approach is required to address their interactions, including addressing nonlinearities in micro-machining, and using tools with the smaller diameters. Improved productivity in micromilling operations requires a chip thickness greater than the minimum chip thickness, while keeping below the plastic deformation limit of the work piece or tool. If this cannot be achieved, the tool design should be improved to increase its strength and stiffness to permit cutting conditions, where chips will always form.

2.3 Micro-cutting auxiliary processes

Impeding the commercialization of micro-systems is a lack of understanding of the needs and differences in testing and modeling of 2D and 3D micro-components. Microcomponents require special equipment to directly measure and handle them. Many products such as hard disk drive heads, inkjet printer heads, chemical sensors and micromotors consist of a system of micro-parts, each with different functionality. In most cases, it is impractical to produce a single product with multiple functions [55]; therefore, assembled systems play an important role in the micro-products industry. Currently, the testing, modeling, handling and assembly of micro-systems are heavily based on semi-conductor processes. With the advent of 3D components, these existing methods need to be updated to accommodate their complex shapes which, in turn, will result in an increase in system complexity.

2.3.1 Testing and modeling

Determining the dynamic performance and reliability of 3D micro-components is becoming increasingly important to ensure functionality [87]. Often, engineers analyze MEMS designs through FE simulations to evaluate system performance [56, 88]. However, experimental analysis is vital to verify FE simulations and develop mathematical models for vibration damping effects in micro-components and micro-assemblies [87].

Ozdoganlar et al. [87] developed an experimental dynamic test system for micro-structures using a piezoelectric shaker and laser vibrometer. The system consists of a vacuum chamber and an open-cell neoprene foam rubber block, in order to minimize external noise such as vibration, temperature, force and pressure, all of which can easily distort the response of the micro-structure. While

they were able to acquire frequency response functions and natural frequencies of structures, they were not able to correlate force and displacement. Further research is required to identify dynamic parameters such as damping ratio and the dynamic stiffness of structures.

2.3.2 Handling and assembly

Micro-assembly issues include the dominating force, joining methods, tolerance, and interference factors. In micro-assembly, the main differences between the macro and micro-scale are a dominant force that exists between a manipulator and its object, as well as the positioning accuracy of the assembly machine [55]. In general, gravity forces dominate at the macro-scale. However, adhesive forces such as surface tension, friction, electrostatic, and Van der Waals forces become dominant in the micro-scale [54,55]. The electrostatic forces are less significant when feature sizes range from $10mm$ to $1mm$. On a nano-scale (i.e. parts less than $10nm$ in size), Van der Waals force become dominant. Since micro-mechanical components made with micro-cutting processes range from a few micrometers and up, the effect of Van der Waals force is not as significant [55,89].

When micro-products measure below $1mm$, conventional manipulation methods cannot be used since measurement and control of sensors and actuators are difficult [55]. Alting et al. [12] classified micro-manipulators into contact and non-contact types. Contact-type manipulators, developed for silicon MEMS, are known as mechanical manipulators and include piezo, shape memory alloy (SMA), thermal bimorph and tweezers [90–96]. Suction systems are also used to pick, hold and place planar microparts. Non-contact manipulators include magnetic fields, optical trap or laser tweezers, electric fields, and aerostatics, but are not as desirable in handling micro-products due to the lack of holding forces [12,55]. Popa et al. [54] presented various micro-grippers, including piezo and SMA types.

Joining of micro-parts is an essential part of microassemblies. Common joining methods include glue, snap fit, key lock, and miniature nut and bolt fasteners [55]. When micro-parts are joined together, small joining tolerances are required. To facilitate the joining of micro-parts, a visual servo system, such as CCD cameras is typically used to increase the position accuracy of the micro-parts [12]. Vibration, which can cause positioning errors, is also a critical

factor during assembly processes.

In summary, in contrast to macro-handling, the assembly, handling and assembly of micro-components and micro-systems require new concepts. The manipulation of micro-components to create assemblies will likely require physical contact, which must consider new dominant forces, as well as joining methods dependant on the components and the size of its features. Vibration, which can cause positioning errors, are also a critical factor during the assembly process.

2.4 Micro-machining from macro-machining knowledge

The translation of the wealth of knowledge developed for macro-machining operations to micro-processes is critical, both for the efficient development of practical micro processes and for the understanding of the limitations of its application. Mechanically removing material using carbide tools can produce countless desired feature shapes and sizes. The micro-cutting process is challenging; however, the experiences learned from macro-processes provide a valuable resource for future micro-machining research.

This section examines the feasibility of translating macro-knowledge into the micro-realm by identifying the similar problems faced in the macro- and micro-domains. For example, regenerative chatter also occurs in the micro domain, but its investigation has been limited due to inaccurate measurement of dynamics between the tool and work piece. Problems that are generally minor in the macro domains, such as tool run-out, are amplified in the micro domain. One of the biggest challenges is maintaining machining forces below a critical limit to prevent excessive tool wear and breakage while improving productivity. Lastly, the sensing and monitoring of micro-machining processes has limitations. It is anticipated that there will be more challenges associated with the micro-machining than macro-machining, and new paradigms may be required to overcome obstacles.

2.4.1 Cutting forces

As with the macro-machining theories, micro-cutting forces consist mainly of shearing and plowing components [75]. However, as mentioned in previous sections, microcutting forces are quite different from macro-forces, especially

the static (dc component) of force. In a preliminary experiment of slot machining aluminum 7075 T-6, micro-cutting forces were compared to their predicted results using the conventional sharp-edge cutting force model [75], with compensation for the run-out forces, and the assumption that the machined materials were uniform (Fig.2.9). The dynamic component, which is mainly due to shearing forces, is similar to conventional cutting force simulations when the depth of cut is greater than the minimum depth of cut. However, the offset static component between the experiment and the predictions clearly indicated that plowing forces in micro-machining processes cannot be fully expressed in the macro-cutting model.

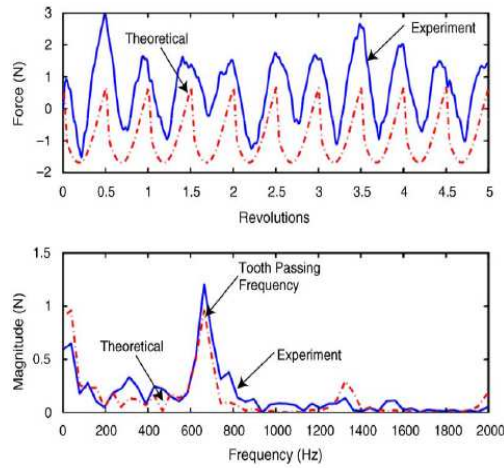


Figure 2.9: Micro-cutting forces in feed direction (cutting conditions: 20,000rpm, 0.002mm/tooth, 200 μ m diameter, two fluted end mill; theoretical, sharp edge theorem; experiment, measured using a Kistler table dynamometer) [75]

Making a small depth of cut in micro-machining is impeded by the requirement to maintain cutting forces below the plastic deformation limit of the micro-tool; therefore, reducing the cutting forces in micro-operations significantly improves material removal productivity. However, driving cutting forces-up is the requirement for a minimum chip thickness necessary for chip formation. Mori-waki et al. [32] presented the possibility of significantly reducing cutting forces in macro-turning and milling by providing an ultrasonic elliptical vibration that is synchronized with the chip flow direction to reduce cutting forces. However, their tool rotational speed was limited by the elliptical vibration speed. This could be addressed by utilizing a high-frequency piezoelectric actuator stage

with higher bandwidth than the rotational speed in the micromachining domain.

Friction between the tool and work piece has not been thoroughly investigated in micro-machining. Several researchers investigated the effects of flank tool wear by monitoring the plowing forces [97,98] in macro-machining. In the macro-process, increased flank wear is caused by high friction and its consequent thermal load between the tool tip and work piece material. This results in tensile residual stresses and creates a white layer with an extremely fine microstructure [47]. With an increase in the chip thickness in micro-machining, the plowing forces decrease as the chip forms [1]. In addition, the elastic deformation of the work piece affects changes in the plowing (or rubbing) forces.

Kountanya et al. [98] examined the flank wear of edgeradiused macro-cutting tools in orthogonal machining conditions. They report that the cutting force decreases when the chip thickness is less than the edge radius of the tool until the edge radius is worn away, then the cutting force increases. The reason for this phenomenon may be due to the sharpening effect on the blunt edge as flank wear increases as illustrated in Fig.2.10. Whether this macro machining phenomenon occurs in the micro-cutting process is not yet known.

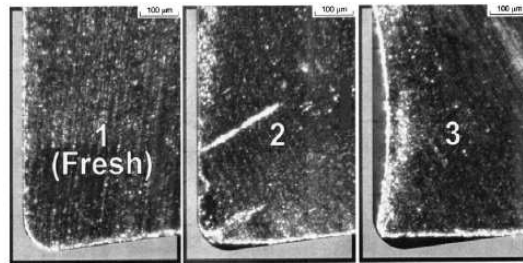


Figure 2.10: Flank wear of edge radiused macro-tool ($70\mu m$ edge radius at the end of test) [98]

2.4.2 Feed rate estimation

Feed rate directly affects cutting forces, with excessive forces resulting in large tool deflection, accelerated tool wear and tool breakage. Thus, the proper selection of the feed rate is very important to maintain desired work piece tolerance limits. Micro-tools, especially carbide end mills, do not plastically deform, having brittle tool failures. When the shear effect is neglected, the tool deflec-

tion and bending stress can be modeled as a simple cantilever beam

Feed rate may be selected based on the two criteria of maximum deflection and/or bending stress. Severe deflection will result in tolerance violation. The carbide strength limit can be evaluated by transverse rupture strength tests (ISO 3327). Based on these two criteria, the maximum allowable force limit can be calculated. Feed rates can then be identified from cutting force models. If tool deflection or breakage are too limiting to the feed rate, tool geometry such as tool length can be changed to increase tool stiffness, permitting maximum chip formation while minimizing elastic effects that result in instability. Therefore, the tool vibration will result in a shorter tool life.

2.4.3 Instability (Chatter)

Chaotic dynamic cutting processes, such as chatter, pose a significant problem in micro-machining because they result in excessive vibration that can lead to catastrophic failure. Chatter is an unstable, self-excited vibration that occurs as a result of an interaction between the dynamics of the machine tool and the work piece [76, 80, 99, 100]. In traditional regenerative chatter stability, the occurrence of chatter is dependent on three factors: cutting conditions, work piece material properties, and the dynamics of the machine tool spindle system. Conventional macro-chatter stability assumes that the feed rate does not significantly affect stability. However in micro-machining, chatter stability needs to consider both the elasticity of the work piece due to low feed rates, as well as the conventional macro-regenerative waves that result in a dynamic change in chip thickness, as shown in Fig.2.11.

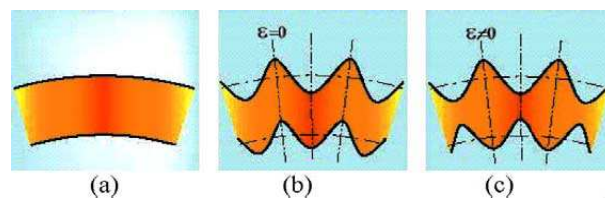


Figure 2.11: Chip Generations due to (a) no vibration; (b) forced vibration; (c) regenerative chatter [75]

An accurate prediction of the overall structural dynamics of the machine tool system is critical to preventing chatter. However, experimental measurement of the dynamics of the machine tool structure at the tool tip is not feasible

for micro-tools. Due to micro-tool size and fragility, impact hammer force tests cannot be applied to measure tool tip vibration. Often, micro-tools are modeled as cantilever beams. However, this may not correctly represent the dynamics at the tool tip. To overcome this, the receptance coupling and joint dynamics identification method developed by Park et al. [101] can be utilized to analytically couple tool and spindle dynamics. To acquire the overall dynamics, the dynamics of the micro-end mill tool is predicted through FE analysis and the dynamics of the spindle-tool holder assembly are measured through the experimental hammer test. The joint dynamics are then indirectly acquired based on two translational measurements using a blank tool.

High-speed machines also present new challenges for micro-machining. At higher speeds, the dynamics of machine tools change, with an unbalanced spindle producing centrifugal and gyroscopic effects. Modeling and analysis of high-speed spindle dynamics with various bearing configurations and thermal expansions are important. The majority of spindle research has dealt with static stiffness optimization rather than dynamic performance. The few papers addressing high-speed spindle dynamics were far below the operation range of micromachining [15].

Finally, in the micro-scale, material property homogeneity cannot be assumed; thus, the cutting coefficients used in chatter control models will vary from macromachining processes due to anisotropy of materials. Instability in micro-machining is a very challenging problem due to various non-linear effects and time-variant dynamics. In particular, the feed rates of micro-milling operations can significantly affect the stability due to elastic deformation [78].

2.4.4 Run-out/unbalance

Tool run-out and unbalance is usually a minor problem in macro-machining operations; however, the problem is severely amplified when the diameter of the tool decreases and spindle speed increases significantly. Tool run-out is caused by a misalignment of the axis of symmetry between the tool and the tool holder or spindle. In macro-machining it is often ignored, as the diameter of cutting tools is relatively large compared to the tool run-out and the speed is relatively slow compared to micro-machining.

The unbalanced component of the rotating spindle can contribute significant noise to force measurements, especially at high rotating speeds. Like run-out,

this noise is caused by the eccentricity (or unbalance) of the rotating spindle that exerts centrifugal forces. Unbalance forces are modeled as Eq.(2.1), where the right hand side of the equation is the centrifugal force acting on the unbalanced mass, m_o , with a distance of the center of the unbalanced mass from the rotational axis, e , and a spindle rotational speed denoted ω_r :

$$M\ddot{x} + C\dot{x} + Kx = m_o e \omega_r^2 \sin \omega_r t \quad (2.1)$$

Thus, the unbalanced forces are a function of the square of the rotational speed, and severe vibration can occur for high-speed micro-machining operations. This unbalance can be also caused by the deflection of the tool due to cutting forces; however, no work has been reported in this area for micro-cutting. This oversight has perhaps contributed to difficulties in measuring micro-cutting forces, as they are severely distorted by the run-out and unbalance.

Several researchers [39,43,102] have investigated tool run-out by investigating cutting forces during cutting and non-cutting. They also investigated different tool holders, and concluded collet-type holders are superior to the setscrew type for reducing run-out. Jun et al. [103,104] used a capacitance sensor to examine tool run-out. Capacitance sensors, however, are inaccurate on round surfaces with the displacement measurement becoming non-linear [105].

Tool deflection due to cutting also affects its accuracy. Lee et al. [106] showed that cutting marks due to tool run-out contribute to surface roughness. These cutting marks had a period of twice the chip load, indicating that one cutting edge is deeper than the other cutting edge. That is, the radius of one cutting edge appears larger than the others. Novel tool holder design may improve micro-tool run-out, and deserves more study. Rivin [107] surveyed tool holders, but active or passive control of tool holders using actuators may be required to compensate for any unbalance and minimize tool run-out. New geometric designs for tools may also be required in micro-machining operations, where the spindle speed is very high.

2.4.5 Sensing methods

Significant research has been conducted on the monitoring of macro-machining processes using various sensors such as: spindle motor current and power [108, 109]; a feed drive measurement [110,111] used to emulate force signals; vibration

signatures [112]; acoustic emissions [113–115]; and cutting forces [75,80]. These sensing methods have very narrow frequency bandwidth requirements and are prone to small disturbances, or not applicable for milling operations due to the highly intermittent nature of the chip removal process [116], Tlustý [80], Byrne [117], and Dimla [118] reviewed various sensors and their limitations for machine monitoring processes using dimensional, cutting force, feed force, spindle motor, and acoustic emission (AE) sensors.

Cutting force measurement is the most effective method for monitoring tool conditions since it provides higher signal-to-noise ratios, and best represents the state of machine tools and machining operations [80]. Despite years of research in this area, reliable, versatile and practical sensors are not yet available for the monitoring and controlling of high-speed machining processes [118]. The most common direct method to measure cutting force in machining operations is through table dynamometers or piezoelectric load cells. Park and Altintas [119] presented a Kalman filter algorithm, which reconstructs cutting forces from the distorted cutting force measurements obtained from a spindle integrated sensor system. Similar filtering techniques are needed to acquire high-frequency bandwidth cutting forces for micro-machining. The bandwidth of sensors needed for micro-cutting operations should be a few times higher than the tooth passing frequencies to reconstruct the cutting forces. This requires the development of new sensors and the fusing of various sensor signals.

2.4.6 Process optimization and monitoring

Most micro-machining processes use conservative feed rates, due to the fragility of micro-tools [16]. To increase overall manufacturing output, micro-cutting requires higher feed rates and spindle speeds for higher volumetric material removal, while minimizing tool deflection and chatter. Adaptive control has been used in macro-machining processes [120,121]. However, it has not been tried in the micro-scale, where it is even more important since tool deflection is considerable.

It is very difficult to detect damage to cutting edges and broken shafts in micro-end mills, making it nearly impossible to stop machining or change the cutting conditions before tool failure. Because feature sizes and cutting tools are small, it is nearly impossible to restart an interrupted machining process by aligning the tool to the work piece. Also, damage to a work piece by a broken

tool may not be observable without special instruments. Tansel et al. [122] have used Smart Work piece holders to prevent work piece damage through the use of a piezoelectric actuator. Using a detected cutting force signal, the actuator can quickly move in the opposite direction in very small increments, thereby creating sufficient time to reduce the motor speed and decrease the cutting forces.

Process monitoring and control in high-speed micromachining applications are very challenging with existing equipment and techniques. Therefore, the fusion and filtering of various process monitoring signals is essential for micro-control to enhance robustness and reconcile the limited frequency bandwidth of currently available sensors and actuators.

2.5 Conclusions

Nano- and micro-electro-mechanical systems (MEMS) are seen as the favored technology for component miniaturization, and its use promises to enhance economic growth, health, and quality of life. However, interfacing to the macro-domain has been a big challenge. Micromechanical cutting is an enabling technology that can bridge the gap between the macro- and nano/micro-domain. The flexibility and efficiency of micro-end milling processes using carbide tools allow the fabrication of small batches compared with other processes. In some cases, the removal of material shows similar trends between the macro- and micro-machining processes, such as regenerative chatter, tool wear, and monitoring strategies. However, in many instances, the direct scaling of macro-knowledge to the micro-domain was not successful. Rather, micro-fabrication requires extensive research in chip removal processes, cutting force predictions, handling, assembly, material properties, modeling and testing in order to provide accuracy and productivity in micro-scales. In addition, extensive commercialization of micro-engineering technology relies on low cost, fast cycle time and high dimensional accuracy production methods. Micro-injection molding processes to produce bio-MEMS are especially attractive, since this process would cost pennies instead of hundreds of dollars. Micro-mechanical machining is well suited to support the development of micro-injection molds because of its promise for accurate, low cost, small batch size processes of 3D molds using ferrous alloys. The development of successful micro-mechanical cutting technologies will provide a catalyst for the broader development of micro-engineered systems.

Chapter 3

Micro Machine Tool (MMT) Development

3.1 Introduction

Due to the special characteristics of micro machining, the demands of the machine tools include the long stroke, micro feed, high positional accuracy, excellent dynamic performances. Therefore, the normal machine tools used for macro scale manufacturing are not suitable for micro scale fabrication. Two types machines are adopted to achieve the micromachining either in the industry or laboratory level. The first one is the traditional precision machine tool [123]. The second one is the micro machine tool (MMT). Due to the huge dimension of the precision machine tool, the machine cost will be much higher in order to achieve the good thermal balance and isolation from the environment effect. In the contrast, the MMT is cost-effective and requires smaller amounts of materials. And due to its lower mass, its natural frequency is higher and with the vibration amplitudes are lower. Hence, since the introduction of Japan's Mechanical Engineering Lab microfactory concept in 1998 [124], more and more researchers resorted to develop several MMTs.

Subrahmanian and Ehmann [125] developed a three-axis meso-scale machine with $15 \times 15 \times 15 \text{mm}^3$ workspace, $0.5 \mu\text{m}$ encoder resolution, and $200,000 \text{rpm}$ spindle. In University of Illinois at Urbana-Champaign (UIUC), after Vogler et al. [30] developed the first generation MMT, Honegger et al. [126] has been developed the seconde prototype. Both of them are 3-axis and actuated by voice-coil actuators. The second one is equipped with $160,000 \text{rpm}$ air-turbine, $0.1 \mu\text{m}$ encoder and reaches $25 \times 25 \times 25 \text{mm}^3$ workspace. Ni and his group [127] has

developed a 3-axis micro/meso machine tool, which is driven by a miniaturized piezoelectric linear stage with $13mm$ stroke and $0.25\mu m$ encoder resolution in each direction, as well as an air-turbine spindle with $120,000RPM$ maximal speed. Some other MMTs development includes the contribution from Bang et al [18], Ashida and Okazaki [9,128], and Filiz et al. [129].

In this chapter, the key technologies of MMT are discussed in detail at the beginning. Then a three-axis MMT prototype is developed. The structural configuration of MMT is selected according to the graph theory and an expert design system. The MMT is driven by three ultra precision linear motors with high resolution linear encoders as feedback. It is equipped with a high speed electro-spindle and a CCD stereo microscope as a monitoring device. Meanwhile, the entire machine is controlled with an open numerical control system based on motion controller. In order to achieve the machining process conveniently, the Human-Machine Interface (HMI) software is developed. The G code can be interpreted by this HMI software to drive the MMT to achieve the complex surface machining. At last, the position accuracy and machining tests have been done on the MMT, and the results are very satisfactory and show its excellent performances.

3.2 Key technologies of MMT

The entire MMT system is contained by some key components, and frequently they can be categorized as feeding system, spindle system, feedback system, control systems, monitoring system et al. How to develop these high quality components is critical to the MMT performance.

3.2.1 Feeding system

Because the feeding system of MMT must satisfy the demands of large feed, precision position, fast response et al, the high quality feeding system is very important to part performances. Some approaches which are primarily adopted to achieve the requirements will be discussed as follows.

Linear driving system

The prismatic DoF is frequently adopted in the machine tool configuration, and the linear driving system can be used without the transferring chain in order

to achieve the direct driving (DD). With the rapid development of the linear driving system, it has been applied in the machine tool industry more and more widely nowadays. The voice-coil actuator, linear motors, and some similar types are included in this category. These motors can supply outstanding dynamic response as much as 5G acceleration, fast-speed positioning, high stiffness and good control ability [30]. Hence they are widely used in the MMT equipment [130, 131].

Rotatory driving unit + ball screw system

This combination is commonly used in the traditional machine tool system. The rotatory driving unit, which is rotatory motor primarily, outputs the torque. Through the coupling unit, the ball screw system leads the stage movement. Compared with the linear driving system, they are less-cost, but the main problems are backlash and creeping phenomena in the ball screw system. So the error compensation devices or algorithms must be developed in order to improve their performances.

Non-motor driving system

The non-motor driving system includes the piezo-electric actuator (PA), shape memory alloy (SMA), etc.. They are well-known for their nano positional precision, and widely used in the fields as MEMS/NEMS, micro operation, sensors, actuators and others. Some researchers adopted them into the MMT systems. Rusnaldy et al. [132] used the PA to drive a three-axis MMT. Malukhin and Ehmann [133] have developed a 2D micro stage by SMA for thin wall structure fabrication. But the strokes of PA and SMA are relative small, the normal value is smaller than $1mm$. The additional motion amplifiers are required. Their dynamic response is lower, so they are not satisfactory when the machining feed rate is higher.

Micro parallel stage

In recent years, the theory of parallel robot has been developed rapidly and realized in many fields. Some researchers have developed the micro parallel stage for micromachining. Their DoFs range from 2 to 6, and the stiffness are higher than the traditional machine tool configuration. Furutani et al. [134] adopted the stacked piezo-electric actuators to form a Stewart parallel platform, which

is used for nanometer cutting research. However, due to the features of the parallel mechanism, the workspace is smaller and it is more expensive to setup a high precision parallel stage.

3.2.2 Spindle system

Due to the miniature size of the micromill tool tip diameter, always smaller than $1mm$, the cutting speed is much smaller than the common sense. In order to improve the cutting speed to prolong the tool life and enhance the surface quality, the high speed spindle ($\geq 10,000rpm$) must be integrated into the MMT system. It can be categorized as bellows [31].

Electro spindle

Today, the electro spindles are the brushless DC motors. Their speed can achieve as high as $500,000rpm$ in the laboratory level, and it is easy to be controlled by the digital signal from inverter. Their output torques are higher. However, they are larger dimensions, heavier mass and the additional cooling system is necessary to decrease the temperature due to the friction between the rotor and bearing system.

Air turbine

The speed of air turbine ranges from $50,000rpm$ to $200,000rpm$. But the size of them are relative larger, about $45mm$ diameter. Due to the driving source is the air flow, they can be cooled by themselves, but their output torques are lower. It is a little difficult to control the speed of the air turbine, because the air flow dynamic property is highly dependent on the temperature.

Dental Handpieces

The dental handpieces are commonly used in the medical field. Their prices are lower than other widespread industrial spindles. The speed is higher up to $500,000rpm$. Their dimensions can be fabricated only $10mm$ diameter, but their output torques are very low.

3.2.3 Sensing system

Because the functions of MMT are in the microscale, the sensors in the conventional range are not capable to detect the signals for MMT. Many special

sensors have been developed to improve the MMT performances. The linear encoder system can reach nanometer resolution in long stroke [135]. The precision dynamometer with $2mN$ resolution and $40KHz$ sampling frequency are already widely used in the laboratory level [136]. Other novel type sensors, such as laser sensor, acoustic emission sensor etc., are integrated in the advanced MMTs.

3.2.4 Control system

Because the MMTs are still not industrialized, there is no standard for the machine development. About 90% MMTs utilize the PC/IPC based hierarchical control system. The operator sends the commands from the PC/IPC in the top level to the motion controller in the middle level. Then the controller compiles and sends the commands in the machine language format to the motor drivers. The feeding system moves according to the commands and the sensors detect the stage movement error and feedback to the controller to form a closed-loop control system.

Nowadays, most researchers work in their controller software environment to drive the MMT motions. Some investigators resorted to develop the interface software between the motion controller and the operator to achieve the manipulation directly. In order to be compatible with the G-code programming, the numerical control (NC) systems for the micromachining must be developed. Hence the MMT can fulfill complex surface fabrication.

3.2.5 Monitor system

Due to the tiny tool size, the tool wear and breakage issues are really important the micromilling operation [49, 84]. Meanwhile, according to some tool catalogs, the tool life of micromill is only a few hours [137]. Therefore, monitoring the machining process online is very useful to check the tool condition. In microscale machining process, the CCD stereo microscope is capable to supply large field-of-view and accepted depth-of-view. And the other sensors can also be used for the process monitor, such as cutting force and acoustic emission sensors.

3.3 Structural configurations and selections reduction

To systematically generate the various machine tool configurations for evaluation purposes, a modular representation of the MMT is essential. Employing the direct graph method, a machine tool can be defined as an integrated assembly of various structural components, all interconnected, with inter-connectivity based on their individual functionality, and flow of force between the tool, ground, and workpiece. Directed graph is demonstrated in Fig.3.1, which depicts as a directed edge, represented by force, flowing from the initial vertex (first structural component) toward the terminal vertex (connecting structural component). During machining operations, cutting forces are generated between the cutting tool and the workpiece, flowing through various connected structural components before terminating at the ground frame. In essence, the machine tool can be represented as two distinct paths of force flows, with main-force going from the cutting tool to the ground and the sub-force flow going from the workpiece to the ground [138].

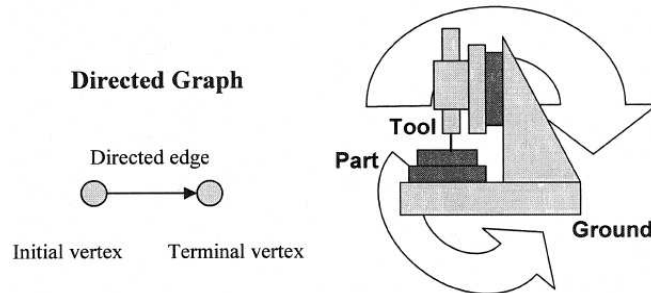


Figure 3.1: Directed edge and force flows inside machine tool

The complete machine tool system can then be broken down into several levels hierarchy (Fig.3.2). The bottom-most level consists of basic machine tool structural components, each with inherent kinematic functionalities. Subsequently higher levels of hierarchy can be reached assembly of the basic structural components. Ultimately, the tool-to-ground and workpiece-to-ground structural chains complete the machine tool system. By extending and incorporating kinematic functionalities into structural components, the generated machine tool configuration can later be assessed and evaluated.

A sample set of basic structural components, and their inherent kinemat-

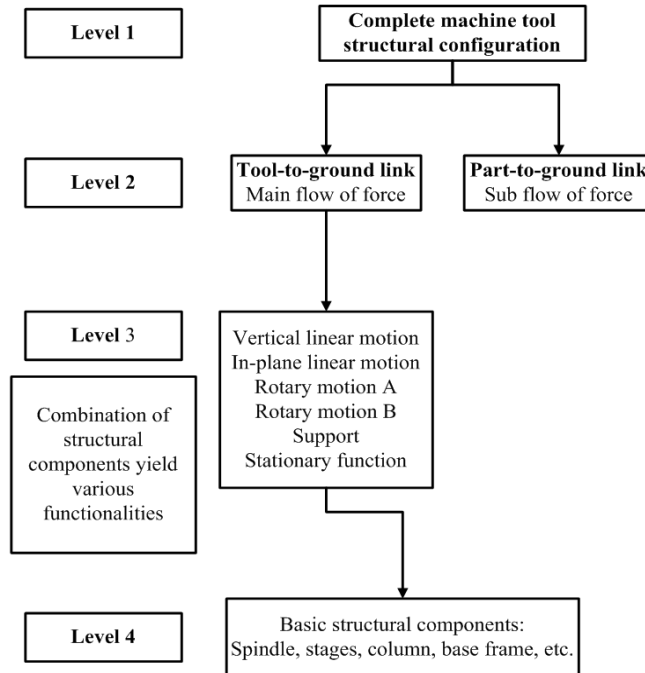


Figure 3.2: Machine tool hierarchy with graph theory

ics functionality, is shown in Fig.3.3. The next step is to formulate the sub-assemblies by defining the inter-connectivity between the structural components. The definition will depend on the user's interpretation as to how the previously selected structural components can be physically mated to each other, and will affect the resulting MMT configurations generated.

Table.3.1 lists all the possible connectivity, or force-flow, between the structural components previously defined in Fig.3.3. For example, initial vertex 1, the spindle, can be jointed to any of the listed vertices, 2,3,4,6,7 (linear slide, rotary joint A, rotary joint B, cross-slide, or base frame). The same definition can be extended to the rest of the structural components listed in the Table.3.1. When two components are inter-connected, the sub-assembly's kinematic functionalities may be modified or extended. One example would be when component 6, the cross-slide, which is connected with component 8, the longitudinal slide, resulting in an in-plane motion stacked on top of a cross-plane motion, which is orthogonal to each other. Another example would be when component 2, the linear slide, which produces a vertical motion, is connected to the component 5, the vertical column, resulting in a linear motion across-plane when connected

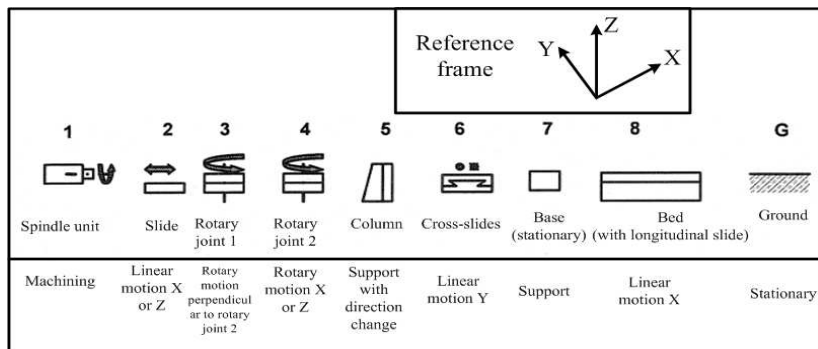


Figure 3.3: Sample set of structural components with kinematic functionalities

to component 8, the bed frame.

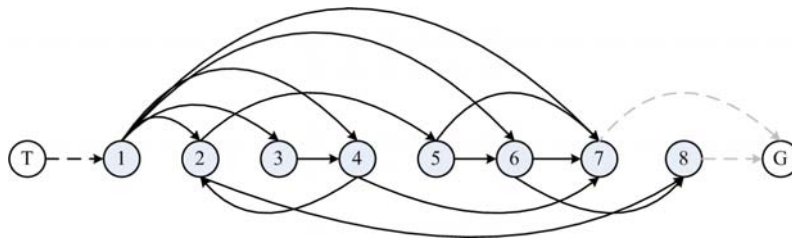


Figure 3.4: Connectivity of tool to ground structural chain

Fig.3.4 depicts all the connectivity in the tool-to-ground structural chain, with the cutting tool connectable to the spindle and ground connectable to either component 7 (base frame) or component 8 (bed with longitudinal slide).

For the connectivity in the part-to-ground structural chain (Fig.3.5), the workpiece is connectable to component 2 (linear slide), component 3 (rotary joint A), component 4 (rotary joint B), component 6 (cross-slide) and component 7 (base frame).

An exhaustive set of the structurally feasible configurations can be systematically generated by iterating through all possible permutations of the force flows through the tool-to-ground structural chain and part-to-ground structural chain. With the sample structural component list and connectivity previously

Table 3.1: Declared connectivity between sample structural components

Initial vertex	Connectivity	Initial vertex to terminal vertex
①	② ③ ④ ⑥ ⑦	
②	⑤ ⑧	
③	④	
④	② ⑦	
⑤	⑥ ⑦	
⑥	⑦ ⑧	
⑦	G	
⑧	G	

defined, fourteen possible force-flow paths of the part-to-ground chain yield two hundred and eighty-nine structurally unique configurations, containing kinematic functionalities ranging from zero to ten degrees-of-freedom. As every generated structural configuration contains information on the structural component's connectivity, the overall kinematic functionalities of the configuration can be assessed and the configuration set can be filtered into a subset of preferred configurations by exercising user-specified functional requirements and expert design rules.

Functional requirements can be derived by detailed examination of the target workpiece, including, for example, shape, form, surfaces, and features. For the purpose of demonstrating the methodology, three axes of linear motors, each orthogonal to the others, is required. The previously generated set of two hundred eighty-nine configurations is then reduced to a subset of six (Fig.3.6).

Of the six configurations shown in Fig.3.7, three configurations have the spindles mounted vertically, and three horizontally, with zero to three orthogonal linear motions distributed in between the tool branch and the workpiece branch.

Further reduction of the sub-set of candidate designs can be achieved by

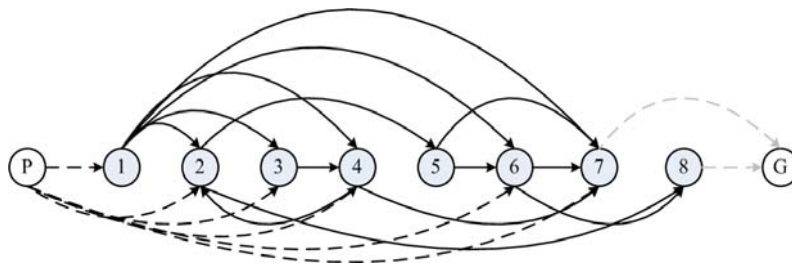


Figure 3.5: Connectivity of part to ground structural chain

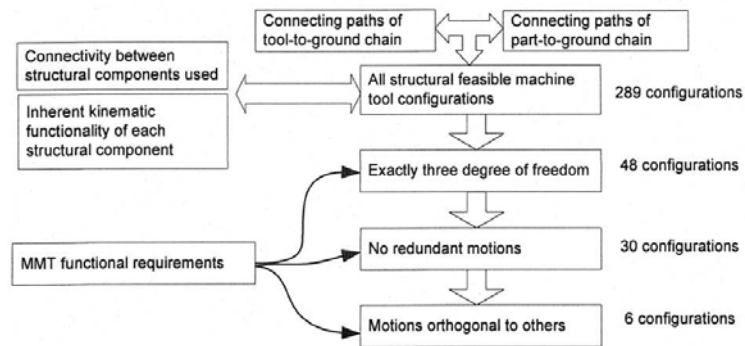


Figure 3.6: Reduction of configurations with functional requirements

implementing an expert system, containing a heuristic rule set that captures accepted design methodologies. An expert design system has the advantage of: ease of implementation, the ability to condense experience, rules of thumb, and judgement in heuristics, and has been demonstrated in the literatures [139–141] in kinematic structural syntheses of mechanisms, design of material handling equipment, and water retaining structures.

An expert system can provide a novice designer with an efficient method of selecting and reducing the candidate MMT configurations, as well as offer advice on the selection of design parameters to satisfy pre-defined attributes based on knowledge accumulated during the development of MMT. Attributes may include, for example: higher kinematic accuracy and lower energy consumption. To evaluate these attributes, the properties of the MMT structural representation are analyzed; specifically, the inter-connectivity, relative and absolute placement of structural components and DoF within the machine tool links.

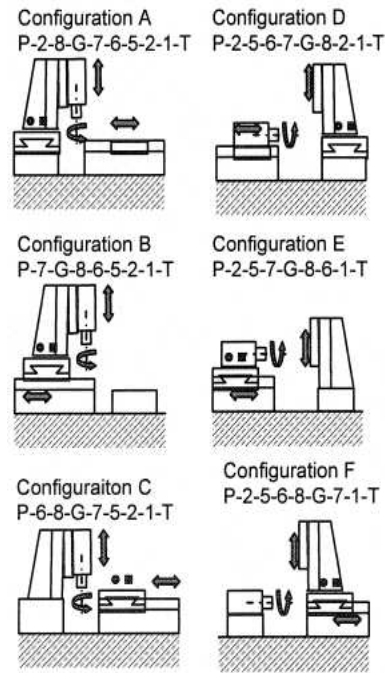


Figure 3.7: Reduced set of MMT configurations

In as much as the development of advanced design methodologies for the micro-scale machine tool remains an active research area, this study incorporates a greatly simplified sample rule set based on conventional-scale machine tool design methodologies. The rule set includes two fundamental design to govern the selection of acceptable design candidates. Rule 1 stipulates the need for even distribution of the kinematic links. Stacked axes and joints will compound the kinematics error and reduce the machine tool structure's rigidity. Rule 2 stipulates that motion stages should move the lightest mass in order to improve accuracy and response of the motion and reduce the power consumption of the system. The application of this rule set reduces the sub-set of candidate designs from six concepts down to two plausible candidate designs, as shown in Fig.3.8. Configurations B and F, each with three stacked axes on its tool-to-ground chain or part-to-ground chain, are eliminated by rule 1 while configurations A and E are eliminated by rule 2, as the spindle is much heavier than the micro-workpiece and these configurations have two moving links on the tool-to-ground chain. The two remaining configurations, candidate C (with vertical spindle), and candidate D (with horizontal spindle) each has two degrees of linear motion

on the part-to-ground chain and one linear motion on the tool-to-ground chain. Hence, these two configurations are widespread used in the MMT prototype design with three translational axes. Chen [142], Rusnaldy et al. [132] and Lee et al. [127] adopted the configuration C in their design. The configuration D has been utilized in the MMT designs of Vogler et al. [30] and Lee et al. [143].

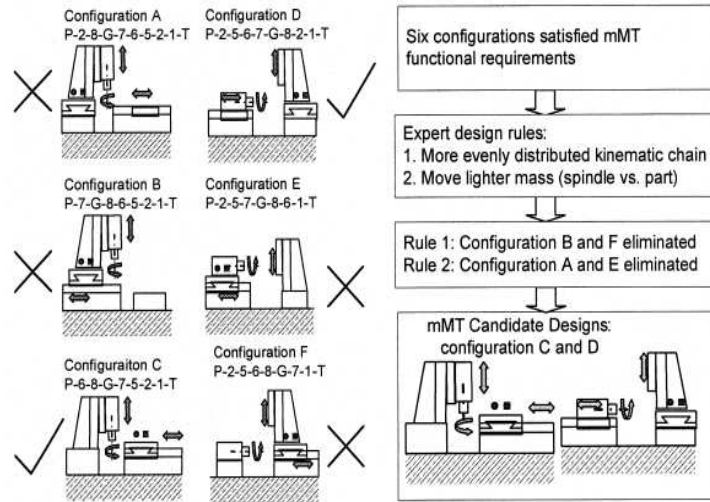


Figure 3.8: Reduction of configuration set with expert design rules

In this research, the configuration C with vertical spindle is adopted to design the prototype. The primary reason is the dynamometer installation. Because the maximal force capacity of the slide is less than the dynamometer gravity so that it must be installed perpendicular to the translational directions of the cross-slide.

3.4 Prototype development

In this thesis, the three-axis micromilling machine prototype is composed by a high speed electro spindle, three ultra precision linear motors, three linear encoders, an open numerical control system, a 3-component precision cutting force dynamometer, a CCD stereo microscope with $40\times \sim 240\times$ magnification, a HMI with G-code programming function, a vibration-isolation system and a spindle-cooling system. The entire prototype is shown in Fig.3.9. The dimension of the prototype is $400 \times 320 \times 100mm^3$ with $50 \times 50 \times 50mm^3$ workspace.

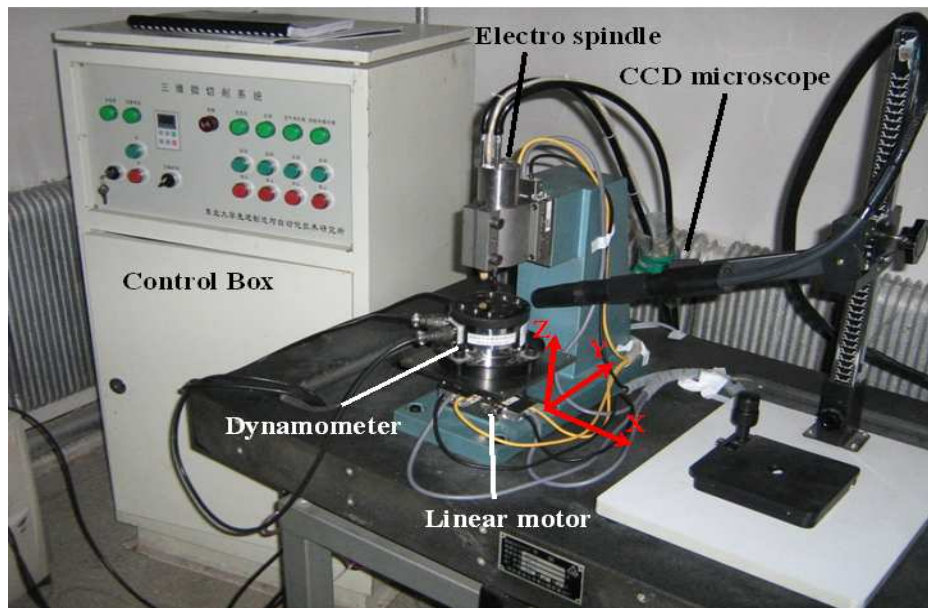


Figure 3.9: Three-axis MMT system

3.4.1 Feeding system

In order to realize the requirements of the machine motion, three micro feeding units MX80L are adopted to achieve long stroke, high precision position and excellent dynamic performance. Each unit is composed by a Parker permanent magnet servo linear motor and a Reinshaw linear encoder. The feeding unit shape is shown in Fig.3.10. Its length and width are 80mm , height is 25mm . The cross roller bearings are utilized to support the moveable platform. The stroke is 50mm . Two limit switches are installed in each two ends of the stroke. The home sensor is assembled in the middle point. The detailed inner structure is shown in Fig.3.11. The specifications of MX80L are listed in Table.3.2.

The resolution of Reinshaw linear encoder is 10nm . This configuration forms a closed-loop control of the feeding system, and improves the performance of the micromilling process.

In our design, the spindle unit will be installed on the Z direction slide, this will increase the static load in the translational direction of Z axis platform due to its gravity. Therefore, one extra air balance system is integrated into the Z platform in order to keep the Z motion smooth and fast response as Fig.3.12.



Figure 3.10: MX80L micro feeding unit

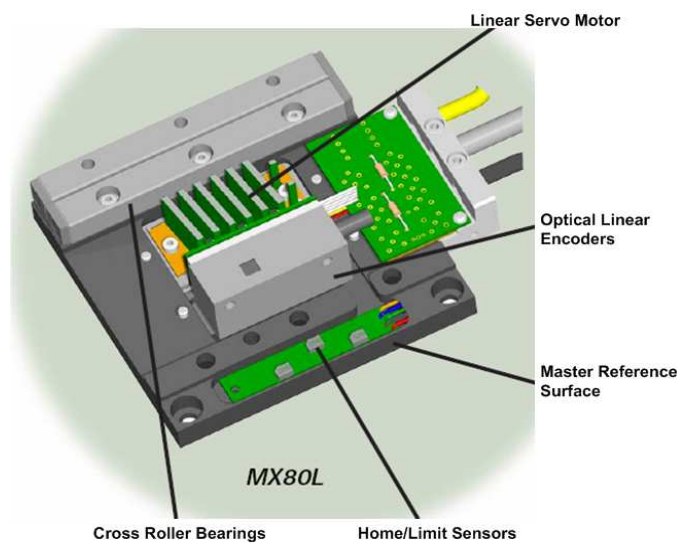


Figure 3.11: MX80L structure

3.4.2 Spindle system

A high speed electro spindle is integrated into the MMT system and moving in Z direction. The maximal rotating speed is $60,000rpm$. It is controlled by HMI interface and driven by inverter. The run-out in radial and axial directions are $3\mu m$, which is satisfactory with the requirements of micromilling operation.

3.4.3 Control system.

This control system structure is PC + 6K multi axis motion controller + VIX linear motor driver, shown in Fig.3.13. The PC can communicate with the 6K motion controller either by ethernet or serial port. Meanwhile the other I/O

Table 3.2: Linear motor specifications

Specifications	Unit	Value
Normal load capacity	Kg	8
Maximum acceleration	G	4
Normal velocity	mm/s	30
Peak force	N	12
Continuous force	N	4
Duty cycle		100%
Straightness & Flatness	μm	4
Unit mass	g	590
Carriage mass (unloaded)	g	282

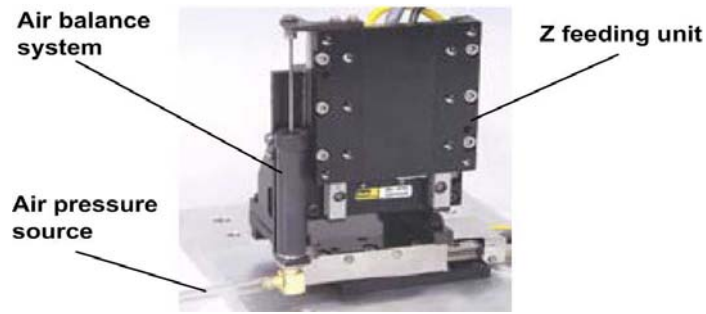


Figure 3.12: Z axis

signals also connected from the control panel to the motion controller. With the feedback of the linear encoders, the PID control are formed to improve the motion performance and the motor status are transferred into the PC to do the real-time monitoring. The entire control scheme adopts the multi-closed-loop principle, as shown in Fig.3.14.

3.4.4 Human machine interface (HMI)

Because 6K motion controller couldn't provide the interface for numerical control of the micromilling process with G-code compatibility, a specialized HMI software, Micromilling NC System (MNCS), is developed by Visual Basic (VB) 6.0. It includes 5 function module, communication, parameters setup, manual manipulation, program checking and auto manipulation. The MNCS structure is shown in Fig.3.15. MNCS can replace the programming environment of the 6K controller, and the G-code can be interpreted into the corresponding commands to the motion controller. The Fig.3.16 is one interface sample of the auto manipulation module which is working with G-code.

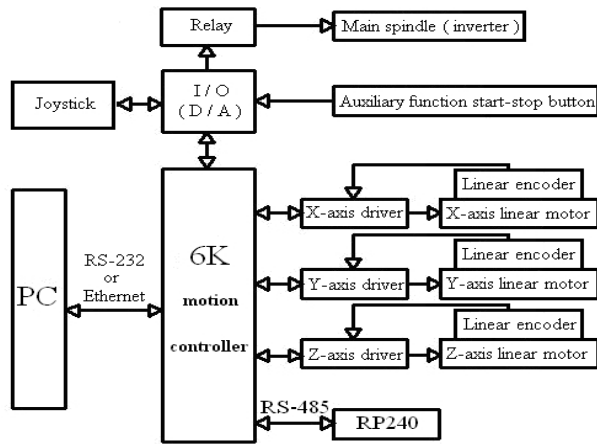


Figure 3.13: MMT control system

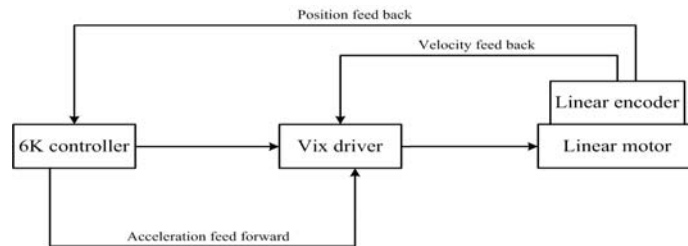


Figure 3.14: Multi-closed-loop control scheme

3.4.5 Microscope monitoring system

In the micromilling process, naked eye is unable to view the machining process due to the tiny tool size and workpiece feature. The microscope system is widely used in the monitoring of micro scale machining and operations.

In this design, a CCD microscope monitoring system is integrated in the entire test-bed. It is composed by a PC, an optical microscope, a Charge Couple Device (CCD), a light source, an image card, and a monitor. Its working principle is shown in Fig.3.17. The light source provides enough light on the objective, the optical microscope magnifies the view field and forms the image in the CCD pixel arrays. The image is transferred into the image card as the digital data and displayed in the monitor. The operator can do the monitoring and measurement through the PC and monitor.

In the microscope specifications, the most important parameters are mag-

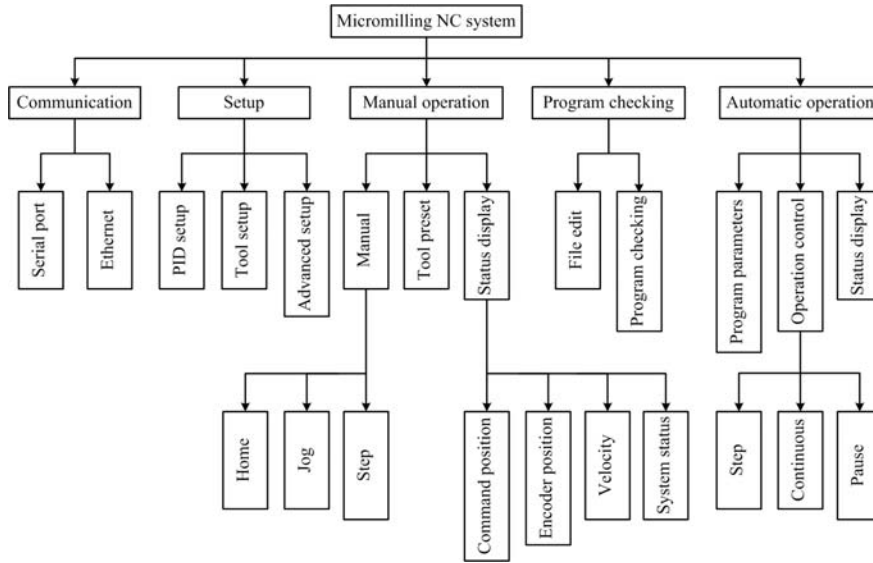


Figure 3.15: MNCS structure

nification and resolution. The magnification is the ratio between the image dimension and the actual objective dimension. It is composed by two factors. The first one is the optical magnification ratio, which is property of the lens in the optical scope. The second one is the digital magnification ratio, which is the diagonal length ratio between the CCD pixel array and the monitor screen. The actual magnification ratio is the product of these two factors values. The resolution is dependent on the optical magnification, image quality and CCD pixel array density. In one aspect, when the total CCD pixel number is a constant, which means the image size of the object in the CCD pixel array is a constant, so the pixel number for image is more, the image resolution is higher. In the other aspect, when the CCD pixel density is a constant, the higher magnification, the image size of the object on the CCD pixel array is larger. The image contains more pixels, hence the image resolution is higher.

Notice that the higher magnification means smaller depth of field (dof). This is a inherency of optical microscope. The dof is very critical to the image definition in 3D sense. Therefore, the variable magnification is obligatory to monitor the machining process, in order to achieve the best combination of magnification, resolution and definition.

A CCD stereo microscope VM-01, with $40\times \sim 240\times$ magnification is used to monitor the micromilling process and to do the workpiece measurement online.

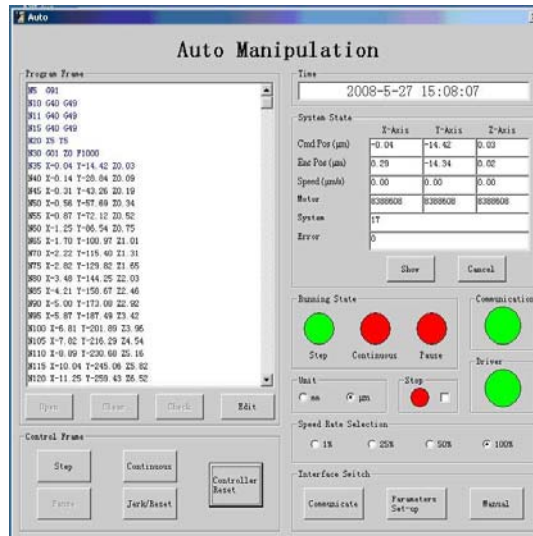


Figure 3.16: HMI of MMT prototype

3.4.6 Dynamometer

To the machining mechanism research, cutting force is very critical. Due to the tiny tool dimension, smaller depth of cut and feedrate per tooth, the cutting force is much smaller to the levels of several micro Newtons to a few Newtons. At the same time, the frequency of the cutting force is much higher due to the high speed rotation and other external disturbances. The dynamometer is the best option to record the cutting force exactly.

In the world wide cutting force research, the dynamometer sensor can be categorized into two classes, piezoelectric type and strain gauge type. The representative of the former one is the Kistler series. In our design, a strain gauge dynamometer, SDC-CJ3SAS, is chosen and integrated into the entire system. The performance comparisons between SDC-CJ3SAS and the corresponding Kistler piezoelectric sensor (type 9256 MiniDyn) are listed in Table.3.3.

The merits of piezoelectric dynamometer are higher natural frequency, finer resolution and higher sampling frequency. However, compared with the piezoelectric dynamometer, the strain gauge dynamometer has better linearity. So in the whole measurement range, one step calibration is enough to the strain gauge sensor. Due to the non-linearity of the the piezoelectric sensor, multi-step calibration is required, so the its actual measurement range is smaller than the nominal one [2]. The sensor calibration curves are shown in Fig.3.18.

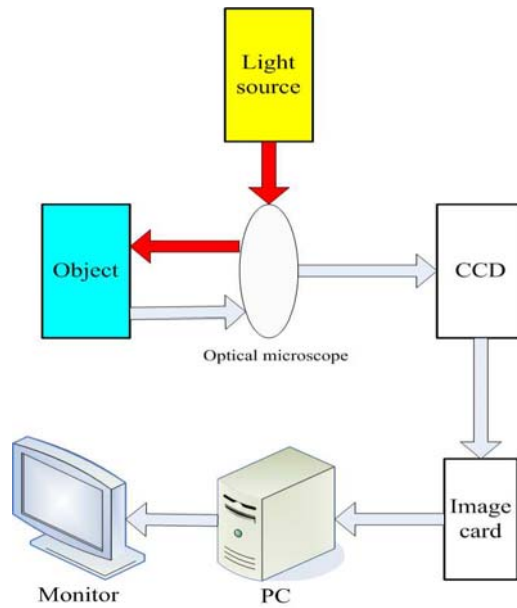


Figure 3.17: CCD microscope scheme

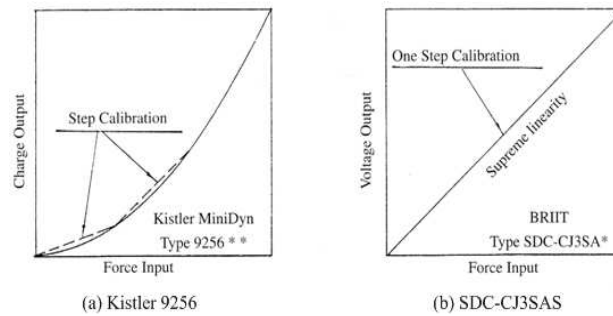


Figure 3.18: Calibration comparison between cutting force sensors [2]

The dynamometer system consists of a force sensor (type SDC-CJ3SAS), a 4-channel strain gauge amplifier (type FS-21/4), an analog to digital converter (A/D board type 1261K2), and a cutting force processing software (FAS-4D-3). The entire system is shown in Fig.3.19.

3.4.7 Other components

A granite platform is used as the base of machine tool in order to isolate the environmental vibration.

A water cycling system is used for cooling of the spindle temperature.

Table 3.3: Dynamometer comparison

Specifications	Kistler 9256	MiniDyn Type	SDC-CJ3SAS
Range of measurement: F_x, F_y, F_z	$\pm 250N$		$\pm 250N$
Linearity	Step calibration is necessary, within one step: $\leq \pm 0.4\%$ FSO (one step: $0 \sim 25N$)		$\leq \pm 0.3\%$ FSO Supreme linearity, one step calibration is enough
Crosstalk	$\leq \pm 2\%$		$\leq \pm 2\%$
Hysteresis	-		$\leq \pm 0.3\%$ FSO
Natural frequency	X,Y,Z: $\geq 5.0KHz$		X,Y,Z: $\geq 4.0KHz$
Operating temperature range	$0 \sim 70^\circ C$		$-20^\circ C \sim 100^\circ C$
Resolution	$2mN$		$10mN$
Sampling frequency	$40KHz$		$8KHz$

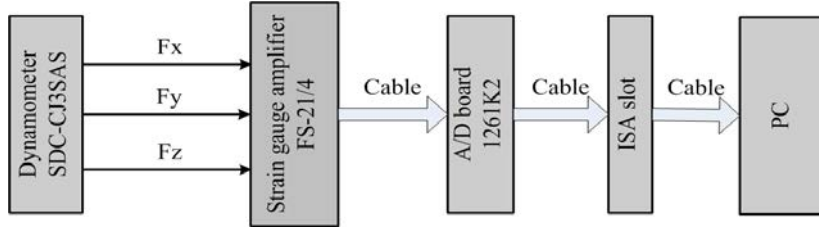


Figure 3.19: The entire dynamometer system

An air supply system is equipped to supply enough pressure to keep the Z platform moving smoothly.

3.5 MMT prototype test

All the linear motors are adjusted by the Proportional-Integral-Derivative (PID) controllers. The step impulse is used to test the appropriate PID parameters set. For each linear motor, the PID parameters are chosen with best dynamic performances and memorized into the motor drivers.

In order to evaluate the performances of the MMT prototype, the positional accuracy test and the machining test have been conducted on it.

3.5.1 Positional accuracy test

The evaluation criteria of the machine tool positional accuracy includes bi-directional positional accuracy, bi-directional repeatability and reversal value. According to the international standard ISO-230-2:1997, the positional accuracy tests of the motion platform utilized bidirectional evaluation method and linear circulation measurement. The target location points number $n = 10$, numbered sequentially by $j = 1, 2, \dots, n$, and the target measurement interval $t = L/n = 5mm$, with the cycle number $m = 5$.

The motion stage in each direction stopped steadily after it arrives the target point, the actual position is feedback from the linear encoder to the PC and displayed in the HMI. The data obtained from the test for Z axis are shown in Fig.3.20, and the X and Y directions are tested in the same way.

Point j	1		2		3		4		5		
P_j (mm)	0		5.510		10.025		14.953		20.042		
Direction	↑	↓	↑	↓	↑	↓	↑	↓	↑	↓	
Positional error	-0.38	-0.36	-0.46	-0.48	-0.38	-0.54	-0.55	-0.55	-0.33	-0.32	
	-0.54	-0.44	-0.44	-0.41	-0.36	-0.40	-0.35	-0.32	-0.42	-0.43	
X_{ij}	i	-0.44	-0.36	-0.38	-0.36	-0.38	-0.36	-0.37	-0.40	-0.50	-0.42
		-0.38	-0.46	-0.52	-0.42	-0.36	-0.56	-0.38	-0.36	-0.38	-0.39
(μm)		-0.54	-0.52	-0.42	-0.51	-0.48	-0.36	-0.57	-0.57	-0.37	-0.38
Point j	6		7		8		9		10		
P_j (mm)	25.051		30.066		34.879		40.027		45.048		
Direction	↑	↓	↑	↓	↑	↓	↑	↓	↑	↓	
Positional error	-0.53	-0.54	-0.43	-0.36	-0.51	-0.52	-0.49	-0.49	-0.44	-0.42	
	-0.37	-0.38	-0.42	-0.43	-0.37	-0.38	-0.41	-0.42	-0.52	-0.51	
X_{ij}	i	-0.43	-0.39	-0.33	-0.37	-0.43	-0.43	-0.38	-0.46	-0.39	-0.38
		-0.53	-0.42	-0.45	-0.45	-0.42	-0.43	-0.36	-0.36	-0.41	-0.41
(μm)		-0.42	-0.46	-0.46	-0.45	-0.43	-0.42	-0.41	-0.42	-0.44	-0.42

Figure 3.20: Positional accuracy test data for Z axis

In this test, X_{ij} is the positional deviation, which is the difference between the actual position and the theoretical position of the motion stage. \uparrow and \downarrow represent the test data are obtained from the positive and negative directions respectively, for example $X_{ij} \uparrow$ and $X_{ij} \downarrow$. Based on the evaluation approach in ISO-230-2:1997, the positional accuracy of the MMT is listed in Table.3.4. The test results show the bi-directional positional accuracy and the bi-directional repeatability of the prototype are in sub-micron level, which is satisfactory to

Table 3.4: The positional accuracy of the MMT prototype

Direction	Bi-directional positional accuracy μm	Bi-directional repeatability μm	Reversal value μm
X	0.2734	0.2682	0.04627
Y	0.2800	0.2618	0.0347
Z	0.4534	0.4510	0.0520

the requirements of micromilling operation.

3.5.2 Micromilling experimental tests

Some micromilling tests are done by the prototype. The 4-flute tungsten carbide micromill with $0.4mm$ diameter is chosen for most tests except the micro column machining. The workpiece is a specialized Mg-Zn-Y alloy for biomedical application [144]. Here, the slab, micro column, micro hexagonal spark and thin wall array micromilling tests are described in detail.

Slab experiment

In this test, the machining parameters are $30,000rpm$ spindle speed, $3\mu m$ feed rate per tooth and $15\mu m$ axial depth. With this setting, three slabs with $3 \times 2mm^2$ dimension are fabricated. The surface quality was measured by optical profiler and the average roughness value is $R_a = 0.123 \pm 0.0181\mu m$. The 2D and 3D surface figures from the profiler of one sample are shown in Fig.3.21. Obviously, the MMT prototype is able to produce the surface with high quality.

Micro column experiment

In this test, in order to achieve ultra high aspect ratio (> 10) micro column, a 2-flute tungsten carbide small diameter mill ($\phi 1.5mm$) is used, due to its longer flute length ($3.5mm$). The step by step deeper machining approach is adopted to create the final feature. The spindle speed is $30,000rpm$, feed rate per tooth is $0.5\mu m$, and the axial depth of cut in each step is $20\mu m$. The fabricated final results captured by SEM are shown in Fig.3.22. Its length is $3mm$, and the column diameter is $200\mu m$, the aspect ratio is 15. Due to the its length is longer than the field of view of SEM, it has to be viewed by two figures.

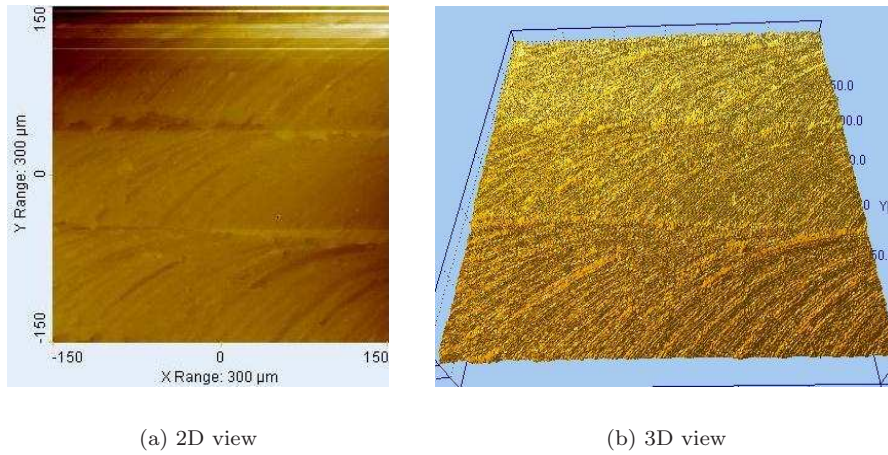


Figure 3.21: The micro slab surface figures from optical profiler

Micro thin wall array experiment

Through adopting the step by step deeper milling strategy, three micro thin walls are fabricated to form an array. The parameters setting are $30,000rpm$ spindle speed, $1.5\mu m$ feed rate per tooth and $20\mu m$ axial depth of cut in each step. Fig.3.23 includes the top view and front view of the thin wall array structure by SEM. The width of each wall is $100\mu m$, and the height is $500\mu m$.

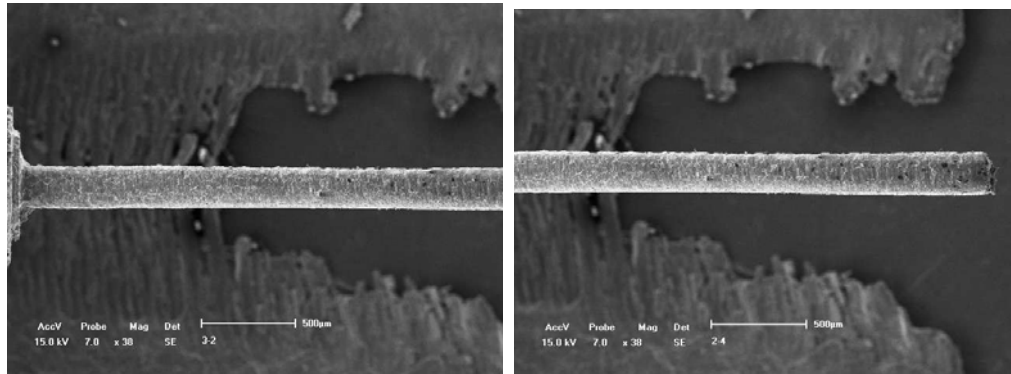
Micro hexagonal spark experiment

The strategy to fabricate a micro hexagonal spark is same with the micro thin wall array test. Its top and front views captured by SEM are shown in Fig.3.24. The diagonal length is $500\mu m$, and the height is $350\mu m$.

Therefore, these tests show the prototype are capable to fabricate the high aspect ratio and complex geometric microstructures on this material.

3.6 Conclusions

In this work, the critical technologies of MMT are discussed in detail. A 3-axis MMT prototype is developed with large workspace, precision resolution. Its structural configuration is selected by an expert design system. It is driven by three linear driving units, which is composed by a linear motor and a ultra precision linear encoder. The HMI interface is developed with compatibility

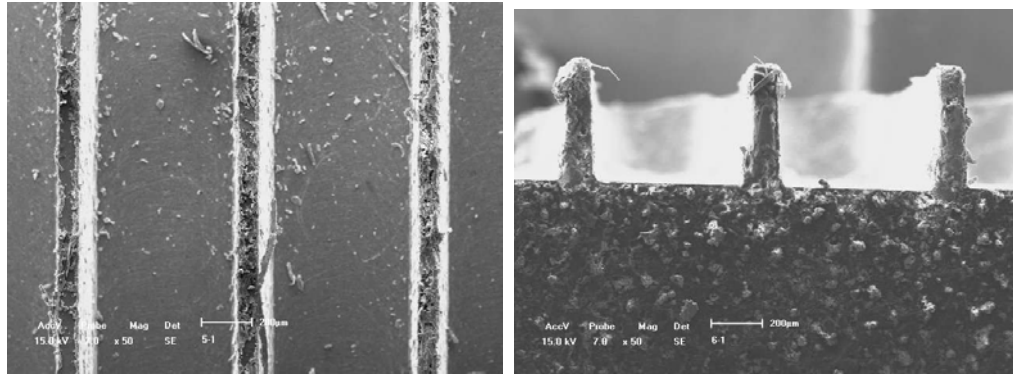


(a) Column bottom

(b) Column top

Figure 3.22: Micro column

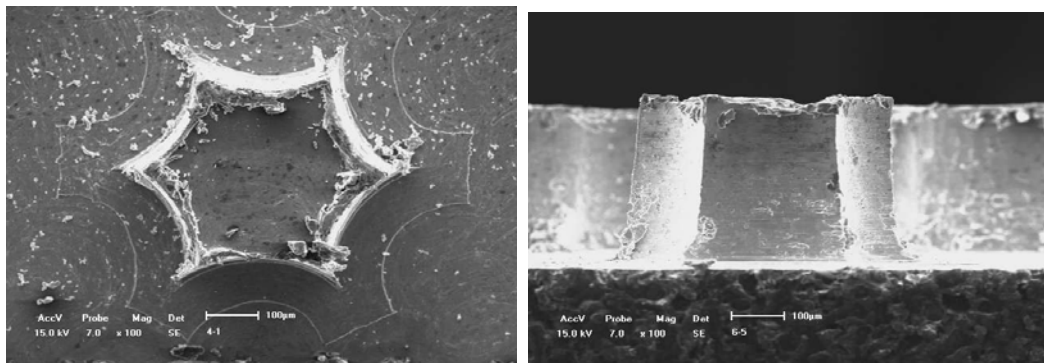
of G-code programming. Through the positional accuracy test of the motion stage, the prototype expressed the excellent performances. In the machining test, the MMT prototype is able to produce high quality surface with suitable machining parameters setting. Meanwhile, it is capable to create high aspect ratio and complex geometric structures as micro column, micro thin wall array and micro hexagonal spark.



(a) Top view

(b) Front view

Figure 3.23: Micro thin wall array



(a) Top view

(b) Bottom view

Figure 3.24: Micro hexagonal spark

Chapter 4

Workpiece Microstructure Effects in Micromilling

4.1 Introduction

In the micro scale machining, due to the huge dimension shrink of the cutting tool and machining parameters, the material microstructure affects the machining process greatly [23]. Therefore, the microstructure of workpiece material must be considered in order to understand the micromilling mechanism deeply and truly.

From the view point of material microstructure, the materials can be classified into three types, multi-phase polycrystalline, single-phase polycrystalline and single crystal. To the single crystal materials' effect to the micro cutting or precision cutting, some scholars have investigated in the laboratory level [81, 106, 145]. To the multi-phase polycrystalline material, the different grains have different metal phases, corresponding to different physical and mechanical properties. But to the single-phase polycrystalline material, the difference between each grain is just their crystal orientation. In this chapter, the Al-6061-T6 alloy is chosen as material for the workpiece to represent the multi-phase polycrystalline workpiece, and the researches on it are described in Sections 4.2 and 4.3. To the single-phase polycrystalline material, three types Oxygen Free High Conductive coppers are selected to do the experimental study.

4.2 Modeling of micromilling multi-phase polycrystalline material

4.2.1 Conventional cutting model

The conventional cutting principles are researched more and more, which is a classical model. A conventional orthogonal cutting model is depicted in Fig.4.1. The main factors are the tool geometry, cutting parameters and the workpiece macro physical characteristics.

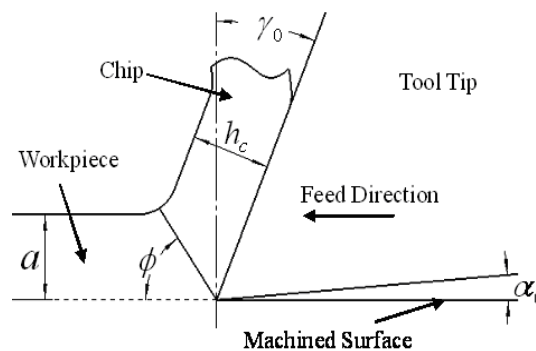


Figure 4.1: Conventional Orthogonal Cutting

Tool geometry

From the Fig.4.1, when the tool tip is engaged into the workpiece, because the cutting depth is much greater than the edge radius, the tool tip is considered as a sharp wedge. The tool geometric angles play very important roles in the cutting process.

Rake angle γ_0 : The effects of γ_0 are reducing the chip deformation, reducing the sliding friction between the rake face and the chip, making the tool tip sharper, improving the machining precision and reducing the machined surface roughness. The γ_0 is larger, the shear angle ϕ is larger, and the deformation of the chip is smaller, the cutting heat is less, but the tool tip stiffness is declining.

Clearance angle α_0 : The principles to choose a suitable α_0 are guaranteeing the tool stiffness and heat dispersion ability, making the tool tip sharper, and reducing the sliding friction between the flank face and the machined surface. The α_0 is smaller, the friction heat between the flank face and the machined surface is more, and the machined hardening phenomenon and residual stress are more.

Workpiece material

In macro scale, when the tool tip is cutting the workpiece, there are lots of grains with different metal phases being cut. Statistically, the influences of the material microstructure are neglected. The macro physical characteristics of the workpiece play important roles, such as the hardness, tensile strength, elastic module and thermal conductivity, so the workpiece material is regarded as isotropic.

4.2.2 Micro Cutting features

In the micro cutting process, because the cutting parameters and the tool tip geometric parameters are less than the grain size. The micro cutting principles are obviously different to the conventional cutting principles.

Micro tool geometry

An orthogonal micro cutting process is depicted in Fig.4.2 when the tool tip is engaged into the workpiece. Because the cutting depth is asymptotic with the edge radius r , the edge radius is important to the micro-cutting process. In a certain moment, when the tool tip is engaged into a grain, the cutting depth is a . When $a < h_m$, where h_m is the minimum chip thickness, the extruding and ploughing are dominant between the tool and the workpiece. Lots of materials are compressed and recovered on the flank face after the tool passed. Some materials are accumulated in front of the tool tip to change the cutting depth. Only when $a \geq h_m$, the chip is formed, and the material is removed. In micro cutting, when $a < r$, the effective rake angle γ_e is a function of r and a , as Eq.(4.1).

$$\gamma_e = \arccos\left(\frac{r-a}{r}\right) - 90^\circ \quad (4.1)$$

Multi-phase polycrystalline workpiece effects

Influence of the Grains with Different Metal Phases: In common, the grain sizes are between $10\mu m$ and $300\mu m$, and the edge radii of the tool tip are less than $5\mu m$. In the micro cutting operation, the cutting depth and the feed rate per tooth are in the order of the micron, even to the sub-micron level. When the tool passes the workpiece, along the length of the tool edge,

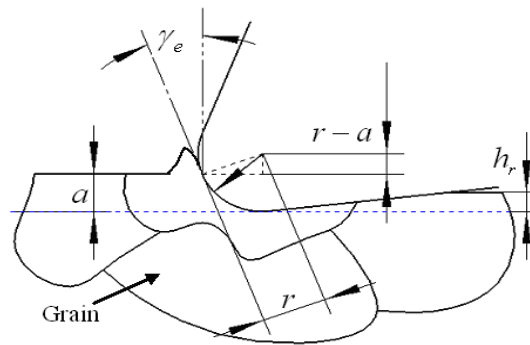


Figure 4.2: Orthogonal micro cutting

there are a few grains being cut, and the number of them are countable. Their influences are different because of their pronounced different physical properties, so the workpiece is regarded as anisotropic. Fig.4.3 is an illustration of the cutting zone in the micro mill's tool tip, when the influences of the metal grains are considered. Their influences are displayed in two aspects, which will be calculated in the Section 4.2.3. One is the chip formation process of different grains with minimum chip thicknesses h_m . The other one is the elastic recover heights h_r of the different grains after they are cut.

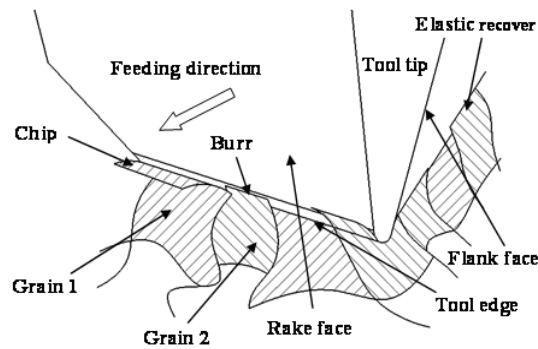


Figure 4.3: Micro cutting zone

Influence of the Grain boundary: The metal atoms, which exist in the grain boundary, arrange very abnormally. There are lots of impurities in the grain boundary, so the deform resistance of the grain boundary is greater than the normal grains, and it is not easy to be removed. Therefore, the chips usually break on the boundary.

4.2.3 Calculations of minimum chip thickness and elastic recover height

Calculation of minimum chip thickness

Fig.4.2 shows the orthogonal micro cutting process, which is a section view of the micro cutting zone (Fig.4.3). From this angle of view, the tool tip engages only one grain, which is isotropic. Because the cutting depth a is always smaller than the edge radius r , it is a large negative rake cutting process. In this process, the minimum chip thickness h_m plays an important role. Before achieving the h_m , some materials accumulate and form a little heave to increase the instantaneous cutting depth, until the material remove occurs. Thus there is a severe ploughing phenomenon and a large part of materials are compressed and recovered along the flank face. When h_m is achieved, the chip is formed and slips along the rake face. According to the reference [37], h_m is related to two factors. The first factor is the friction coefficient μ between workpiece and tool, which correlates with the physical properties of the grain and the tool material in this analysis. The second factor is the tool tip edge radius r . Given these two parameters of each grain, its corresponding h_m is governed by Eq.(4.2).

$$h_m = r(1 - \cos(1 - \cos(\pi/4 - \beta/2))) \quad (4.2)$$

where β is the friction angle between the tool and the workpiece as determined in Eq.(4.3).

$$\cos \beta = \frac{1}{\sqrt{1 + \mu^2}} \quad (4.3)$$

Calculation of elastic recover height

The tool edge passes and removes a part of these grains, and these grains under the flank face will recover with different recovery heights h_r due to different elastic moduli E they possess. h_r can be given by

$$h_r = \begin{cases} a, & \sigma \leq \sigma_P \\ h_m - \frac{\sigma_P \sqrt{r^2 - (r - h_m)^2}}{E}, & \sigma > \sigma_P \end{cases} \quad (4.4)$$

where σ_P is the proportional stress limit of each grain. r is the tool tip edge radius. σ is the compressing stress inflicting on the grain, which is calculated by

$$\sigma = \frac{E \cdot h_m}{\sqrt{r^2 - (r - h_m)^2}} \quad (4.5)$$

Eq.(4.4) demonstrates when σ is smaller than or equal to its σ_P , only elastic deformation occurs, and it will recover completely. When σ is greater than σ_P , it results in the elastic deformation accompanied with plastic deformation. This process is explained by the material compression strain-stress curve (Fig.4.4).

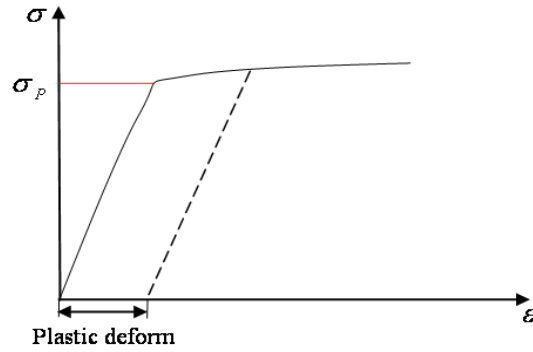


Figure 4.4: Material compression strain-stress curve

4.2.4 Micromilling Model

The micromilling process is as Fig.4.5. The workpiece is composed with many grains, which are classified by their metal phases. When the edge radius is known, different metal phases correspond to different minimum chip thicknesses due to different friction factors.

In per revolute of the micro mill, the tool tip passes a few grains. In order to simplify the model, assume only 2 grains in the path of the tool rotary as Fig.4.5. In Fig.4.5(a), there is no material removed. With the tool feeding, as depicted in Fig.4.5(b), the minimum chip thicknesses of two grains are still not achieved, and there are only ploughing between the tool tip and the workpiece. After the tool passed, the elastic recover of the grains occur. In Fig.4.5(c), the tool feeds continuously. To the grain 1, its minimum chip thickness is achieved, and the chip is formed. Except in the entrance of the engagement, where the cutting depth is small. But to the grain 2, its minimum chip thickness is still not achieved, and the process likes the last step. In Fig.4.5(d), when the tool tip passes 2 grains again, because the grain 1 is cut in the last step, so the tool tip ploughs the machined surface, but the material in the entrance may

be removed. At this revolte, the minimum chip thickness of the grain 2 is achieved, and the material remove occurs in grain 2, except the exit of the engagement, also because the cutting depth here is smaller too.

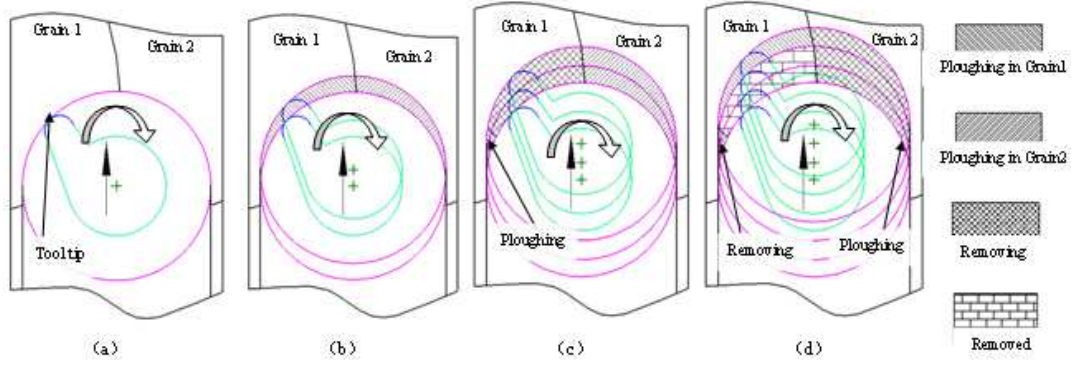


Figure 4.5: Micromilling process

Cutting forces predication

According to the traditional milling theory, when the cutting speed is kept as constant, the milling force F is proportional to the axial depth of cut a_P , and feed rate per tooth f , as Eq.(4.6). K_P is the machinability factor, which depends on the machining condition and workpiece material properties [146]. Because of the machining ability differences of different metal phases, they have different K_P , which induce different cutting forces amplitudes occur on the edge radius when the tool engages into them, and this causes a vibration with low frequency. When the edge moves in a grain, the minimum chip thickness plays an important role. There are obvious cutting forces differences between ploughing process and cutting process, which corresponds to the minimum chip thickness influences in one grain. This is high frequency vibration of the cutting forces. Actually, both of these two cutting forces vibrations are added together.

$$F = K_P * a_P * f \quad (4.6)$$

Surface generation predication

Except for the tool passing traces, there is an obvious influence from different grain phases on the machined surface. Because their different elastic modules, after the tool passing, they will recover to different heights. So there are lots of

heaves with different heights on the machined surface. And some friction traces caused by ploughing exist on the surface, which correspond to the minimum chip thickness influence.

4.3 Experiments of micromilling multi-phase polycrystalline material

4.3.1 Experimental setup

A four-flute tungsten carbide micromill with 0.4mm diameter is used. Its edge radius is $1.36\mu\text{m}$ measured by SEM (Fig.4.6).

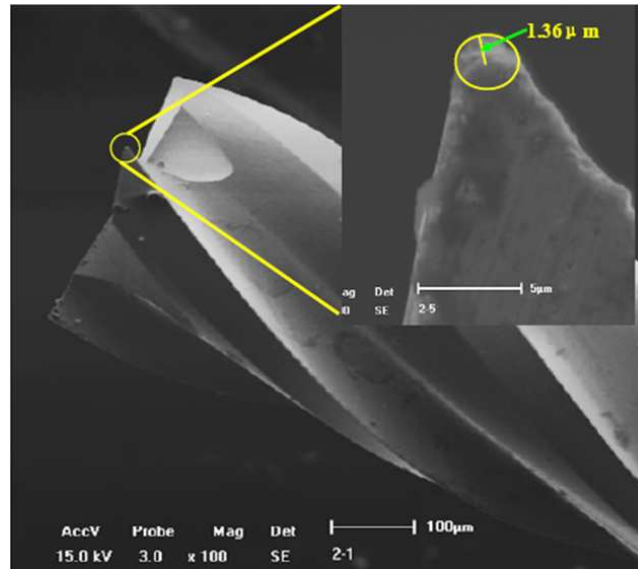


Figure 4.6: Micromill with cutting edge

The workpiece is Al6061-T6 alloy, and its microstructure is shown in Fig.4.7. It is composed by two phases, soft phase and brittle phase. The white part is the soft phase, which is mainly composed by Al, and its average grain intercept length is $10.238\mu\text{m}$. The black part is the brittle phase dispersing on the Al base, which mainly is acicular silicon. The material properties [147] and the calculation results of h_m and h_r based on Eqs.(4.2-4.5) for the soft phase and brittle phase are listed in the Table.4.1. From the comparison, h_m in the brittle phase grain is smaller than the soft phase grain, which means the chip forms easier in the brittle phase grain. h_r is smaller in brittle phase grain than in soft phase grain, which means the recovery height is lower in the brittle phase

Table 4.1: Al6061-T6 material characteristics and calculated results

Item	Soft phase	Brittle phase
E (GPa)	70	8.7
μ	0.3	0.5
σ_P (MPa)	240	0.04
h_m (μm)	0.2689	0.2031
h_r (μm)	0.2655	0.2021

grain. These calculations reflect the physical prosperities of different phases will lead to different machining phenomena, although it is just a qualitative calculation, because many other material properties and machining variables are not contained in Eqs.(4.2-4.5).

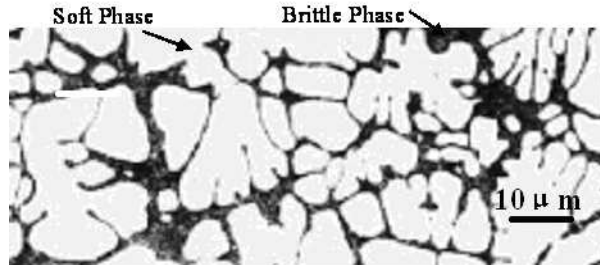


Figure 4.7: Microstructure of Al6061-T6

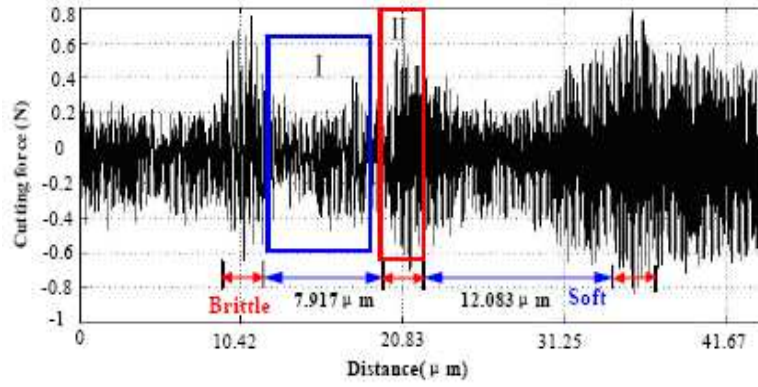
4.3.2 Experimental results

A series full slot micromilling experiments are conducted to validate the model. The experimental results of cutting force, surface generation and chip formation are discussed.

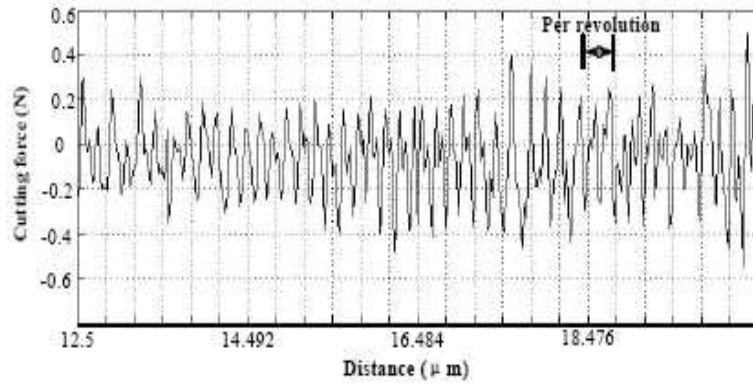
Cutting forces analysis

The tangential cutting force of a test is shown in Fig.4.8. In this case, the spindle speed is 30,000rpm, feedrate is 10mm/min, and the axial depth of cut is 20μm.

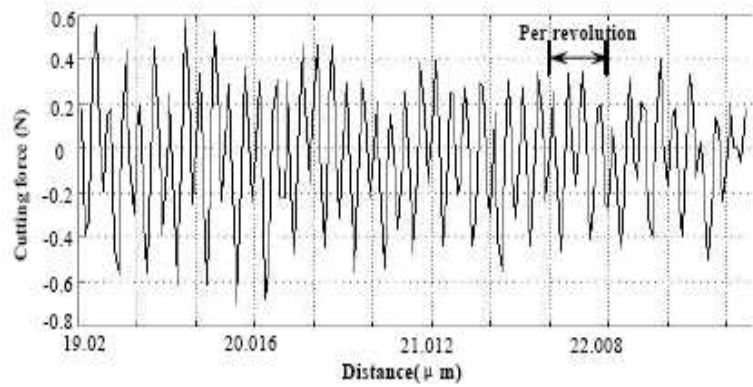
Because different grains with different machining abilities, the cutting forces in different grains are different. From Fig.4.8(a), the cutting force is small when the tool center engages into the soft phase grain, and to the brittle phase, the cutting force is great. The distances of the soft phase correlate its average



(a) Origin



(b) I magnification



(c) II magnification

Figure 4.8: Tangential cutting force

intercept length. The Fig.4.8(b) and Fig.4.8(c) are the local magnifications of the I and II parts, and they display the cutting forces corresponding to the soft phase and brittle phase respectively. In Fig.4.8(b), in per revolute, there is less than 4 large-scale peaks, because the feedrate per tooth is smaller than the minimum chip thickness of soft phase. Many teeth passing are just plowing and extruding, so there are some small-scale peaks in the signal history. In Fig.4.8(c), the large-scale peak number in per revolute is more than the one in Fig.4.8(b), this is because that the minimum chip thickness of brittle phase is smaller than the soft phase, which means that it is easier to be removed.

Surface generation analysis

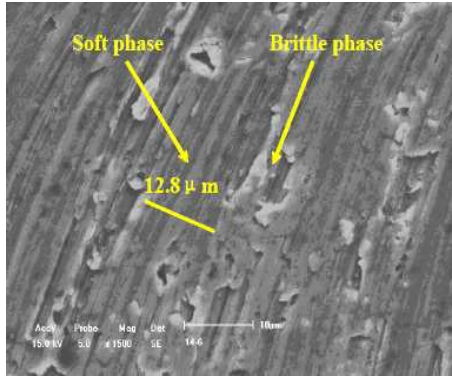
SEM and CHR 150 Stil Micromasure 2 optical surface profiler are used to measure the machined slot bottom surface. In this case, the spindle speed is 25,000rpm, feed rate is 20mm/min, axial depth of cut is 10 μ m.

The SEM photo of the micromilled bottom surface is shown in Fig.4.9(a). Fig.4.9(b) is the surface measured result using CHR 150 Stil Micromasure 2 optical surface measurement system. Fig.4.9(c) is the roughness curve corresponding to the line in the Fig.4.9(b).

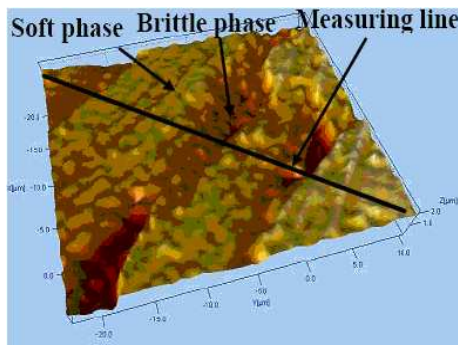
In Fig.4.9(a), the tool passing paths can be seen. And a few concaves formed on the brittle phase grains with chips around them, which correlate well with the previous description. In Fig.4.9(b) and Fig.4.9(c), the large-scale curves correspond to the brittle phases. And the small-scale curves correspond to the influence of the minimum chip thickness. And the distances shown in Fig.4.9(a) and Fig.4.9(c) strongly correlate with the average intercept length of the soft phase.

Chip formation

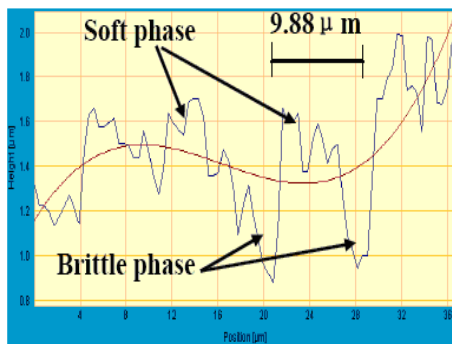
Fig.4.10 shows the chips attached on the bottom of the micro end-mill. These chips are highly fragmented, and discontinuous, indicating the interrupting nature of the grain boundaries in the chip formation process.



(a) SEM photo



(b) 3D figure



(c) Surface profile

Figure 4.9: Micromilled bottom surface

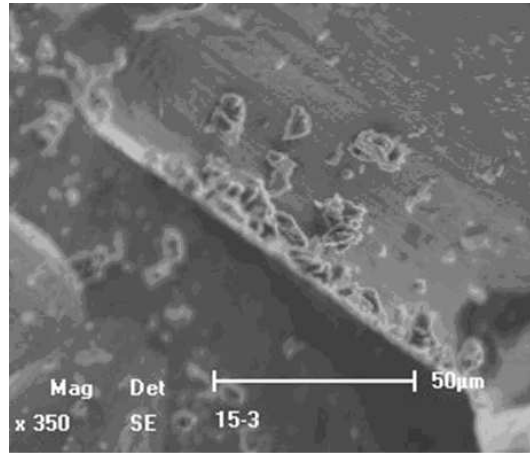


Figure 4.10: Chips in micromilling

4.4 Micromilling single-phase polycrystalline material research

In the previous study of this chapter, micromilling on multi-phase polycrystalline material is investigated. We found that the material microstructure affects the surface generation in the micromilling process, so the surface quality will be degraded due to the material anisotropy. In this section, the single-phase polycrystalline materials with different grain sizes are chosen as workpiece, in order to understand the grain size and crystal orientation effects to the surface roughness.

4.4.1 Workpiece material

The workpiece is Oxygen Free High Conductive (OFHC) copper. They are processed by Equal Channel Angular Pressing (ECAP) to achieve different grain sizes [3, 148]. All the workpieces are provided by Prof. Tóth at Laboratoire de Physique et Mécanique des Matériaux (LPMM) in the Université Paul Verlaine de Metz.

ECAP process

Equal channel angular pressing (ECAP) in particular has drawn considerable attention due to its potential to produce ultrafine-grained or in some cases nanometer grain size materials in bulk form. It is now well known that materials with such small grain sizes have extraordinary properties, such as simultaneous

ultrahigh strength and high ductility as well as the capability of superplastic forming. They therefore have great potential for technological applications [3].

In ECAP, a billet is deformed in a narrow deformation zone at the plane of intersection of two die channels whose cross sections are of equal area, and the strain mode approximates closely to simple shear (ideal case, Fig.4.11). As the overall billet geometry remains nearly constant during ECAP, multiple passes and different routes are possible without any reduction in cross-sectional area. This allows materials to be deformed to very high plastic strains that cannot be readily obtained via more conventional manufacturing processes, such as rolling or extrusion. In general, plastic deformation takes place in a broad zone the shape of which sensitively depends on factors such as contact friction, material flow response, backpressure and die design. It appears that the simple shear viewpoint is approached when the inner and outer corners of the die are sharp, there is no friction at the die walls, backpressure is applied, and the material behaves in a rigid plastic fashion. In practice, however, these conditions may only be partly fulfilled [3].

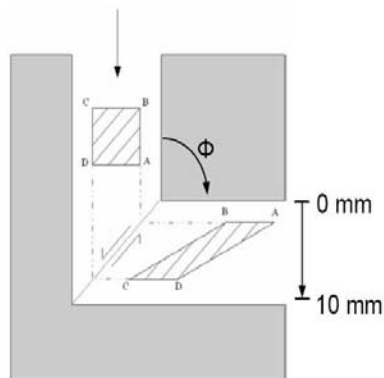


Figure 4.11: ECAP principle [3]

The grains with initial type as sphere in the billet will be extruded to the elliptical sizes after a few passes of ECAP. With the increase of the ECAP pass numbers, the elliptical grains are extruded and split into many smaller size grains. This progress is shown in Fig.4.12.

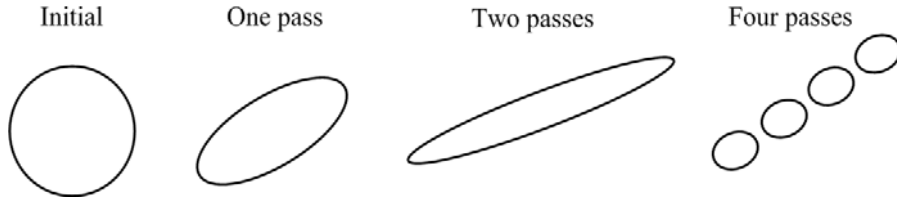


Figure 4.12: Grain shape and size evolution during ECAP

Workpiece preparation

Three billets of OFHC copper (99.99% purity) with dimensions of $9.9 \times 9.9 \times 100mm^3$ are cut by WEDM from extruded 4N copper rods (Provided by Goodfellow). The channels of the ECAP die have a square cross section of $10 \times 10mm^2$ meeting at an angle $\Phi = 90^\circ$. All corners and edges of the die are sharp as Fig.4.11. The ECAP is done at room temperature (homologous temperature = 0.22) with a crosshead speed of $1mm/s$ using MoS_2 as lubricant.

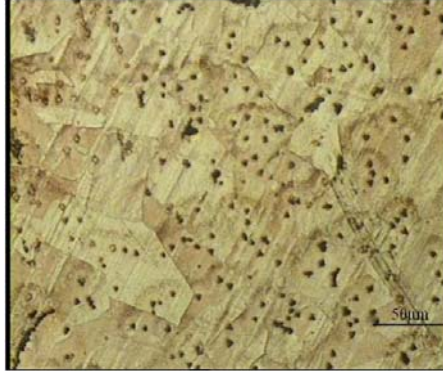
In this test, the first billet doesn't experience ECAP and keep it as the initial grain size. The second and third billets are processed by ECAP with two and eight passes respectively. Therefore, their grain sizes are obviously different. Their metallographic and average grain size are shown in Fig.4.13. They coincide with the grain size evolution progress described in Fig.4.12.

4.4.2 Experimental design

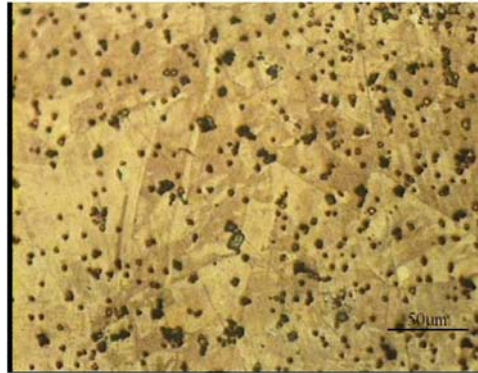
From the literatures' study, the feedrate per tooth is critical to the bottom surface roughness in the milling operation [149], as indicated by Eq.(4.7), where FPT is the feedrate per tooth, r is the tool nose radius, T_N is the number of teeth of the cutter, C is the ratio between the average roughness R_a and the Peak-to-Valley roughness R_t .

$$R_a = \frac{FPT^2}{8C[r \pm (FPT \cdot T_N/\pi)]} \quad (4.7)$$

Therefore, the feedrate per tooth and material grain size are chosen as the machining variables, and their effects to the average surface roughness (R_a) are investigated. The other machining parameters are set to constant and listed in Table.4.2.



(a) 0 pass ($55.66\mu m$)



(b) 2 passes ($35.54\mu m$)



(c) 8 passes ($4.32\mu m$)

Figure 4.13: OFHC copper with different grain size

Table 4.2: Experimental setup

Item	Value
Tool type	4-flute carbide micromill
Tool size	0.4mm diameter
Edge radius	1.36 μm
Rotating speed	40,000rpm
Axial depth of cut	10 μm
Machining type	Slot milling

Table 4.3: Experimental design and R_a results

Test No.	Workpiece type (Pass number)	Feedrate per tooth (μm)	R_a (μm)	STD (μm)
1	0	0.1	0.077933	0.016398
2	0	0.2	0.090946	0.008289
3	0	0.3	0.13047	0.030014
4	0	0.6	0.149074	0.091042
5	0	1	0.158083	0.020598
6	2	0.1	0.153807	0.059501
7	2	0.2	0.137	0.021166
8	2	0.3	0.086833	0.006804
9	2	0.6	0.152333	0.028868
10	2	1	0.164	0.040112
11	8	0.1	0.0828	0.01254
12	8	0.2	0.1116	0.022642
13	8	0.3	0.094867	0.021499
14	8	0.6	0.110967	0.021703
15	8	1	0.168714	0.017623

The friction coefficient between the carbide and the OFHC copper is 0.35 from Ref. [147]. According to Eq.(4.2), the corresponding minimum chip thickness is about 0.2508 μm . Hence the feedrate per tooth is chosen from 0.1 μm to 1 μm in order to cover the minimum chip thickness. The experimental design is according to the Taguchi's orthogonal array in Table.4.3.

4.4.3 Experimental surface roughness result and discussion

For each milled test slot, the bottom surface was scanned by CHR 150 Stil Micromasure 2 optical surface profiler three times, with scanning area $0.1 \times 0.1mm^2$ each time. The average surface roughness (R_a) value for this slot is their

average measurement results, also listed in Table.4.3 and shown in Fig.4.14.

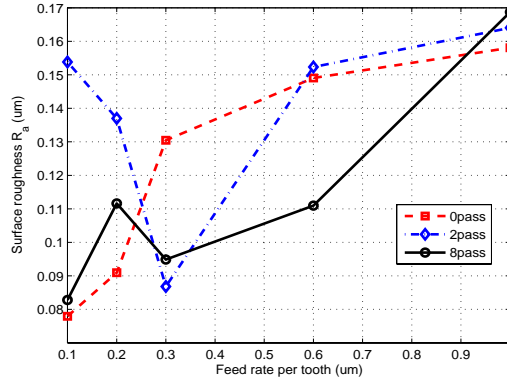


Figure 4.14: R_a experimental results

Through the experimental average surface roughness results, we found there is no obvious discipline for each workpiece. It means to the micromilling on single-phase polycrystalline material. The grain size and crystal orientation effects to the surface roughness would require further investigations to find the deeper discipline.

4.5 Conclusions

Through micromilling on multi-phase and single-phase polycrystalline materials, the material microstructure effects to the micromilling mechanism are understood deeply. Some important results are listed as follows:

1. The grains with different metal phases in the multi-phase polycrystalline material induce the cutting force with additional vibration.
2. To the multi-phase material, different metal phases correspond to the different minimum chip thicknesses and elastic recover heights, which degrade the surface quality.
3. The crystal orientation and grain size effects are very little, which would require further investigations.

Based on the research results, we suggest if the grain size in the multi-phase polycrystalline material can be reduced into nano-scale, the dimension

of workpiece microstructure could be much smaller than the tool edge radius. Therefore, the workpiece can be regarded as homogeneous, which is similar to the conventional machining theory. This research will be conducted in future.

Chapter 5

Micromill Tip Trajectories Investigation

5.1 Introduction

Due to the special geometric features of micromill, the tool flute trajectories are obviously different to the common sense. In this chapter, an exact model is developed to predict the tool tip trajectories for a two-flute cutter, and their effects to the machining error, surface quality, and tool life are discussed in detail.

In the macro scale, Thusty and Bryan [150] were the pioneers focusing on this issue. The machining error caused by the rotating mill were evaluated by them. Kline et al. [151] have reported the effect of cutter run-out on the shifting of cutting force from tooth passing frequency to spindle frequency. Kim et al. [152] built the end mill as a rotating tapered, loment-wound composite, Timoshenko shaft for its vibration and stability analysis, but this tool shape was used very few in the industry. Altintas and Budak [153] proposed a speed-dependant transfer function for the stability analysis in milling operation. Montgomery and Altintas [154] developed a trochoidal tooth path trajectory model for the tool center and flutes of mill, including the influences of the process geometry and dynamic vibration. Lee et al. [155] proposed a simple run-out measuring method for a four-flute mill cutter. They adopted a dial gauge to do the measurement and calculate the run-out parameters. However, these approaches were not suitable for the high speed machining. Gagnol et al. [156] integrated the approach in the Ref. [153] to elaborate the new stability lobes for a high speed spindle. Nakkiew et al. [157] proposed a simple and practical method

to quantify the radial error of the cutter/spindle system at high speed rotation through measuring the size of the cutting marks produced by the end mill.



Figure 5.1: Geometric comparison between (a) macro mill and (b) micromill

Unfortunately, these macro scale methods are not suitable to the micromilling operation. The most important reason is the geometric difference between the micromill and the macro mill. As compared in Fig.5.1, the milling tool in the macro scale, its tip dimension is in the same scale with the shank dimension, a few millimeters. So it has much stronger stiffness to resist its radial bending deformation, and its assembling error in the tool holder is very little compared to its tool tip diameter, which can be neglected actually. To the micromill, the tool shank is in the millimeter order, which is adapted to the commercial tool holder. A big taper with slope ratio almost more than 10 transits the tool profile from the shank in a few millimeters to the tool tip with reduced diameter in the sub-millimeter level, even to the several microns. The tiny tool tip dimension is the pronounced feature of the micromill, which is used to create the micro size structures on the workpiece. The dimensional difference between the tool shank and tool tip is more than 20.

In addition, the rotating speed during the micromilling process is always exceeding $20000rpm$. Therefore the micromill tip dimension in milling status is larger than its nominal diameter obviously (Fig.5.2). This phenomenon is induced by some reasons and has attracted some researchers' interests. Antoine et al. [158] calculated the first vibration frequency on a small size high speed rotor which is suitable for the micromilling. Bao and Tansel [102] evaluated the tool run-out influences in the micromilling process. They calculated the run-out value by the experimental cutting force for two tool holders. Jun et al. [104] employed a capacitive sensor to measure the tool shank faults and a high magnification optical scope to measure the tool tip faults. But due to the smaller depth of field of the microscope and the high speed revolution, the uncertainty of the tool tip faults measurement was greater. They found the micromill stability was significantly affected by the second mode of the

micromill. Filiz and Ozdoganlar [159] used the measurements results of spindle-axis offsets and tool tilt angles from [160] to understand the effects of the tool setup errors on the dynamic tool tip run-out for varying spindle speeds.

From the literatures' study, the researchers resorted to understand the effects of run-out and vibration to the machining process. The run-out can be defined by a offset value ρ and a phase angle λ [155]. To the conventional mill tool, the tool tip run-out value can be obtained directly through the shank measurement. But to the micromill, the tool tip run-out is calculated because it is very difficult to be measured directly [102, 159].

In this chapter, the tool tip trajectories of a two-flute micromill are investigated in detail considering the effects of the tool radial error motion and the tool tip vibration at high speed rotation. A tool tip trajectories model is developed to predict the cutter flute positions in the corresponding rotating instant. The model includes the effects of geometrical errors, such as spindle run-out, tool assemble error due to the chuck inaccuracy, tool fabrication error in the tool grinding process. In order to integrate the tool tip vibration effects under high speed rotation to the trajectory model, a rotor dynamic model is developed for the cutter/spindle system. Based on the tool flute trajectories prediction, the chip thickness, cutting force, machining error, and surface generation are predicted too. This work is useful to the tool condition optimization [161], machining error compensation [43], and workpiece burr minimization [162].

5.2 Model development

A model is developed to predict the tool tip trajectories of a 2-flute micromill under high speed rotation. The model hierarchical structure is shown in Fig.5.3, including "Input", "Model" and "Output" layers.

In the "Input layer", the tool tip radial error motion and tool unbalance are obtained based on the measurement results and proposed calculation approaches described in Section 5.3. Two models, a rotor dynamics model and a tool tip trajectories model, are contained in the "Model layer". The tool tip radial translation is calculated from the rotor dynamic model and input to the trajectories model. In the "Output layer", the results of flute trajectories, chip thickness, cutting force, slot width and surface quality can be obtained from the tool tip trajectories model. The vibration modes and the stability of the

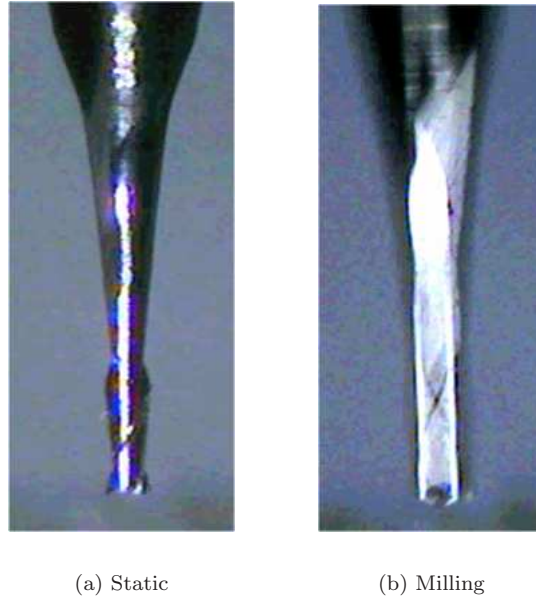


Figure 5.2: Tool tip dimensions comparison

cutter/spindle system can be acquired from the rotor dynamic model directly, but they will not be described in this thesis.

5.3 Measuring method

After setting the micromill to the spindle/clamp system, measuring the tool tip radial error motion and the rotor unbalance are critical to calculate the tool tip trajectories. Due to the sub-millimeter dimension of the tool tip and the complex shape of the twisted fluted section, it is impossible to find a proper instrument to do the measurement directly on the tool tip. Hereby, new methods are required to detect the tip radial error motion.

The dial gauge [155], capacitive probe [163] and laser sensor [159] are widely used to examine and quantify the spindle/cutter system radial error motion, especially the run out, in conventional milling. The dial gauge setup is cheaper but with greater uncertainty and veteran experiences are required. Because the commercial capacitive probes almost require a flat target in square millimeter order as its sensing area, but the micromill shank diameter is only 3 or 4 millimeters, to our tool is 3.175mm ($1/8''$), which can't supply so large

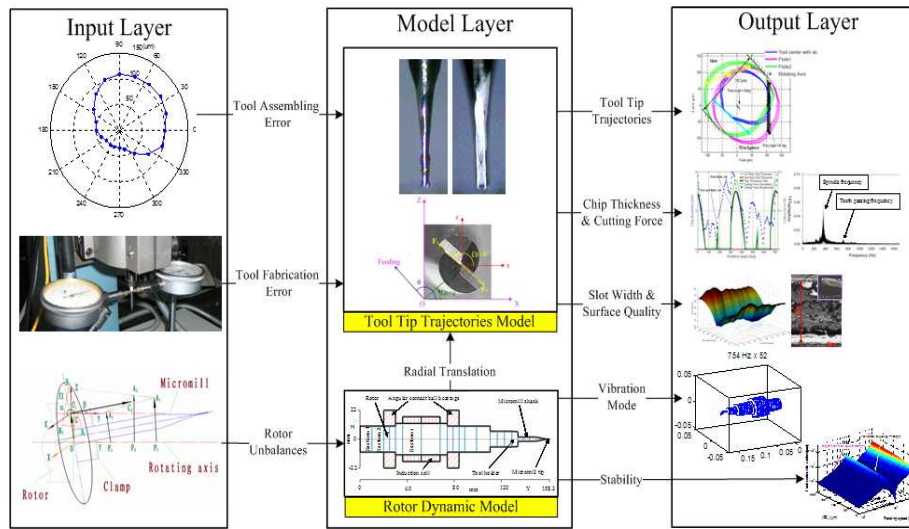


Figure 5.3: Trajectory model hierarchical structure

flat sensing area. So according to Vallance’s work [105], the measurement with capacitive sensor under this condition will be not accurate. The detecting point of laser can be as small as a few micron size. It is very important to do the non-contact measurement on the tool shank, but the laser experimental setup is expensive. And the precision arbor, like reference ball or cylinder, is not used in our measurement, because it can’t reflect the actual running accuracy of the cutter/spindle system [157]. In this chapter, the dial gauges are adopted to do the measurement, and the measured results are validated by the laser test.



Figure 5.4: Measurement setup

5.3.1 Measurement setup

The proposed measurement setup is shown in Fig.5.4. Two dial gauges are employed with elaborately aligning and contact. Their probes press on the tool shank with the same pressure in the opposite directions, in order to eliminate

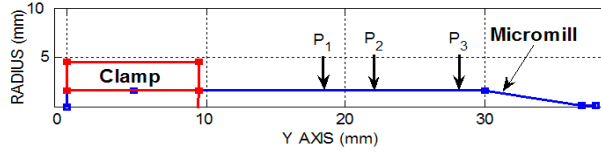


Figure 5.5: Measuring points distribution

Item	Value
Tool length	38mm
Shank diameter	3.175mm
Shank length	30mm
Taper length	7.5mm
Tip diameter	152 μ m
Tip length	0.5mm
Flute No.	2

the tool bending caused by contact pressure.

The micromill used for the model and experiment in this study is a two-flute tungsten carbide tool. The tool geometry is shown in Fig.5.5. The detailed tool geometric features are listed in the Table.5.1

The measurement is conducted on three different positions P_1 , P_2 and P_3 on the tool shank as Fig.5.5. In this test, the tool clamp length is 9.5mm, the Y coordinates of P_1 , P_2 and P_3 are 18mm, 22.2mm and 28.7mm respectively.

In each measuring point, the multi-step method is adopted, with 5 revolutions and 20 steps per revolute in this work in order to reduce the measurement uncertainty [164]. The measurement results of each point are averaged as their radial error motion value and shown in Fig.5.6 with 18° interval in their section polar frames.

5.3.2 Tool tip radial error motion

By linear interpolation, 20 straight lines are formed to connect the radial error profiles of P_1 and P_3 along the Y axis (the spindle rotating axis). Then, the tip radial error motion is represented by the points of these 20 lines corresponding to the tool tip Y coordinate (Fig.5.7), which is used for this analysis. The largest radial error value is about 110 μ m from 20° to 90°, which is in the

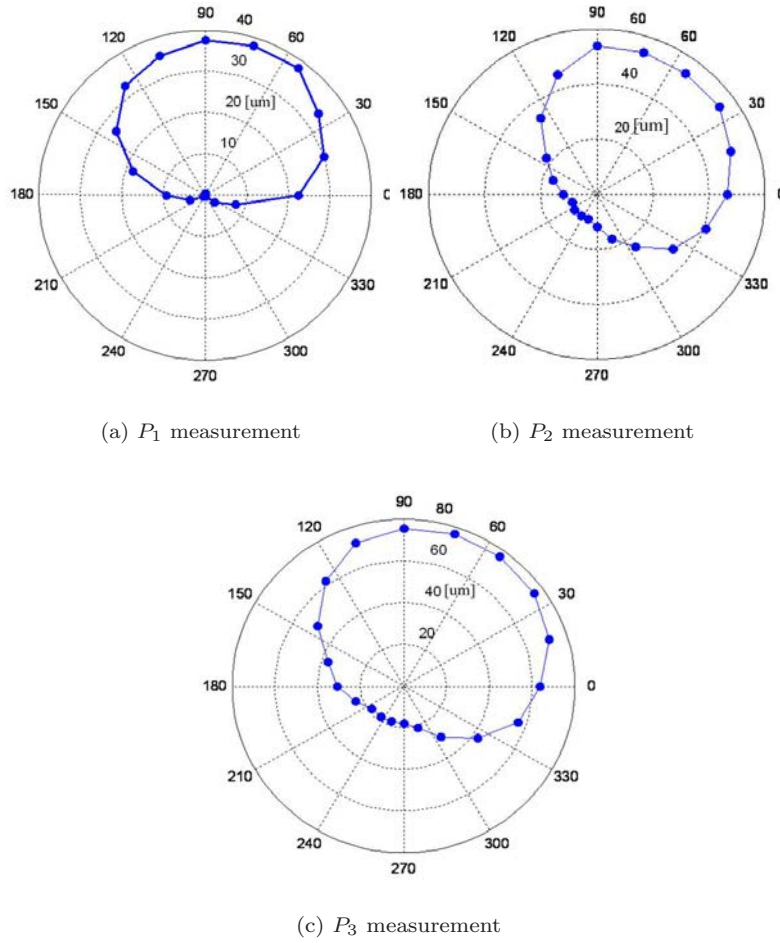


Figure 5.6: Tool shank radial error motion measurement

asymptotic level of the tool tip diameter. In order to clarify the tool radial error motion, the tool assembling is not elaborately adjusted, and a spring tool clamp with three slots is adopted in this test. In [102], the run-out value ranges from $40\mu m$ to $345\mu m$. In [159], the maximal dynamic run-out is about $50\mu m$. These literatures' results show the tool radial error motion is very sensitive to the clamp precision and tool assembling accuracy.

5.3.3 Tool unbalance

Due to the high speed rotation, the rotor unbalance induces great centrifugal forces effect, which causes tool vibration and affects the tip trajectories. In the rotor dynamic model, which will be described in the Section 5.4, the unbal-

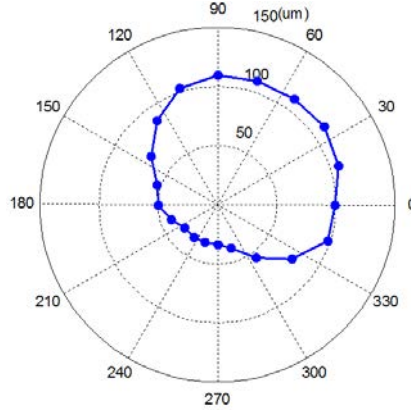


Figure 5.7: Tool tip radial error motion

ance of each section must be obtained to do the vibration analysis. However, measuring the unbalance radius of each section on the micromill is very time-consuming, and the tool tip unbalance is impossible to be measured directly as aforementioned.

In this section, a simple method to calculate the unbalance radii of all sections is proposed based on the measurement results of P_1 , P_2 and P_3 . The measurement principle is shown in Fig.5.8, which can be separated into three steps. The first step is the vector summarization of the radial error values on P_1 , P_2 and P_3 respectively. The vectors $\overrightarrow{P_1A_1}$, $\overrightarrow{P_2A_2}$ and $\overrightarrow{P_3A_3}$ represent the unbalance radii in the P_1 , P_2 and P_3 sections. The end points of these three vectors form a triangle $\triangle A_1A_2A_3$, with its shape center C_2 . The second step is to connect A_1A_2 , A_1A_3 , and A_2A_3 , to intersect the tool set plane Π at B_1 , B_2 and B_3 , which form a triangle $\triangle B_1B_2B_3$ too, with its shape center C_1 . The third step, connect the shape centers C_1 and C_2 of triangles $\triangle B_1B_2B_3$ and $\triangle A_1A_2A_3$, to form a vector $\overrightarrow{C_1C_2}$. $\overrightarrow{C_1C_2}$ represents the unbalance radii of all tool sections approximately.

$\overrightarrow{C_1C_2}$ can be defined by three parameters in the $O - XYZ$ frame, $|OC_1|$, α and β . $|OC_1|$ represents the unbalance radius of the tool in the plane Π . α stands of the angle location of $\overrightarrow{C_1C_2}$ in the XOZ frame, which is angle between $\overrightarrow{C_1C_2}$ and X axis. And β is the inclination angle between $\overrightarrow{C_1C_2}$ and Y axis. Among them, β and $|OC_1|$ are decisive to the tool's unbalance.

In this test, the unbalance vectors of these three measured points $\overrightarrow{P_1A_1}$, $\overrightarrow{P_2A_2}$ and $\overrightarrow{P_3A_3}$ and the micromill unbalance vector $\overrightarrow{C_1C_2}$ calculated by the

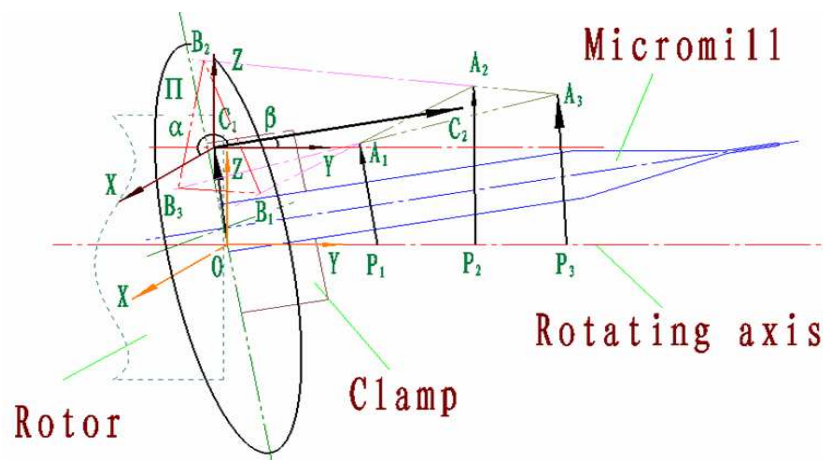


Figure 5.8: Tool unbalance calculation principle

aforementioned algorithm are shown on Fig.5.9. The parameters of the tool unbalance radii vector $\overrightarrow{C_1C_2}$ are $|OC_1| = 100.7\mu\text{m}$, $\alpha = 90.39^\circ$, and $\beta = 0.67^\circ$.

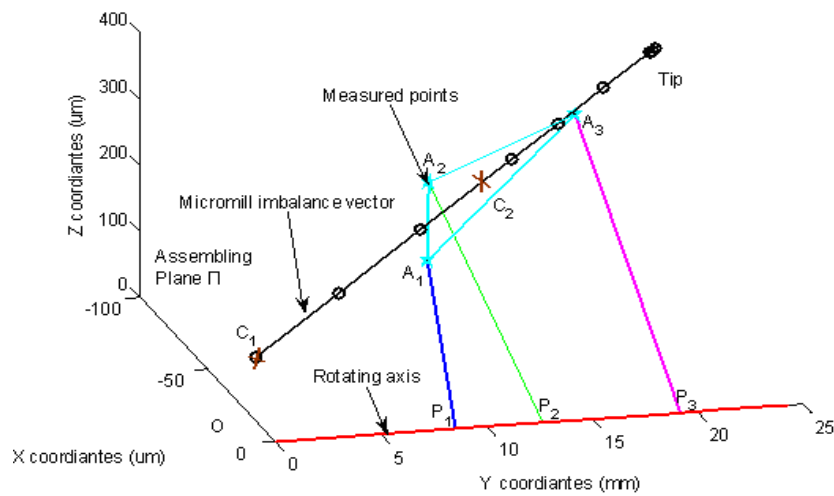


Figure 5.9: Tool unbalance calculation results

Obviously, this approach is an approximate calculation method. Because A_1 , A_2 and A_3 don't locate on the vector $\overrightarrow{C_1C_2}$, but they are very close to $\overrightarrow{C_1C_2}$. The unbalance vectors of all sections can be expressed by a simple vector $\overrightarrow{C_1C_2}$ utilizing this method, so this a little error is acceptable. Meanwhile, this method is easy to be operated, because measurement on each section of the micromill is very time-consumable and the cost-effectively compared with other approaches.

5.4 Vibration analysis

5.4.1 Rotor dynamic model

In order to understand the tool unbalance effects to the tool tip vibration, a rotor dynamic model is developed for the cutter/spindle system. The geometric dimension of the rotor is shown in Fig.5.10. The bearing stiffness in radial direction is $1.885e^7 N/m$, provided from NSK. The rotor is dispersed into a few sections, and the mass of each section is lumped into their corresponding node. The rotor is modeled as a Timoshenko beam. The rotor inertia effect, the gyroscopic moment, the transverse deformation, and the shear deformation are considered into the Lagrange formulation. Specially developed MATLAB program [165] gives stiffness, damping and mass matrixes related to the rotor geometry and the setting of bearings.

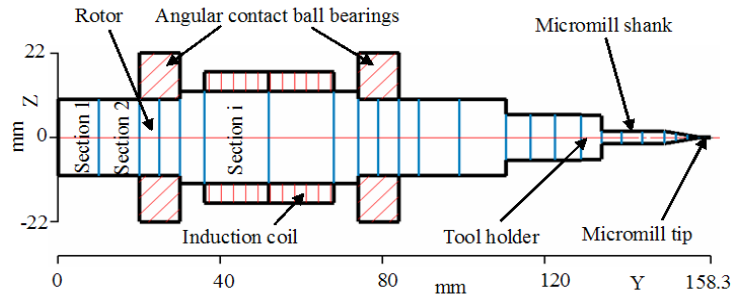
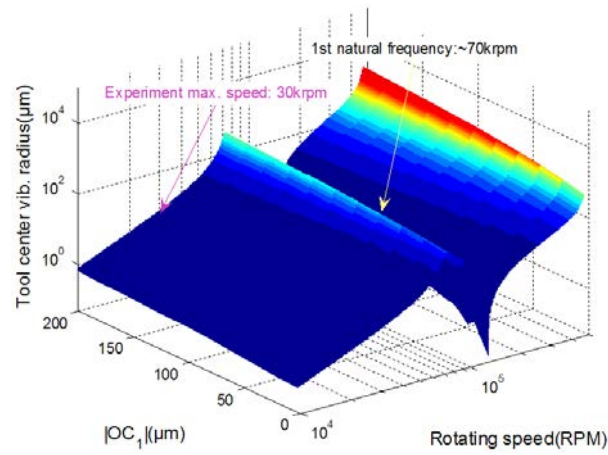


Figure 5.10: Cutter/spindle system model

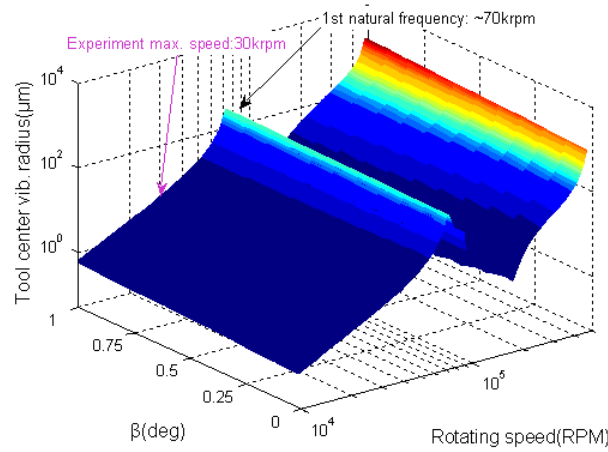
5.4.2 Natural frequency and tool tip vibration

The rotor unbalance is included in the model. The unbalance radius of spindle rotor is $3\mu m$ according to its catalog [166]. Based on the previous calculation results, the parameters of the tool unbalance radii vector $\overrightarrow{C_1C_2}$ are $|OC_1| = 100.7\mu m$, $\alpha = 90.39^\circ$, and $\beta = 0.67^\circ$. Then the unbalance radius of each section on the tool is calculated by $\overrightarrow{C_1C_2}$ according to its Y coordinate. By multiplying the lumped mass of each section and its corresponding unbalance radius, the unbalance of the rotor is calculated and input to the model. Because $|OC_1|$ and β are critical to the tool unbalance vector, their effects are discussed in detail. The tool tip vibration mode diagrams are shown in Fig.5.11. Fig.5.11(a) reflects the influence of $|OC_1|$, and Fig.5.11(b) expresses the influence of β . We found that even if the unbalance changes the vibration amplitude, it does not

affect the natural frequency. In this research, the maximal experimental speed is $30,000rpm$. It is much smaller than the rotor's natural frequency, about $70,000rpm$. Therefore, the rotor is assumed as a rigid body. The tool tip vibration amplitude is less than $10\mu m$ in our spindle speed range and this effect will be included into the trajectories analysis.



(a) $|OC_1|$ effect, when $\beta = 0.6691^\circ$



(b) β effect, when $|OC_1| = 100.7\mu m$

Figure 5.11: Tool tip vibration bode diagram

Table 5.2: LK-G10 specification

Item	Value
Reference distance	10mm
Measurement range	$\pm 1mm$
Light source wave length	650nm
Light spot diameter	$\sim 20\mu m$
Linearity	$\pm 0.03\%$
Resolution	0.02 μm
Sampling frequency	$\sim 50KHz$
Weight	$\sim 190g$

5.5 Validation of measurement and calculation

In order to validate the measurement in Section 5.3 and calculation results in Section 5.4. The Keyence laser sensor (type LK-G10) is adopted in this test. The detailed sensor specifications are listed in Table.5.2. The validations include static and dynamic tests. In the static test, the laser sensor is used to detect the radial error motion at three points corresponding to the three positions shown in Fig.5.5. In the dynamic test, when the spindle is under high speed rotation, the Y coordinate of laser sensor is set to 29mm. This axial position is much near to the tool taper. Because the measurement on the tool tip with twisted section can't reflect the actual location of the tool tip center. So this point is chosen to validate the comprehensive effect of tool radial motion and vibration under high speed rotation.

5.5.1 Validation test setup

The test scheme is designed as Fig.5.12. The laser is shot on the tool shank. The microscope is used to monitor the laser spot position on the tool shank. The measurement data from the sensor is transferred to the data recorder, and it is shown in the digital displayer simultaneously. Meanwhile, the measurement process is captured under the microscope and top-level monitor. The positions of the laser sensor and the microscope are set to be perpendicular. Entire test setup is shown in Fig.5.13.

Due to the locations of the laser sensor and the microscope are perpendicular, when we found the laser spot was on the tangential generatrix of the tool under microscope, as Fig.5.14, it means the sampled data from the laser sensor are

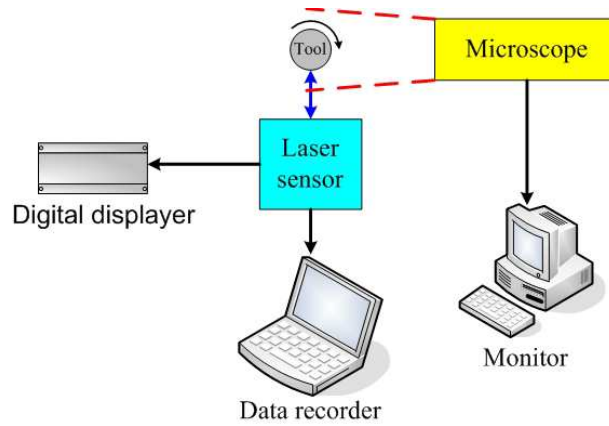


Figure 5.12: Laser test scheme

reliable to reflect the tool radial error motion.

5.5.2 Static test results

In the static test, the tool is rotated by hand operation, and the radial error motion data in three measurement points are shown in Fig.5.15. Meanwhile, the measurement results from the dial gauges are also shown in Fig.5.15 as comparison.

From Fig.5.15, we found that the measurement results from dial gauge and laser sensor correlated very well. Actually, the measurement error of dial gauge should be greater than the laser sensor, due to the its contact measurement inherits and the assemble errors of dial gauges. But in this test, the installation of the dial gauges are very careful to avoid the additional error. Therefore the measurement error of the dial gauge compared with the radial error motion is less. Hence, these two sensors show good agreement measurement results.

5.5.3 Dynamic test results

In the dynamic test, the measurements are conducted on two rotating speeds, $20,000rpm$ and $30,000rpm$, respectively. The sampling frequency is $50KHz$ and the corresponding laser measurement results are shown in Fig.5.16.

Using the calculation algorithm in the Section 5.3.2, the radial error motion value of this test point is calculated. We found its average value is $47.135\mu m$ with $29.535\mu m$ amplitude. Therefore, the up-limit and the down-limit of the radial error motion are $76.67\mu m$ and $17.6\mu m$ respectively. Through the ro-



Figure 5.13: Laser test setup

tor dynamic model, the vibration amplitudes in this point under $20,000rpm$ and $30,000rpm$ are $4.3\mu m$ and $6.2\mu m$. Hence, the corresponding displacement ranges are $67.67\mu m$ and $71.47\mu m$. From Fig.5.16, the average displacement ranges of $20,000rpm$ and $30,000rpm$ are about $71\mu m$ and $75\mu m$. The model gives the good prediction with relative errors around 4.7%. The laser test validates the proposed radial error motion measurement and tool tip vibration calculation. Here the data obtained in the Section5.3 and Section 5.4 are used in the tool tip trajectory model.

5.6 Trajectories investigation

In order to analyze the trajectories of the tool center and each flute, the coordinate frames and some important vectors are defined in the tool tip plane, shown in Fig.5.17.

XOZ is the fix frame as mentioned in Fig.5.8. $x'o'z$ frame is always parallel to XOZ frame, but rotates with the tool, and o' is the tool tip center. Ω is the rotating speed. Flute angle θ is defined between the first flute $o'F_1$ and the $o'x$ axis in the static condition (before rotating). It is a constant value after the

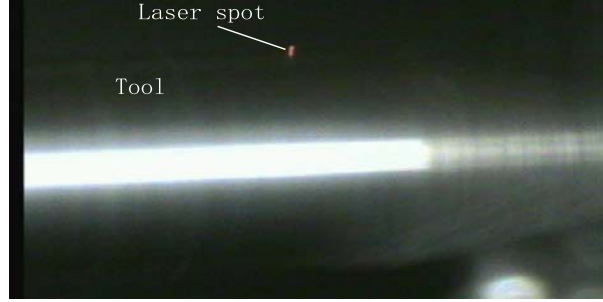


Figure 5.14: Laser point location under microscope

tool assembling. Feed angle ϕ is defined between the tool feeding direction and the OX axis. The domains of these two variables range from 0° to 360° and symmetry to 180° . F_1 and F_2 are the flute positions. And the tool radius R equals to $\overrightarrow{o'F_1}$ and $\overrightarrow{o'F_2}$. Later, the trajectories of o' , F_1 and F_2 will be discussed in detail.

5.6.1 Trajectories without feeding

According to the assumption that the cutter/spindle system is a rigid body in this research, the tool tip plane can be regarded as a single freedom system. Thus, in this instance, the tool rotates around the Y axis (rotating center) in the speed Ω , accompanied with the tool self rotating in the Ω too [167]. Based on this principle, the trajectories without feeding of o' , F_1 and F_2 can be described in the time domain by

$$\begin{cases} x_{o'}(t) = |Oo'(\Omega t)| \cos(\Omega t) \\ z_{o'}(t) = |Oo'(\Omega t)| \sin(\Omega t) \end{cases} \quad (5.1)$$

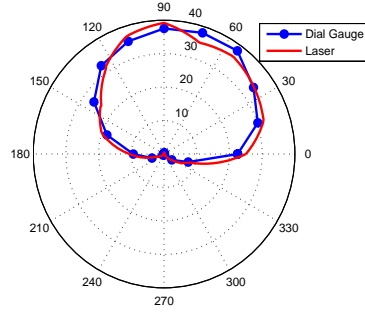
$$\begin{cases} x_{F_1}(t) = |Oo'(\Omega t)| \cos(\Omega t) + R \cos(\Omega t + \theta) \\ z_{F_1}(t) = |Oo'(\Omega t)| \sin(\Omega t) + R \sin(\Omega t + \theta) \end{cases} \quad (5.2)$$

$$\begin{cases} x_{F_2}(t) = |Oo'(\Omega t)| \cos(\Omega t) - R \cos(\Omega t + \theta) \\ z_{F_2}(t) = |Oo'(\Omega t)| \sin(\Omega t) - R \sin(\Omega t + \theta) \end{cases} \quad (5.3)$$

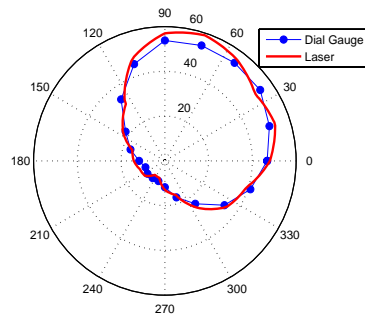
Then change Eqs.(5.1 ~ 5.3) to their curve expressions, as Eqs.(5.4 ~ 5.6):

$$x_{o'}(t)^2 + z_{o'}(t)^2 = |Oo'(\Omega t)|^2 \quad (5.4)$$

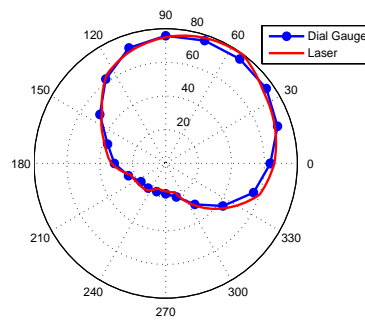
$$x_{F_1}(t)^2 + z_{F_1}(t)^2 = |Oo'(\Omega t)|^2 + 2|Oo'(\Omega t)|R \cos \theta + R^2 \quad (5.5)$$



(a) P_1

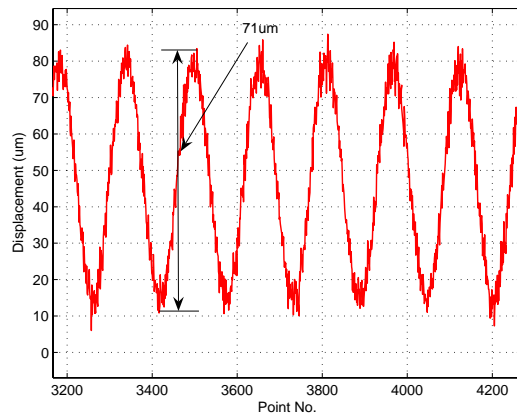


(b) P_2

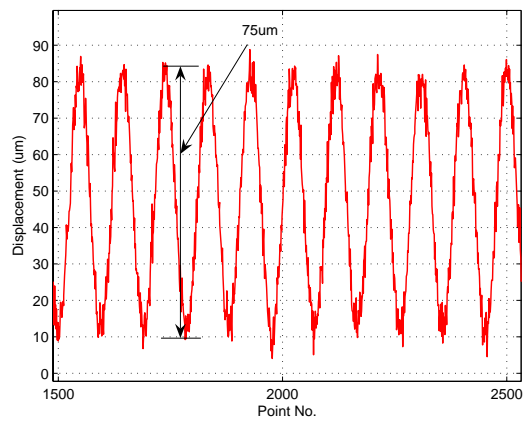


(c) P_3

Figure 5.15: Static test results comparison



(a) 20,000rpm



(b) 30,000rpm

Figure 5.16: Dynamic laser test

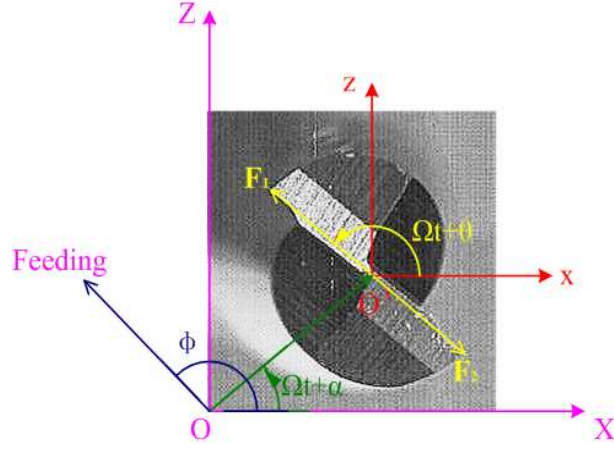


Figure 5.17: Frames and vectors in the tool tip plane

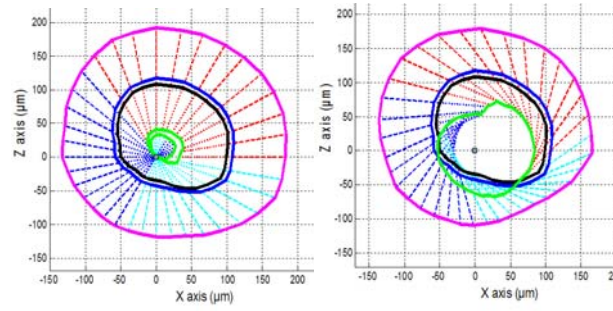
$$x_{F_2}(t)^2 + z_{F_2}(t)^2 = |Oo'(\Omega t)|^2 - 2|Oo'(\Omega t)|R \cos \theta + R^2 \quad (5.6)$$

Note that $|Oo'(\Omega t)|$ is the distance from the tool tip center to the rotating axis. In fact, it is the summarization of the tool tip radial error motion and the tip vibration amplitude. Because the tool tip radial error motion is calculated based on the measurement on the actual tool assemble, it can't be described by any analytical function. Using numerical fitting technique, they form a close-loop in the simulation. It is obviously that the flute angle θ affects the tool tip trajectories without feeding in Eqs.(5.4 ~ 5.6). Fig.5.18 shows some simulation results with different θ under 30000rpm rotating speed. The radial error motion and the unbalance radii vector $\overrightarrow{C_1C_2}$ used for all simulations in this research are shown in Fig.5.7 and given in the Section 5.4.2 respectively.

In addition to the legend information in Fig.5.18, the lines with red, blue, and cyan colors stand for the flute positions in each trisection in a rotation. Dash lines and dot lines represent the vectors from the tool center to the first and second flutes respectively.

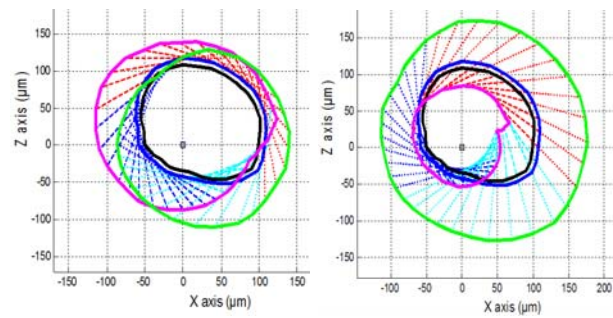
As shown in the Fig.5.18, the tool tip center trajectory without vibration is purely induced by the radial error motion, which has greater effect than the vibration amplitude under this speed.

Only when $\theta = \pm 90^\circ$ (Fig.5.18(c)), the trajectory of one flute is not be enclosed entirely by the other one. In many other conditions (Figs.5.18(a,b,d,e)), the trajectory of one flute is enclosed by the other one entirely. It means the



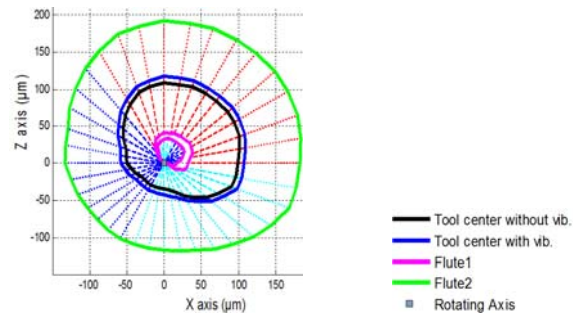
(a) $\theta = 0^\circ$

(b) $\theta = 45^\circ$



(c) $\theta = 90^\circ$

(d) $\theta = 135^\circ$



(e) $\theta = 180^\circ$

Figure 5.18: Tool tip trajectories simulation without feeding

single flute cutting always occur in the micromilling. Only except when $\theta = \pm 90^\circ$, there is the possibility for double flute cutting.

5.6.2 Trajectories With Feeding

In the actual micromilling operation, the tool moves relative with the workpiece, named feeding motion. With different feed angle ϕ , the tool tip trajectories are shown in Fig.5.19, in which the rotating speed is $30000rpm$, flute angle $\theta = -90^\circ$, and the two sets of feed angles are 40° and 310° , which coincide with the experimental parameters.

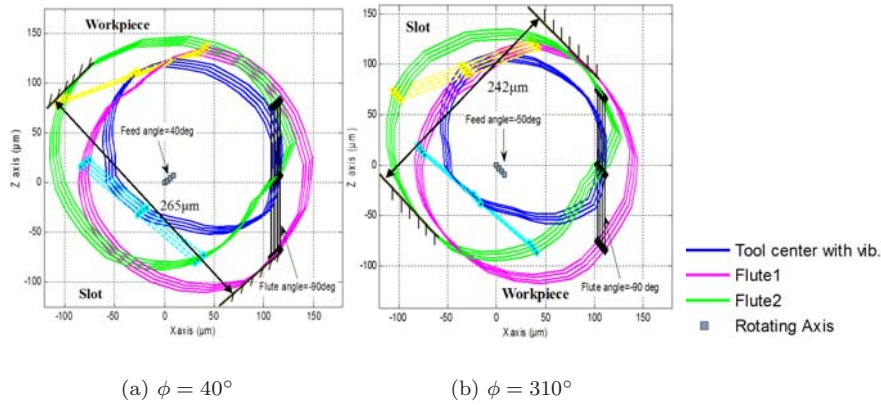


Figure 5.19: Tool tip trajectories simulation with feeding

In the Fig.5.19, the straight lines connect the tool center's trajectory and the first and second flutes' trajectories with black, yellow, and cyan color represent the tool center locations in 0° , 120° and 240° respectively. Actually, when the flute angle θ is determined, with different feed angles ϕ , the slot widths and flute chip loads are different as shown in the Fig.5.19. In the Fig.5.19(a), all the chip loads almost inflict on two flutes equally, but the slot width is $265\mu m$. In the Fig.5.19(b), most part of chip loads inflict on the first flute, and the second flute only affords a little. Fortunately, the slot width is $242\mu m$. Comparing with the tool nominal diameter ($152\mu m$), the machining error in the Fig.5.19(a) ($113\mu m$) is greater than the Fig.5.19(b) ($90\mu m$).

5.6.3 Parameters Analysis

From the previous simulation, it is clear that under the same rotating speed and radial error motion, the slot width (machining error) and flute chip loads are influenced by the flute angle θ and feed angle ϕ simultaneously. The quantificational analysis of their effects are given in this section.

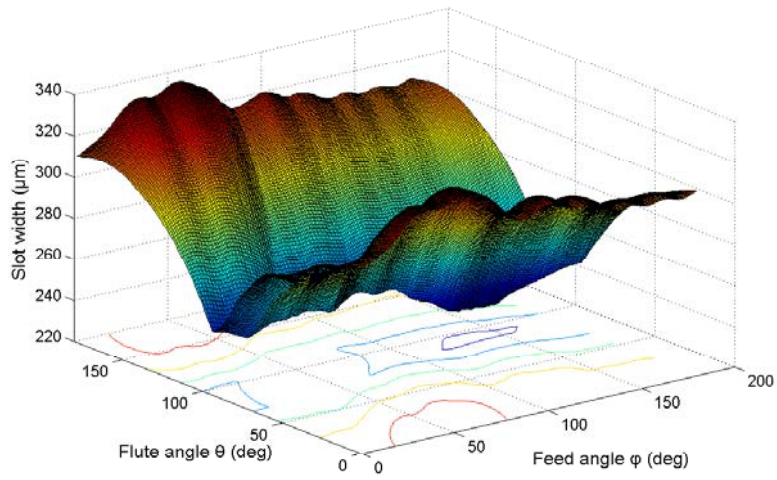
Slot width

Assuming the micromilling operation is used to fabricate the slots, using the tool tip trajectories model to calculate the slot width in the direction perpendicular to the feeding direction. Fig.5.20 gives the 3D and contour expression of the slot width varying with θ and ϕ from 0° and 180° . It is obvious that the flute angle θ affects on the slot width much more than the feed angle ϕ . The machining error is smaller when $\theta = \pm 90^\circ$. The minimum slot width value is about $235\mu m$, when θ near 90° , and ϕ is about 135° . This condition corresponds to the tool tip trajectories shown as Fig.5.19(b). The maximum slot width is about $330\mu m$, when θ near 0° or 180° , and ϕ is about 150° .

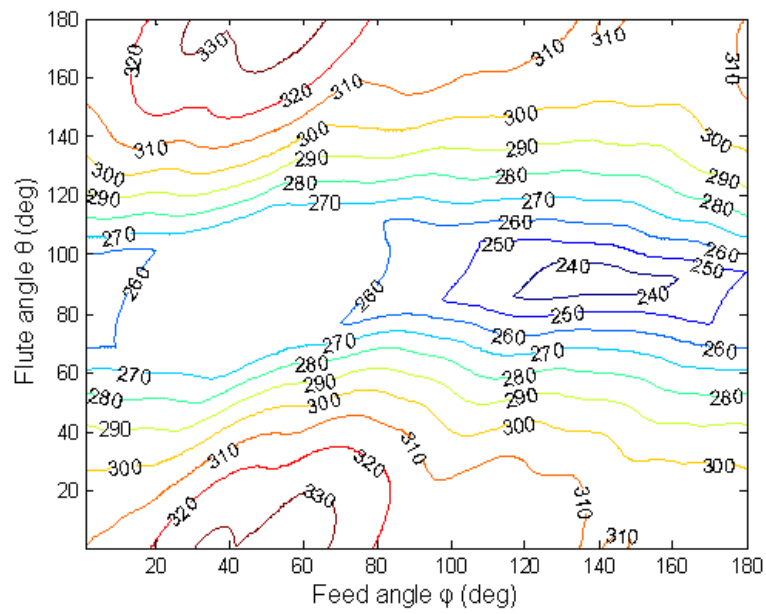
Flute angle θ influence. Fig.5.21 shows the influence of flute angle θ to the slot width with four different feed angles ϕ . It is significantly that the peak-valley values for each feed angle ϕ are about $70\mu m$. It means that the great influence from the flute angle. The differences between each line for the same flute angle variable are not large. It also means that the feed angle effect is less.

The valley value of slot width in each line is when the flute angle θ near 90° or 270° . In the contrast, when the flute angle θ is about 0° or 180° , the slot widths (machining errors) are greatest. Because the flute angle is depending on the tool assemble, it means that adjusting the flute angle carefully to about 90° or 270° is very critical to decrease the machining error.

Feed angle ϕ influence. Fig.5.22 reflects the influence of the feed angle ϕ to the slot width, with four different flute angles. These peak-valley (PV) values of these curves are between $25\mu m$ and $40\mu m$. They are obviously less than the PV values of the flute angle θ influence. There is almost no discipline can be found among these curves. Except the large curves, there are lots of small oscillations in each curve.



(a) 3D expression



(b) Contour

Figure 5.20: Slot width varying with θ and ϕ

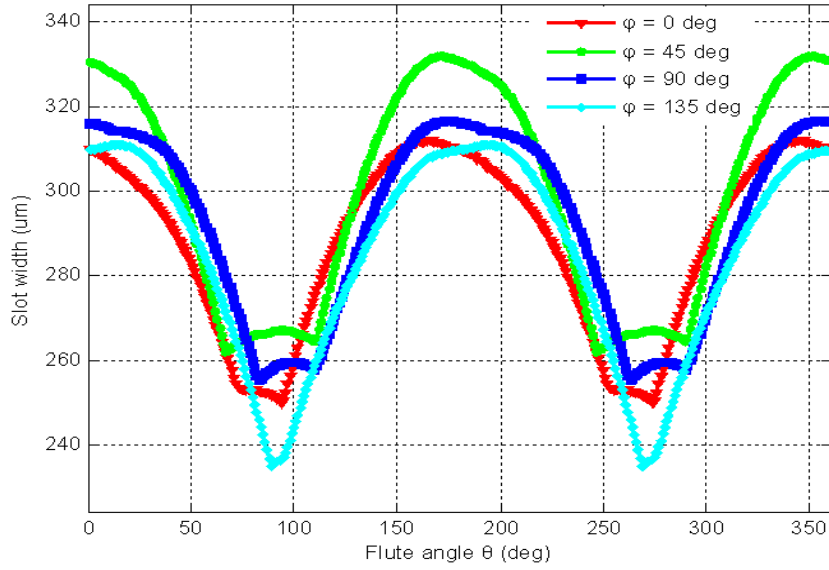


Figure 5.21: Flute angle θ influence to the slot width

Table 5.3: Feed Angle Influences to Micromilling, When $\theta = \pm 90^\circ$

Feed Angle ϕ	Chip Load	Cutting Condition	Machining Error
45° 225°	$1^{st} = 2^{nd}$	Double Flute	Largest
$45^\circ \sim 135^\circ$ $135^\circ \sim 225^\circ$	$2^{nd} > 1^{st}$	Double Flute	Middle
135°	2^{nd}	Single Flute	Least
$225^\circ \sim 315^\circ$ $315^\circ \sim 45^\circ$	$1^{st} > 2^{nd}$	Double Flute	Middle
315°	1^{st}	Single Flute	Least

Chip loads

From the trajectory simulation in the Fig.5.18 and Fig.5.19, it is easy to know that the chip load of each flute is also affected strongly by the flute angle θ and feed angle ϕ , which is important to the tool wear and tool life.

In the Fig.5.18, only one flute cuts the material in Figs.5.18(a,b,d,e). In the Fig.5.18(c), when $\theta \simeq \pm 90^\circ$, there is the possibility of double flute cutting. The cutting condition, chip load on each flute and the machining error depend on the feed angle ϕ as Table.5.3. The results show when ϕ is 135° or 315° , the machining error is the least, but only one flute cuts material and decreases the tool life. When ϕ is 45° or 225° , the chip load are almost distributed on two flutes equally, but the machining error is greatest.

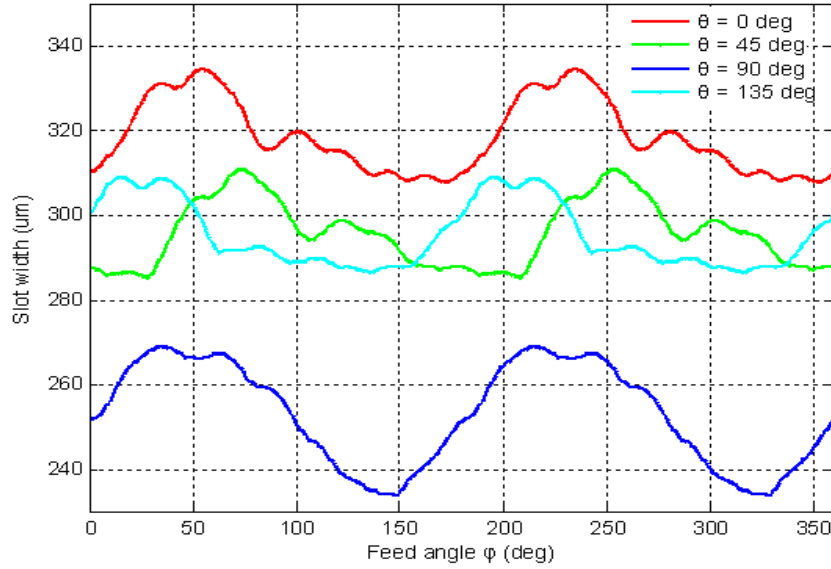


Figure 5.22: Feed angle ϕ influence to the slot width

These results indicate us the single flute cutting condition always occur in the micromilling process. And the micromill assemble is important to adjust the flute angle θ near $\pm 90^\circ$, for the purpose of decrease the machining error and tool wear. In this condition, the feed direction should be chosen according to the machining objective. If the operator pursues the machining accuracy, single flute cutting condition should be chosen, but it accelerates the tool-wear on the cutting edge. On the contrary, double flute cutting condition can be chosen to extend the tool life, but the machining error would be greater.

5.7 Experimental Study

According to the analytical results presented in the Fig.5.20, the tool tip trajectories are complex due to the influences of the flute angle θ and feed angle ϕ . Validating all cases by experiments would be very expensive and time-consumable. Here, the case study is given. The cutting force, chip thickness, slot width and slot bottom surface quality are analyzed.

5.7.1 Experimental design

A two-flute M.A.Ford tungsten carbide micromill with $152\mu\text{m}$ diameter is used in the experiments. In these case studies, all experiments are done on

Table 5.4: Experimental plan for the tool tip trajectories model

Series No.	Test No.	Feed angle ϕ ($^{\circ}$)	Spindle speed (<i>rpm</i>)
1	1	310	17500
1	2	310	20000
1	3	310	25000
1	4	310	30000
2	5	40	17500
2	6	40	20000
2	7	40	25000
2	8	40	30000

Aluminum 6061 workpiece with $10\mu m$ axial depth of cut, $60mm/min$ feed rate, and the flute angle $\theta = -90^{\circ}$. The rotating speed and the feed angle ϕ are variables. The reasons of choosing these experimental parameters are to reduce the minimum chip thickness effect because of great feedrate per tooth according to Ref. [130], and neglect the tool's helix angle effect due to the small axial depth of cut. The detailed experimental plan is listed in Table.5.4. The first series experiments are designed for single-flute cutting, and the second series are for double-flute cutting.

5.7.2 Cutting forces and chip thickness

The cutting forces are recorded for all experiments, and similar results have been found for each series. Here, we present one case for the single flute cutting in the first series. In this case, the rotating speed is $20000rpm$, and $\phi = 310^{\circ}$, with test no. is 2, and the flute trajectories are shown in Fig.5.19(b). Through the feeding trajectories analysis, the instantaneous chip thickness is plotted in Fig.5.23 with the left Y axis. Based on the micromilling force model in Ref. [168], the main cutting force is presented in Fig.5.23 accompanied with the corresponding experimental force data with the right Y axis. The force model is modified from Ref. [169], in which the cutting force is proportional to the chip thickness, and contained the friction effects caused by the tool chip contact and the workpiece material spring back. With this parameters set, almost the minimal machining error is obtained, but more than 90% of chip load is concentrated on the first flute. From Fig.5.23, the model gives good prediction to the experimental cutting force.

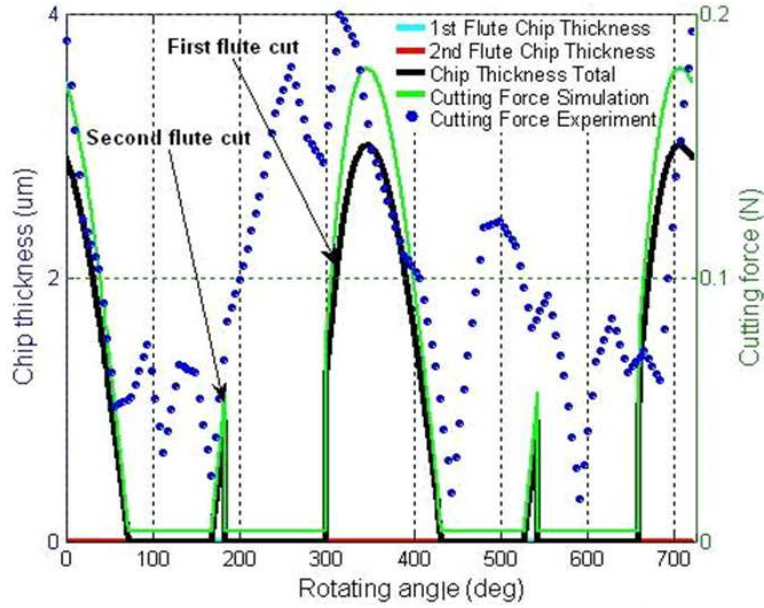


Figure 5.23: Chip thickness and cutting force

In the macro-scale milling, the dominant frequency of the cutting force is the tooth passing frequency, other than the spindle frequency. For example, using a two-flute mill, the tooth passing frequency, twice of the spindle frequency, should be dominant. However, the FFT analysis on this experimental micromilling force reflects that the main frequency component transfers from the traditional tooth passing frequency to the traditional spindle frequency as shown in Fig.5.24. This is due to the single flute cutting condition. Only one flute removes the material, and the tooth passing frequency caused by single flute cutting equals to the spindle frequency. Hence, the amplitude of the traditional spindle frequency is higher, and the amplitude of the traditional tooth passing frequency is lower. The similar results are reported in Refs. [151,170].

5.7.3 Slot width and surface quality

The slot widths of two series experiments measured by SEM are shown in Fig.5.25. Their feed angles are 40° and 310° , and the rotating speed ranges from $17500rpm$ to $30000rpm$. The trajectory model performs good prediction of the slot width, which is very important to make the error compensation.

An example of the experimental slot bottom surface is shown in Fig.5.26, with $30000rpm$ and $\phi = 40^\circ$ setting. And the SEM photo of the micromill with

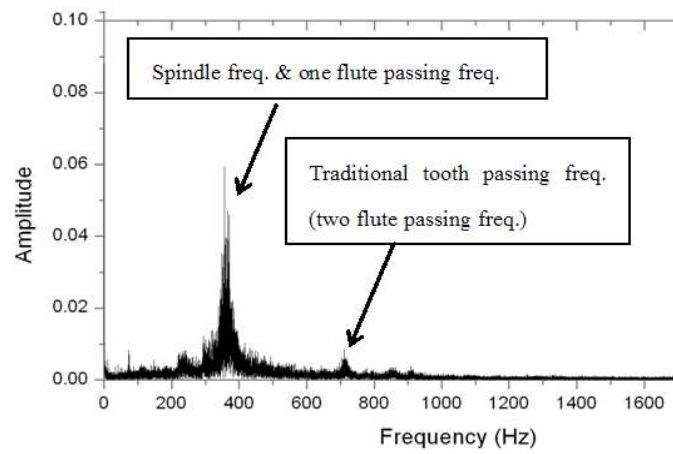


Figure 5.24: Frequency analysis of the experiment cutting forces

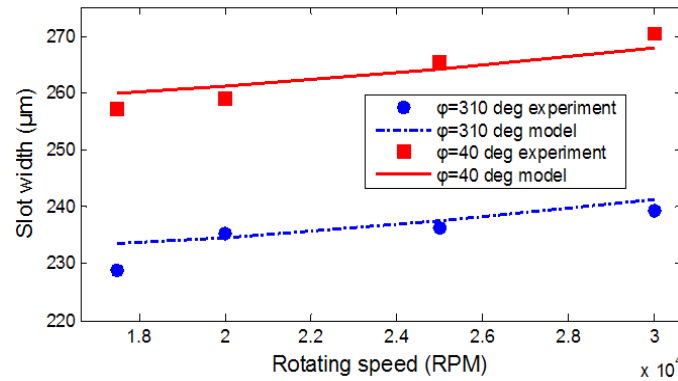


Figure 5.25: Slot width comparison between experiment and model

152 μm tool tip diameter is also shown in the right up corner of the Fig.5.26. The tool tip trajectories analysis of this case is shown in Fig.5.19(a). The width of this slot is about 270 μm , which validated the model prediction too.

The surface quality of the slot bottom is not satisfactory, especially the slot center. This is because the radial position of each flute is different, then induce their axial height differences. The outer flute locates far from the rotating axis in the radial direction, which cuts material, and has higher axial location. But the inner flute locates near the rotating axis, and has lower axial location, but it contacts the slot center to destroy the machined surface.

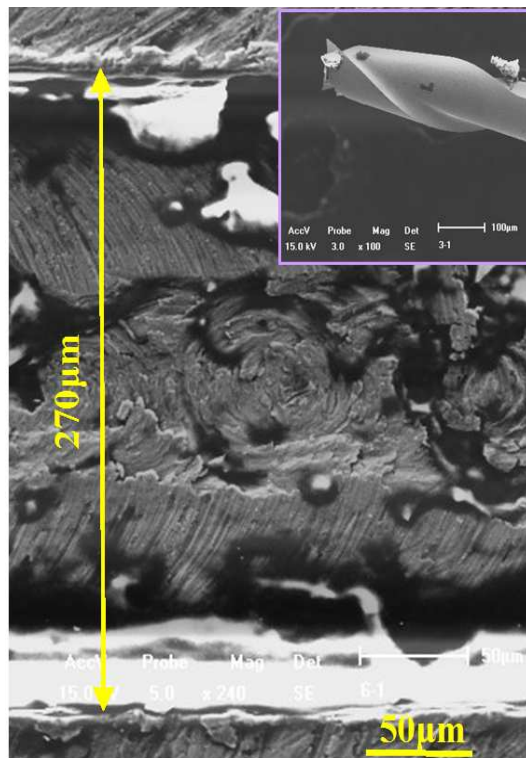


Figure 5.26: Bottom surface and tool tip

5.7.4 Tool breakage

As the analysis in the Section 5.6.3, in most cases, the chip load burden inflicts on one flute. Its wearing speed is much faster than the other flute, and the tool life is dependent on this flute wear condition.

In the first series experiments, with $\phi = 310^\circ$ setting, the tool is broken (Fig.5.27), after machining 157.5mm slots on the workpiece. From the fracture image, the tool breaks because the chip loads of each flute are extremely unequal. The cutting force inflicted on the 1st flute causes the tool body bearing the bending stress much stronger in one side.

5.8 Conclusions

A tool tip trajectories model is developed for a two-flute micromill. It contains the effects of the tool radial error motion and the tool tip vibration under high speed rotation. The model gives good prediction to the experimental results. It is useful to understand the micromilling mechanism, and to minimize

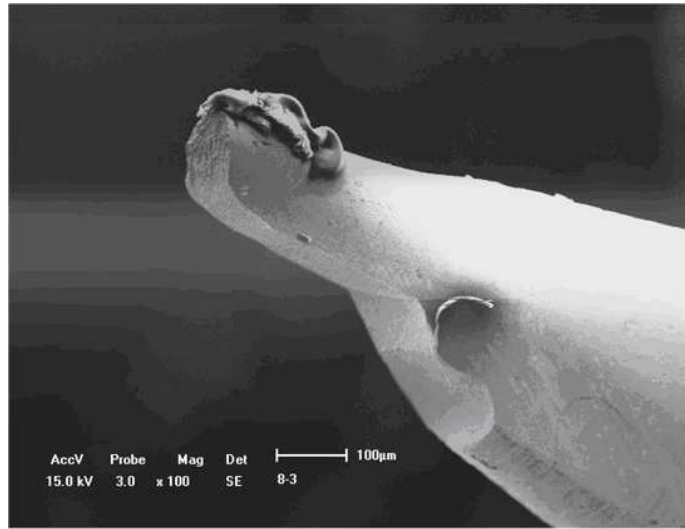


Figure 5.27: Tool breakage fracture in the first series experiments

the machining error. Some important conclusions in this chapter are listed as below:

1. The single flute cutting condition always occur in the micromilling by using a two-flute cutter, which is obviously different from the common sense.
2. The tool set precision is very important to the machining accuracy and the tool life. The optimal condition is to set the flute angle $\theta = \pm 90^\circ$.
3. After optimizing the flute angle θ , choosing appropriate feeding direction (feed angle ϕ) is also critical to the machining error and the chip load distribution.

Chapter 6

Wavy Chip Formation Analysis

6.1 Introduction

Understanding the chip formation is the first step to achieve the good chip control, a necessity for automated machining. Moreover, a lack of chip control often leads to coarse surface finish, poor machining accuracy, and problems with chip removal from the machining zone [171]. The well-known concept of the chip formation classification was proposed by Ernst [172] from the point of view of chip geometry, as discontinuous, continuous, and continuous with a built-up edge interposed between the chip and tool in the vicinity of cutting edge. Recently Astakhov [173] redefined the categories of chip formation by a generalized model.

To the conventional scale machining processes, much work has been done to investigate the chip formation. Most of early researches were based on the mechanics model [145, 174]. With the enhancement of the digital computer industry, more and more numerical methods, especially the Finite Element Method (FEM), were resorted to understand the chip formation in a multi-physics field [175–179]. To the 1990s, most researchers developed their own FEM code. From the last two decades, the commercial FEM packages have been dramatically used for this purpose, due to their easy application in industry and allowing engineers to concentrate on their concerned problems not on the programming issues [180].

FEM is also a powerful tool to simulate the manufacturing process in micro scale. However, it costs more computational resources and longer duration

because of the finer element mesh and more elements to emulate the actual micromachining condition. In this aspect, Vogler et al. [34, 35] used a customized FEM code developed by Chuzhoy et al. [181, 182], which is capable to embed the heterogeneous material into the FEM environment, to determine the minimum chip thicknesses (MCT) for ferrite and pearlite metallographies respectively. Simoneau et al. [183, 184] assigned different hardness parameters to different metal phase components of steel, and explained the chip formation and surface defects in microscale cutting. Özel et al. [185] analyzed the temperature of micromilling process, and found that a lower value compared to the one of conventional cutting. Woon et al. [186] analyzed the edge radius effect in microcutting and showed that the ratio of uncut chip thickness (UCT) to edge radius influences the material flow stress and effective negative rake angle strongly. Except for the FEM, Molecular Dynamics (MD) is another way to simulate the machining process in the microscale even to nanoscale [187, 188].

In the microcutting operation, due to its scale shrinking, most of the micro parts are finished only in one procedure, not multi-procedure processing. In another word, optimization the processing variables to achieve the best surface quality and form accuracy is quite important to the microfabrication. In microcutting, the residual burrs on the workpiece are not easily eliminated by the conventional burr removal processes. They are huge obstacles of the parts behavior. Therefore, understanding the chip formation mechanism and optimizing the machining parameters based on the mechanism are pivotal to improve the application and performances of microcutting. Ueda et al. [189] found the lamellar chip structure when microcutting of an amorphous metal due to the periodical formation of localized shear band. However, the tool edge radius effect was neglected. Kim et al. [190] investigated the MCT effects on chip formation in micromilling. And it showed that not all tool passes would produce the chip when the feed rate per tooth was smaller than MCT. Only when the accumulated UCT was larger than MCT, the chip was formed. Lee and Dornfeld [162, 191] conducted a large amount of experiments to investigate the relationship between burr formation and machining variables in micromilling. Based on analytical results, the parameters were optimized to achieve better surface quality and longer tool life. However, so many experiments were very time consuming and expensive. Therefore, simulations are very helpful to investigate the chip formation in micromilling and accelerate its industrialization.

In this chapter, the FEM approach is utilized to investigate the chip formation process in slot micromilling Al6061-T6 alloy by a carbide tool. The chip is found to be wavy type, which is similar to the Ueda's findings. The chip morphology is verified by experimental observation of the burr and chip shapes. Furthermore, the simulation cutting force correlates well with the experimental one. Through the detailed analysis on the simulation results, the wavy chip formation process is described from the viewpoint of chip velocity, together with the variations of the tool chip contact length (l_T) and shear band length (l_S). It has been found the maximal chip velocity location changes from the chip root to chip tip, then back to chip root again in this process. Then the chip formation mechanism is studied quantitatively by means of hybrid analytical-FEM approach. After calculating and analyzing the chip moments, including the "Tool Rake Moment" M_{Tool} and "Shear Band Moment" M_{Work} , it is proved that the main reasons of wavy chip generation are the variations of the l_T and l_S . Before the chip bending, l_T and l_S increase simultaneously. In the chip bending process, the l_T decreases faster than l_S . The Merchant model (MM model) [192] and Arcona-Dow model (AD model) [169] are adopted respectively to calculate the M_{Work} as a comparison. The AD model shows a good performance in the microcutting scale. In the wavy segment generation occasion, the average chip velocity magnitude in chip bending process is much greater than the one before chip bending which is about the nominal cutting speed. The chip root velocity is almost constant in the entire micromilling process, and the chip tip velocity increases too much in the chip bending instant due to the chip angular acceleration. The chip angular acceleration is acquired respectively from FEM and analytical model based on the M_{Tool} and M_{Work_AD} calculations. The excellent agreement between these two approaches validates the correctness of the chip moments calculations. The results of this chapter are very useful to understand the micromilling mechanism and improve the workpiece performances.

6.2 FEM Model

In the material removal processes using geometrically defined cutting edges, workpiece material undergoes severe deformations and shearing at very high deformation rates and sometimes high temperatures. Hence, adopting the reliable workpiece material flow stress data, also as well known as the constitutive model,

A(MPa)	B(MPa)	n	C	m	Others
324	114	0.42	0.002	1.34	$T_{melt} = 582^{\circ}\text{C} = 855.15\text{K}$ $T_{room} = 20^{\circ}\text{C} = 293.15\text{K}$

which covers the large strain rate and temperature range, is very important to characterize the material behavior in the vicinity of cutting edge [193]. As well as the material flow stress model, the friction between the tool and workpiece is also important in the cutting simulation [194]. In this section, the constitutive and friction models are chosen based on the literatures and suitable machining conditions in micromilling operation.

6.2.1 Material constitutive model

The flow stress at which the workpiece material starts to plastically deform is influenced by strain, strain rate, temperature factors and sometimes strain paths. The Johnson-Cook (JC) model [195,196], is widely accepted in machining simulation due to its good fit for strain-hardening and thermal softening behavior of metals and its numerical robustness and can be easily used in finite element simulation models [197,198]. It is represented as follows, with the constants for Al6061-T6 [196] listed in Table.6.1.

$$\bar{\sigma} = [A + B(\bar{\varepsilon})^n][1 + C \ln(\frac{\dot{\varepsilon}}{\dot{\varepsilon}_0})][1 - (\frac{T - T_{room}}{T_{melt} - T_{room}})^m] \quad (6.1)$$

$\bar{\sigma}$, Von Mises flow stress

$\bar{\varepsilon}$, equivalent plastic strain

$\dot{\varepsilon}$, strain rate. $\frac{\dot{\varepsilon}}{\dot{\varepsilon}_0}$, is the dimensionless plastic strain rate for $\dot{\varepsilon}_0 = 1.0\text{s}^{-1}$

T , workpiece temperature

T_{room} , room temperature

T_{melt} , workpiece melt temperature

A , yield stress

B and n , effects of the strain hardening with B is hardening constant and n is hardening exponent

C , strain rate constant

m , thermal softening exponent

6.2.2 Friction model

Friction properties are almost as important as the material flow stress model in the cutting simulation process. Even if many works have been done on this topic [175, 199–201], the friction behavior in the cutting zone is still not clear.

In the low cutting speed range, the friction stress τ_f on the tool rake face is assumed proportional to the normal stress σ_n , with a coefficient of friction μ . This is the sliding friction based on Coulomb's law as

$$\tau_f = \mu \cdot \sigma_n \quad (6.2)$$

According to Trent and Wright's work [202], they observed the sliding condition is dominant during low speed machining, and during high speed machining the sticking condition is dominant. In micromilling, even if a high speed spindle is adopted to improve cutting speed, due to the tiny tool diameter, the cutting speed remains much lower than the conventional one. In this case, the cutting speed is 238.8mm/s . For this reason, the Coulomb's law of sliding friction is dominant in the micromilling operation. In this chapter, for the combination of the tool workpiece materials, carbide and Al6061-T6, the friction factor μ is chosen as 0.7 as obtained from experiments by Medaska et al. [203].

6.2.3 Simulation setup

In this study, the FEM software DEFORM-2D from SFTC is used to simulate the cutting process. It is based on an updated Lagrangian formulation that employs implicit integration method designed for large deformation simulations. The strength of this FEM software is its ability to automatically remesh and generate a very dense grid of nodes near the tool tip so that large gradients of strain, strain rate and temperature can be handled. In this approach, no chip separation criterion is required, which makes it highly effective in simulating metal cutting process. Furthermore, a high mesh density zone is defined around the cutting edge as a moving window allowing an excessively distorted mesh in the primary and secondary shear zones to be automatically remeshed without interruption. Thus, the chip formation is simulated step by step per tool advance with a minimum number of remeshing.

In this simulation parameters setting, due to the small cutting depth, the

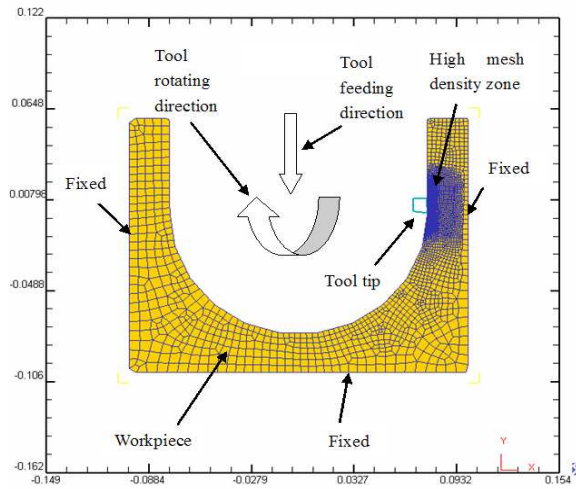


Figure 6.1: FEM model

effect of the helix angle is neglected and then the flute is assumed to be straight. Due to the small feed rate, cutting by the bottom edge is not included, and only the side edge is considered. Hence, the micromilling process is simplified as a plane strain problem, and modeled by DEFORM-2D. The workpiece is treated as elastic-plastic type, and the tool is considered as a rigid body. In our simulation, total element number of the meshed workpiece is 18404. Supported by the mesh density window technique, the tool work contact region is highly meshed with the smallest element size reducing to 80nm approximately and the whole slot cutting process by one flute is simulated. Fig.6.1 shows the detail of this FEM model, with the boundary condition, mesh of the workpiece and tool movement information.

The JC constitutive model is embedded into the simulation engine by the user routine, and the friction model is chosen as above. The micromill tool, provided by M.A. Ford, is measured by SEM in order to acquire the exact geometric information for the simulation and experiment. The other material thermal and mechanical properties are obtained from www.matweb.com. The machining parameters are designed coincident with experiment, and the feed rate is chosen very low in order to avoid the tool premature failure and prevent the 2D hypothesis to collapse. These parameters are listed in Table.6.2.

Table 6.2: Simulation and experimental parameters

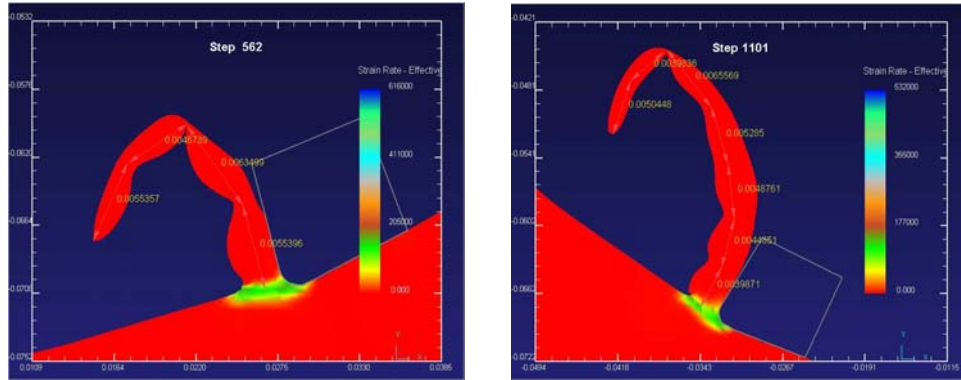
Tool geometry	
Tool diameter (μm)	152
Flutes No.	2
Edge radius (μm)	1.36
Rake angle ($^{\circ}$)	6.5
Clearance angle ($^{\circ}$)	5
Material properties of Al6061-T6	
Young's Modulus (GPa)	68.9
Poisson ratio	0.33
Thermal conductivity($W/m - K$)	167
Heat capacity($J/g - ^{\circ} C$)	0.896
Machining parameters	
Rotating speed (RPM)	30000
Feed rate(mm/min)	10
Cutting depth(μm)	20
Room temperature($^{\circ}C$)	20

6.3 Simulation results and experimental validations

Through the FEM simulation, a lot of results about the machining process are obtained by the post processor. In this chapter, we focus on those concerning the chip formation process.

6.3.1 Simulation results

The chip with wavy type formation is found. Fig.6.2(a) and Fig.6.2(b) showed the chip morphology in micromilling process with 4 segments and 7 segments respectively. The length of each segment in millimeter unit is labeled on the figure. Length values on them are approximate because the shapes of the segments depend on the mesh density. When chip moves out of the mesh density window, it may lose the real shape due to remesh. However, the newly formed segment with finer element has exact shape, and its length is measured simultaneously after their formation. When the tooth exits the machined slot, the chip is composed by 11 segments. The average segment length is $4.7835\mu m$, with $0.6645\mu m$ standard deviation.



(a) After rotating 72.2°

(b) After rotating 121°

Figure 6.2: The wavy type chip formation in micromilling simulation

6.3.2 Experimental results

All the experimental parameters are listed in the Table.6.2. Fig.6.3 is the free surface of the top burr on the slot down milling side, which is left on the workpiece when the tool leaves the workpiece [191]. From the SEM photo of the top burr, it is clearly that there are many parallel wavy segments distributed on the burr free surface. In order to obtain more powerful evidences, the micro chips were collected and embedded in the resin, then polished and viewed under the optical scope. Fig.6.4 shows two chip examples. The wavy segment is observed, with $5.79\mu\text{m}$ average segment length and $1.36\mu\text{m}$ standard deviation. The chip shape is quite similar with the simulation results. Although the average segment length value is a little greater than the FEM result, the error is in the acceptable range.

Meanwhile, the micromilling experimental force signals were recorded by the ultra precision three-component dynamometer. The peak-to-valley values of the experimental X and Y forces averaged over 50 revolutions were calculated and compared with the simulation results. The X and Y forces in the experimental are 0.462N and 0.475N . The corresponding simulation results are 0.446N and 0.453N . The relative errors of them are within 5%. Therefore, the simulation results are believed correct, and the FEM results are capable to provide better understanding of the chip formation mechanism [183].

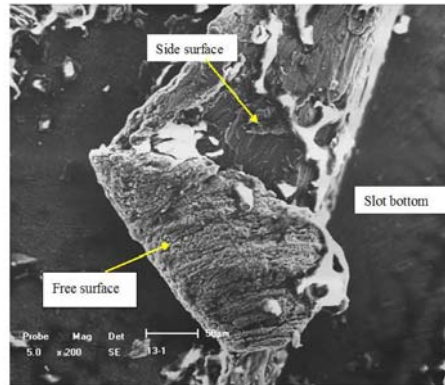
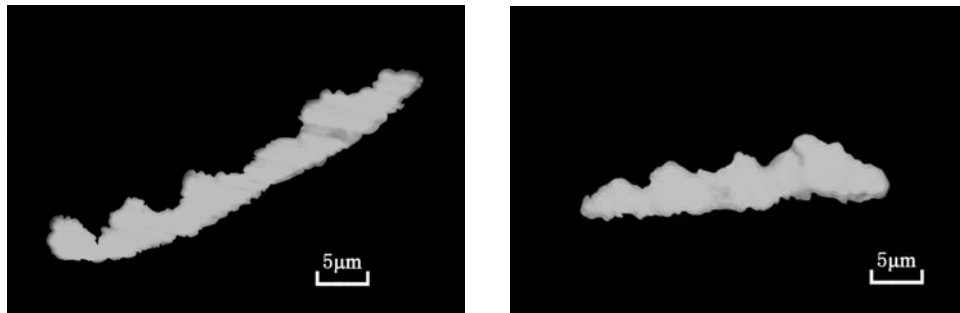


Figure 6.3: The top burr on the down milling side of the micromilled slot



(a) Chip sample 1

(b) Chip sample 2

Figure 6.4: The section view of the wavy chip

6.4 Chip formation process

The wavy chip formation is also known as laminar type [204], continuous fragmentary type [171]. It was first reported by Bickel [205], who used a high frequency flash lamp to produce a series of pictures showing the development of what is generally referred to as a wavy chip. He found that this phenomenon is the result of a repetition of the cycle of variation in shear angle, forces and chip thickness. It had the same appearance as a continuous “flow” type chip except that there were signs of greater and less strain having taken place in the thin and thick chip vicinities respectively [206]. Similar cyclic chips were described by Eugene [207] and Albrecht [208]. Recently, Astakhov et al. [209] analyzed the bending moment effect in chip forming process and regarded that this is the reason of wavy chip. However, these explanations are suitable to the steady

cutting condition in conventional scale with relative greater UCT, in which the mass of the formed chip is enough to bear the continuously impact from the tool. But in the milling operation, in each tooth pass, the chip experiences forming, growing, and breaking procedures, which is a typical transient cutting procedure. The chip mass varies in the entire process, especially in micromilling it is much smaller than the one in conventional scale milling.

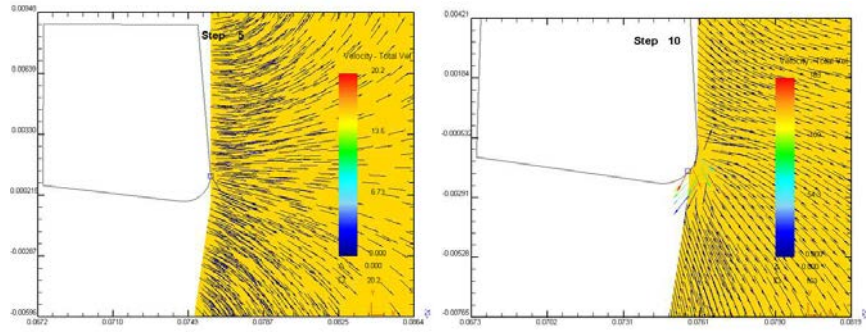
In this section, the process of wavy chip formation in the micromilling process is described in detail through chip velocity analysis by FEM.

6.4.1 Chip formation process

The first four segments formation processes, Figs.6.5 ~ 6.8, are described in detail. The state variable of these series is the total node velocity obtained from the FEM.

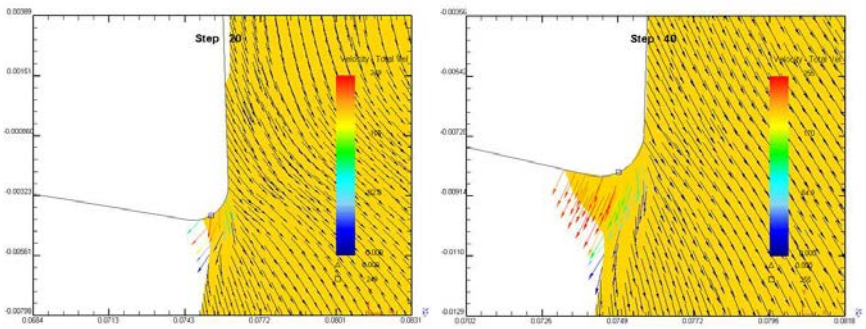
At the beginning of tool workpiece engagement, the UCT is quite small, and the ploughing effect is dominant in the tool work contact region. The tool edge presses workpiece, but the node velocity magnitude is smaller due to the tool moves in the tangential direction, Fig.6.5(a). As the tool advancing, the UCT increases. When the tool rotates around 1.8° , a very critical UCT is achieved, Fig.6.5(b). In this moment, a small amount material in front of the tool tip moves upward along the edge radius, the other fraction of workpiece is compressed beneath the tool edge and slides to the tool flank face. This critical UCT, which is defined as MCT in most cases, is very important in microcutting operation. After this transition point, the shearing effect appears between the tool and workpiece. In this simulation, the MCT is about $0.268\mu m$ examined by FEM. It coincides with the calculation results by Wang et al. [210]. However, in this simulation the feed rate per tooth is about $0.17\mu m$, it seems impossible to achieve the MCT just after the tool only rotates about 1.8° . One reason of this problem is due to the workpiece shape error caused by the remesh in FEM environment. The other reason is caused by material deformation due to the tool edge indenting, and it will be discussed qualitatively in Section. 6.5 by another FEM analysis.

With the continuous steps, the tool advances gradually as shown in Fig.6.5(c) and Fig.6.5(d). After the transition of MCT, shearing becomes more significant than the ploughing effect gradually, which induces the chip growth. In Fig.6.5(c), the workpiece material is piled up in front of the tool edge. The



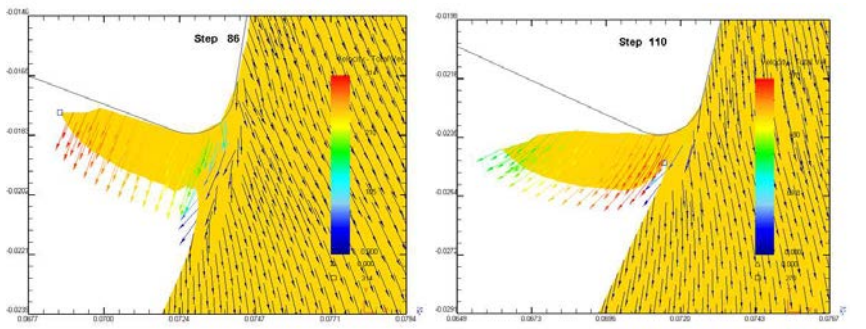
(a) 0.5°

(b) 1.8°



(c) 3.24°

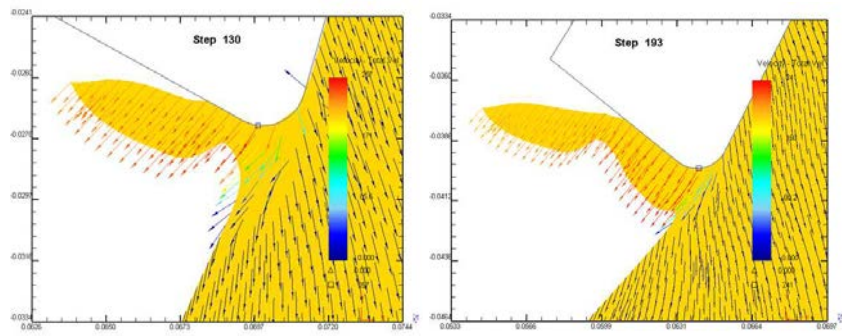
(d) 6.55°



(e) 14.14°

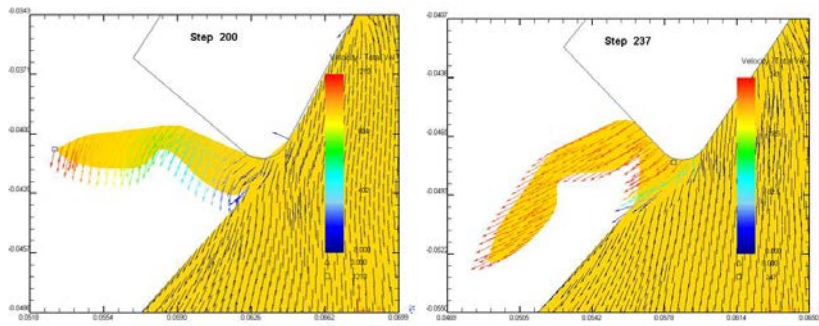
(f) 18.17°

Figure 6.5: The first segment formation process



(a) 21.41°

(b) 32.02°



(c) 33.28°

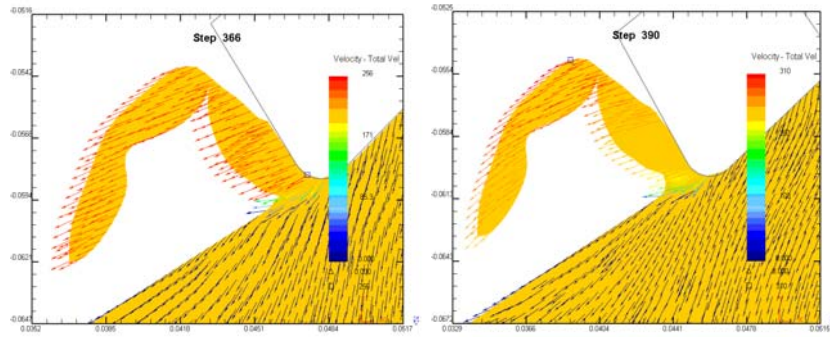
(d) 39.22°

Figure 6.6: The second segment formation process

node velocity vectors show an upward trend which represent the chip growth, indicate a possible extruded-like behavior. This effect is similar to the indentation operation, with a rigid ball pressing on the material. With the gradual chip growth, the velocity of deformed material ahead of the tool tip direct toward almost parallel to the tool tangential movement direction, Fig.6.5(d). The chip is formed and the shearing effect becomes dominant to the chip formation process hereafter. With the chip growth, both the tool chip contact length l_T and the shear band length l_S increase continuously, and more kinetic energy transferring into the chip from tool tip. In Fig.6.5(e), the chip starts to separate from the rake face, and bend forward and downward to the uncut workpiece surface. This angular motion causes the maximal chip velocity location transferring from the chip root in previous steps to the chip tip in this step. Then the chip accelerates to bend, which causes the l_T reducing and concentrating on a small section between the chip root and tool edge, as well as shortening l_S , Fig.6.5(f). Large portion of the kinetic energy is transferred to the chip root by the edge radius, which leads the chip starting to move upward. Meanwhile, the maximal chip velocity location changes to the chip root again. Till now, the first segment is formed completely, and the second segment formation process begins.

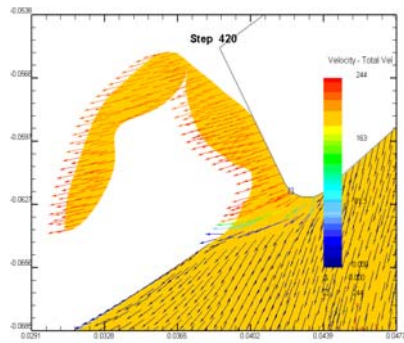
As the tool advancing, the tool edge indents the material continuously, the extruding phenomenon occurs again. The newly deformed materials move forward and upward, and they impel the first segment moving with them. With the increase of the l_T and l_S , Figs.6.6(a,b), the maximal chip velocity locates on the chip root. Until both l_T and l_S reach their local maximal value, the chip bending phenomenon takes place once again as shown in Fig.6.6(c). The maximal chip velocity locates on the chip tip in this occasion because of the additional chip angular acceleration. The second segment is produced until l_T and l_S decrease to their local minimal value and the maximal chip velocity location transfers to the chip root again, Fig.6.6(d).

The third and fourth wavy segments formation procedures are similar to the first and second one, as presented in Fig.6.7 and Fig.6.8. The maximal velocity location changes from the chip root to chip tip then back to chip root in each wavy segment generation. But due to the increase of chip mass m_{Chip} as well as its moment of inertia J_{Chip-O} , and since the difference, $M_{Tool-Max} - M_{Work-Max}$, remains almost constant as analyzed in Section. 6.6, the chip can not get much greater angular acceleration as the first two segments.



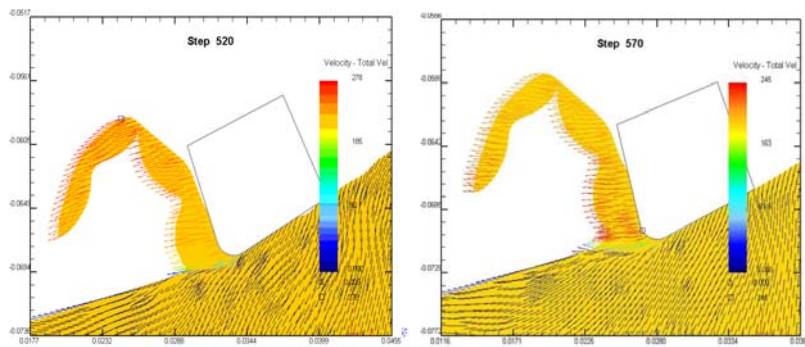
(a) 50.91°

(b) 53.07°



(c) 55.77°

Figure 6.7: The third segment formation process



(a) 64.59°

(b) 68.9°

Figure 6.8: The fourth segment formation process

The next a few segments formation procedures are similar to the first four. But due to the increase of the chip mass and moment of inertia, the milling process enters the steady status gradually. In the next a few wavy segments generation occasions, although the chip maximal velocity location also varies and the chip bending movement occurs, they are not as obvious as before. The wavy chip formation in the entire micromilling process is shown in Fig.6.9.

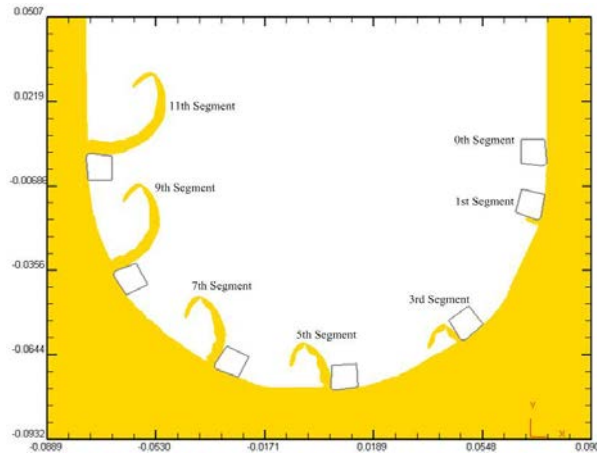


Figure 6.9: The entire chip formation process

6.5 Tool edge radius effect

In the microcutting operation, due to the small UCT, the tool edge radius effect can not be neglected. When the ratio of the UCT to tool edge radius is smaller than 1, the nominal rake angle of the tool doesn't work, and the effective rake angle is negative in reality [130,211,212]. In this section, the edge radius effect to the uncut surface deformation is investigated qualitatively, in order to explain the change of uncut chip thickness in the micromilling process in Fig.6.5(b).

This process is modeled as an indentation operation by FEM, with a rigid ball pressing into the material. This is an axis symmetric problem, Fig.6.10. The rigid ball moves downward ($-Y$ direction), with $1.36\mu m$ radius and constant speed $238.8mm/s$. The workpiece is Al6061-T6, with the Johnson-Cook flow stress model and the Coulomb's friction model. All of the settings are as same as the micromilling simulation.

After the rigid ball indenting about $616nm$ depth, the material deformation

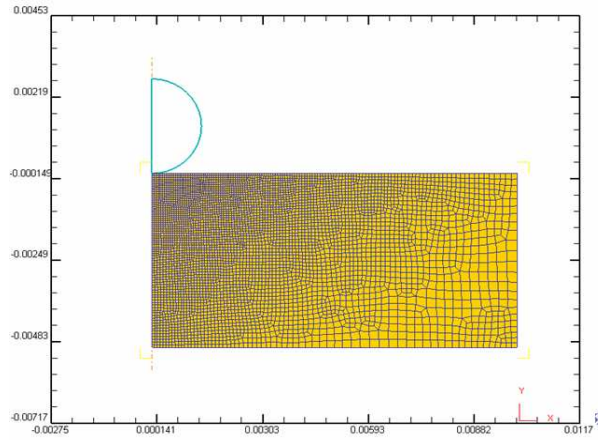


Figure 6.10: Indentation FEM model

is shown as Fig.6.11 with nodal displacement contour. The maximum material deformation locates in the symmetric axis with the nominal indentation depth. However, due to the material plastic flow, the surface which is not pressed by the rigid ball is deformed in the reverse indentation direction, (+Y direction). After sampling the displacement data along the top surface of workpiece, Fig.6.11(a), their values are shown in Fig.6.11(b). In Y displacement curve, the material out of the indentation zone is deformed in the reverse direction after the ball movement. The maximal upheaving is about $100nm$, $1/6$ of indentation depth, and the maximal X deformation value is more than $200nm$, $1/3$ of indentation depth. In micromilling process, the tool round edge first contacting material is similar with the indentation process. Although the material is not removed, it is deformed with tool advancing, and some materials heave in front of tool edge. Therefore the instantaneous UCT changes. This is the reason that in Fig.6.5(b), although the nominal UCT is less than the MCT, the actual UCT is greater than the nominal value after some materials begin to move upward with tool pressing.

6.6 Chip moments calculations

6.6.1 Modeling of the chip formation

In this section, the chip is modeled as a cantilever to explain the chip formation process, as shown in Fig.6.12. Two moments about the chip separating

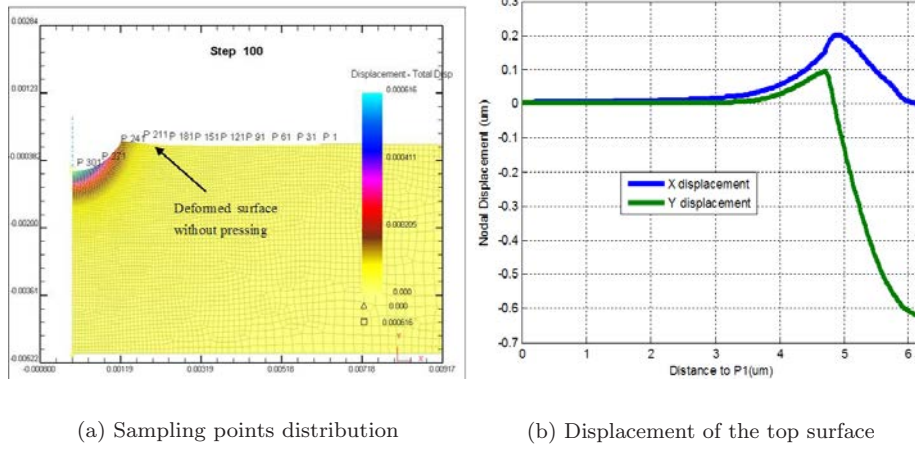


Figure 6.11: The displacement contour of the indentation process

point O are inflicted on the chip. The first one is the “Tool rake moment”, M_{Tool} , from the tool rake to chip by the tool movement. The second one is the “Shear plane moment”, M_{Work} , from the workpiece to chip due to the normal stress on shear plane. Both of them are scalars, and their directions are shown in Fig.6.12. So that the chip angular motion around \vec{OZ} axis is governed by Eq.(6.3). The chip mass is m_{Chip} , and its moment of inertia in the XY plane about \vec{OZ} is $J_{Chip,O}$, and the corresponding angular acceleration around \vec{OZ} is $\dot{\omega}_{Chip}$.

$$(M_{Tool} - M_{Work}) = J_{Chip,O} \dot{\omega}_{Chip} \quad (6.3)$$

From the previous analysis, it has been found that the chip velocity varied in the chip formation process, and it can be explained if $\dot{\omega}_{Chip}$ can be obtained from from Eq.(6.3). Therefore, understanding the moments inflicted on the chip and their fluctuations are very critical to clarify the segments formation mechanism. In the subsequent sections, the hybrid FEM-analytical approach which comprises both FEM simulation results and some analytical models, is adopted to calculate the M_{Tool} and M_{Work} .

6.6.2 M_{Tool} calculation

M_{Tool} is produced by the normal pressure distributed on the chip-rake contact surface. It can be calculated as follows.

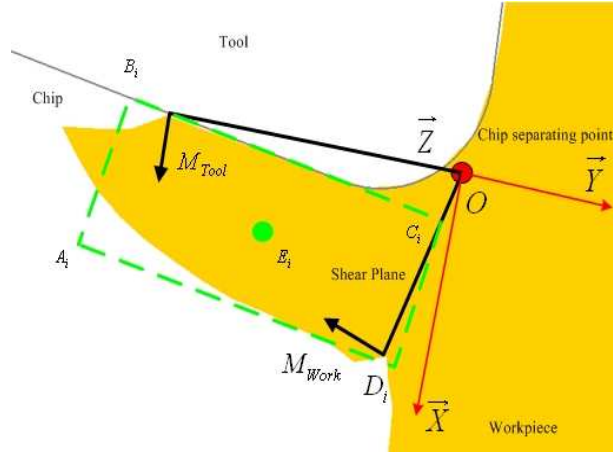


Figure 6.12: Chip cantilever modeling

First, disperse the tool chip contact surface to many infinitesimal elements from the chip separating point O , to the tool chip separating point F , Fig.6.13. To each element, the normal pressure value is obtained from FEM simulation, so M_{Tool} can be calculated by Eq.(6.4).

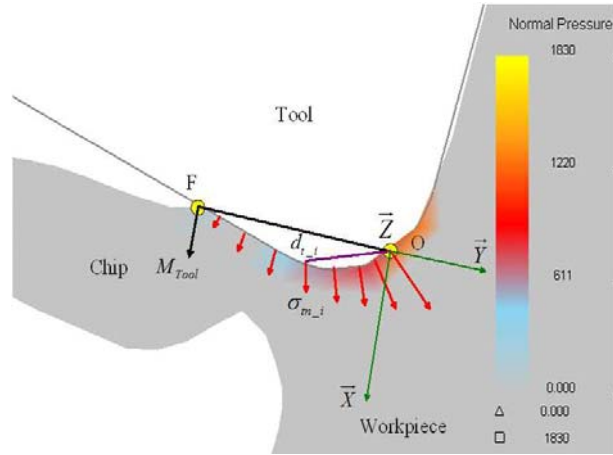


Figure 6.13: M_{Tool} and tool rake normal pressure

$$M_{Tool} = \int_O^F w \sigma_{tn-i} d_{t-i} dl \quad (6.4)$$

σ_{tn-i} is the normal pressure acting on the i_{th} element. d_{t-i} is distance from the i_{th} element to point O . dl is arc length of the i_{th} element. And w is the chip width along the \overrightarrow{OZ} axis, in this case $w = 20\mu m$.

6.6.3 M_{Work} calculation

M_{Work} is generated from the normal stress distribution on the shear plane, Fig.6.14. Since in the shear plane, strain rate is significantly greater than the other parts of workpiece, the shear plane can be determined by the equivalent strain rate distribution plot in FEM [213]. The M_{Work} can be calculated by Eq.(6.5). σ_{wn_i} is the normal stress from the i_{th} element acting on the shear plane. d_{w_i} is distance from the i_{th} element to the point O . ds is the length of the i_{th} element. Because the normal stress varies in a linear relationship along the shear plane, with the maximum value on point G at chip free surface, and reduces towards the chip separating point O [201]. However, the value of σ_{wn_i} in the point O or G and the slope of σ_{wn_i} distribution are very difficult to obtain till now, one of the simplifications is to assume the normal force N_S inflicted on the middle point of the shear plane [214]. In this work, we continue this assumption, and the Eq.(6.5) is reduced to Eq.(6.6), in which the average shear plane normal pressure $\sigma_{wn_{aver}}$ is easier to be calculated by dividing N_S by the shear plane area A_S , Eq.(6.7). A_S is calculated by Eq.(6.8). l_S is the shear band length. Noticing the assumption of N_S acting on the middle point of the shear plane induces some errors when calculating the M_{Work} , due to the actual acting point depending on real σ_{wn_i} distribution. The maximal relative error is 0.33 when σ_{wn_i} in point O is zero, but in the machining process this value is always much greater than zero, so the error caused by this simplification can be accepted.

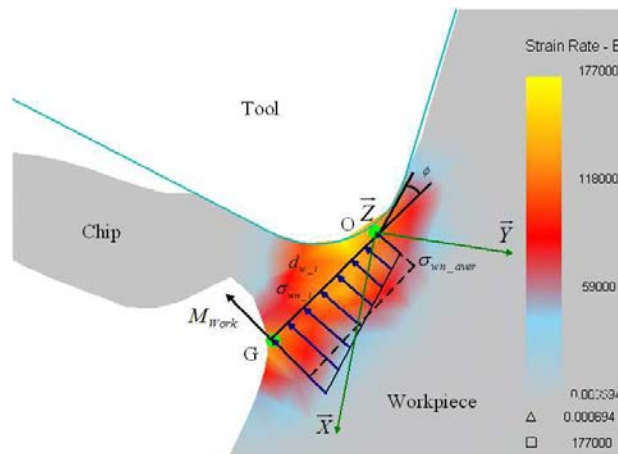


Figure 6.14: M_{Work} and shear plane normal stress

$$M_{Work} = \int_O^G w\sigma_{wn.i}d_{w.i}ds \quad (6.5)$$

$$M_{Work} = \frac{w\sigma_{wn.aver}l_s^2}{2} \quad (6.6)$$

$$\sigma_{wn.aver} = \frac{N_S}{A_S} \quad (6.7)$$

$$A_S = wl_S \quad (6.8)$$

In this work, because the $\sigma_{wn.i}$ can not be obtained from FEM, therefore two models, MM model and AD model are used to calculate the N_S respectively, and result in different M_{Work} , renamed as M_{Work_MM} and M_{Work_AD} . The comparison between them gives deeper understanding of microcutting mechanism.

M_{Work_MM} calculation

In this section, N_S is calculated based on the Merchant theory [192], renamed N_{S_MM} . It assumes that the cutting forces originated from the shear work consumed in shear plane and the friction work between the chip and tool rake. This theory is widely accepted and suitable to the conventional orthogonal cutting with greater UCT and neglects the effects of the tool edge radius [214–216].

According to the Merchant's force circle [192], N_{S_MM} is expressed by cutting force F_{P_MM} , thrust force F_{Q_MM} , and shear angle ϕ , Eq.(6.9). However, only orthogonal force components F_X and F_Y can be obtained directly from the FEM simulation results. In case of orthogonal cutting hypothesis, F_{P_MM} and F_{Q_MM} in milling operation are transformed from F_X and F_Y by tool rotating angle θ with Eq.(6.10). The shear angle ϕ , defined between the tool rotating tangential direction and the shear band in XY plane, is also obtained from FEM. Then, the final M_{Work_MM} expression, Eq.(6.11), is deduced with all components from FEM analysis.

$$N_{S_MM} = F_{P_MM} \sin \phi + F_{Q_MM} \cos \phi \quad (6.9)$$

$$\begin{bmatrix} F_{P_MM} \\ F_{Q_MM} \end{bmatrix} = \begin{bmatrix} \sin \theta & \cos \theta \\ -\cos \theta & \sin \theta \end{bmatrix} \begin{bmatrix} F_X \\ F_Y \end{bmatrix} \quad (6.10)$$

$$M_{Work-MM} = \frac{[-\cos(\theta + \phi)F_X + \sin(\theta + \phi)F_Y]l_s}{2} \quad (6.11)$$

$M_{Work-AD}$ calculation

Due to the machining parameters and tool geometric features in micromilling operation are obviously different from the conventional cutting, it has been found that the microcutting forces are produced not only by the shearing effect ahead of the tool tip, but also by the tool workpiece ploughing, friction, and workpiece springback effects. The most important reason of these effects is the reduced ratio of UCT to the cutting edge radius, along with the specific cutting energy increases exponentially to approximately 100-times than that at conventional sizes. Arcona and Dow [169] proposed a cutting force model for diamond machining based on elastic contact and friction between the tool and some workpiece materials, including Al6061-T6 alloy. While the model also included shearing forces for a very sharp and rigid tool, the results showed that as the UCT reduced, the shearing contribution to the total cutting forces greatly decreases while the elastic contact and friction components approached an asymptotic level. These parasitical forces were attributed to elastic springback of the workpiece as it was compressed and moved under the cutting edge without being removed. The AD model required the hardness and Young's modulus of the workpiece and two empirical constants were obtained from cutting measurements. Therefore, it is much easier to be imbedded into the NC system than other complex mechanics model for the online manufacturing error compensation. Although it was first developed for the diamond turning force calculation purpose, some later investigators resorted to modify and employed the AD model into the micromilling process. Dow et al. [43] integrated the AD model into the NC system to predict the cutting and thrust forces of the small ball end milling of S-7 tool steel, and compensated shape error induced by the tool deflection. Friedrich et al. [168] modified the AD model to investigate the workpiece springback effect to the micromilling force components. Gong et al. [217] used the AD model to calculate the micromilling force with the consideration of the tool radial error motion.

The major differences between the micromilling and diamond cutting are that the milling tool edge radii are in the order of several micrometers, the milling tool has a variable UCT for each edge, and the milling tool has multiple

edges in contact with the workpiece with time-varying force resultants at any instant of tool rotation [168]. The AD model adopted into one generalized micromill tool edge, either the side edge or the bottom edge, is illustrated in Fig.6.15.

The AD model is expressed as Eq.(6.12). H and E are the hardness and Young's modulus of the workpiece material respectively. A_C is the face area of the chip. A_f is the tool flank contact area with the workpiece. μ is the friction coefficient between tool rake face and workpiece. μ_f is the friction coefficient between flank face and workpiece. ϕ is the shear angle. The cutting force F_{P_AD} in the Eq.(6.12) consists two terms. The first is the force on the rake face and is a function of the workpiece material and the area of the chip, A_C . The second term originates from the friction on the flank face of the tool and is a function of the workpiece material, the tool flank contact area A_f and the friction coefficient μ_f . The thrust force F_{Q_AD} in Eq.(6.12) is similar to the cutting force with the first term originating from friction on the rake face and the second from the direct force on the flank face. The constants in Eq.(6.12) were experimentally obtained as a best-fit for several materials including Al6061-T6 [169]. In this model, it is obviously that the second term of each force component is the contribution of the workpiece springback on the flank face. The first term has related to the effects of the rake face.

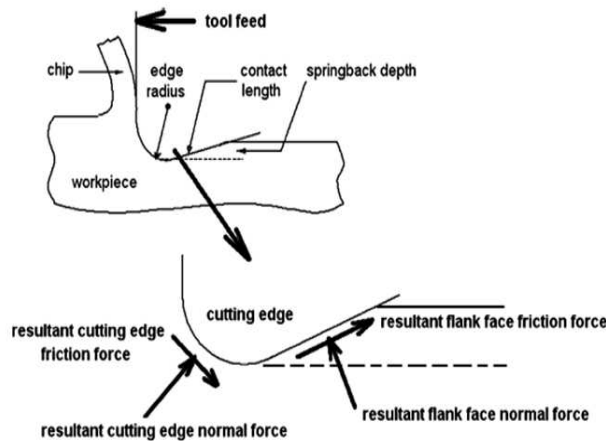


Figure 6.15: Generalized micromilling tool cutting edge and flank with resultant normal contact forces and friction forces. Magnitude and orientation of resultant force vectors depend on tool geometry and work piece springback depth [168]

In order to calculate the cutting force only due to the effects from tool rake,

each second item in Eq.(6.12) is ignored, and the final expressions of F_{P_AD} and F_{Q_AD} are reduced to Eq.(6.13). Integrating them into the normal force on the shear plane N_{S_AD} , Eq.(6.14), and input N_{S_AD} into Eq.(6.7), the M_{Work_AD} is given in Eq.(6.15).

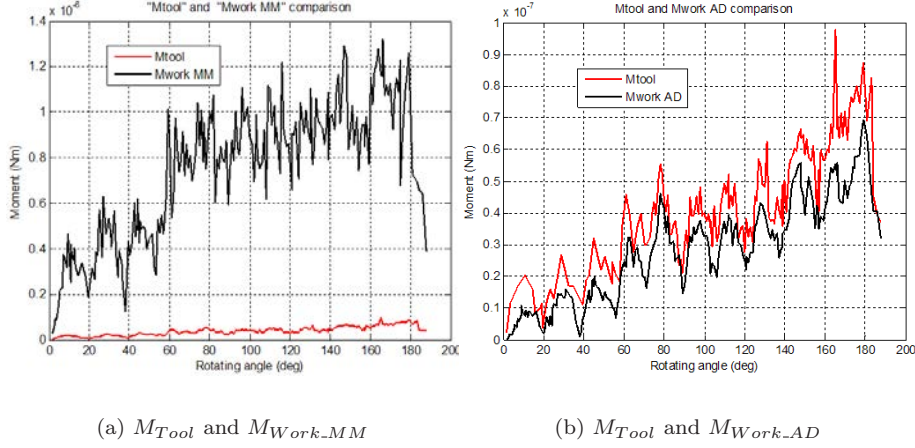


Figure 6.16: M_{Tool} Vs M_{Work_MM} and M_{Tool} Vs M_{Work_AD}

$$\begin{cases} F_{P_AD} = \frac{HAC}{3} \left(\frac{\cot \phi}{\sqrt{3}} + 1 \right) + \mu_f A_f \left[(4.1H) \sqrt{\frac{H}{E}} \right] \\ F_{Q_AD} = \mu \left[\frac{HAC}{3} \left(\frac{\cot \phi}{\sqrt{3}} + 1 \right) \right] + A_f \left[(4.1H) \sqrt{\frac{H}{E}} \right] \end{cases} \quad (6.12)$$

$$\begin{cases} F_{P_AD} = \frac{HAC}{3} \left(\frac{\cot \phi}{\sqrt{3}} + 1 \right) \\ F_{Q_AD} = \mu \left[\frac{HAC}{3} \left(\frac{\cot \phi}{\sqrt{3}} + 1 \right) \right] \end{cases} \quad (6.13)$$

$$N_{S_AD} = F_{P_AD} \sin \phi + F_{Q_AD} \cos \phi \quad (6.14)$$

$$M_{Work_AD} = \frac{wl_s^2 H \sin \phi}{6} \left(\frac{\cot \phi}{\sqrt{3}} + 1 \right) (\sin \phi + \mu \cos \phi) \quad (6.15)$$

6.7 Chip moments calculation results

In this section, the calculation results of the M_{Tool} and M_{Work} (M_{Work_MM} and M_{Work_AD}) are given in detail. Fig.6.16 gives the comparisons between M_{Tool} and M_{Work_MM} and between M_{Tool} and M_{Work_AD} .

From Fig.6.16(a), it is obviously that M_{Work_MM} is much greater than M_{Tool} . Should this fact be, the chip wouldn't form the wavy segment and

grow up. This is contradictory with the simulation results and experimental observation.

In Fig.6.16(b), M_{Tool} is a little greater than M_{Work_AD} with the similar variation curves. When the chip segment starts to occur, both of them are in the local minimum values, and reaches the local maximum values when it starts to bend. Then with the decrease of the l_T and l_S , both of them reduce to another local minimum values. The curves have 11 waves, which correspond to the 11 segments formations. This is similar with the definition of “Self induced vibration in metal cutting” by Albrecht [208]. From Eq.(6.3), it is seen that the difference of M_{Tool} and M_{Work_AD} , $M_{Tool} - M_{Work_AD}$, induces the chip angular motion and segment generation. These three variables are given in the Fig.6.17. Although the difference $M_{Tool} - M_{Work_AD}$ fluctuates, but its deviation is small, and it doesn't increase as the chip moments. Only when the M_{Tool} and M_{Work_AD} reach their local maximal values, the chip starts to bend in this instant, some peak values exist to induce the additional chip angular acceleration. This procedure repeats for each segment generation in the entire micromilling process, and coincides with the FEM simulation and experimental results.

The comparison of the chip moments calculation results also indicates that widely accepted MM model is not valid in the microcutting. Additional works need to be realized to develop new model adapted to microcutting, and the AD model could be a good candidate.

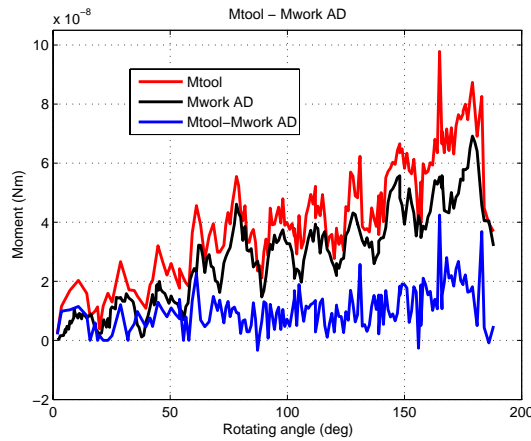


Figure 6.17: M_{Tool} , M_{Work_AD} and $M_{Tool} - M_{Work_AD}$ variations

Therefore, it is important to clarify the main reasons of the M_{Tool} and M_{Work_AD} variations, which are the primary reasons of the wavy chip formation. In the chip moments calculation, the chip width w is a constant, so in Eq.(6.6), we know the M_{Work_AD} is a function of shear band length l_S and average shear plane normal pressure σ_{wn_aver} , $M_{Work_AD} = f(l_S^2/2, \sigma_{wn_aver})$. From Eq.(6.15), the σ_{wn_aver} is caused by the shear angle ϕ . Similar with M_{Work_AD} , we simplify the M_{Tool} in Eq.(6.4) as a function of tool chip contact length l_T and the equivalent tool rake normal pressure σ_{tn_equ} , $M_{Tool} = f(l_T^2/2, \sigma_{tn_equ})$.

The Fig.6.18 gives the variations of σ_{tn_equ} and σ_{wn_aver} in the entire milling process. Obviously, they don't follow the same trends as the M_{Tool} and M_{Work_AD} . Their magnitudes are not great although there are some exceptions as below. At the beginning of tool workpiece engagement, the σ_{tn_equ} value is much greater. This is the so called size effect due to extra small uncut chip thickness. Then in the first three segments generation occasions, there are some greater values, because the shorter l_T to increase the specific cutting energy. Especially when the second segment occurs, after the tool rotating about 40° , because the l_T and l_S are shortest in this occasion as shown in Fig.6.19, both σ_{tn_equ} and σ_{wn_aver} are higher due to the higher specific cutting energy. From Fig.6.19, it is obviously that l_T and l_S fluctuate in the similar trends as the M_{Tool} and M_{Work_AD} . Before the chip bending, l_T and l_S accompanied with the M_{Tool} and M_{Work_AD} increase simultaneously. According to Childs [218] and Astakhov [173], the normal stress distributed on the shear plane has an upper limit. When the M_{Work_AD} reaches its local maximal value, the l_S achieves its local maximal value too. But due to the continuous tool advancing, the M_{Tool} still increases along with the l_T . Then the difference $M_{Tool} - M_{Work_AD}$ increases to great enough to make the chip get the additional angular acceleration and bend. The M_{Tool} and l_T achieve their local maximal values when the chip begins to bend. After chip separates from the tool rake in the chip bending process, the l_T decreases faster and induces the decreasing of other variables, such as M_{Tool} , M_{Work_AD} and l_S . From Fig.6.19, we found the l_T decreases faster than l_S in the chip bending process. It means the decrease of l_T is the main reason of the chip bending. After the chip bending angular motion finish, all of these variables achieve their local minimal values, the chip starts to grow again, and the wavy segment is formed. This procedure repeats and repeats for each wavy segment generation. Due to the smaller chip mass and moment of inertia, these

phenomena are obvious especially in the first a few segments generation processes. Therefore, the l_S and l_T induce the M_{Tool} and M_{Work_AD} fluctuating with the same trend as them. It means the main reasons of the wavy segment chip are the variations of l_S and l_T .

6.8 Chip velocity analysis

From the analysis of chip formation process, in each segment generation the maximal chip velocity changes from the chip root to chip tip, then back to chip root. This phenomenon is obviously when the chip mass and moment of inertia are smaller.

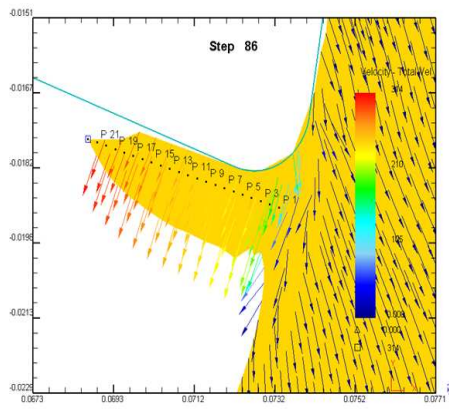
Fig.6.20 and Fig.6.21 give the comparison of chip velocity distribution before and after the chip separating with the tool at the first segment generation instant. The average velocity value in Fig.6.21 is $424.6mm/s$, but in Fig.6.20, this value is only $256.2mm/s$, which is similar with the cutting speed, $238.8mm/s$. The chip velocity ranges from $138.8mm/s$ to $314.4mm/s$ in Fig.6.20 and from $130.8mm/s$ to $665.3mm/s$ in Fig.6.21 respectively.

As same as the Fig.6.20 and Fig.6.21, the Fig.6.22 and Fig.6.23 represent the chip velocity distribution when the second segment forms. The similar results are found as the comparison between the Fig.6.20 and Fig.6.21. The average velocity value is $662.9mm/s$ in Fig.6.23, much higher than the corresponding value in Fig.6.22, $215.7mm/s$, which is also about the cutting speed. The chip velocity ranges from $167.5mm/s$ to $235.8mm/s$ in Fig.6.22, and from $133.8mm/s$ to $1206mm/s$ in Fig.6.23.

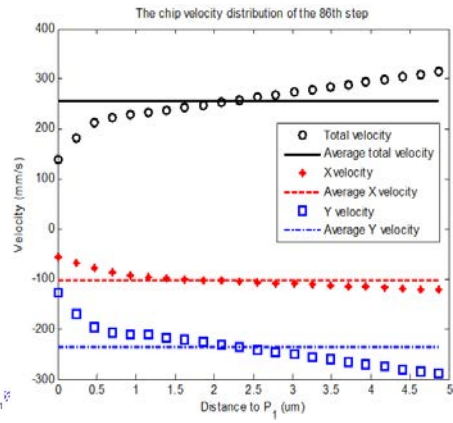
From the analysis in this section, we know the average chip velocity magnitude after the chip separating from the tool, Fig.6.21 and Fig.6.23, is much greater than one before the chip bending, Fig.6.20 and Fig.6.22, which is about the nominal cutting speed. Meanwhile, the velocity in the shear plane is almost constant for all cases, but during the chip bending process the chip tip velocity in Fig.6.21 and Fig.6.23 are greater because of the chip angular acceleration as calculated in the Section 6.9.

6.9 Chip angular acceleration analysis

After acquiring the chip velocity distribution in the adjoining steps from FEM, the chip angular acceleration obtained from FEM analysis $\dot{\omega}_{Chip_FEM}$

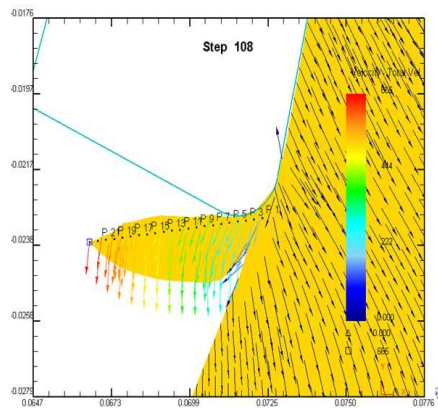


(a) Sampling points

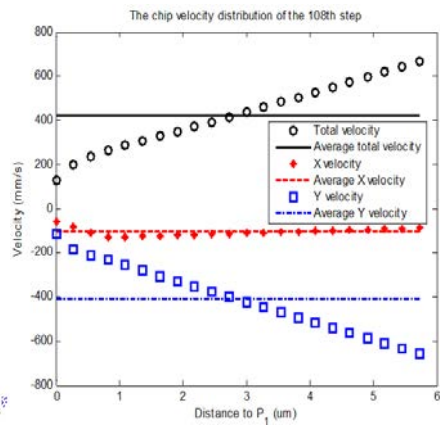


(b) Chip velocity distribution

Figure 6.20: Chip velocity distribution before the first segment separating with tool

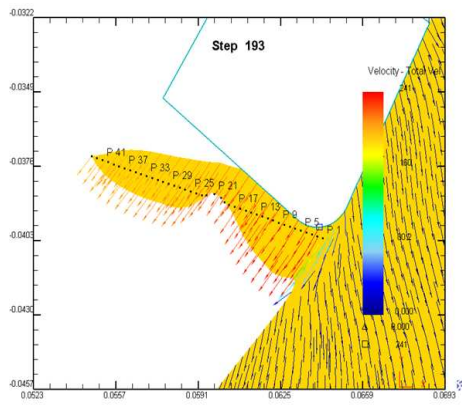


(a) Sampling points

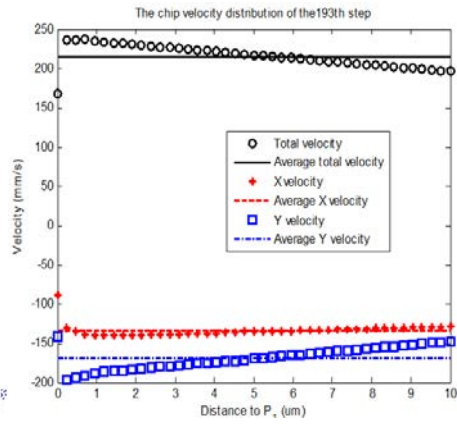


(b) Chip velocity distribution

Figure 6.21: Chip velocity distribution after the first segment separating with tool

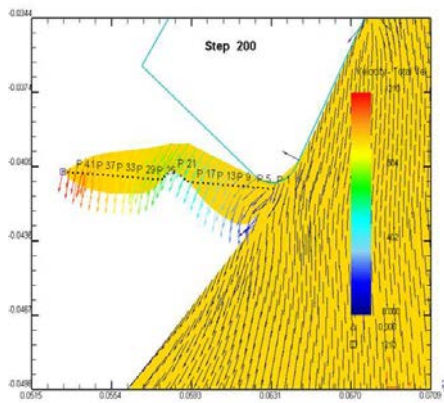


(a) Sampling points

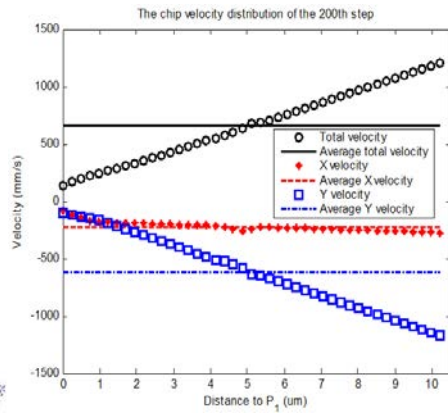


(b) Chip velocity distribution

Figure 6.22: Chip velocity distribution before the second segment separating with tool



(a) Sampling points



(b) Chip velocity distribution

Figure 6.23: Chip velocity distribution after the second segment separating with tool

can be calculated as follows.

$$\dot{\omega}_{Chip_FEM} = \frac{\frac{V_{tip_e} - V_{root_e}}{D_e} - \frac{V_{tip_b} - V_{root_b}}{D_b}}{T_e - T_b} \quad (6.16)$$

In Eq.(6.16), V_{tip_b} is the chip tip velocity in the beginning step. V_{tip_e} is the chip tip velocity in the end step. V_{root_b} is the chip root velocity in the beginning step. V_{root_e} is the chip root velocity in the end step. D_b is distance from the chip root to chip tip in the beginning step. D_e is distance from the chip root to chip tip in the end step. T_b is the time of the beginning step. T_e is the time of the end step. All of these elements can be obtained from FEM results, and for the first and second segment, they are shown in Figs.6.20 ~ 6.23.

Meanwhile, due to M_{Tool} and M_{Work_AD} can be calculated as above. If the chip moment of inertia J_{Chip_O} is obtained, the Eq.(6.3) can be used to calculate $\dot{\omega}_{Chip}$ in another way. Then the comparison between $\dot{\omega}_{Chip}$ and $\dot{\omega}_{Chip_FEM}$ can be utilized to validate the correctness of M_{Tool} and M_{Work_AD} calculations. As shown in Fig.6.12, the chip is modeled as a cantilever with a series segments. Hence, the J_{Chip_O} can be calculated approximately as follows. First, assuming the chip is homogeneous, without the density change in the cutting process. Then simplify the i^{th} chip segment to a rectangular shape $A_i B_i C_i D_i$, with length l_i , width b_i , and geometric shape center E_i . The subscript i represents the segment sequence number, from 1 to n, here $n = 11$. For the i^{th} segment, its moment of inertia about the \overrightarrow{OZ} axis across their own geometric shape center E_i is J_{E_i} , which is calculated by Eq.(6.17). Then according to the ‘‘Parallel Axis Theorem’’, to the entire formed chip, J_{Chip_O} is expressed by Eq.(6.18), in which d_i is the distance from E_i to point O , and m_i is the mass of the i^{th} segment, which is the product of the work density ρ and the chip volume, estimated by Eq.(6.19).

$$J_{E_i} = \frac{m_i(l_i^2 + b_i^2)}{12} \quad (6.17)$$

$$J_{Chip_O} = \sum_{i=1}^n (J_{E_i} + m_i d_i^2) \quad (6.18)$$

$$m_i = \rho l_i b_i w \quad (6.19)$$

When each segment forms, J_{Chip_O} is calculated at the corresponding rotating angle. Due to the chip curling, the J_{Chip_O} increases in a non-linear trend.

At the beginning of the micromilling, J_{Chip-O} is smaller. This is the reason that the chip acquires great velocity in the first a few segments formation processes. By polynomial curve fitting, the J_{Chip-O} is found to be a third order function with reference to the rotating angle in the entire process, Fig.6.24. Due to the fact of $J_{Chip-O} = 0$ when the rotating angle is 0° , the fitting function utilizes J_{Chip-O}/θ versus θ instead of J_{Chip-O} versus θ . Therefore, the coefficient for the zero-order item in this function shown in Fig.6.24 is set to zero, and its final expression is Eq.(6.20).

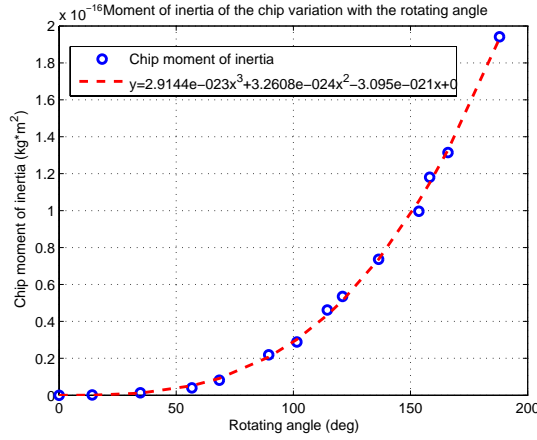


Figure 6.24: The moment of inertia of the chip variation with the rotating angle

$$J_{Chip-O} = 2.9144e^{-23}\theta^3 + 3.2608e^{-24}\theta^2 - 3.095e^{-21}\theta \quad (6.20)$$

Then, the comparison between the $\dot{\omega}_{Chip-FEM}$ calculated by Eq.(6.16) and the $\dot{\omega}_{Chip}$ calculated by Eq.(6.3) is shown in Fig.6.25. Two calculation results show good agreement, and the error between them can be accepted. It validates the calculations of the M_{Tool} and $M_{Work-AD}$.

6.10 Conclusions

In this chapter, the chip formation in the slot micromilling process by one flute cutter is investigated by FEM and experiment. Based on the suitable assumptions, the micromilling operation is modeled in DEFORM-2D. The JC constitutive and Coulomb's friction models are adopted in the FEM simulation. The wavy type chip has been found when micromilling Al6061-T6 by carbide

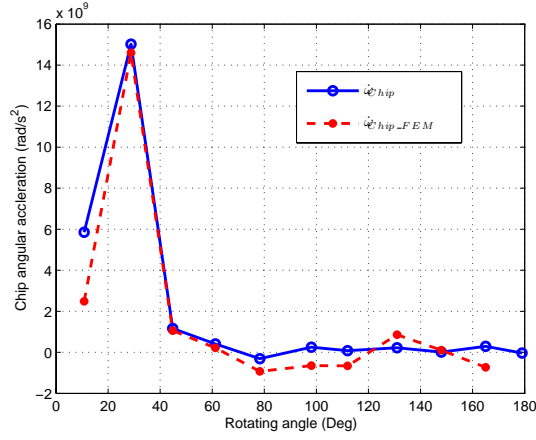


Figure 6.25: The chip angular acceleration comparison between $\dot{\omega}_{Chip-FEM}$ and $\dot{\omega}_{Chip}$

tool under this set of machining parameters. The simulation results of chip shapes, segment length, and cutting force agree well with the experimental verification. Through analyzing the chip velocity results from FEM, the chip formation process is described in detail. And the chip formation mechanism is studied quantitatively via hybrid FEM-Analytical approach. Some important results are found as follows:

1. The fluctuations of the tool chip contact length l_T and the shear band length l_S are the main reasons of wavy segment formation. They induce the variations of the M_{Work} and M_{Tool} .
2. The variation of the difference between M_{Tool} and M_{Work} , $M_{Tool} - M_{Work}$, causes the additional chip angular acceleration, and induces the chip velocity increase when the wavy segment forms.
3. The maximal chip velocity locates in the chip root before and after segment generation. In the wavy segment forming instant, the maximal chip velocity location changes to the chip tip because the chip gets additional angular acceleration caused by the increase of chip moments difference.
4. The MM and AD models are used to calculate the M_{Work} respectively. The comparison between their results shows the MM model is not suitable in microcutting scale, although it is widely accepted in conventional scale. The AD model could be a good candidate in this field.

5. When the wavy segment occurs, the average chip velocity magnitude is much greater than the one before the segment generation, which is about the cutting speed. And the chip root velocity is almost constant in the entire micromilling process, and the chip tip velocity increases too much when the chip bending.
6. When the chip segment forms, it acquires additional angular acceleration and induces the increase of chip velocity. The chip angular acceleration is obtained respectively by FEM and analytical model based on the M_{Tool} and M_{Work_AD} calculation results. The agreement of these two approaches validates the M_{Tool} and M_{Work_AD} calculations.
7. By an indentation FEM model, the uncut surface deformation under the influence of tool edge radius is studied qualitatively. This analysis is useful to explain the UCT greater than the nominal value in the micromilling process.

Chapter 7

Surface Roughness Prediction Based on Neural Network

7.1 Introduction

In the conventional scale, the parts are fabricated by multi-procedure, from rough machining to finishing, in order to achieve the required surface quality and dimensional accuracy. But in the micro-scale, the tool exchange between different procedures will induce great machining error due to the tiny tool size. Therefore, most micro components are machined by one chuck and one tool. So choosing suitable machining variables is important to improve the machined surface quality, and further widen their application. In the factory workshop level, the machinists set the parameters based on their experience and trial-and-error approach, which induces the additional production cost and the veteran requirement. Therefore, some researchers developed surface roughness model based on manufacturing geometry to predict the workpiece surface quality under different machining parameters combination [149]. But due to the complexity of the mechanical machining process, the geometrical models can not take all the surface roughness factors into account [219].

With the development of neural network (NN) technique, the non-linear problems have been studied deeply in various fields. The NN method has been carried out by Sanjay et al. [220] to predict the tool wear considering feed rate, spindle speed, torque, machining time and thrust force as process parameters during drilling of mild steel workpieces using HSS twist drills. A similar study

has been presented by Singh et al. [221] to predict drill wear by employing NN model when drilling copper workpieces. Xu et al. [222] used a NN model to study the effects of PV factor and contact temperature on the dry sliding tribological behavior of 30 wt.% carbon-fiber-reinforced polyetheretherketone composite (PEEK-CF30). El-Sonbaty et al. [223] used a NN model and fractal geometry method to study the surface roughness profiles of the milled surface. Korosec et al. [224] used a self-organized NN to improve the surface quality when do a free form surface machining. Huang et al. [225] integrated the NN model into a milling machine control system to adjust the machining parameters automatically to improve the workpiece surface quality. Markopoulos et al. [226] used this method for the Electrical Discharge Machining (EDM). Except for the machining process application, the NN method is also widely used in the control field for the motors, robots, and machine tools [227–231]. These literatures reflect that the NN is a generalized methodology in many applications.

The objective of NN method is to imitate the human brain so as to implement the functions such as association, self-organization and generalization. The ability of NN is to approximate any functions accurately and hence it is suitable to use the model for highly non-linear processes. The NN has the advantages of learning ability as well as generalization, thus can capture non-linear and complex input-output relationships. A NN is made up of some neurons connected together via synaptic links. The information is processed within neurons and propagated to other neurons through weighted connection links. NN is expected to be capable of solving a complicated problem in a very efficient manner by distributing the knowledge over the neurons and conducting parallel processing on information.

The aim of this chapter is to analyze the effects of spindle speed (n), feedrate (f) and axial depth of cut (a_P) on average surface roughness value (R_a) in the micromilling process. Compared with the conventional milling operation, the non-linearity of micromilling is more obviously due to the minimum chip thickness [130], tool radial error motion [217], and workpiece inhomogeneous inherent [210]. In this chapter, the Taguchi's approach is utilized for the design of experiment (DoE) to acquire enough training information with minimal experiment number. Based on the experimental results, the NN model is developed, trained and used to predict the micromilled bottom surface roughness. Finally, the effects of the single machining parameter and two-factor interaction

are analyzed in detail.

7.2 Experimental works

7.2.1 Experimental Conditions

A number of micromilling experiments in dry cutting condition are carried out in order to obtain the experimental data. A fresh four-flute M.A.Ford carbide micromill with $400\mu\text{m}$ diameter is employed. The slot milling experiments are conducted on Al 6061-T6 according to the DoE. The length of each experimental slot is about 6mm .

The machined slot bottom surfaces are cleaned by air-pressure before the measurement. The average roughness R_a is measured under Stil Micromasure 2 optical surface profiler. For each evaluation, the measurements were repeated at least three times with approximate $0.1 \times 0.1\text{mm}^2$ area. The step length of the profiler is set to the nanometer scale, so the surface features can be detected in detail. Fig.7.1 shows one measurement example with $n = 32500\text{rpm}$, $f = 15\text{mm}/\text{min}$ and $a_P = 15\mu\text{m}$ setting.

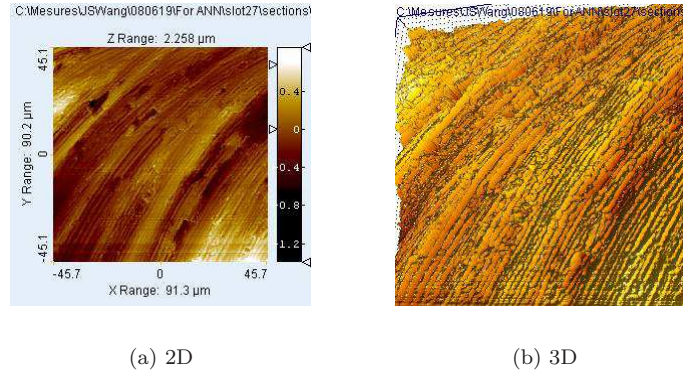


Figure 7.1: Slot bottom surface measurement example

7.2.2 Design of Experiments

In slot milling operation, the most important machining parameters are spindle speed (n), feedrate (f), and axial depth of cut (a_P). In this test, they are chosen as the experimental factors and the inputs of NN model. In this work, the tool wear is not considered as the criterion affecting the result of the cutting

Table 7.1: Experimental R_a results for NN training

Test No.	$n(rpm)$	$f(mm/min)$	$a_P(\mu m)$	$R_a(\mu m)$
1	30000	10	10	0.2303
2	30000	20	15	0.2023
3	30000	30	20	0.4435
4	30000	40	25	0.4982
5	30000	50	30	0.7168
6	35000	10	15	0.1556
7	35000	20	20	0.2129
8	35000	30	25	0.3548
9	35000	40	30	0.7113
10	35000	50	10	0.1525
11	40000	10	20	0.1543
12	40000	20	25	0.3363
13	40000	30	30	0.2167
14	40000	40	10	0.1945
15	40000	50	15	0.1360
16	45000	10	25	0.1805
17	45000	20	30	0.3233
18	45000	30	10	0.1980
19	45000	40	15	0.1793
20	45000	50	20	0.5300
21	50000	10	30	0.2443
22	50000	20	10	0.2260
23	50000	30	15	0.2565
24	50000	40	20	0.1923
25	50000	50	25	0.4543

process since a new tool is used, the total machining length is short and the material being utilized is soft [232].

In this chapter, the ranges of the model variables are $30000 \sim 50000rpm$ for n , $10 \sim 50mm/min$ for f , and $10 \sim 30\mu m$ for a_P respectively. Five levels are defined for each factor according to the micro machining conditions and machine tool limits. Hence, Taguchi's $L_{25}(5^6)$ orthogonal array is selected [233] for experimentation. The first three columns are assigned to n , f , and a_P respectively. The experimental layout plan of Taguchi array along with the R_a measurement results are listed in the Table.7.1, and they are used to train the NN model.

7.3 Neural Network Model

7.3.1 Neural Network Structure

A mathematical model that expresses the average surface roughness (R_a) in terms of machining parameters (n, f, a_p) is established utilizing NN method. NN is a multilayered architecture. In this chapter, the feed forward NN of Fig.7.2 consists of neurons divided into the input, output and hidden layers. It consists of 3 neurons in the input layer (corresponding to 3 process inputs, n, f , and a_p), 1 neuron in the output layer (corresponding to 1 outputs, R_a). One hidden layer with 10 neurons is employed in the present study. The neurons between the layers are connected by variable weights and biases to be determined. In the network, each neuron receives total input from all of the neurons in the previous layer as

$$net_j = \sum_{i=0}^N w_{ij}x_i \quad (7.1)$$

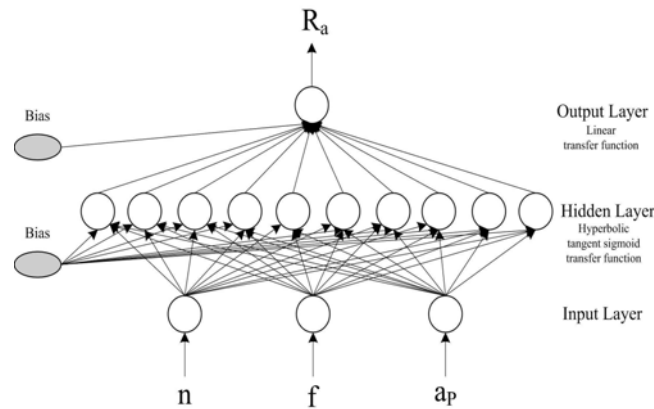


Figure 7.2: Neural network structure

The net_j is the total or net input and N is the number of inputs to the j^{th} neuron in the hidden layer. w_{ij} is the weight of the connection from the i^{th} neuron in the forward layer to the j^{th} neuron in the hidden layer and x_i is the input from the i^{th} neuron in the preceding layer. A neuron in the network produces its output (out_j) by processing the net input through an activation (transfer) function f . In this work, f for the hidden layer and output layer are the tangent hyperbolic function and linear function respectively. The tangent

hyperbolic function leads to minimum the mean square error (MSE) and is represented as Eq.(7.2).

$$out_j = f(net_j) = \frac{1 - e^{-net_j}}{1 + e^{-net_j}} \quad (7.2)$$

The Levenberg-Marquardt algorithm selected for training the NN, is a variation of the classic back propagation algorithm, unlike other variations that use heuristics, relies on numerical optimization techniques to minimize and accelerate the required calculations, resulting in much faster training. More specifically, the direction in which the search is made is described by

$$x_{k+1} = x_k - A_k^{-1} g_k \quad (7.3)$$

Where A_k is the Hessian matrix of the error function at the current values of weights and biases and g_k is the gradient of the error function. Since the error function is a form of sum of squares, the Hessian matrix can be approximated as Eq.(7.4), and the gradient as Eq.(7.5).

$$A_k = J^T J \quad (7.4)$$

$$g_k = J^T e \quad (7.5)$$

Where J is the Jacobian matrix, which contains first derivatives of the network errors with respect to the weights and biases, and e is a vector of network errors. Finally, the search direction is given by

$$x_{k+1} = x_k - [J^T J + \mu I]^{-1} J^T e \quad (7.6)$$

When the scalar μ is zero, this is just a Newtons method using the approximate Hessian matrix. When μ is large, Eq.(7.6) becomes a gradient descent with a small step size. Newtons method is faster and more accurate near an error minimum, so the aim is to shift towards Newtons method as quickly as possible. Thus, μ decreases after each successful step (reduction in performance function) and increases only when a tentative step would increase the performance function. In this way, the performance function will always be reduced at each iteration of the algorithm.

Furthermore, in order to improve the generalization, a technique called “early stopping” was implemented. The complete set of data is divided into three subsets, the training subset, the validation subset and the testing subset. The first is used to train the NN. The second subset practically determines when the training stops by monitoring the training subset error during training. At first, the validation error will, of course, decrease following the error of the training subset. But as the NN begins to over fit the training data, the validation error will increase. If this increase continues for a specified amount of epochs, the training stops and the values of the weights that correspond to the minimum validation error are restored.

7.3.2 Neural Network Performances

Neural Network Training

The experimental data in the Table.7.1 are used to train the NN model. The variation of training error during the training process is depicted in Fig.7.3. In the present study, the training goal, 10^{-3} Sum-Squared Error, is achieved after 103 epochs.

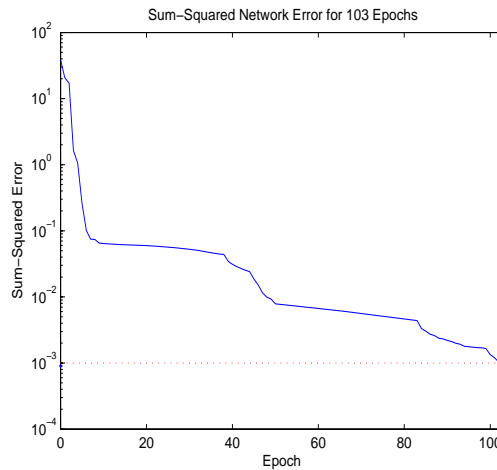


Figure 7.3: Training error epoches

Neural Network testing

The trained NN is initially tested by presenting 25 input patterns, which are employed for the training purpose. The comparison between the NN predicted

and experimental R_a results is given in Fig.7.4, associated with the prediction error. It has been found that the predicted and experimental values are very fairly close to each other. The maximal prediction error is about $0.02\mu m$ corresponding to the 4th test set. The relative error is only 4.8%.

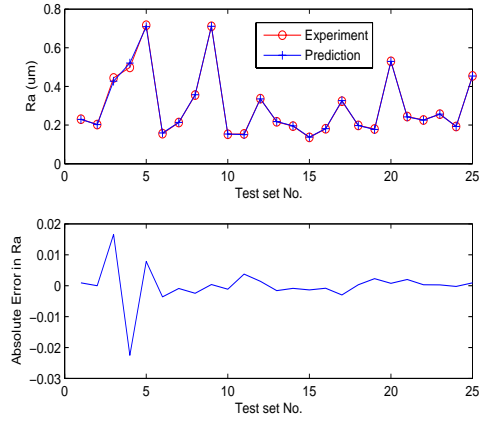


Figure 7.4: R_a comparison between prediction and experiment

For the validation purpose, 5 new trials are executed to test the NN model, which are not in the training data set. Fig.7.5 shows the workpiece which contains all the experimental results, including 25 slots for training, and 5 slots for validation. The detailed experimental settings, and the R_a values from prediction compared with the measurement are listed in the Table.7.2. It is observed that the prediction results are validated by experimental works. The maximal prediction error is about 10%, when the machining variables are out of the range which is used for training.

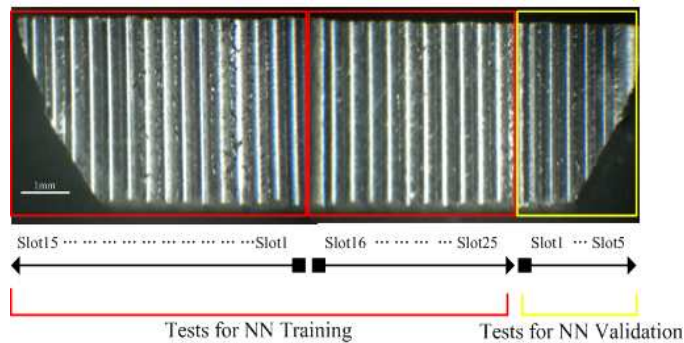


Figure 7.5: Experimental slots

Table 7.2: Experimental validation of NN R_a Prediction

Test No.	$n(rpm)$	$f(mm/min)$	$a_P(\mu m)$	Pred. $R_a(\mu m)$	Exp. $R_a(\mu m)$	Error (%)
1	25000	10	10	0.8518	0.7626	10.47
2	33500	15	15	0.7443	0.7233	2.1
3	43000	27	22	0.0639	0.072	6.56
4	49000	5	35	0.1785	0.179	0.5
5	52000	35	8	0.5220	0.5823	10.36

Therefore, we know the NN model is capable to predict the average micromilling surface roughness R_a in the machining variable ranges which are used for training.

7.4 Results and Discussions

Based on the Taguchi's DoE and the NN model, the effects of the machining variables, including spindle speed (n), feedrate (f), and the axial depth of cut (a_P), to the average micromilled surface roughness (R_a) are discussed in detail.

7.4.1 Single Factor Influence

Based on the experimental results of the Taguchi's orthogonal array, the influences of different levels for each factor to R_a is shown in Fig.7.6. It is clearly that the effects of these three factors are in the asymptotic level.

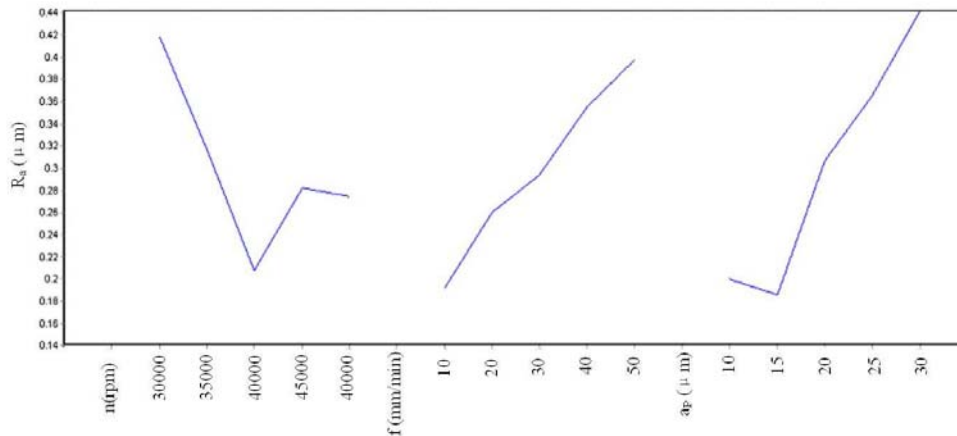


Figure 7.6: Main effect of R_a

Normally, in the milling operation, the slot bottom surface roughness R_a is influenced most important by the feedrate per tooth (FPT) as Eq.(7.7) [149]. In Eq.(7.7), C is the ratio between the average roughness R_a and the Peak-to-Valley roughness. r is the tool nose radius. FPT can be calculated as Eq.(7.8), with the number of the teeth T_N . Here, $T_N = 4$.

$$R_a = \frac{FPT^2}{8C[r \pm (FPT \cdot T_N/\pi)]} \quad (7.7)$$

$$FPT = \frac{f}{n \times T_N} \quad (7.8)$$

From Fig.7.6, it is clearly that R_a decreases with the increase of the spindle speed n . R_a reaches its minimal value when $n = 40000rpm$. After that R_a increases with the increase of n . The reason is that in the low spindle speed range, the feedrate per tooth (FPT) is larger, which degrades the R_a . However, when $n > 40000rpm$, the surface quality is reduced due to the increased effect of vibration induced by the spindle rotor imbalance.

From Fig.7.6, it is obviously that there is almost a linear relationship between the feedrate and R_a . This phenomenon is induced by the increase of FPT, which can be explained by the Eq.(7.7) clearly.

In the conventional scale milling operation, the effect of a_P to the surface quality is very little, due to its main effect is to the cutting force in the feed direction. But in the micromilling operation, due to the tiny tool size, its stiffness in the radial direction is relative lower than the traditional tool. Hence, before the $a_P = 15\mu m$ point, the micromill can afford the cutting force in the feed direction. But after the $a_P = 15\mu m$ point, the R_a value rises rapidly with the increase of the a_P . It means that the radial deformation of the tool is increased, then the tool inclined an angle to cut the material and degrading the surface quality.

7.4.2 Interaction Effect

The results of NN model and Taguchi's DoE can be used to analyze the effects of the selected process parameters to surface roughness R_a . In order to determine the their interaction effects to the micromilling operation. The contour plots were generated considering each two-parameter combinations. These interaction effects are depicted in Figs.7.7-7.9. These figures are very important

to choose suitable process parameters in order to achieve the desirable surface quality.

Fig.7.7 reflects the interaction effect of spindle speed (n) and feedrate (f) to R_a . We found that there are two regions which will induce bad surface quality. The first region is when the $n > 40000RPM$ and feedrate $f < 15\mu m$. The second one is when the $n \approx 50000RPM$ and feedrate $f \approx 25\mu m$. It is clearly that the spindle speed will induce more vibration effects to degrade the workpiece quality. However, we found the minimum R_a locates on the region when $n \approx 50000RPM$ and $f \approx 20\mu m$. It means choosing suitable feedrate will eliminate the cutting force in feed direction and eliminate the vibration effects.

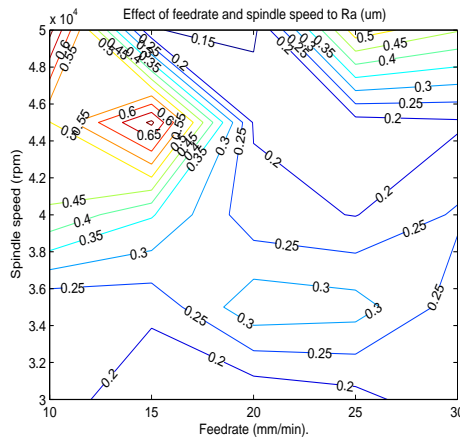


Figure 7.7: Interaction Effects of spindle speed and feedrate on R_a

Fig.7.8 expresses the interaction effect to R_a from the spindle speed (n) and the axial depth of cut (a_P). With the increase of spindle speed (n) in the low axial depth of cut, R_a increases rapidly. The maximal R_a occurs when the $n = 50000rpm$, and $a_P = 15\mu m$. It means when a_P is smaller, the cutting force is smaller. The vibration effect due to the spindle speed is greater. We also found when the spindle speed $n \approx 40000rpm$, and the axial depth of cut $a_P = 25\mu m$, R_a is in the second peak location. When we considerate the parameters combination of these two greater R_a value, it seems the chatter happens, because the chatter is a function of the spindle speed and the axial depth of cut.

The interaction effects of the axial depth of cut (a_P) and the feedrate (f) to R_a is shown in Fig.7.9. Compared with the last two interaction effects. This

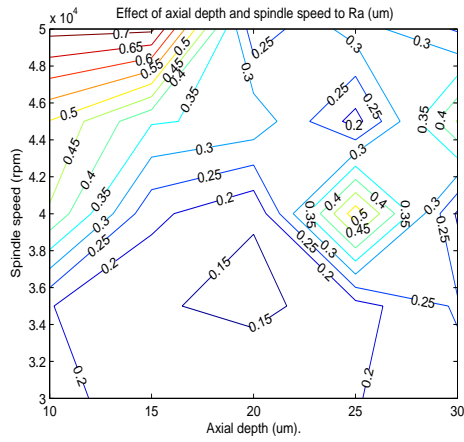


Figure 7.8: Interaction Effects of spindle speed and axial depth on R_a

combination effect is easier to be understood. Both of these two variables are almost linear to R_a . The maximal R_a occurs when the a_P and f are maximum.

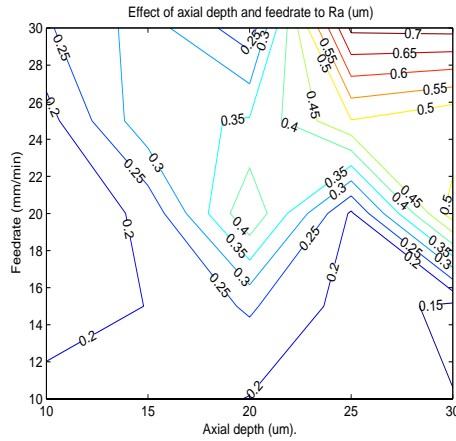


Figure 7.9: Interaction Effects of feedrate and axial depth on R_a

7.5 Conclusion

In this chapter, a neural network model is developed to predict the slot bottom surface roughness in the micromilling operation. The Taguchi's design of experiment was adopted to provide enough training information with minimal experiment times. The validation tests have been conducted to verify the NN model. The maximal prediction error is about 10%, when the machining

variables are chosen out of the variables range which is used for the NN model training. It means the model is capable to predict the surface roughness well. Based on the results of NN prediction and the DoE, the influence of single parameter and interaction effect of each two-parameter combinations to R_a are discussed in detail.

Chapter 8

Conclusions and Perspectives

8.1 Conclusions

In this research, a micro machine tool test-bed is developed for the micromilling research. Based on the experimental study on the test-bed, the other works completed in this dissertation reveals valuable information about the micromilling principles, such as workpiece microstructure effects, micromill tip trajectories, chip formation mechanism, and surface roughness problem.

1. Micromilling on multi-phase polycrystalline material has been conducted. Through the modeling and experimental study on Al6061-T6, we found the mechanical properties differences of different metal phases induce the vibration of cutting force and difference of surface generation heights. To the single-phase polycrystalline material, the experimental results show the effects of crystal orientation and grain size to the surface roughness is very little.
2. An exact tool tip trajectories model for a two flute micromill is developed including the influences of tool tip radial error motion and vibration. In this model, a cost-effective method is proposed to measure and calculate the tool tip radial error motion and tool unbalance by two dial gauges. This method is validated by laser measurement. A rotor dynamic model considering the unbalance is utilized to calculate the tool tip vibration. The tool flute trajectories are predicted and their effects to the chip thickness, cutting force, chip load, machining error, surface quality and tool

breakage are validated by experiments. This study found the single flute cutting condition is very common in the micromilling process by a two flute cutter. In the tool assembling process, the flute angle is the most important parameter to machining error and chip load. Its optimal value is $\pm 90^\circ$. In the actual milling process, the feed angle effect is also critical.

3. The wavy type chip has been found by the FEM simulation and micromilling experiments. The chip formation mechanism is studied quantitatively by means of hybrid analytical-FEM approach. After calculating and analyzing the chip moments, “Tool Rake Moment” M_{Tool} and “Shear Band Moment” M_{Work} , it is proved that the main reasons of wavy chip formation are the variations of the tool chip contact length (l_T) and shear band length (l_S). The Merchant model (MM model) and Arcona-Dow model (AD model) are adopted respectively to calculate the M_{Work} as a comparison. The AD model shows a good performance in the microcutting scale. In the wavy segment generation occasion, the average chip velocity magnitude in chip bending process is much greater than the one before the chip bending which is about the cutting speed. The chip root velocity is almost constant in the entire micromilling process, and the chip tip velocity increases too much in the chip bending instant due to the chip angular acceleration. The chip angular acceleration is acquired respectively from FEM and analytical model based on the M_{Tool} and M_{Work_AD} calculations. The excellent agreement of these two approaches validates the correctness of the chip moments calculations.
4. A neural network (NN) model is developed to predict the effects of spindle speed (n), feedrate (f) and axial depth of cut (a_P) on average surface roughness parameters (R_a) in the micromilling operation. The experimental design adopts the Taguchi’s approach to acquire enough training information with minimal experiment number. Based on the experimental results, the NN model is trained and give a good prediction ability in the suitable machining parameter ranges. Through the analysis of the single machining parameter and their interactions to R_a , we found these three variables are in the asymptotic level.

8.2 Perspectives for future work

Based on the results of this work, several areas of future research efforts have been identified:

1. Development of cutter location determination system

In the micromilling operation, most of the parts are fabricated by one tool setup. Because it is very difficult to set the latter tool in the same location of the previous tool, due to the tiny tool tip size and tool assembling error. Therefore, new system needs to be developed to determine the cutter location, no matter radial or axial position.

2. Comprehensive three dimensional FEM simulation of micromilling process

The comprehensive three dimensional finite element simulation model should be developed including the effects of the workpiece microstructure of heterogeneous material, tool flute complex trajectories, and the crystal plasticity constitutive model, the entire tool geometry and the flexibility of tool and workpiece should be integrated to emulate the grain performances truly.

3. Modeling of the surface generation based on the tool tip trajectories model

The mathematical model and simulation works needs to be done in order to determine the exact tool flute axial position based on the tool tip trajectories model proposed in this research. This work is important to determine the profile of the machined bottom surface.

4. Error compensation and controlling system of micromilling process

Based on the tool tip trajectories model, the machining error under this condition is predicted in this thesis. The corresponding error compensation system should be developed and integrated into the MMT control system. Meanwhile, the real-time control system should be embedded into the NC software in order to improve the performances and efficiency of micromilling process.

5. Micro mill-grinding process

Through the experimental study, it has been found that compared with the dimension of micro components, its surface quality is not satisfactory. Hence, the grinding process is an alternative way to improve the surface quality of the machined surface. However, due to the low material removal rate of the grinding operation. The author proposed a new machining process, named micro mill-grinding, which electroplates the ultra-fine grits on the flank face of the micromill tool and combined the advantages of the high efficiency as milling and good surface quality as grinding.

Bibliography

- [1] X. Liu, R. DeVor, S. Kapoor, K. Ehman, The mechanics of machining at the micro scale: assessment of the current state of the science, *ASME Journal of Manufacturing Science and Engineering* 126 (2004) 666–678.
- [2] B. R. I. of Inertial Technology, Dynamometers:based on strain gauge technology, measuring cutting and grinding forces on machine tools.
- [3] W. Skrotzki, N. Scheerbaum, C. Oertel, R. Arruffat-Massion, S. Suwas, L. Toth, Microstructure and texture gradient in copper deformed by equal channel angular pressing, *Acta Materialia* 55 (6) (2007) 2013–2024.
- [4] J. Wang, Y. Gong, G. Abba, J. Cao, J. Shi, G. Cai, Micro milling technologies for mems, in: *Proceeding of 3rd MEMSTECH, Lviv-Polyana, Ukraine, 2007*, pp. 86–95.
- [5] J. Corbett, P. McKeon, G. Peggs, R. Whatmore, Nanotechnology: International developments and emerging products, *Annals of CIRP* 49 (1) (2000) 523–546.
- [6] M. Madou, *Fundamentals of Microfabrication*, CRC Press, 1997.
- [7] M. Weck, S. Fischer, M. Vos, Fabrication of micro components using ultra precision machine tools, *Nanotechnology* 8 (1997) 145–148.
- [8] W. Lang, Reflexions on the future of microsystems, *Sensor and Actuators* 72 (1999) 1–15.
- [9] Y. Okazaki, N. Mishima, K. Ashida, Microfactory-concept, history, and developments, *ASME Journal of Manufacturing Science and Engineering* 126 (2004) 837C844.

- [10] P. Picart, J. Michel, Effects of size and texture on the constitutive behavior for very small components in sheet metal forming, in: Proceedings of the Sixth International Conference on Technology of Plasticity, 1999.
- [11] V. Lemiale, P. Picart, Modelling and simulation of precision blanking for very thin components, *Journal of Steels and Related Materials* 1 (2004) 413–416.
- [12] L. Alting, F. Kimura, H. Hansen, G. Bissacco, Micro engineering, *Annals of CIRP* 52 (2) (2003) STC–O.
- [13] T. Masuzawa, State of the art of micromachining, *Annals of CIRP* 49 (2) (2000) 473–488.
- [14] G. Benavides, D. Adams, P. Yang, Meso-machining capabilities, Tech. rep., Sanding Report (2001).
- [15] R. Howe, Micro systems research in japan, Tech. rep., World Technology Evaluation Center (WTEC) (2003).
- [16] A. El-Fataty, Euspen vision online: Transferring microsystems technology, Tech. rep., NEXUS Report (2003).
- [17] M. Tanaka, Development of desktop machining microfactory, Tech. Rep. 34, Riken Review (2001).
- [18] Y. Bang, K. Lee, S. Oh, 5-axis micro milling machine for machining micro parts, *International Journal of Advanced Manufacturing Technology* 25 (2005) 888–894.
- [19] E. Kussul, T. Baidyk, L. Ruiz-Huerta, A. Caballero-Ruiz, G. Velasco, L. Kasatkina, Micromechanical engineering: a basis of the low-cost manufacturing of mechanical micro devices using micro equipment, *Journal of Micromechanics and Microengineering* 6 (1996) 410–425.
- [20] E. Kussul, T. Baidyk, L. Ruiz-Huerta, A. Caballero-Ruiz, G. Velasco, L. Kasatkina, Development of micromachine tool prototypes for microfactories, *Journal of Micromechanics and Microengineering* 12 (2002) 795–812.

- [21] J. Hesselbach, A. Raatz, J. Wreg, International state of the art of micro production technology, *Production Engineering* 11 (1) (2004) 29–36.
- [22] J. Chae, S. Park, T. Freiheit, Investigation of micro-cutting operations, *International Journal of Machine Tools & Manufacture* 46 (2006) 313–332.
- [23] D. Dornfeld, S. Min, Y. Takeuchi, Recent advances in mechanical micro-machining, *Annals of CIRP* 55 (2) (2006) 745–768.
- [24] H. Onikura, O. Ohnishi, Y. Take, Fabrication of micro carbide tools by ultrasonic vibration grinding, *Annals of CIRP* 49 (1) (2000) 257–260.
- [25] F. Fang, H. Wu, X. Liu, Y. Liu, S. Ng, Tool geometry study in micro-machining, *Journal of Micromechanics and Microengineering* 13 (2003) 726–731.
- [26] <http://www.mikrotools.com/product DT110.htm>.
- [27] www.kuglerofamerica.com/micro_m.htm.
- [28] <http://www.makino.com/default.asp>.
- [29] www.moriseiki.com/english/index.html.
- [30] M. Vogler, X. Liu, S. Kapoor, R. DeVor, K. Ehmann, Development of meso-scale machine tool (mmt) systems, *Transactions of North American Manufacturing Research Institution* 30 (2002) 1–9.
- [31] S. Kapoor, Current state of micro-scale machine tool systems and machining research, Workshop on micromanufacturing, natural science foundation, University of Illinois at Urbana-Champaign (2004).
- [32] T. Moriwaki, N. Sugimura, S. Luan, Combined stress material flow and heat analysis of orthogonal micromachining of copper, *Annals of CIRP* 42 (1) (1993) 75–78.
- [33] J. Kim, D. Kim, Theoretical analysis of micro-cutting characteristics in ultra-precision machining, *Journal of Materials Processing Technology* 49 (1995) 387–398.
- [34] M. Vogler, R. DeVor, S. Kapoor, On the modeling and analysis of machining performance in micro-endmilling, part I: Surface generation, *ASME Journal of Manufacturing Science and Engineering* 126 (2004) 684–693.

- [35] M. Vogler, R. DeVor, S. Kapoor, On the modeling and analysis of machining performance in micro-endmilling, part II: Cutting force prediction, *ASME Journal of Manufacturing Science and Engineering* 126 (2004) 695–705.
- [36] K. Liu, X. Li, M. Rahman, Characteristics of high speed microcutting of tungsten carbide, *Journal of Materials Processing Technology* 140 (2003) 352–357.
- [37] S. Son, H. Lim, J. Ahn, Effects of the friction coefficient on the minimum cutting thickness in micro cutting, *International Journal of Machine Tools & Manufacture* 45 (2005) 529–535.
- [38] H. Weule, V. Huntrup, H. Tritschler, Micro-cutting of steel to meet new requirements in miniaturization, *Annals of CIRP* 50 (2001) 61–64.
- [39] B. Ikua, H. Tanaka, F. Obata, S. Sakamoto, Prediction of cutting forces and machining error in ball end milling of curved surfacesI theoretical analysis, *Journal of International Societies of Precision Engineering and Nanotechnology* 25 (2001) 266–273.
- [40] W. Bao, I. Tansel, Modeling microend-milling operations. part I: analytical cutting force model, *International Journal of Machine Tools & Manufacture* 40 (2000) 2155–2173.
- [41] J. Grum, M. Kisin, Influence of microstructure on surface integrity in turning-part 2: the influence of a microstructure of the work piece material on cutting forces, *International Journal of Machine Tools & Manufacture* 43 (2003) 1545–1551.
- [42] W. Lee, C. Cheung, S. To, Materials induced vibration in ultraprecision machining, *Journal of Materials Processing Technology* 89-90 (1999) 318–325.
- [43] T. Dow, E. Miller, K. Garrard, Tool force and deflection compensation for small milling tools, *Precision Engineering* 28 (2004) 31–45.
- [44] A. Dugas, J. Lee, J. Hascoet, An enhanced machining simulator with tool deflection error analysis, *Journal of Manufacturing Systems* 21 (6) (2002) 451–463.

- [45] X. Liu, R. DeVor, S. Kapoor, Model-based analysis of the surface generation in microendmilling-part I: Model development, *ASME Journal of Manufacturing Science and Engineering* 129 (3) (2007) 453–460.
- [46] X. Liu, R. DeVor, S. Kapoor, Model-based analysis of the surface generation in microendmilling-part II: Experimental validation and analysis, *ASME Journal of Manufacturing Science and Engineering* 129 (3) (2007) 461–469.
- [47] G. Byrne, D. Dornfeld, B. Denkena, Advancing cutting technology, *Annals of CIRP* 52 (2) (2003) 483–507.
- [48] T. Schaller, L. Bohn, J. Mayer, K. Schubert, Microstructure grooves with a width of less than $50\mu m$ cut with ground hard metal micro end mills, *Precision Engineering* 23 (1999) 229–235.
- [49] I. Tansel, T. Arkan, W. Bao, N. Mahendrakar, B. Shisler, D. Smith, M. McCool, Tool wear estimation in micro machining. part 2: neural-network-based periodic inspector for non-metals, *International Journal of Machine Tools & Manufacture* 40 (2000) 609–620.
- [50] K. Weinert, V. Petzoldt, Machining of niti based shape memory alloy, *Materials Science and Engineering A* 378 (2004) 180–184.
- [51] S. Shabouk, T. Nakamoto, Micro machining of single crystal diamond by utilization of tool wear during cutting process of ferrous material, *Journal of Micromechatronics* 2 (1) (2003) 13–26.
- [52] B. Kim, M. Schmittdiel, F. Degertekin, T. Kurfess, Scanning grating micro interferometer for mems metrology, *ASME Journal of Manufacturing Science and Engineering* 126 (2004) 807–812.
- [53] M. Hart, R. Conant, K. Lau, R. Muller, Stroboscopic interferometer system for dynamic mems characterization, *Journal of Microelectromechanical Systems* 9 (4) (2000) 409–418.
- [54] D. Popa, B. Kang, J. Wen, H. Stephanou, Dynamic modeling and input shaping of thermal bimorph mems actuators, in: *IEEE Conference Robotics and Automation*, 2003, pp. 1470–1475.

- [55] H. V. Brussel, J. Peirs, D. Reynaerts, A. Delchambre, G. Reinhart, N. Roth, M. Weck, E. Zussman, Assembly of microsystems, *Annals of CIRP* 49 (2) (2000) 451–472.
- [56] D. Cox, G. Newby, H. Park, S. Liang, Performance evaluation of a miniaturized machining center for precision manufacturing, in: *Proceedings ASME International Mechanical Engineering Congress and Exposition*, 2004.
- [57] S. Kalpakjian, S. Schmid, *Manufacturing Processes for Engineering Materials*, Prentice-Hall, New Jersey, USA, 2002.
- [58] D. Adams, M. Vasile, G. Benavides, A. Cambell, Micromilling of metal alloy with focused ion beam-fabricated tools, *Journal of International Societies of Precision Engineering and Nanotechnology* 25 (2001) 107–113.
- [59] <http://www.mmsonline.com/articles/010504.html>.
- [60] B. Rooks, The shrinking sizes in micro manufacturing, *Assembly Automation* 24 (4) (2004) 352–356.
- [61] www.kernmicrotechnic.com.
- [62] Y. Takeuchi, Y. Sakaida, K. Sawada, T. Sata, Development of a 5-axis control ultra precision milling machine for micromachining based on non-friction servomechanisms, *Annals of CIRP* 49 (1) (2000) 295–298.
- [63] <http://www.willeminmacodel.com/>.
- [64] www.nanowave.co.jp.
- [65] H. Tonshoff, Developments and trends in monitoring and control of machining processes, *Annals of CIRP* 37 (2) (1988) 611–622.
- [66] M. Shaw, Precision finishing, *Annals of CIRP* 44 (1) (1995) 343–348.
- [67] T. Schmitz, M. Davies, M. Kennedy, Tool point frequency response prediction for high-speed machining by rcsa, *ASME Journal of Manufacturing Science and Engineering* 123 (2002) 700–707.
- [68] Y. Furukawa, N. Moronoki, Effect of material properties on ultra precise cutting processes, *Annals of CIRP* 37 (1) (1988) 113–116.

- [69] D. Lucca, R. Rohrer, R. Komanduri, Energy dissipation in the ultraprecision machining of copper, *Annals of CIRP* 40 (1) (1991) 69–72.
- [70] A. Matsubara, Y. Kakino, T. Ogawa, H. Nakagawa, T. Sato, Monitoring of cutting forces in end-milling for intelligent machine tools, in: *Proceedings of the Fifth International Conference on Progress of Machining Technology*, 2000, p. 615.
- [71] M. Vogler, R. Devor, S. Kapoor, Microstructure-level force prediction model for micro-milling of multi-phase materials, *ASME Journal of Manufacturing Science and Engineering* 125 (2002) 202–209.
- [72] M. Davies, C. Evans, K. Harper, Chip segmentation in machining aisi 52100 steel, in: *ASPE*, Vol. 11, 1995, pp. 235–238.
- [73] M. Davies, Y. Chou, C. Evans, On chip morphology, tool wear and cutting mechanism in finish hard turning, *Annals of CIRP* 45 (1) (1995) 77–82.
- [74] W. Konig, A. Berktold, K. Koch, Turning versus grinding - a comparison of surface integrity aspects and attainable accuracies, *Annals of CIRP* 42 (1) (1993) 39–43.
- [75] Y. Altintas, *Manufacturing Automation: Metal Cutting Mechanics, Machine Tool Vibrations, and CNC Design*, Cambridge University Press, Cambridge, 2000.
- [76] E. Budak, Improving productivity and part quality in milling of titanium based impellers by chatter suppression and force control, *Annals of CIRP* 49 (1) (2000) 31–36.
- [77] V. Jardret, H. Zahouani, J. Loubet, T. Mathia, Understanding and quantification of elastic and plastic deformation during a scratch test, *Wear* 218 (1998) 8–14.
- [78] C. Kim, J. Mayor, J. Ni, A static model of chip formation in microscale milling, *ASME Journal of Manufacturing Science and Engineering* 126 (2004) 710–718.
- [79] J. Tlustý, P. Macneil, Dynamics of cutting forces in end milling, *Annals of CIRP* 24 (1) (1975) 21–25.

- [80] J. Tlustý, G. Andrews, A critical review of sensors for unmanned machining, *Annals of CIRP* 32 (2) (1983) 563–572.
- [81] W. Lee, C. Cheung, S. To, A microplasticity analysis of micro-cutting force variation in ultra-precision diamond turning, *ASME Journal of Manufacturing Science and Engineering* 124 (2002) 170–177.
- [82] M. Xiao, K. Sato, S. Karube, T. Soutone, The effect of tool nose radius in ultrasonic vibration cutting of hard metal, *International Journal of Machine Tools & Manufacture* 43 (2003) 1375–1382.
- [83] C. Liu, S. Mittal, Single-step super finish hard machining: feasibility and feasible cutting conditions, *Robotics Computer-Integrated Manufacture* 12 (1996) 15–27.
- [84] I. Tansel, T. Arkan, W. Bao, N. Mahendrakar, B. Shisler, D. Smith, M. McCool, Tool wear estimation in micro-machining. part 1: tool usage-cutting force relationship, *International Journal of Machine Tools & Manufacture* 40 (2000) 599–608.
- [85] M. Rahman, S. Kumar, J. Prakash, Micro milling of pure copper, *Journal of materials Processing Technology* 116 (2001) 39–43.
- [86] <http://www.mitsubishicarbide.com/mmus/ca/product/article/mzs.pdf>.
- [87] O. Ozdoganlar, D. Epp, P. Reu, H. Sumali, Development of a testing facility for experimental investigation of mems dynamics, in: *Proceedings ASME International Mechanical Engineering Congress and Exposition*, 2004.
- [88] A. Atre, Dynamic response of surface micro machined horizontal beam flexure actuator, in: *Proceedings ASME International Mechanical Engineering Congress and Exposition*, 2004.
- [89] R. Fearing, Grasping for macro-scale and micro-scale, in: *Workshop on Working in the Micro-world: Systems to Enable the Manipulation and Machining of Micro-objects*, 1995, pp. 202–209.
- [90] C. Kim, A. Pisano, R. Muller, Silicon processed overhanging micro gripper, *Journal of Microelectromechanical Systems* 1 (1) (1992) 31–36.

- [91] H. T. K. Suzumori, S. Likura, Flexible micro actuator for miniature robots, in: Proceedings of IEEE MEMS Workshop, 1991, pp. 204–209.
- [92] J. Peirs, D. Reynaerts, H. V. Brussel, A micro robotic arm for a self propelling colonoscope, in: Proceedings Actuator, 1998, pp. 576–579.
- [93] M. Weck, J. Hummler, B. Petersen, Assembly of hybrid micro systems in a large chamber electron microscope by use of mechanical grippers, in: Proceedings of SPIE, Micromachining and Micro fabrication Process Technology III, 1997, pp. 223–229.
- [94] J. Breguet, S. Henein, R. Mericio, R. Clavel, Monolithic piezoceramic flexible structures for micromanipulation, in: Proceedings of the Ninth International Precision Engineering Seminar, 1997, pp. 397–400.
- [95] Y. Furuya, H. Shimada, Shape memory actuators for robotic applications, in: Engineering Aspect of Shape Memory Alloys, 1990, pp. 338–355.
- [96] G. Greitmann, R. Buser, Tactile micro gripper for automated handling of micro parts, *Sensors and Actuators* 53 (1996) 410–415.
- [97] Y. Yao, X. Fang, G. Amdt, Comprehensive tool wear estimation in finish-machining via multivariate time-series analysis of 3-d cutting forces, *Annals of CIRP* 39 (1990) 57–60.
- [98] R. Kountanya, W. Endres, Flank wear of edge-radiused cutting tools under ideal straight-edged orthogonal conditions, *ASME Journal of Manufacturing Science and Engineering* 126 (2004) 496–505.
- [99] S. Tobias, *Machine Tool Vibrations*, Blackie and Sons, Glasgow, 1965.
- [100] S. Tobias, W. Fishwick, *A Theory of Regenerative Chatter*, The Engineer, London, 1958.
- [101] S. Park, Y. Altintas, M. Movahhedy, Receptance coupling for end mills, *International Journal of Machine Tools & Manufacture* 43 (2003) 889–896.
- [102] W. Bao, I. Tansel, Modeling micro-end-milling operations. part II: tool run-out, *International Journal of Machine Tools & Manufacture* 40 (2000) 2175–2192.

- [103] M. Jun, X. Liu, R. DeVor, S. Kapoor, Investigation of the dynamics of microend milling-part I: Model development, *ASME Journal of Manufacturing Science and Engineering* 128 (2006) 893–900.
- [104] M. Jun, X. Liu, R. DeVor, S. Kapoor, Investigation of the dynamics of microend milling-part II: Model validation and interpretation, *ASME Journal of Manufacturing Science and Engineering* 128 (2006) 901–912.
- [105] R. Vallance, E. Marsh, P. Smith, Effects of spherical targets on capacitive displacement measurements, *ASME Journal of Manufacturing Science and Engineering* 126 (4) (2004) 822–829.
- [106] W. Lee, C. Cheung, A dynamic surface topography model for the precision of nano-surface generation in ultra-precision machining, *International Journal of Mechanical Sciences* 43 (2001) 961–991.
- [107] E. Rivin, Tooling structure - interface between cutting edge and machine tool, *Annals of CIRP* 49 (2) (2000) 591–634.
- [108] K. Matsushima, P. Bertok, T. Sata, In process detection of tool breakage by monitoring the spindle current of a machine tool, *ASME Journal of Measurement and Control* (1982) 145–154.
- [109] N. Constantinides, S. Bennett, An investigation of methods for on line estimation of tool wear, *International Journal of Machine Tools & Manufacture* 27 (2) (1987) 225–237.
- [110] Y. Altintas, Prediction of cutting forces and tool breakage in milling from feed drive current measurements, *ASME Journal of Engineering of Industry* 114 (1992) 386–392.
- [111] T. Kim, J. Kim, Adaptive cutting force control for a machining center by using indirect cutting force measurements, *International Journal of Machine Tools & Manufacture* 36 (1996) 925–937.
- [112] T. El-Wardany, D. Gao, M. Elbestawi, Tool condition monitoring in drilling using vibration signature analysis, *International Journal of Machine Tools & Manufacture* 36 (6) (1996) 687–711.
- [113] T. Moriwaki, Detection for tool fracture by ae measurement, *Annals of CIRP* 29 (1980) 35–40.

- [114] A. Sampath, S. Vajpayee, Tool health monitoring using acoustic emission, *International Journal of Production Research* 25 (5) (1996) 703–719.
- [115] D. Choi, W. Kwon, C. Chu, Real time monitoring of tool fracture in turning using sensor fusion, *International Journal of Advance Manufacturing Technology* 15 (5) (1999) 305–310.
- [116] D. Yan, T. El-Wardany, M. Elbestawi, A multi-sensor strategy for tool failure detection in milling, *International Journal of Machine Tools & Manufacture* 35 (1995) 383–398.
- [117] G. Byrne, D. Dornfeld, I. Inasaki, W. Konig, R. Teti, Tool condition monitoring (tcm)-the status of research and industrial application, *Annals of CIRP* 44 (2) (1995) 541–567.
- [118] D. Dimla, Sensor signals for tool wear monitoring in metal cutting operations-a review of methods, *International Journal of Mechanical Science* 40 (2000) 1073–1098.
- [119] S. Park, Y. Altintas, Dynamic compensation of cutting forces measured from the spindle integrated force sensor system, in: *Proceedings ASME International Mechanical Engineering Congress and Exposition*, 2002.
- [120] A. Ulsoy, Y. Koren, Applications of adaptive control to machine tool process control, *IEEE Control Systems Magazine* 9 (4) (1989) 33–37.
- [121] Y. Koren, *Computer Control of Manufacturing Systems*, McGraw Hill, New York, 1983.
- [122] I. Tansel, A. Nedbouyan, M. Trujillo, B. Tansel, Micro-endmilling-extending tool life with a smart work piece holder, *International Journal of Machine Tools & Manufacture* 38 (1998) 1437–1448.
- [123] X. Luo, K. Cheng, D. Webb, F. Wardle, Design of ultraprecision machine tools with applications to manufacture of miniature and micro components, *Journal of Materials Processing Technology* 167 (2005) 515–528.
- [124] K. Furuta, Y. Ishikawa, Y. Mikuriya, Y. Takahashi, The microfactory system in national r&d project of miti, in: *Proceedings of the International Workshop on Microfactories*, Tsukuba, Japan, 1998, pp. 193–196.

- [125] R. Subrahmanian, K. F. Ehmann, Development of a meso-scale machine tool (mmt) for micro-machining, in: Proceeding of Japan-USA Symposium on Flexible Automation, Vol. 1, Hiroshima, Japan, 2002, pp. 163–169.
- [126] A. Honegger, S. Kapoor, R. DeVor, A hybrid methodology for kinematic calibration of micro/meso-scale machine tools (mts), *ASME Journal of Manufacturing Science and Engineering* 128 (2006) 513–522.
- [127] S. W. Lee, R. Mayor, J. Ni, Dynamic analysis of a mesoscale machine tool, *ASME Journal of Manufacturing Science and Engineering* 128 (2006) 194–203.
- [128] K. Ashida, N. Mishima, H. Maekawa, T. Tanikawa, K. Kaneko, M. Tanaka, Development of desktop machining microfactory, in: Proceeding of Japan-USA Symposium on Flexible Automation, 2000, pp. 175–178.
- [129] S. Filiz, C. Conley, M. Wasserman, O. Ozdoganlar, An experimental investigation of micro-machinability of copper 101 using tungsten carbide micro-endmills, *International Journal of Machine Tools & Manufacture* 47 (2007) 1088–1100.
- [130] J. Wang, J. Shi, Y. Gong, G. Abba, G. Cai, A micro milling model considering metal phases and minimum chip thickness, *Key Engineering Materials* 375-376 (2008) 505–509.
- [131] L. Zhang, D. Zhao, J. Zhang, X. Sun, C. Pang, Development of miniaturized numerical control milling machine tool used in micro cutting, *Journal of Southeast University (Natural Science Edition)* 137 (1) (2007) 26–29.
- [132] Rusnaldy, J. K. Tae, H. S. Kim, An experimental study on microcutting of silicon using a micromilling machine, *International Journal of Advanced Manufacturing Technology* 39 (2008) 85–91.
- [133] K. Malukhin, K. Ehmann, Identification of direct metal deposition (dmd) process parameters for manufacturing thin wall structures from shape memory alloy (niti) powder, *Transactions of the North American Manufacturing Research Institution of SME* 35 (2007) 481–488.

- [134] K.Furutani, M.Suzuki, R.Kudoh, Nanometer-cutting machine using stewart-platform parallel mechanism, *Measurement Science and Technology* 15 (2) (2004) 467–474.
- [135] www.renishaw.com.
- [136] www.kistler.com.
- [137] www.precisiondormer.com.
- [138] H. Shinno, Y. Ito, Computer aided concept design for structural configuration of machine tools: variant design using directed graph, *Transactions of ASME* 11 (1987) 311–318.
- [139] F. Chan, Design of material handling equipment selection system: an integration of expert system with analytic hierarchy process approach, *Integrated Manufacturing Systems* 13 (2003) 58–68.
- [140] K. Chau, F. Albermani, Expert system application on preliminary design of water retaining structures, *Expert Systems with Applications* 22 (2003) 169–178.
- [141] M. Chew, S. Shen, G. Issa, Kinematic structural synthesis of mechanisms using knowledge-based systems, *Transaction of ASME, Journal of Mechanical Design* 117 (1995) 96–103.
- [142] H. Chen, Generation and evaluation of meso-scale machine tool designs for micro-machining applications, Ph.D. thesis, University of Michigan (2005).
- [143] J. Lee, S. Park, S. Yang, Machining a micro/meso scale structure using a miniaturized machine tool by using a conventional cutting process, *ASME Journal of Manufacturing Science and Engineering* 128 (2006) 820–825.
- [144] E. L. Zhang, W. W. He, H. Du, K. Yang, Microstructure, mechanical properties and corrosion properties of mg-zn-y alloys with low zn content, *Materials Science and Engineering: A* 488 (1-2) (2008) 102–111.
- [145] E. Lee, B. Shaffer, The theory of plasticity applied to a problem of machining, *ASME Journal of Applied Mechanics* 18 (1951) 405–413.

- [146] R. Walsh, Handbook of Machining and Metalworking Calculations, McGraw-Hill, New York, 2001.
- [147] Z. Wu, Handbook of mechanical design, Chemical Industry Press, Beijing, 1999.
- [148] L. Toth, R. Massion, L. Germain, S. Baik, S. Suwas, Analysis of texture evolution in equal channel angular extrusion of copper using a new flow field, *Acta Materialia* 52 (7) (2004) 1885–1898.
- [149] M. Shaw, Metal Cutting Principles, Oxford University Press, Oxford, 1984.
- [150] J. Tlustý, System and methods of testing machine tools, *Microtechnic* 13 (1959) 162.
- [151] W. Kline, R. DeVor, The effect of runout on cutting geometry and forces in end milling, *International Journal of Machine Tool Design and Research* 23 (2/3) (1983) 123–140.
- [152] W. Kim, A. Argento, R. Scott, Forced vibration and dynamic stability of a rotating tapered composite timoshenko shaft: bending motions in end-milling operations, *Journal of Sound and vibration* 246 (4) (2001) 583–600.
- [153] Y. Altintas, E. Budak, Analytical predication of stability lobes in milling, *Annals of CIRP* 44 (1) (1995) 357–362.
- [154] D. Montgomery, Y. Altintas, Mechanism of cutting force and surface generation in dynamic milling, *ASME Journal of Engineering for Industry* 113 (2) (1991) 160–168.
- [155] K. Lee, H. Kim, S. Park, A run-out measuring method using modeling and simulation in four-fluted end milling, *Journal of Materials Processing Technology* 187-188 (2007) 207–211.
- [156] V. Gagnol, B. Bouzgarrou, P. Ray, C. Barra, Model-based chatter stability predication for high-speed spindles, *International Journal of Machine Tools & Manufacture* 47 (2007) 1176–1186.

- [157] W. Nakkiew, C. Lin, J. Tu, A new method to quantify radial error of a motorized end-milling cutter/spindle system at very high speed rotations, *International Journal of Machine Tools & Manufacture* 46 (2006) 877–889.
- [158] J. Antoine, G. Abba, C. Sauvey, Approximate explicit calculation of first vibration frequencies of an unsymmetrical high speed rotor, *American Society of Mechanical Engineers, Design Engineering Division (Publication) DE 116 (2) (2003) 1141–1149.*
- [159] S. Filiz, O. Ozdoganlar, Microendmill dynamics including the actual fluted geometry and setup errors-part II: Model validation and application, *ASME Journal of Manufacturing Science and Engineering* 130 (2008) 031120–1–031120–13.
- [160] A. Tulsian, M. Wasserman, O. Ozdoganlar, Measurement of dynamic runout characteristics of ultra-high-speed miniature spindles for micromachining, in: *International Conference on Micro Manufacturing, Greenville, South Carolina, USA, 2007.*
- [161] X. Li, R. Du, B. Denkena, J. Imiela, Tool breakage monitoring using motor current signals for machine tools with linear motors, *Industrial Electronics, IEEE Transactions on* 52 (5) (2005) 1403–1408.
- [162] K. Lee, D. Dornfeld, Micro-burr formation and minimization through process control, *Precision Engineering* 29 (2005) 246–252.
- [163] T. Schmitz, J. Couey, E. Marsh, N. Mauntler, D. Hughes, Runout effects in milling: Surface finish, surface location error, and stability, *International Journal of Machine Tools & Manufacture* 47 (5) (2007) 841–85.
- [164] W. Estler, C. Evans, L. Shao, Uncertainty estimation for multiposition form error metrology, *International Journal of the Japan Society for Precision Engineering* 21 (1997) 72–82.
- [165] J. Antoine, C. Visa, G. Abba, C. Sauvey, Electerspindle design for high speed machining, in: *5th Int. congress on High Speed Machining, Metz, France, 2006, pp. 329–340.*
- [166] GWD300 high speed electro spindle specifications.

- [167] B. Wen, *Mechanical Vibration*, Metallurgy Industry Press, 2000.
- [168] C. Friedrich, V. Kulkarni, Effect of workpiece springback on micromilling forces, *Microsystem Technologies* 10 (2004) 472–477.
- [169] C. Arcona, T. Dow, An empirical tool force model for precision machining, *ASME Journal of Manufacturing Science and Engineering* 120 (1998) 700–707.
- [170] J. Wang, S. Liang, W. Book, Convolution analysis of milling force pulsation, *ASME Journal of Engineering for Industry* 116 (1994) 17–25.
- [171] V. Astakhov, S. Shvets, M. Osman, Chip structure classification based on mechanics of its formation, *Journal of Materials Processing Technology* 71 (2) (1997) 247–257.
- [172] H. Ernst, *Physics of metal cutting, machining of metal*, American Society for Metals (1938) 24.
- [173] V. Astakhov, *Metal Cutting Mechanics*, CRC Press, Boca Raton, 1998.
- [174] M. Shaw, N. Cook, I. Finnie, The shear-angle relationship in metal cutting, *ASME Journal of Engineering for Industry* 75 (1953) 273–288.
- [175] E. Usui, T. Shirakashi, Mechanics of machining from descriptive to predictive theory, on the art of cutting metals, *ASME PED* 7 (1982) 13–35.
- [176] J. Strenkowski, J. Carroll, A finite element model of orthogonal metal cutting, *ASME Journal of Engineering for Industry* 107 (1985) 347–354.
- [177] E. Ceretti, P. Fallbohmer, W. Wu, T. Altan, Application of 2d fem to chip formation in orthogonal cutting, *Journal of Materials Processing Technology* 59 (1996) 169–180.
- [178] T. Özel, T. Altan, Process simulation using finite element method - prediction of cutting forces, tool stresses and temperatures in high-speed flat end milling, *International Journal of Machine Tools & Manufacture* 40 (5) (2000) 713–738.
- [179] P. Rosa, O.Kolednik, P. Martins, A. Atkins, The transient beginning to machining and the transition to steady-state cutting, *International Journal of Machine Tools & Manufacture* 47 (12-13) (2007) 1904–1915.

- [180] J. Mackerle, Finite element analysis and simulation of machining: an addendum a bibliography (1996-2002), *International Journal of Machine Tools & Manufacture* 43 (2003) 103–114.
- [181] L. Chuzhoy, R. DeVor, S. Kapoor, A. Beaudoin, D. Bammann, Machining simulation of ductile iron and its constituents. part I: Estimation of material model parameters and their validation, *ASME Journal of Manufacturing Science and Engineering* 125 (2003) 181–191.
- [182] L. Chuzhoy, R. DeVor, S. Kapoor, Machining simulation of ductile iron and its constituents. part II: Numerical simulation and experimental validation of machining, *ASME Journal of Manufacturing Science and Engineering* 125 (2003) 192–201.
- [183] A. Simoneau, E. Ng, M. Elbestawi, Chip formation during microscale cutting of a medium carbon steel, *International Journal of Machine Tools & Manufacture* 46 (2006) 467–481.
- [184] A. Simoneau, E. Ng, M. Elbestawi, Surface defects during microcutting, *International Journal of Machine Tools & Manufacture* 46 (2006) 1378–1387.
- [185] T. Özel, X. Liu, A. Dhanorker, Modelling and simulation of micro-milling process, in: *Proceeding of 4th International Conference and Exhibition on Design and Production of Machines and Dies/Molds*, Cesme, Turkey, 2007.
- [186] K. Woon, M. Rahman, F. Fang, K. Neo, K. Liu, Investigations of tool edge radius effect in micromachining: A fem simulation approach, *Journal of materials processing technology* 195 (2008) 204–211.
- [187] R. Komanduri, L. Narulkar, R. Raff, Monte carlo simulation of nanometric cutting, *Philosophical Magazine* 84 (11) (2004) 1155–1183.
- [188] K. Cheng, X. Luo, R. Ward, R. Holt, Modeling and simulation of the tool wear in nanometric cutting, *Wear* 255 (7-12) (2003) 1427–1432.
- [189] K. Ueda, K. Manabe, Chip formation mechanism in microcutting of an amorphous metal, *Annals of CIRP* 41 (1) (1992) 129–132.

- [190] C. Kim, M. Bono, J. Ni, Experimental analysis of chip formation in micro-milling, Transactions of North American Manufacturing Research Institution of SME 30 (2002) 247–254.
- [191] K. Lee, D. Dornfeld, An experimental study on burr formation in micro milling aluminium and copper, Transactions of North American Manufacturing Research Institution of SME 30 (2002) 255–262.
- [192] M. Merchant, Mechanics of the metal cutting process 1: orthogonal cutting and a type 2 chip, Journal of Applied Physics 16 (5) (1945) 267–275.
- [193] J. Shi, C. Liu, The influence of material models on finite element simulation of machining, ASME Journal of Manufacturing Science and Engineering 126 (4) (2004) 849–857.
- [194] T. Özel, The influence of friction models on finite element simulations of machining, International Journal of Machine Tools & Manufacture 46 (5) (2006) 518–530.
- [195] G. Johnson, W. Cook, A constitutive model and data for metals subjected to large strains, high strain rates and high temperatures, in: Proceedings of the 7th International Symposium on Ballistics, Hague, Netherlands, 1983, pp. 541–547.
- [196] G. Johnson, R. Stryk, T. Holmquist, S. Beissel, User instruction for the 1996 version of the epic code, Tech. rep., Alliant Techsystems Inc. (1996).
- [197] J. Hamann, V. Grolleau, F. L. Maitre, Machinability improvement of steels at high cutting speeds - study of tool/work material interaction, Annals of CIRP 45 (1996) 87–92.
- [198] T. Özel, E. Zeren, Determination of work material flow stress and friction properties for fea of machining using orthogonal cutting tests, Journal of Materials Processing Technology 153-154 (2004) 1019–1025.
- [199] N. Zorev, Interrelationship between shear processes occurring along tool face and on shear plane in metal cutting, in: Proceedings of the international research in production engineering conference, New York, USA, 1963, pp. 42–49.

- [200] K. Iwata, K. Osakada, Y. Terasaka, Process modeling of orthogonal cutting by the rigid plastic finite element method, *ASME Journal of Engineering for Industry* 106 (1984) 132–138.
- [201] T. Childs, Friction modelling in metal cutting, *Wear* 260 (2006) 310–318.
- [202] E. Trent, P. Wright, *Metal Cutting*, fourth ed., Butterworth-Heinemann, Woburn, MA, USA, 2000.
- [203] M. Medaska, L. Nowag, S. Liang, Simultaneous measurement of the thermal and mechanical effectiveness of cutting fluid, *Journal of Machining Science and Technology* 3 (2) (1999) 221–237.
- [204] J. Black, Flow stress model in metal cutting, *ASME Journal of Engineering for Industry* 101 (1979) 403.
- [205] E. Bickel, Hochfrequenten zeitlupenaufnahmen, *Annals of CIRP* 3 (1954) 90–91.
- [206] M. Shaw, Chip formation in the machining of hardened steel, *Annals of CIRP* 42 (1) (1993) 29–33.
- [207] E. Eugene, Etude experimentale sur l'influence conjointe de la pente d'affutage de l'outil et de la vitesse de coupe sur les modalites de la formation de copeau, *Annals of CIRP* 4 (1957) 121.
- [208] P. Albrecht, Self induced vibration in metal cutting, *ASME Journal of Engineering for Industry* 84 (1962) 405.
- [209] V. Astakhov, S. Shvets, M. Osman, The bending moment as the cause of chip formation, in: *Proceeding of American Society of Mechanical Engineers International Mechanical Engineering Congress and Exposition*, Vol. 6 of 2, Dallas, TX, UA, 1997, p. 53.
- [210] J. Wang, Y. Gong, G. Abba, K. Chen, J. Shi, G. Cai, Surface generation analysis in micro end-milling considering the influences of grain, *Microsystem Technologies* 14 (7) (2008) 937–942.
- [211] K. Liu, S. Melkote, Material strengthening mechanisms and their contribution to size effect in micro-cutting, *ASME Journal of Manufacturing Science and Engineering* 128 (2006) 730–738.

- [212] I. Kang, J. Kim, J. Kim, M. Kang, Y. Seo, A mechanistic model of cutting force in the micro end milling process, *Journal of Materials Processing Technology* 187-188 (2007) 250–255.
- [213] H. Bil, S. Kiliç, A. Tekkaya, A comparison of orthogonal cutting data from experiments with three different finite element models, *International Journal of Machine Tools & Manufacture* 44 (2) (2004) 933–944.
- [214] A. Moufki, A. Molinari, D. Dudzinski, Modelling of orthogonal cutting with a temperature dependent friction law, *Journal of the Mechanics and Physics of Solids* 35 (9) (1998) 1092–1027.
- [215] P. Venuinod, W. Jin, Three-dimensional cutting force analysis based on the lower boundary of the shear zone. part 1: Single edge oblique cutting, *International Journal of Machine Tools & Manufacture* 36 (3) (1996) 307–323.
- [216] P. Venuinod, Three-dimensional cutting force analysis based on the lower boundary of the shear zone. part 2: Edge oblique cutting, *International Journal of Machine Tools & Manufacture* 36 (3) (1996) 325–338.
- [217] Y. Gong, J. Wang, G. Abba, J. Antoine, J. Shi, Tool tip trajectories investigation and its influences in micromilling operation, *IEEE Review on Advances in Micro, Nano and molecular Systems*.
- [218] T. Childs, K. Maekawa, T. Obikawa, Y. Yamane, *Metal machining: theory and applications*, Arnold, London, UK, 2000.
- [219] A. Diniz, R. Micaroni, Cutting conditions for finish turning process aiming: the use of dry cutting, *International Journal of Machine Tools & Manufacture* 432 (2002) 899–904.
- [220] C. Sanjay, M. Neema, C. Chin, Modeling of tool wear in drilling by statistical analysis and artificial neural network, *Journal of Materials Processing Technology* 170 (2005) 494–500.
- [221] A. Singh, S. Panda, D. Chakraborty, S. Pal, Predicting drill wear using an artificial neural network, *International Journal of Advanced Manufacturing Technology* 28 (2006) 456–462.

- [222] L. Xu, J. Davim, R. Cardoso, Prediction on tribiological behaviour of composite peek-cf30 using artificial neural networks, *Journal of Materials Processing Technology* 189 (2007) 374–378.
- [223] I. El-Sonbaty, U. Khashaba, A. Selmy, A. Ali, Prediction of surface roughness profiles for milled surfaces using an artificial neural network and fractal geometry approach, *Journal of Materials Processing Technology* 200 (2008) 271–278.
- [224] M. Korosec, J. Kopac, Improved surface roughness as a result of free-form surface machining using self-organized neural network, *Journal of Materials Processing Technology* 204 (2008) 94–102.
- [225] B. Huang, J. Chen, Y. Li, Artificial-neural-networks-based surface roughness pokayoke system for end milling operations, *Neurocomputing* 71 (2008) 544–549.
- [226] A. Markopoulos, D. Manolakos, N. Vaxevanidis, Artificial neural network models for the prediction of surface roughness in electrical discharge machining, *Journal of Intelligent Manufacturing* 19 (2008) 283–292.
- [227] D. Zhang, H. Li, A stochastic-based fpga controller for an induction motor drive with integrated neural network algorithms, *Industrial Electronics, IEEE Transactions on* 55 (2) (2008) 551–561.
- [228] T. Pajchrowski, K. Zawirski, Application of artificial neural network to robust speed control of servodrive, *Industrial Electronics, IEEE Transactions on* 54 (1) (2007) 200–207.
- [229] K. Kiguchi, T. Fukuda, Position/force control of robot manipulators for geometrically unknown objects using fuzzy neural networks, *Industrial Electronics, IEEE Transactions on* 47 (3) (2000) 641–649.
- [230] X. Li, A. Djordjevich, P. Venuvinod, Current-sensor-based feed cutting force intelligent estimation and tool wear condition monitoring, *Industrial Electronics, IEEE Transactions on* 47 (3) (2000) 697–702.
- [231] C. Hudson, N. Lobo, R. Krishnan, Sensorless control of single switch-based switched reluctance motor drive using neural network, *Industrial Electronics, IEEE Transactions on* 55 (1) (2008) 321–329.

- [232] H. Oktem, T. Erzurumlu, F. Erzincanli, Prediction of minimum surface roughness in end milling mold parts using neural network and genetic algorithm, *Materials & Design* 27 (2006) 735–744.
- [233] P. Ross, *Taguchi Techniques for Quality Engineering*, McGraw-Hill, New York, 1996.



UNIVERSITE DE METZ



NORTHEASTERN UNIVERSITY



ECOLE DOCTORALE EMMA

Énergie, Mécanique, Matériaux

THÈSE DE DOCTORAT
PRÉSENTÉE A
L'UNIVERSITÉ DE METZ
POUR L'OBTENTION DU TITRE DE
DOCTEUR DE L'UNIVERSITÉ DE METZ
SPÉCIALITÉ : GENIE MÉCANIQUE

PAR

Jinsheng WANG

ETUDE DES MÉCANISMES DE
COUPE EN MICRO-USINAGE :
APPLICATION AU MICRO-FRAISAGE

SOUTENUE LE 13 Janvier 2009 DEVANT LE JURY COMPOSÉ DE :

P. PICART Rapporteur
Y. YAO Rapporteur
J. ANTOINE Examineur
M. WANG Examineur, Président
G. ABBA Directeur de Thèse
Y. GONG Directeur de Thèse

THIS WORK WAS DONE WITH THE SUPPORT OF FRENCH CHINESE DOCTORAL COLLEGE

Laboratoire de Génie Industriel et
de Production Mécanique (LGIPM),
Université de METZ,
Île du Sauley, F-57045 METZ Cedex 1

Laboratory of Advanced Manufacturing
and Automation (LAMA),
Northeastern University,
Shenyang, Liaoning, 110004, China

Résumé de thèse étendu en français

Jinsheng WANG

January 22, 2009

Etude des Mécanismes de Coupe en Micro-Usinage : Application au Micro-Fraisage

Laboratoire de Génie Industriel et de Production Mécanique
Université Paul Verlaine, Metz, France
Directeur de thèse: Professor Gabriel ABBA

Laboratory of Advanced Manufacturing and Automation
Northeastern University, Shenyang, China
Directeur de thèse: Professor Yadong GONG

1 Introduction

La technique du micro-fraisage apporte de nombreux avantages à la fabrication de pièces de petites dimensions. L'un de ses principaux avantages est la flexibilité de mise en œuvre [1]. Contrairement au fraisage classique, le micro-fraisage peut être facilement modifié pour répondre à la production et aux exigences d'exploitation. En outre, il n'exige pas de montages onéreux comme les méthodes lithographiques et ne nécessite pas de masques qui demande de temps de réalisation important. Le seuil de rentabilité est de ce fait réduit. Le procédé peut s'utiliser aisément pour la réalisation de pièces unitaires comme de grandes séries. Il offre la possibilité de surveiller la qualité des pièces en cours de fabrication et de corriger d'éventuelles dérives. Il permet de réaliser des surfaces gauches autorisant ainsi la production, par exemple de moules à injection plastique. Par ailleurs, on peut fabriquer une grande variété de produits fonctionnels en alliages métalliques, en matériaux composites, en polymères ou en matériaux céramiques. Par conséquent, il est nécessaire de comprendre en profondeur le procédé de micro-fraisage.

Les objectifs de cette thèse sont d'étudier les mécanismes physiques intervenant en micro-fraisage pour l'amélioration de la fabrication de produits miniaturisés. Un certain nombre de phénomènes et de grandeurs physiques influence le processus de micro-fraisage : les efforts de coupe, la dynamique et la stabilité de la broche et de l'outil, la formation du copeau et les caractéristiques des machines-outils.

Plusieurs thématiques de recherche ont été abordés par les chercheurs afin d'améliorer la technologie de micro-usinage tant en terme de qualité que de productivité. Parmi ces thématiques, on peut citer le développement de micro-machines-outils, l'étude de l'influence de la microstructure des pièces, l'étude des trajectoires de l'extrémité de la micro-fraise, l'analyse numérique et

analytique de la formation d'un copeau segmenté, la modélisation de la rugosité de la surface usinée, par exemple par réseau de neurones ou la conception de bancs d'essais.

Durant cette thèse, les études ont été réalisées au laboratoire "Advanced Manufacturing and Automation" (LAMA) de la *Northeastern University* (NEU) en Chine et au Laboratoire de Génie Industriel et de Production Mécanique (LGIPM) de l'Université Paul Verlaine (UPV) de Metz en France. Les motivations, les objectifs et les méthodologies de recherche sont résumés sur la figure 1.

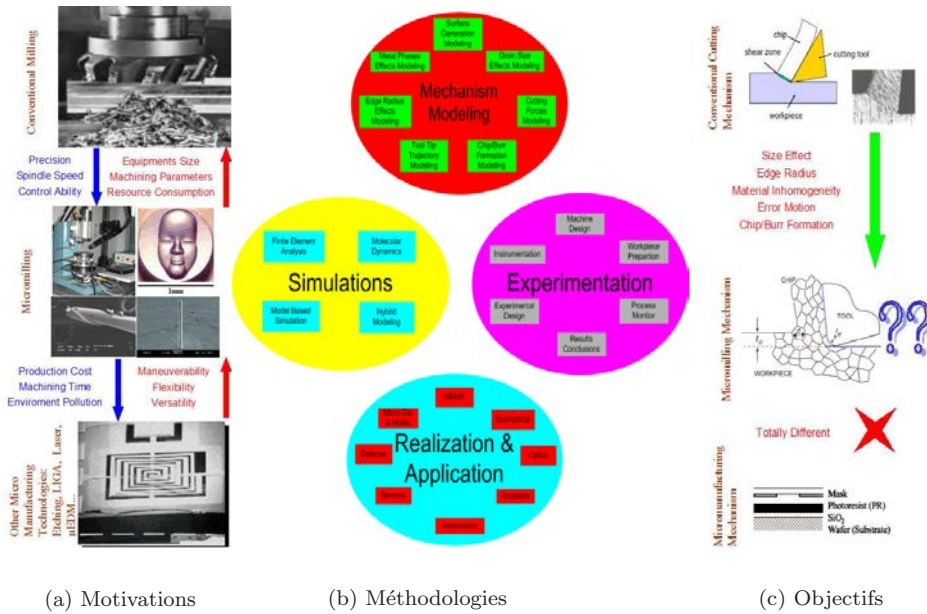


Figure 1: Motivations, objectifs et méthodologie de nos recherches

2 Développement d'une micro-machine d'usinage

Une Micro-Machine-outil (MMT pour *Micro-Machine Tools*) est rentable car elle nécessite pour sa réalisation de plus petites quantités de matériaux qu'une machine-outil de précision traditionnelle. En raison alors de sa faible masse, les fréquences propres sont plus élevées et les amplitudes des vibrations sont plus faibles. Ainsi, depuis l'introduction du concept de "microfactory" par le *Japan's Mechanical Engineering Lab* en 1998 [2], de plus en plus de chercheurs tentent de développer des MMT. Dans ce travail, un prototype de MMT trois-axes a été développé afin de disposer d'un banc d'essai pour les tests de micro-fraisage.

2.1 Conception de configuration

Après avoir déterminé les composants de la structure de base et les degrés de liberté nécessaires pour la micro-machine-outil, un système-expert [3] est utilisé pour optimiser la configuration de la MMT sélectionnée. Ce système intègre un ensemble de règles très simplifiées fondé sur la méthodologie de conception des machines-outils conventionnelles. Le jeu de règles inclut deux concepts fondamentaux pour sélectionner les configurations candidates acceptables. La règle numéro 1 stipule le besoin d'une répartition paire des degrés de liberté cinématiques. En effet, les axes et les liaisons montés en série vont accentuer les erreurs cinématiques et réduire la rigidité de la structure. La règle numéro 2 indique que les axes en mouvement doivent déplacer des masses les plus légères possibles pour améliorer la précision et la rapidité de réponse du système, et diminuer la puissance des moteurs installés. L'application de ces règles réduit le sous-ensemble des configurations de conceptions plausibles de 6 à 2, comme présentés sur la figure 2.

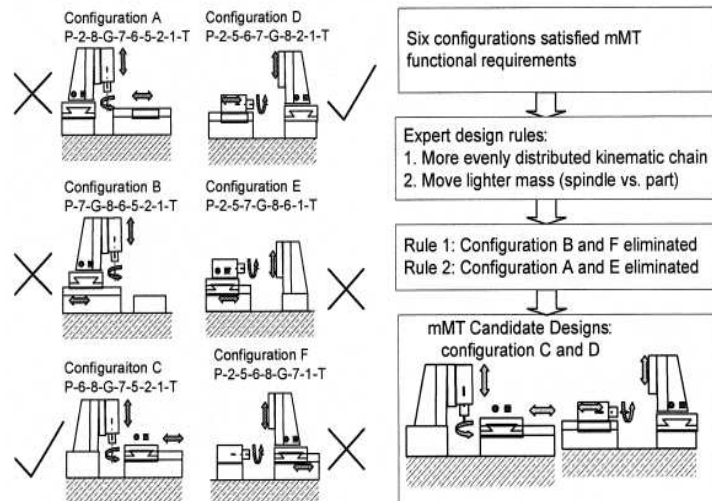


Figure 2: Réduction par système-expert du nombre de configurations acceptables

Dans l'étude présentée, la configuration C à broche verticale est adoptée pour la conception du prototype. La principale raison qui a conduit à ce choix est le besoin d'installer la dynamomètre. Sur le banc d'essai, la capacité maximale de la glissière est inférieure au poids du dynamomètre, qui doit alors être installé perpendiculairement à la direction de translation de la table croisée.

2.2 Développement de la micro-machine-outil

Le prototype réalisé de machine d'usinage trois-axes est composé d'une électrobroche grande vitesse, de trois moteurs linéaires de grande précision, de règles linéaires, d'une commande numérique, d'un dynamomètre de précision pour la mesure de forces tridimensionnelles, d'un microscope stéréo à caméra CCD, d'une interface à fonction programmable en code G, d'un système d'isolation antivibratoire et d'un système de refroidissement de la broche. L'ensemble du système est présenté sur la figure 3. Les performances et les principales caractéristiques de la machine-outil sont rassemblées dans le tableau 1. Un exemple d'usinage de micro-colonne de $200\ \mu\text{m}$ de diamètre et 3 mm de long est présenté sur la figure 4.

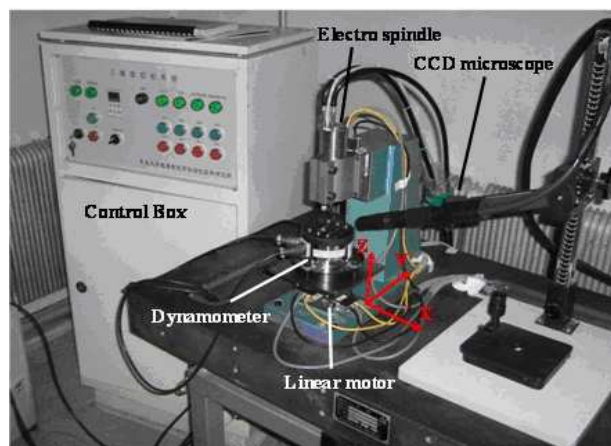


Figure 3: Système MMT 3-axes

Table 1: Performances et caractéristiques de la machine

Systèmes	Éléments	Valeurs
Avances	Moteurs linéaires	MX80L
	Course du moteur linéaire	50 mm
	Règle linéaire	Reinshaw
	Résolution de la règle	10 nm
	Charge maximale	8Kg
	Accélération maximale	4G
	Vitesse nominale	30 mm/s
	Force maximale	12 N
	Force permanente admissible	4 N
	Cycle d'utilisation	100%
	Rectitude et planéité	4 μ m
	Masse	590 g
	Masse en mouvement	282 g
Broche	Vitesse de rotation maximale	60 000 tr/mn
	Faux-rond axial et radial	3 μ m
Microscope	Amplifications	40 \times ~ 240 \times
Dynamomètre	Dynamomètre	SDC-CJ3SAS
	Plage de mesure: F_x, F_y, F_z	± 250 N
	Linéarité	$\leq \pm 0,3\%$ FSO Supreme linearity, one step calibration is enough
	Couplage	$\leq \pm 2\%$
	Hystérésis	$\leq \pm 0,3\%$ FSO
	Fréquences propres (X,Y,Z)	$\geq 4,0$ kHz
	Plage de température de fonctionnement	-20° C ~ 100° C
	Résolution	10 mN
	Fréquence d'échantillonnage	8 kHz
MMT	Dimensions	400 \times 320 \times 100 mm ³
	Espace utile	50 \times 50 \times 50 mm ³
	Précision de positionnement bi-directionnel	X: 0,2734 μ m, Y: 0,2800 μ m, Z: 0,4534 μ m
	Répétabilité de positionnement bi-directionnel	X: 0,2682 μ m, Y: 0,2618 μ m, Z: 0,4510 μ m
	Valeur de retournement	X: 0,04627 μ m, Y: 0,0347 μ m, Z: 0,0520 μ m

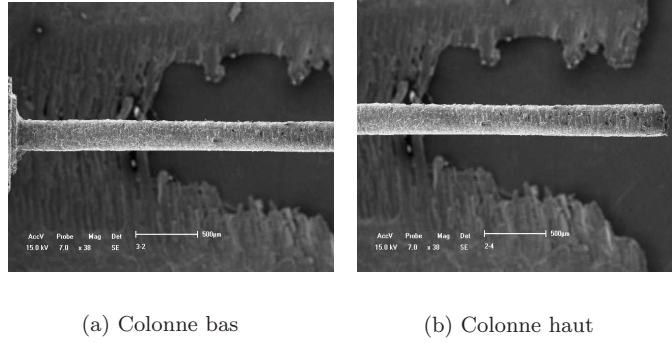


Figure 4: Exemple de micro-colonne réalisé par la MMT

3 Effets de la microstructure de la pièce

A l'échelle du micro-usinage, en raison de l'énorme diminution de la taille de l'outil et des conditions de coupe, la structure microcristalline de la pièce à usiner joue un rôle important dans le processus d'usinage [4]. Par conséquent, la microstructure doit être étudiée afin de véritablement bien comprendre les mécanismes du micro-fraisage. Dans ce travail, un alliage d'aluminium Al6061-T6 est choisi pour étudier les effets de la microstructure des matériaux polycristallins. Trois types de cuivre exempt d'oxygène à haute conductivité ont été sélectionnés pour faire l'étude de matériaux polycristallins monophasés.

3.1 Modèle pour le micro-fraisage des matériaux polycristallins

Dans le processus de micro-usinage, le rayon de l'arête de coupe et la taille des grains sont plus d'importances que les paramètres usuels d'usinage. Par conséquent, leurs effets doivent être pris en compte dans le modèle, ainsi que la zone présentée figure 5 o se concentre les phénomènes liés à la micro-coupe .

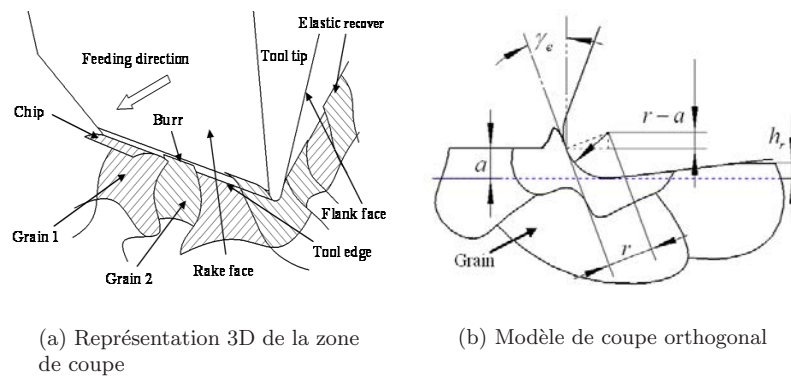


Figure 5: Processus de micro-coupe

La première modification concerne l'angle nominal d'inclinaison qui est remplacé par une valeur calculée en fonction de la profondeur de passe a et du rayon de l'arête de coupe et qui est donné par la formule suivante:

$$r_e = \arccos\left(\frac{r-a}{r}\right) - \frac{\pi}{2} \quad (1)$$

Deuxièmement, puisque les phases métalliques varient d'un grain à l'autre, avec des propriétés mécaniques très variables, la pièce doit être considérée comme anisotrope. En raison des différences de modules d'élasticité E et de coefficient de frottement μ , le copeau minimum h_m et le retour élastique h_r seront variables d'un grain à l'autre. h_m sera calculés [5] par les équations (2) et (3) . La hauteur h_r sera obtenue grâce aux équations (4) et (5).

$$h_m = r(1 - \cos(1 - \cos(\pi/4 - \beta/2))) \quad (2)$$

$$\cos \beta = \frac{1}{\sqrt{1 + \mu^2}} \quad (3)$$

$$h_r = \begin{cases} h_m, & \sigma \leq \sigma_P \\ h_m - \frac{\sigma_P \sqrt{r^2 - (r - h_m)^2}}{E}, & \sigma > \sigma_P \end{cases} \quad (4)$$

$$\sigma = \frac{E \cdot h_m}{\sqrt{r^2 - (r - h_m)^2}} \quad (5)$$

La figure 6 présente la modélisation du micro-fraisage. La pièce est composée de nombreux grains, classés selon leur phase métallique. En raison des variations de copeau minimum h_m , les grains auront besoin, pour être enlevés, d'un nombre de passes variable. Par conséquent, des vibrations vont se produire : en basse fréquence pour celles dues aux différentes phases métalliques et à haute fréquence pour celles générées par les variations de hauteur de coupe. Par ailleurs, la surface générée sera également modifiée par la nature des phases métalliques.

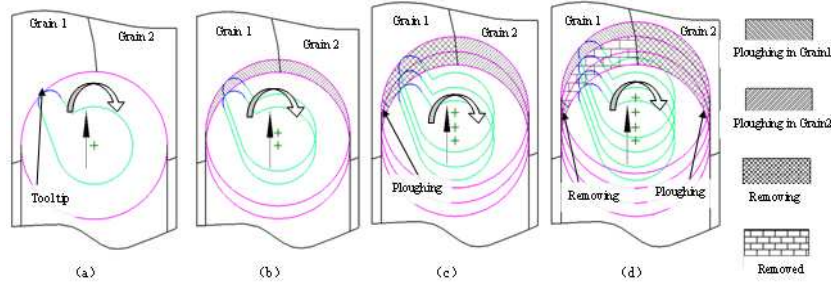


Figure 6: Processus de micro-fraisage

3.2 Etude expérimentale du micro-fraisage d'un matériau polycristallin multi-phase

3.2.1 Montage expérimental

Une micro-fraise à 4 dents en carbure de tungstène de 0,4 mm de diamètre a été utilisée. Le rayon de l'arête de coupe mesuré par microscope électronique à balayage est de $1,36 \mu\text{m}$. La pièce à usiner est en Al6061-T6. Sa microstructure est présentée sur la figure 7. L'alliage est composée de 2 phases, l'une ductile et l'autre fragile. La partie qui apparaît blanche, est la phase ductile composée principalement d'aluminium. Le diamètre moyen des grains est de $10,238 \mu\text{m}$. La partie noire est la phase fragile rejetée de la phase au refroidissement, essentiellement constitué de silicium, souvent appelée silicium aciculaire. Les propriétés du matériau [6] et le calcul des résultats de h_m et h_r pour les deux phases sur la base des équations (2-5) sont listés dans le tableau 2. Si l'on compare les valeurs, h_m est plus petit pour la phase fragile que pour la phase ductile, ce qui veut dire que le copeau se formera plus facilement dans la phase fragile. h_r est plus petit dans la phase fragile que dans la phase ductile, par conséquent le retour élastique sera plus faible dans les joints des grains.

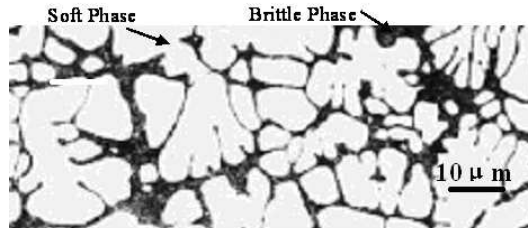


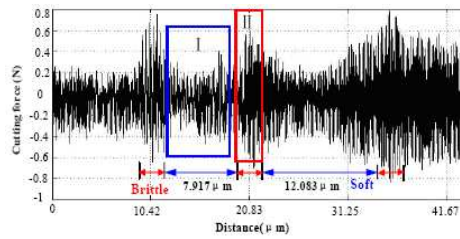
Figure 7: Microstructure de Al6061-T6

Table 2: Les propriétés du matériau Al6061-T6 et les valeurs du modèle

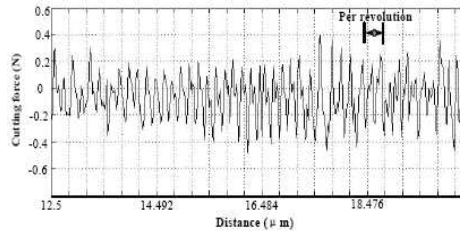
Éléments	Phase ductile	Phase fragile
E (GPa)	70	8,7
μ	0,3	0,5
σ_P (MPa)	240	0,04
h_m (μm)	0,2689	0,2031
h_r (μm)	0,2655	0,2021

3.2.2 Effort de coupe

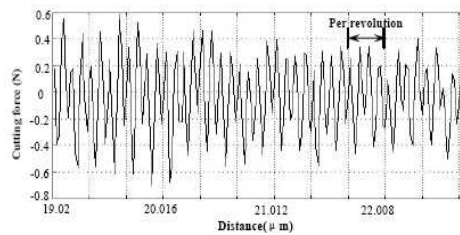
La figure 8 présente les résultats de mesure d'efforts de coupe suivant une des trois directions du dynamomètre. Il a été constaté que la force de coupe dans la phase fragile était supérieure à celle dans les grains. Dans le même temps, pour chaque tour de l'outil, quatre pics de différentes amplitudes apparaissaient en raison des phénomènes de copeau minimum.



(a) Signal d'origine



(b) Agrandissement zone I



(c) Agrandissement zone II

Figure 8: Effort de coupe (vitesse de rotation : 30 000 tr/mn, vitesse d'avance : 10 mm/min, profondeur de passe axiale : 20 μm)

3.3 Génération de surface

La surface en fond d'une rainure usinée est présentée sur la figure 9. En plus des stries d'usinage dues au passage de l'arête de coupe, on remarque des cavités formées sur la phase fragile avec des copeaux autour d'elles, qui sont en bonne corrélation avec la description précédente. La distance mesurée sur la figure 9 concorde bien avec la taille moyenne des grains.

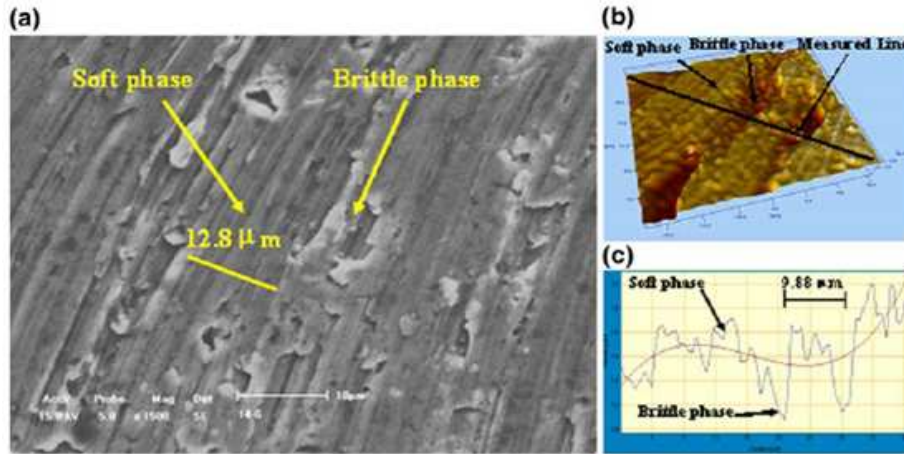


Figure 9: Fond d'une rainure fraisée (vitesse de rotation : 25 000 tr/min, vitesse avance : 20 mm/min, profondeur de passe axiale : 10 µm)

3.4 Fraisage de matériaux monophasés polycristallins

Trois pièces de cuivre haute conductivité exempt d'oxygène, qui est un matériau polycristallin monophasé, générés par un nombre variable de passe d'extrusion angulaire à aire égale (ECAE) afin d'obtenir différentes tailles de grains, sont utilisées pour comprendre les effets de la taille des grains, de l'orientation cristallographique et de la rugosité de la surface micro-fraisée.

4 Etude des trajectoires des arêtes de coupe de la micro-fraise

En raison des caractéristiques géométriques particulières de la micro-fraise et sa haute vitesse de rotation, les trajectoires des dents de l'outil sont manifestement différentes de celles que l'on obtient communément. Dans cette partie, un modèle précis est développé pour prévoir les trajectoires d'une fraise à 2 dents. Leurs effets sur l'erreur d'usinage, la qualité de la surface et la durée de vie de l'outil seront décrits en détails.

4.1 Structure du modèle

La structure du modèle est montrée sur la figure 10, incluant les étapes en entrée du modèle et en sortie. Dans l'étape "entrée", le faux rond en bout d'outil et son balourd sont obtenus à partir de mesure et des approches proposées pour le calcul. Deux modèles, un modèle de la dynamique des rotors tournants et un modèle de trajectoires des dents de l'outil, sont contenus dans l'étape "modèles". Les déformations radiales de l'outil en rotation sont calculées par le premier modèle, et servent d'entrée au second lors du calcul des trajectoires. En sortie, les résultats concernant les trajectoires des dents de l'outil, l'épaisseur du copeau, les forces de coupe, la largeur de la rainure et la qualité de la surface peuvent être obtenus à partir de la trajectoire de l'outil.

4.2 Méthode de mesure

L'approche de mesure proposée utilise deux comparateurs à aiguilles pour réaliser des mesures en trois endroits différents de l'axe de l'outil. Un capteur laser est utilisé pour valider les résultats des mesures. Les résultats sont en bonne concordance.

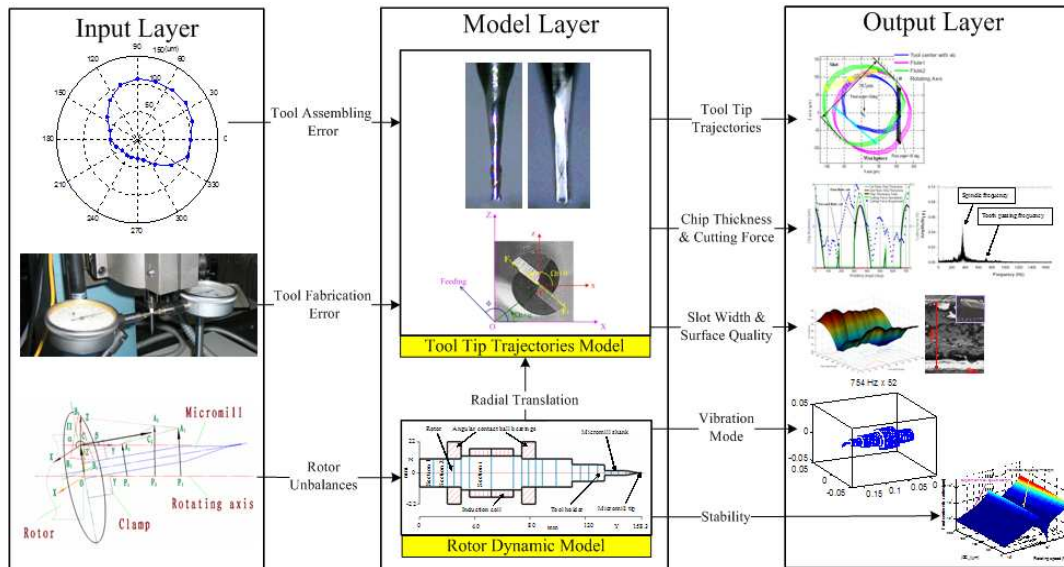


Figure 10: Structure du modèle de détermination des trajectoires d'outil

4.2.1 Faux rond du bout de l'outil

L'interpolation linéaire des résultats de mesure donne le faux-rond de l'outil qui est représenté sur la figure 11.

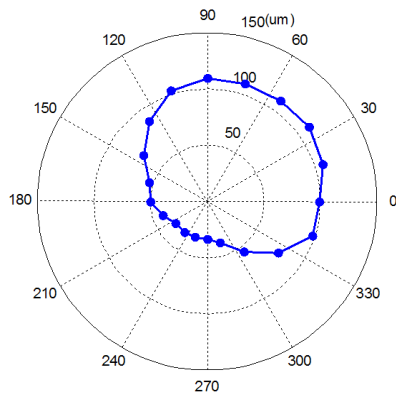


Figure 11: Faux rond du bout de l'outil

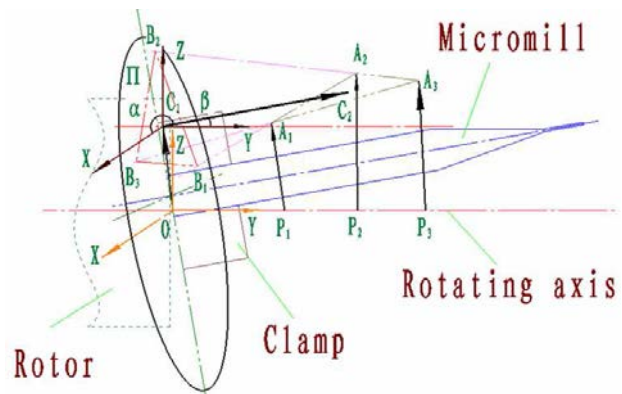


Figure 12: Principe de calcul du faux rond de l'outil

4.2.2 Balourd de l'outil

Déterminer le balourd de chaque section de l'outil est primordial pour l'analyse des vibrations du rotor. Une méthode simple de calcul des balourds utilisant les résultats précédents est présentée sur la figure 12. Le vecteur $\vec{C_1C_2}$ permet d'obtenir le balourd sur chaque section.

4.2.3 Vibrations du rotor

Un modèle de dynamique du rotor [7] a été développé pour calculer les vibrations en bout d'outil. La première fréquence propre est trouvée à environ 70 000 tr/mn, alors que la vitesse maximale de la broche est de 30 000 tr/mn. Le rotor peut être considéré comme un corps rigide dans cette étude et on supposera que seul le balourd du rotor affecte l'amplitude des vibrations en bout d'outil.

4.3 Étude des trajectoires

A partir de l'hypothèse précédemment développée, la trajectoire de l'extrémité de l'outil est vu comme un système à un degré de liberté. Les vecteurs et repères liés à l'outil sont définis sur la figure 13. Les deux angles principaux sont l'angle de l'arête θ et l'angle d'avance ϕ . Ils varient de 0° à 360° . Les deux arêtes sont confondues lorsqu'on effectue une rotation de 180° . Le faux-rond et les vibrations du bout de l'outil sont incluses dans le modèle des trajectoires. Les équations (6 ~ 8) donnent les trajectoires du centre de l'outil o' et des deux arêtes F_1 et F_2 quand l'avance est nulle. La figure 14 présente des exemples avec différents angles θ quand la vitesse de rotation est de 30 000 tr/min. Dans le même temps, la figure 15 présente les trajectoires avec avance pour $\theta = -90^\circ$ et toujours pour une vitesse de 30 000 tr/min.

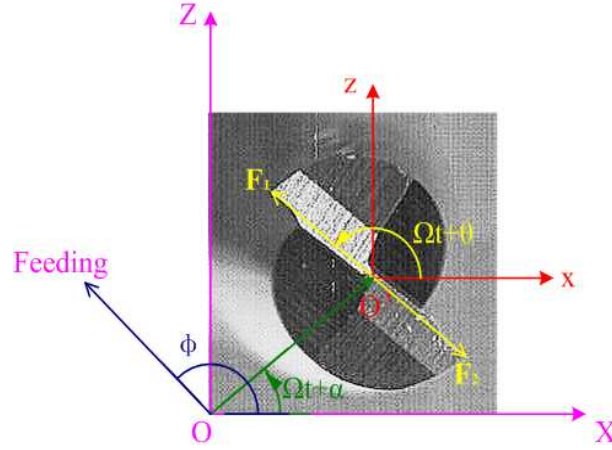


Figure 13: Les vecteurs et repères liés à l'outil

$$x_{o'}(t)^2 + z_{o'}(t)^2 = |Oo'(\Omega t)|^2 \quad (6)$$

$$x_{F_1}(t)^2 + z_{F_1}(t)^2 = |Oo'(\Omega t)|^2 + 2|Oo'(\Omega t)|R \cos \theta + R^2 \quad (7)$$

$$x_{F_2}(t)^2 + z_{F_2}(t)^2 = |Oo'(\Omega t)|^2 - 2|Oo'(\Omega t)|R \cos \theta + R^2 \quad (8)$$

4.4 Analyse des paramètres les plus influents

A partir des trajectoires simulées, il a été mis en évidence que les effets de l'angle des arêtes θ et de la direction d'avance ϕ sur la largeur de la rainure et sur les forces de coupe sont importants.

4.4.1 Largeur de rainure

La figure 16 présente la variation de la largeur de la rainure en fonction des paramètres θ et ϕ . Il est évident que l'angle d'arête affecte beaucoup plus la largeur de rainure que l'angle d'avance. La valeur optimale de $\theta = \pm 90^\circ$ a été déterminée.

4.4.2 Interaction avec le copeau

Les simulations montrent que, dans bien des cas, seule une des arêtes de l'outil est active. La force de coupe est donc toujours sur la même arête. L'angle d'avance ϕ a une importance dans la distribution des efforts et dans l'erreur d'usinage seulement lorsque $\theta = \pm 90^\circ$ (Tableau 3). L'erreur d'usinage est moindre avec seule une arête coupe que lorsque les deux arêtes sont actives.

4.5 Étude expérimentale

Une fraise 2 dents de $152 \mu\text{m}$ de diamètre a été utilisée. Les conditions de coupe choisies sont une profondeur de passe de $10 \mu\text{m}$, une vitesse d'avance de 60 mm/mn et un angle d'arête de $\theta = -90^\circ$. La vitesse de rotation et la direction d'avance varient.

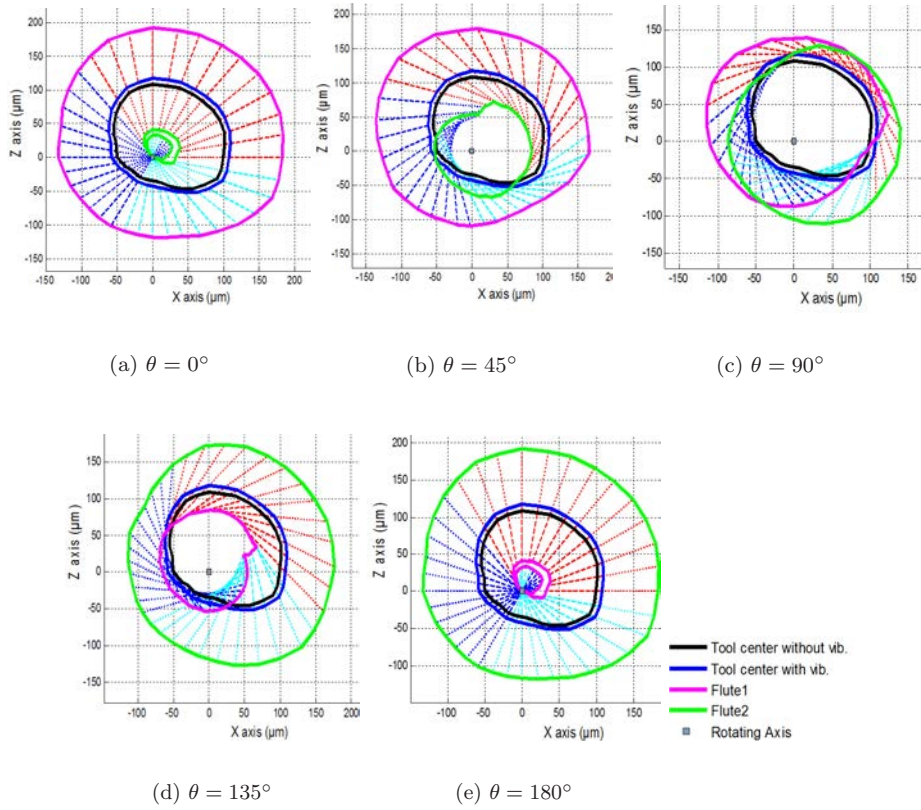


Figure 14: Trajectoires statiques

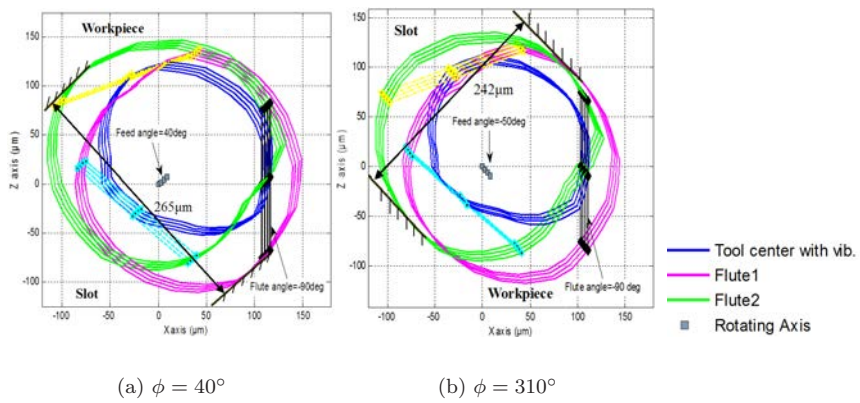


Figure 15: Trajectoires avec vitesse d'avance

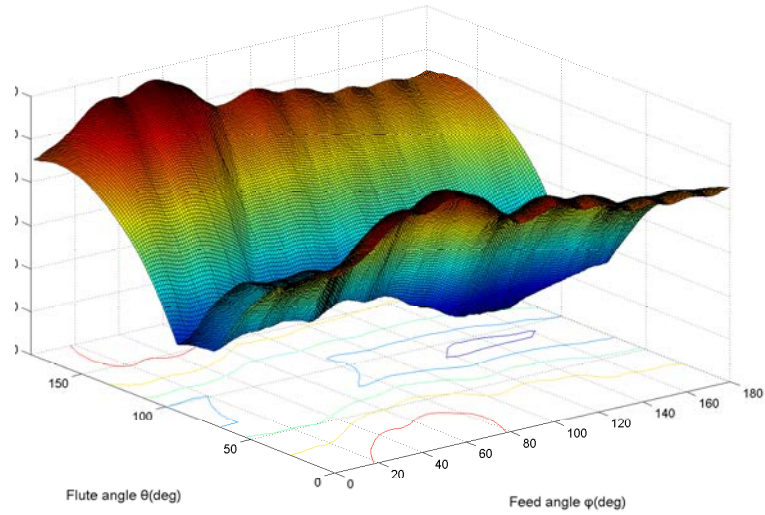


Figure 16: Variation de la largeur de la rainure en fonction des paramètres θ et ϕ

Table 3: Influence de l'angle d'avance ϕ sur les efforts ($\theta = \pm 90^\circ$)

Angle d'avance ϕ	Interaction avec le copeau	Distribution des efforts	Erreur d'usinage
45° 225°	$1^{er} = 2^{ème}$	2 dents	importante
$45^\circ \sim 135^\circ$ $135^\circ \sim 225^\circ$	$2^{ème} > 1^{er}$	2 dents	moyenne
135°	$2^{ème}$	1 dent	faible
$225^\circ \sim 315^\circ$ $315^\circ \sim 45^\circ$	$1^{er} > 2^{ème}$	2 dents	moyenne
315°	1^{er}	1 dent	faible

Efforts de coupe et épaisseur du copeau

Un exemple d'efforts de coupe et d'épaisseur de copeau est présenté sur la figure 17. Une seule arête coupe. Les résultats expérimentaux sont en bonne corrélation avec les simulations. Plus de 90% des efforts sont concentrés sur la première arête. De plus, l'analyse FFT de la force met en évidence que la principale composante du signal n'est pas la fréquence de passage des dents mais celle de rotation de la broche comme présenté sur la figure 18.

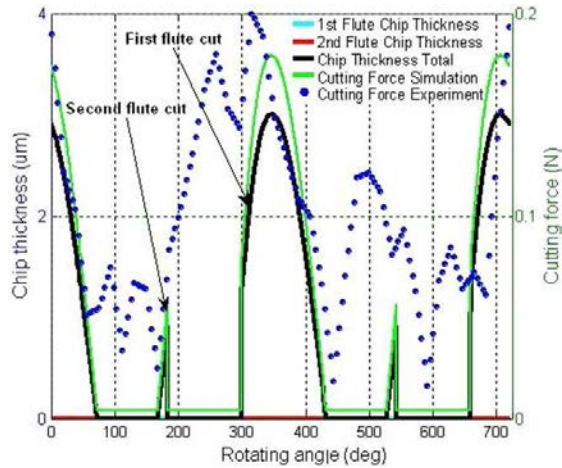


Figure 17: Efforts de coupe et épaisseur du copeau (Vitesse de rotation: 30 000 tr/mn, $\phi = 310^\circ$)

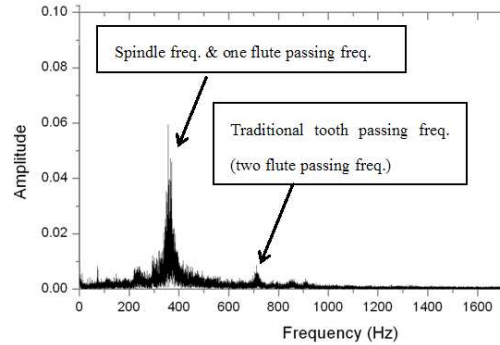


Figure 18: L'analyse FFT de la force

4.5.1 Largeur de rainure et état de surface

La figure 19 présente les résultats de la mesure par SEM pour deux séries d'essai. Le modèle prédit très bien les variations de la largeur de rainure en fonction de la vitesse de rotation et pour les deux directions d'avance étudiées. Le cas d'une largeur de rainure de $270 \mu\text{m}$ usinée avec un outil de diamètre $\phi 152 \mu\text{m}$ est présenté sur la figure 20. L'état de surface du fond de la rainure est très mauvais en raison de la différence de hauteur des deux arêtes.

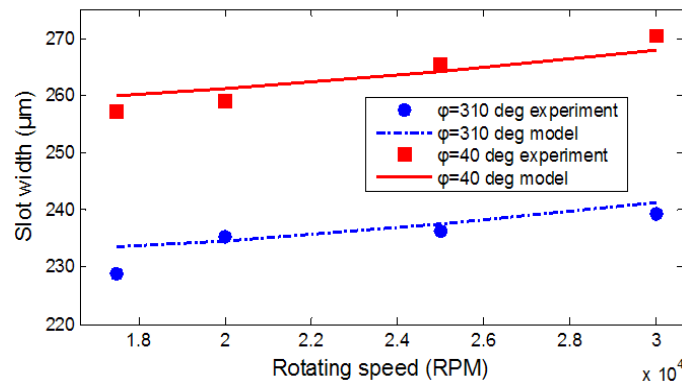


Figure 19: Comparaison de largeur de rainure

5 Formation d'un copeau segmenté

Les essais et les simulations par éléments finis ont mis en évidence un type de copeau segmenté. Afin de comprendre le mécanisme de formation du copeau, une approche hybride analytique et numérique est utilisée pour étudier les moments appliqués, la vitesse et l'accélération du copeau.

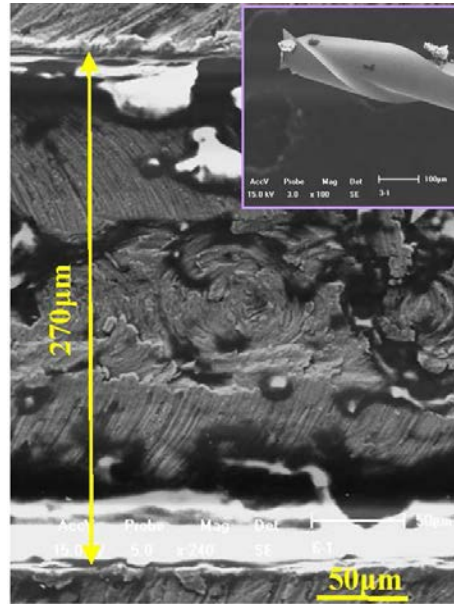


Figure 20: Qualité de surface de rainure (Vitesse de rotation : 30000 tr/mn, $\phi = 40^\circ$)

5.1 Simulation par éléments finis et validation expérimentale

Le logiciel de simulation DEFORM 2D est utilisé. Le modèle de Johnson-Cook de Al6061-T6 et un coefficient de frottement de Coulomb de 0,7 est implanté dans la routine par l'utilisateur. Les simulations de formation du copeau et les essais sont présentés sur les figures 21 et 22. Ils montrent un bon accord tant dans la forme du copeau que dans sa longueur. À partir de l'analyse numérique des vitesses, on montre que la localisation du point de vitesse maximale alterne de la racine du copeau à sa pointe à chaque segmentation de celui-ci.

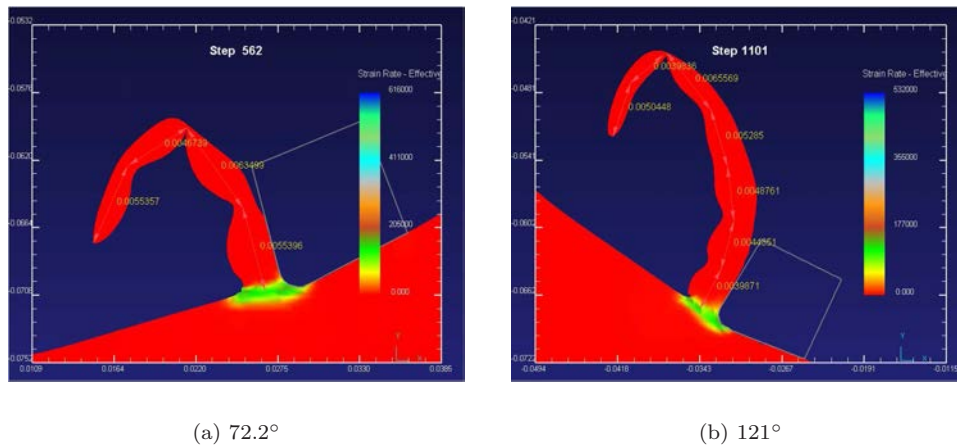
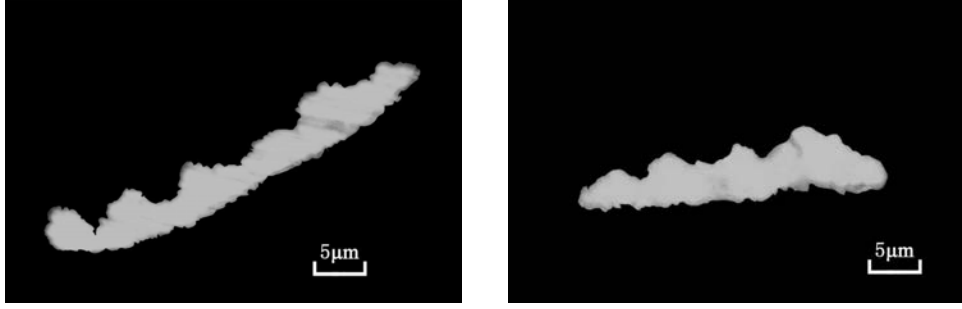


Figure 21: Simulations de formation du copeau

5.2 Étude du mécanisme de formation du copeau

5.2.1 Calcul des moments appliqués sur le copeau

Le copeau est modélisé comme une poutre comme représentée sur la figure 23 et géré par l'équation 9. Le plus important est de calculer le moment appliqué sur le copeau par l'outil



(a) exemple 1 de copeau

(b) exemple 2 de copeau

Figure 22: Simulations de formation du copeau

M_{Tool} , et le moment appliqué par le plan de cisaillement M_{Work} .

$$(M_{Tool} - M_{Work}) = J_{Chip-O} \dot{\omega}_{Chip} \quad (9)$$

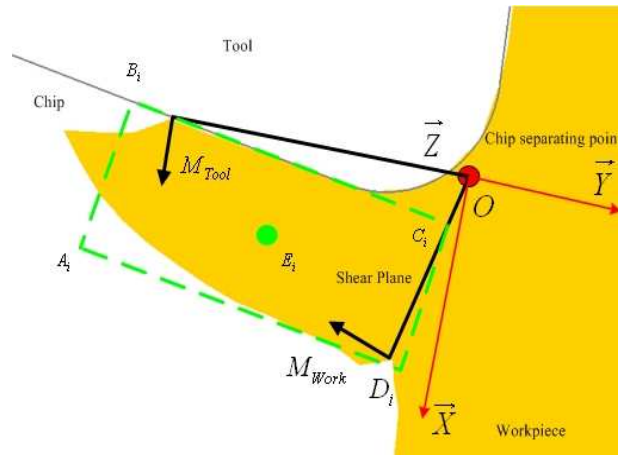


Figure 23: Poutre équivalente de modélisation du copeau

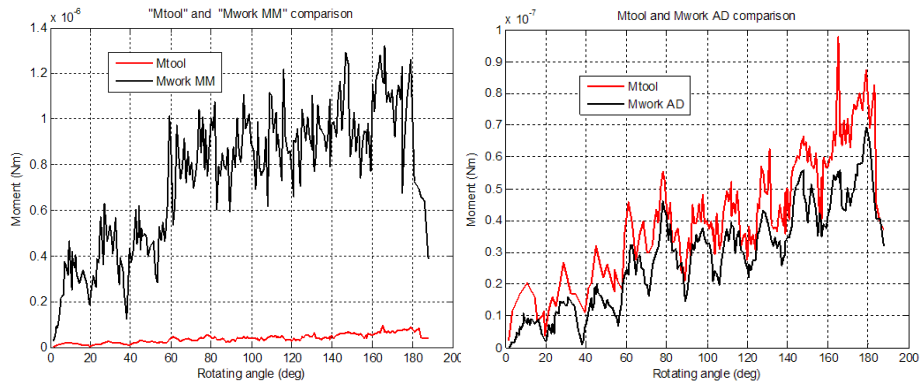
Le couple M_{Tool} est calculé par intégration de la pression normale au contact sur la surface de contact avec l'outil par l'équation 10 dont les éléments sont obtenus par la simulation.

$$M_{Tool} = \int_O^F w \sigma_{tn,i} dt_i dl \quad (10)$$

Le couple M_{Work} est calculé par l'équation 11 grâce à deux modèles analytiques: le modèle de Merchant (MM) [8] et le modèle d'Arcona-Dow (AD) [9]. Ces modèles sont comparés sur la figure 24. Les résultats montrent que le modèle AD développé pour le tournage au diamant est mieux adapté que le modèle MM destiné à l'échelle macroscopique.

$$M_{Work} = \frac{w \sigma_{wn,aver} l_s^2}{2} \quad (11)$$

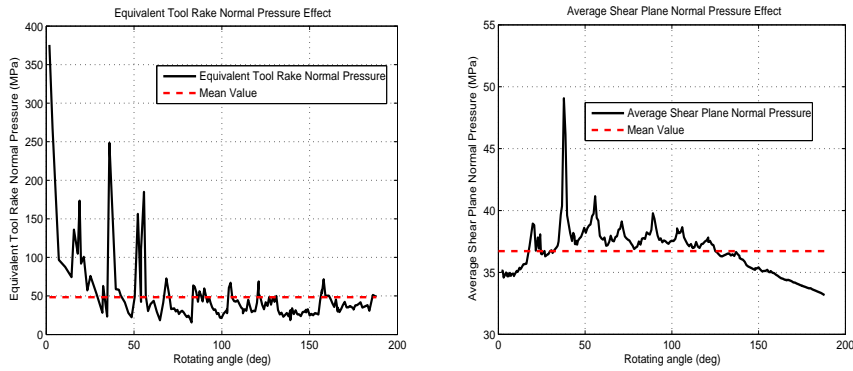
Les moments appliqués au copeau peuvent être considérés comme des fonctions des couples $M_{Work-AD} = f(l_s^2/2, \sigma_{wn,aver})$ et $M_{Tool} = f(l_T^2/2, \sigma_{tn,equ})$ respectivement. Les variations de $\sigma_{tn,equ}$, $\sigma_{wn,aver}$, l_T et l_S sont présentées sur les figures 25 et 26. De toute évidence, l_T et l_S suivent les mêmes tendances que M_{Tool} et $M_{Work-AD}$. En conclusion, on remarque que les variations des longueurs l_T et l_S sont les raisons principales des moments et donc de la formation du copeau segmenté.



(a) M_{Tool} et M_{Work_MM}

(b) M_{Tool} et M_{Work_AD}

Figure 24: M_{Tool} fonction de M_{Work_MM} et M_{Tool} fonction de M_{Work_AD}



(a) Tracé de σ_{tn_equ}

(b) Tracé de σ_{wn_aver}

Figure 25: Allure de σ_{tn_equ} et σ_{wn_aver}

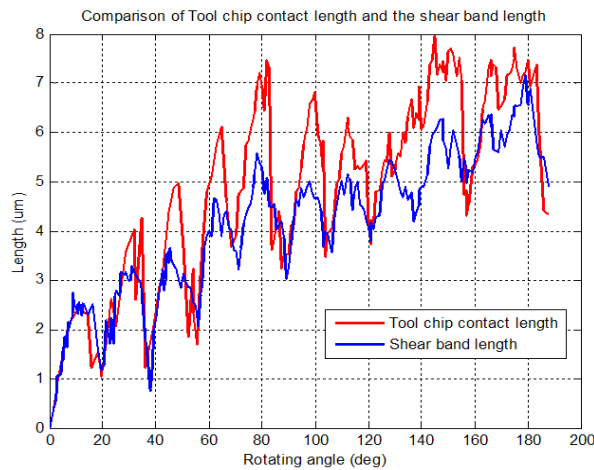


Figure 26: l_T et l_S

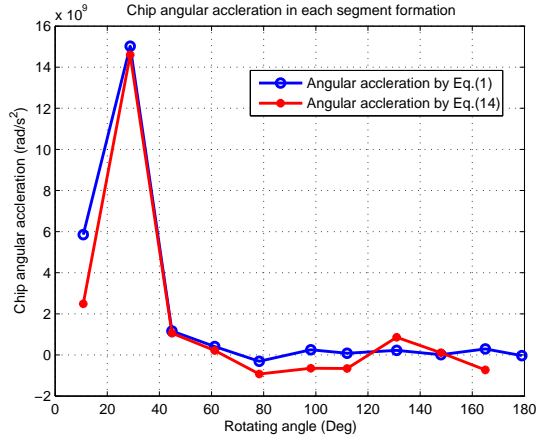


Figure 27: Accélérations angulaires du copeau $\dot{\omega}_{Chip_FEM}$ et $\dot{\omega}_{Chip}$

5.2.2 Analyse de la vitesse du copeau

À partir de l'analyse des vitesses du copeau, nous savons que la vitesse moyenne du copeau après séparation d'avec l'outil est bien supérieure à celle avant la flexion du copeau, qui est de l'ordre de la vitesse de coupe. Dans le même temps, la vitesse dans le plan de cisaillement est pratiquement constante pour l'ensemble du processus. La principale raison est que la vitesse de l'extrémité du copeau est plus importante lors du processus de flexion à cause de l'accélération angulaire.

5.2.3 Analyse de l'accélération angulaire du copeau

L'accélération angulaire du copeau est calculée par deux approches. La première est basée sur l'équation 12. la seconde utilise l'équation 9 après avoir calculé le moment d'inertie du copeau J_{Chip_O} . La figure 27 montre que les deux résultats concordent bien.

$$\dot{\omega}_{Chip_FEM} = \frac{\frac{V_{tip_e} - V_{root_e}}{D_e} - \frac{V_{tip_b} - V_{root_b}}{D_b}}{T_e - T_b} \quad (12)$$

6 Prédiction de la rugosité par réseaux de neurones et plan d'expérience

Un modèle de réseau de neurones à propagation inverse est développé pour prédire les effets de la vitesse de rotation n , de la vitesse d'avance f et de la profondeur de passe a_p sur la rugosité moyenne de la surface R_a usinée par un procédé de micro-fraisage. L'approche de Taguchi est utilisée pour le plan d'expérience (DoE) pour acquérir suffisant d'informations avec un nombre minimum d'essais, pour former le réseau de neurones (NN). Enfin, le modèle NN donne de bonnes prédictions de la rugosité de la surface et les effets d'un facteur ou de l'interaction entre deux facteurs sont discutés.

7 Conclusion

Dans cette étude, le mécanisme de micro-fraisage est étudié en profondeur par certains aspects, incluant le développement d'une micro-machine-outil pour le fraisage, l'influence de la microstructure de la pièce usinée, les effets de la trajectoire de l'extrémité de la micro-fraise, l'étude de la formation du copeau segmenté et la prédiction de la rugosité. Certains résultats importants obtenus durant ce travail sont rappelés ci-dessous :

1. Les différences de phases métalliques dans un matériau polycristallin multiphase affectent beaucoup le processus de micro-fraisage, induisant des variations dans les efforts de coupe et influençant la surface générée.

2. Pendant le processus de micro-fraisage, seule une seule arête coupe la matière. L'angle de l'arête θ et la direction d'avance ϕ sont importants pour réduire l'erreur d'usinage et pour répartir les efforts de coupe.
3. Le mécanisme de formation du copeau est étudié par une méthode hybride analytique-numérique. Le copeau acquiert une accélération angulaire additionnelle au moment de la génération du segment. Les variations de la longueur de contact entre l'outil l_T et le copeau et de la longueur de la bande de cisaillement l_S sont les raisons principales qui expliquent l'apparition du copeau segmenté.

References

- [1] M. Weck, S. Fischer, M. Vos, Fabrication of micro components using ultra precision machine tools, *Nanotechnology*, 8 (1997), 145–148.
- [2] K. Furuta, Y. Ishikawa, Y. Mikuriya, Y. Takahashi, The microfactory system in national r&d project of miti, in: *Proceedings of the International Workshop on Microfactories*, Tsukuba, Japan, 1998, pp. 193–196.
- [3] H. Chen, Generation and evaluation of meso-scale machine tool designs for micro-machining applications, Ph.D. thesis, University of Michigan (2005).
- [4] D. Dornfeld, S. Min, Y. Takeuchi, Recent advances in mechanical micromachining, *Annals of CIRP*, 55 (2) (2006), 745–768.
- [5] S. Son, H. Lim, J. Ahn, Effects of the friction coefficient on the minimum cutting thickness in micro cutting, *International Journal of Machine Tools & Manufacture*, 45 (2005), 529–535.
- [6] Z. Wu, *Handbook of mechanical design*, Chemical Industry Press, Beijing, 1999.
- [7] J. Antoine, C. Visa, G. Abba, C. Sauvey, Electrospindle design for high speed machining, in: *5th Int. congress on High Speed Machining*, Metz, France, 2006, pp. 329–340.
- [8] M. Merchant, Mechanics of the metal cutting process 1: orthogonal cutting and a type 2 chip, *Journal of Applied Physics*, 16 (5) (1945), 267–275.
- [9] C. Arcona, T. Dow, An empirical tool force model for precision machining, *ASME Journal of Manufacturing Science and Engineering*, 120 (1998), 700–707.

Abstract

Micromilling technique brings many advantages to the fabrication of micro-sized features. The objectives of this thesis are to investigate the micromilling mechanism for the efficient fabrication of miniaturized products. There are a number of issues that influence micromilling processes: cutting forces, dynamics and stability, chip formation, and machine tools. Several research topics, including Micro Machine Tool (MMT) development, workpiece microstructure influences, micromill tip trajectory investigation, wavy chip formation analysis via FEM-analytical approach, surface roughness prediction based on the neural network and design of experiment are focused in this thesis. Some important results are listed: 1. The metal phase differences in the multi-phase polycrystalline material affect the micromilling process greatly, induce the cutting force variation, and influence the surface generation. 2. The single flute cutting condition always occurs in the micromilling process. The flute angle θ and feed angle ϕ are important to the machining error and chip load distribution. 3. The wavy chip formation mechanism is studied via hybrid analytical-FEM approach. It has been found the chip acquires additional angular acceleration in the segment generation instant. The variations of the tool chip contact length l_T and shear band length l_S are the main reasons of wavy chip segment formation.

Résumé

La technique du micro-fraisage apporte de nombreux avantages à la fabrication de pièces de petites dimensions. Les objectifs de cette thèse sont d'étudier les mécanismes physiques intervenant en micro-fraisage pour l'amélioration de la fabrication de produits miniaturisés. Plusieurs thématiques de recherche ont été abordés par les chercheurs afin d'améliorer la technologie de micro-usinage tant en terme de qualité que de productivité. Parmi ces thématiques, on peut citer le développement de micro-machines-outils, l'étude de l'influence de la microstructure des pièces, l'étude des trajectoires de l'extrémité de la micro-fraise, l'analyse numérique et analytique de la formation d'un copeau segmenté, la modélisation de la rugosité de la surface usinée, par exemple par réseau de neurones ou la conception de bancs d'essais. Certains résultats importants obtenus durant ce travail sont: 1. Les différences de phases métalliques dans un matériau polycristallin multiphase affectent beaucoup le processus de micro-fraisage, induisant des variations dans les efforts de coupe et influençant la surface générée. 2. Pendant le processus de micro-fraisage, seule une seule arête coupe la matière. L'angle de l'arête θ et la direction d'avance ϕ sont importants pour réduire l'erreur d'usinage et pour répartir les efforts de coupe. 3. Le mécanisme de formation du copeau est étudié par une méthode hybride analytique-numérique. Les variations de la longueur de contact entre l'outil l_T et le copeau et de la longueur de la bande de cisaillement l_S sont les raisons principales qui expliquent l'apparition du copeau segmenté.